DEVELOPMENT OF DROP-BASED MICROFLUIDIC METHODS FOR HIGH-THROUGHPUT BIOLOGICAL ASSAYS

by

Geoffrey Kane Zath

A dissertation submitted in partial fulfillment
of the requirements for the degree

of

Doctor of Philosophy

in

Chemical Engineering

MONTANA STATE UNIVERSITY
Bozeman, Montana

April 2021

©COPYRIGHT

by

Geoffrey Kane Zath

2021

All Rights Reserved

DEDICATION

I dedicate this dissertation to my loving parents, Dr. Cynthia Kane and Greg Zath, who supported me throughout my time in graduate school. They always said “it” would get harder, and “it” finally did.

ACKNOWLEDGEMENTS

I would like to acknowledge my advisor Dr. Connie Chang for her support and guidance throughout my time at MSU. I am grateful for the help and support of my past and present lab mates; I could not have done this without you. Thank you, Betsey Pitts, for your assistance with all matters related to microscopy. I would also like to thank the Center for Biofilm Engineering and Dr. Anja Kunze for microscopy access and the Montana Microfabrication Facility for the use of photolithography equipment. Thank you also to my committee who helped guide me through the last year of graduate school. Finally, thank you to my friends in the Bozeman Ultimate Frisbee community who made my time outside of graduate school unforgettable.

This work was all made possible by funding provided by the Montana State University Office of the Provost, the Defense Advanced Research Projects Agency, and the National Science Foundation.

TABLE OF CONTENTS

1. INTRODUCTION 1

Background 1
Funding and Collaborations 2
Dissertation Overview 2

2. LITERATURE REVIEW 7

Literature Review Overview 7
Microfluidic PCR 8
Introduction 8
Quantitative PCR Methods 8
Overview 8
ddPCR 10
qPCR 11
Microfluidic PCR Device Design 12
Overview 12
Static Array 13
Continuous Flow 15
Electrowetting 19
Conclusion 20
Drop Surfactants 21
Introduction 21
Surfactant Requirements and Limitations 22
Emulsion Physics 24
Surfactant Developments 27
Conclusion 30
Transport Between Drops 31
Conclusion 37

3. RAPID PARALLEL GENERATION OF A FLUORESCENTLY BARCODED DROP LIBRARY FROM A MICROTITER PLATE USING THE PRESSURE COOKER CHIP 38

Manuscript Contributions of Authors 38
Manuscript Information Page 40
Abstract 41
Introduction 42
Materials and Methods 45
PCC Design 45
PCC Fabrication 45

TABLE OF CONTENTS CONTINUED

Pressure Chamber 46
Drop Encapsulation....47
Drop Measurements....50
Fluorescent Microbead Barcodes....51
Quantum Dot Barcodes....52
Two Channel Fluorescence Activated Drop Sorting....52
Results and Discussion....53
Drop Formation Characterization....53
Signal Discrimination in Barcoded Drop Libraries....56
Sample Isolation Using Fluorescence-Activated Drop Sorting....63
Conclusion....65
Conflicts of Interest....67
Acknowledgments....67

4. SCREENING OF ADDITIVE FORMULATIONS ENABLES OFF-CHIP DROP REVERSE TRANSCRIPTION QUANTITATIVE POLYMERASE CHAIN REACTION OF SINGLE INFLUENZA A VIRUS GENOMES....68

Manuscript Contributions of Authors....68
Manuscript Information Page....69
Abstract....70
Introduction....71
Experimental Section....75
Virus Strains and Cell Lines....75
PCR Sequences and Reaction Concentrations....75
In Vitro Transcribed RNA....76
Drop Encapsulation....76
Imaging of Drops....77
Analysis of Epifluorescence Images of Drops During OCD RT-qPCR Thermocycling....77
Analysis of Epifluorescence Images of Endpoint OCD RT-qPCR Drops....77
Imaging of Multiplexed OCD-qPCR Drops....78
Virus Infections....78
Results and Discussion....79
OCD RT-qPCR....79
Screening Additive Formulations....80
Dilution Series Verifies Efficiency of Drops Versus Bulk....84
Constructing Amplification Curves Using OCD RT-qPCR....87
Multiplexed OCD RT-qPCR Drop Detection of Target Genomes....90
Quantification of Influenza A Virus Genomes from Infected Cells....92

TABLE OF CONTENTS CONTINUED

Conclusion 93
Acknowledgments....95
Supporting Information....95
Notes 95

5. DROP QPCR ENABLED BY SIGMOIDAL CURVE FITTING USING PCR EFFICIENCY....96

Manuscript Contributions of Authors 96
Manuscript Information Page 97
Abstract....98
Introduction....99
Experimental Section....102
PCR Sequences and Reaction Concentrations....102
In Vitro Transcribed RNA 103
MYCN and Soybean qPCR Dataset 103
Microfluidic Device Fabrication....104
Drop Encapsulation....104
Drop Imaging....105
Drop Detection....105
Amplification Curve Library 106
SCFPE Drop Analysis....107
Results and Discussion 108
qPCR Analysis with SCFPE 108
Validation of SCFPE with Bulk qPCR Datasets....113
SCFPE Applied to Drops Collected at Various Thermocycles 115
M Gene Drop Mixture Measured with SCFPE....118
Conclusion 120
Acknowledgments....121
Supporting Information....121
Notes 121

6. DROP-BASED RT-QPCR REVEALS HIGHLY VARIABLE INFLUENZA A VIRAL BURST SIZE FROM SINGLE CELLS 122

Manuscript Contributions of Authors 122
Manuscript Information Page 123
Abstract....124
Significant Statement....125
Introduction....125
Results....128

TABLE OF CONTENTS CONTINUED

Single Cell RT-qPCR Using Drop-Based Microfluidics 128
Novel qPCR Analysis Using Amplification Curve Mapping 130
Heterogeneous Population of IAV RNA in Drops 134
Single Cell IAV Production Measured with Drop-Based RT-qPCR 135
Discussion 139
Material and Methods 140
Virus Strains and Cell Lines 140
Bulk Virus Infection 140
PCR Sequences and Reaction Concentrations 141
In Vitro Transcribed RNA 142
Sample Preparation for Bulk qPCR 142
Microfluidic Device Fabrication 143
Drop Encapsulation 144
Drop Processing for RT-qPCR 144
Drop Sampling and Imaging 145
Drop Detection 145
Amplification Curve Mapping for Infected Drops Experiments 146
Acknowledgements 147

7. CONCLUSIONS AND OUTLOOK 148

Conclusions 148
Outlook 152

APPENDICES 155

APPENDIX A: Supplemental Information for Chapter 3: Rapid Parallel Generation of a Fluorescently Barcoded Drop Library from a Microtiter Plate Using the Pressure Cooker Chip 156

PCC Fabrication 157
Microbead and Quantum Dot Barcode Label Combinations 159
PCC Drop Formation Characterization 161
Reynolds Number Calculation 161
Convert L_{drop} to V_{drop} 161
Barcoded Drop Detection 163
Discrimination of Discrete Signals in Barcoded Drop Libraries 166
Drop Library Clustering 166
Schottky Equation 166
Calculation of Noise 167

TABLE OF CONTENTS CONTINUED

APPENDIX B: Supplemental Information for Chapter 4: Screening of Additive Formulations Enables Off-Chip Drop Reverse Transcription Quantitative Polymerase Chain Reaction of Single Influenza A Virus Genome 169

Expanded Experimental Details 171
Microfluidic Device Fabrication 171
PCR Sequences and Reaction Concentrations 172
Imaging of Drops Containing PCR Additives 172
Analysis of Endpoint Epifluorescence Images of Drops Containing PCR Additives 173
Imaging of Drops During OCD-qPCR Thermocycling 173
Imaging of Multiplexed OCD-qPCR Drops 174

APPENDIX C: Supplemental Information for Chapter 5: Drop qPCR Enabled by Sigmoidal Curve Fitting Using PCR Efficiency 175

LME Results 178

APPENDIX D: Supplemental Information for Chapter 6: Drop-Based RT-qPCR Reveals Highly Variable Influenza A Viral Burst Size from Single Cells 179

Sigmoidal Curve Fitting Using PCR Efficiency (SCFPE) 180
Amplification Curve Library 182
Validation of Amplification Mapping Analysis with Bulk qPCR Datasets 183
MYCN and Soybean qPCR Datasets 185

APPENDIX E: DropSOAC: Stabilizing Microfluidic Drops for Time-Lapse Quantification of Single-Cell Bacterial Physiology 190

Manuscript Contributions of Authors 191
Manuscript Information Page 192
Image Processing and Analysis 193
Growth Heterogeneity of Pseudomonas Aeruginosa with Single Cells as Inocula 194
The DropSOAC Method Allows for Analysis of Single Cell Growth Kinetics and Quantification of Heterogeneity in Microbial Populations 197

TABLE OF CONTENTS CONTINUED

APPENDIX F: Image Analysis MATLAB Script for Measuring Drop Diameter and Multichannel Fluorescence 198

APPENDIX G: Statistics Based Model for Tracking the Loading of Cells and Virus while Passaging with the Evolution Chip 202
Introduction.....203
Objective: Develop a Drop-Based Microfluidic Platform for the Continual Passaging of MDCK Cells and Influenza Virus in Drops.....205
Preliminary Results.....206
Evolution Chip Drop Loading Model.....206
Initial test of the evolution chip 209
Task 1: Poisson Statistics-Based Cell/Virus Drop Loading Model.....210
Introduction.....211
Task 2: MDCK Cell and Influenza Virus Passaging Study in Drops

APPENDIX H: MATLAB Script for Counting Fluorescent Particles Contained in Drops from Raw Time Trace Detection Data 212

APPENDIX I: Model for Simulating Drop Detection Data 215

APPENDIX J: Model for Predicting the Coalescence Events of Drops.....218

REFERENCES CITED.....221

LIST OF TABLES

Chapter.Table Page

A.1 Green and red microbead barcode concentration combinations 159

A.2 QD625 and QD705 quantum dot barcode concentration combinations 160

B.1 Supplemental data table for Figure 4.2B and 4.2C 170

B.2 Supplemental data table for endpoint analysis Figure 4.3E and 4.5D 170

C.1 SCFPE fitting parameters for Figure 5.1.....176

C.2 SCFPE cycle offset performance 176

C.3 SCFPE cycle conversion performance.....177

C.4 Comparison of single M gene drop populations to GMM fitted distributions.....177

D.1 SCFPE fitting parameters for Figure D.4.....185

D.2 Amplification curve mapping cycle offset performance.....186

D.3 Amplification curve mapping cycle conversion performance 186

LIST OF FIGURES

Chapter.Figure Page

2.1 PCR Amplification of DNA....9

2.2 Instrument schematic for real-time PCR in picoliter droplets....15

2.3 Examples of continuous flow thermal cycling devices....17

2.4 Schematic of a continuous flow PCR device depicting....18

2.5 Images of an electrowetting RT-qPCR device....20

2.6 Role of surfactant micelles in the transport between drops in the case of Ostwald ripening....26

2.7 Dye leakage experiments with F-SiO_2 NP and EA surfactant stabilized drops....30

2.8 Dye diffusion model schematic....34

2.9 Temporal evolution of the signal-to-noise ratio (SNR)....34

2.10 Diffusion time scales in drops....35

2.11 Effect of CMC on diffusion between drops....36

3.1 PCC design and assembly....46

3.2 PCC operation and barcoded drop library production....49

3.3 Characterization of drop sizes produced by the PCC....56

3.4 Analysis of microbead and QD barcoded drop libraries....62

3.5 Fluorescence activated drop sorting of a microbead-barcoded drop library....64

4.1 Off-Chip Drop Reverse Transcription qPCR (OCD RT-qPCR)....79

4.2 Screening of drop additives for PCR....82

4.3 Dilution series of in vitro transcribed IAV M gene in bulk and in drops....85

LIST OF FIGURES CONTINUED

Chapter.Figure Page

4.4 OCD RT-qPCR amplification curves compared to standard qPCR curves 88

4.5 Multiplexed endpoint OCD RT-qPCR detection of target genomes 91

5.1 SCF and SCFPE methods applied to the M gene dilution series amplification curves 111

5.2 Construction of the amplification curve library 112

5.3 Method comparison for bulk M gene, MYCN gene, and soybean gene qPCR datasets 115

5.4 SCFPE conversion applied to drop data 117

5.5 Mixture of M gene drop populations 119

6.1 Workflow for RT-qPCR of IAV from single cells 130

6.2 Homogeneous distributions of RNA measured with drop-based RT-qPCR analysis using amplification curve mapping 133

6.3 Heterogeneous distributions of IAV M gene RNA in drops 135

6.4 Single cell burst size measured with drop-based RT-qPCR for H3N2 and H1N1 138

A.1 Standard curve relating volumetric flowrate ratio to pressure ratio during PCC operation 162

A.2 Confocal image of fluorescent blue, green, and red microbeads in drops 164

A.3 Re-injection of barcoded drops into a detection chip 164

A.4 Schematic of the drop detection process 165

A.5 Manual segmentation, or grouping, of barcoded drop library data 168

A.6 Standard curves of the mean fluorescence intensity versus the concentration of microbeads or quantum dots in drops 168

LIST OF FIGURES CONTINUED

Chapter.Figure Page

B.1 Drops at the exit of a drop making device 170

B.1 Mean normalized background fluorescence intensity for each PCR additive condition 171

C.1 Close up comparison of SCFPE and SCF fits 178

D.1 Cell loading measurements 187

D.2 β-actin released from cells as measured by bulk RT-qPCR 187

D.3 Example of β-actin filtering of burst size data 188

D.4 SCF and SCFPE methods applied to the M gene dilution series amplification curves 188

D.5 Zoomed in comparison of SCFPE and SCF fits to bulk qPCR data 189

D.6 Method comparison for bulk M gene, MYCN gene, and soybean gene qPCR datasets 189

E.1 Summary of *P. aeruginosa* PAO1 and Δ*hpf* growth resuscitation studies 195

F.1 Circle Hough Transform schematic 200

F.2 Image analysis of PCR drops post-thermocycling 200

F.3 Image analysis of drops containing GFP expressing *E. coli* 201

G.1 High-speed video capture of drop merging on the evolution chip 206

G.2 Modeled viral load in drops 208

G.3 Relationship between bulk and drop MOI 208

G.4 Comparison of data obtained from the evolution chip, bulk passaging, and model predictions 210

G.5 Process flow of the Poisson statistics-based model at the device level and drop level for cell and virus loading in drops 211

LIST OF FIGURES CONTINUED

Chapter.Figure Page

H.1 Counting fluorescent particles in drops from time trace data 214

I.1 Simulated data of drops containing fluorescent particles 217

I.2 Fluorescence measurements of red fluorescent microbeads in drops.....217

J.1 Schematic of the coalescence cascade model.....220

J.2 Comparison of measured and modeled drop volume after coalescence 220

ABSTRACT

Drop-based microfluidics allows single-cell biological assays to be performed by encapsulating samples in picoliter scale drops. Adapting biological assays to drop-based microfluidics requires novel approaches to meet the method requirements of each assay. For example, microtiter plates are a common tool for storing many unique samples in some assays. An equivalent strategy for drops involves labeling samples with a barcode prior to drop encapsulation and storing the barcoded drops in a single mixture, thereby creating a drop library. Other assay adaptions, such as drop-based reverse transcription quantitative polymerase chain reaction (RT-qPCR) require that drops be stabilized during the high temperatures used for thermal cycling. Drop-based RT-qPCR is useful for studying single-cell dynamics in drops, such as influenza A virus (IAV) infection. Conventional methods for measuring IAV output from individual cells are labor intensive and low-throughput. Thus, there is a need to adapt RT-qPCR to drop-based microfluidics for the purpose of high-throughput single cell analysis of infected cells.

The research presented here focuses on the characterization of the Pressure Cooker Chip (PCC) to rapidly encapsulate drop libraries and the development of a drop-based RT-qPCR method to measure IAV output from infected cells. The PCC was used to make drop libraries by rapidly generating drops of up to 96 different conditions in parallel by interfacing individual drop makers with a standard microtiter well plate. The drop library was optically barcoded using a two-color combination of fluorescent microbeads or quantum dots with 24 or 192 unique combinations, respectively. To adapt RT-qPCR in drops, known PCR additives were systematically tested to optimize drop stability and limit dye diffusion during thermocycling. A novel qPCR data analysis method was developed to convert drop fluorescence data collected at a single thermocycle to an initial RNA template concentration. Together, the additive screening and novel qPCR data analsyis method enabled the use of drop-based RT-qPCR to quantify the highly heterogeneous IAV burst size from single cells in thousands of drops. Our method is the first to measure single cell IAV burst size using a high-throughput, drop-based RT-qPCR assay.

CHAPTER ONE

INTRODUCTION

Background

The research presented in this thesis contributes to the understanding of adapting biological assays for drop-based microfluidic applications. The thesis is focused on the characterization of a novel 3D device design for rapid encapsulation of drop libraries and the development of a drop-based reverse transcription quantitative polymerase chain reaction (RT-qPCR) method to measure influenza A virus (IAV) output from infected cells. Drop-based microfluidics allows single-cell biological assays to be performed at kilohertz rates by encapsulating samples in pico- to nanoliter sized drops, providing an isolated microenvironment. Part of this thesis is focused on the development of a novel 3D device design for rapidly encapsulating drop libraries. By labeling samples with a barcode prior to drop encapsulation, a drop library is created and composed of an array of sample conditions. A drop library allows for performing multiplexed biological assays or screening a chemical library in parallel, compared to serial processing done with current drop-based microfluidic methods. Adapting biological assays to drops requires novel approaches to ensure drops can withstand the requirements of the assay. For example, developing a drop-based RT-qPCR assay requires that drops be stabilized during the high temperatures used for thermocycling and new analysis methods for the data collected during the assay.

Drop-based RT-qPCR is an attractive method for studying the infection dynamics of IAV at the single-cell level. IAV is notorious for causing seasonal epidemics and sporadic worldwide

pandemics that have resulted in over 100 million deaths during the past century. Understanding how IAV interacts with its host cells is typically performed using tissue culture systems or with animal models. These systems provide bulk measurements of virus production and/or cellular responses, such as interferon activation and production. However, individual cells exist as a heterogeneous population, resulting in cell-to-cell differences in virus production and antiviral responses. Conventional methods for measuring the antiviral response in individual cells during IAV infection are labor intensive, incur high reagent costs, and require extensive serial dilutions to isolate singularly infected cells. Thus, there is a need for high-throughput analysis of single cells to elucidate individual host-cell dynamics. Adapting RT-qPCR into drops for the purpose of measuring IAV output at the single-cell level is the primary focus of the chapters presented in this thesis.

Funding and Collaborations

This research was funded by the Montana State University Office of the Provost, Defense Advanced Research Projects Agency (DARPA) grant W911NF-17-2-0034, and National Science Foundation (NSF) CAREER Grant 1753352. The research was conducted at the Center for Biofilm Engineering (CBE) at Montana State University (MSU) (Montana, USA) with IAV studies in collaboration with the Brooke Lab at University of Illinois at Urbana-Champaign (UIUC) (Illinois, USA).

Dissertation Overview

The remainder of this thesis is organized into six chapters; Chapter 2 is comprised of a literature review providing a summary of PCR applications performed in drops such as droplet

digital PCR (ddPCR) and drop-based qPCR. In addition, the biocompatible surfactants used to stabilize drops and the significance of transport of small molecules is discussed in relation to PCR. Since applications such as ddPCR and drop-based qPCR rely on reporter dyes and heating drops up to 98 °C, maintaining stable drops that do not transport dye between them during thermocycling is critical to drop-based PCR.

Chapter 3 describes the design, fabrication, and characterization of the PCC. A novel 3D device design intended to integrate directly with a standard microtiter well plate. A detailed description of the fabrication and operation of the PCC is included. The PCC was used to rapidly encapsulate up to 192 fluorescently barcoded samples in parallel to create a drop library. The use of fluorescent microbeads and quantum dots to create 24 and 192 barcode labels in the drop library, respectively, is discussed. The latter of which is to our knowledge the highest number of two-color barcode labels to be produced in drops. A comprehensive analysis of drop formation on the PCC led to fitting a drop scaling law, providing a useful tool for tuning the drop diameter based on inlet pressures. Drop libraries created with the PCC will enable multiplexed screening of fluorescence-based assays with a streamlined workflow requiring only a single microfluidic device to encapsulate drops. The journal article is titled "*Rapid Parallel Generation of a Fluorescently Barcoded Drop Library from a Microtiter Plate Using the Pressure Cooker Chip*" and is being prepared for submission to the peer-reviewed journal Lab on a Chip.

Chapter 4 describes a method we call Off-Chip Drop Reverse Transcription quantitative (OCD RT-qPCR) in which drops are thermocycled in a qPCR machine and sampled at various cycle numbers "off-chip", or outside of a microfluidic chip. To adapt RT-qPCR in drops, we first systematically tested known PCR additives to optimize stability and limit dye diffusion during

OCD RT-qPCR. We discovered that an optimal combination of Tween 20 / betaine / BSA is necessary to stabilize drops for amplification of the M gene of influenza A virus (IAV). To demonstrate the utility of our method for droplet RT-qPCR, we tested a wide range of both *in vitro* transcribed viral RNA and viral supernatant from infected cells in drops and showed that our systematic additive testing provided a viable and accurate method for measuring IAV, even down to a single viral genome per drop. The droplet assays were processed using a traditional RT-qPCR machine to measure the overall drop fluorescence during thermocycling. Additionally, we used epifluorescence microscopy to analyze individual drops at various thermocycles in a high throughput manner, aspects that are not possible on a traditional qPCR machine. The amplification curves constructed from the image data correlated well with those from the qPCR machine, indicating quantitative analysis of the drop data may be possible using a variation of current qPCR analysis techniques. This will have impact on future work in single cell virology using drop-based microfluidics for measuring viral output at the single cell level. The journal article is titled "*Screening of Additive Formulations Enables Off-Chip Drop Reverse Transcription Quantitative Polymerase Chain Reaction of Single Influenza A Virus Genomes*" and is published in the peer-reviewed journal Analytical Chemistry, Volume 93, Issue 10.

Chapter 5 describes a novel qPCR data analysis pipeline that was developed to convert drop fluorescence data collected with the OCD RT-qPCR method described in Chapter 4. We call this method Sigmoidal Curve Fitting using PCR Efficiency (SCFPE). Our approach used PCR kinetics modeling and curve fitting to construct an amplification curve library from randomly sampled fluorescence measurements at various thermocycles. The amplification curve library is then used to convert fluorescence measurements collected at individual thermocycles,

thereby removing the need to measure samples at every cycle. We show the analysis technique provides accurate estimations of starting template concentration from 96-well plate measurements on a bench-top qPCR machine and measurements made with our OCD RT-qPCR method. For drop-based experiments, this technique enables the measurement of RNA contained within thousands of individual drops without the need for a custom qPCR device. Furthermore, this technique will enable future high-throughput single cell studies in drops. The journal article is titled "*Drop qPCR Enabled by Sigmoidal Curve Fitting Using PCR Efficiency*" and is being prepared for submission to the peer-reviewed journal Analytical Chemistry.

Chapter 6 describes the application of a novel drop-based RT-qPCR method to measure the amount of influenza A virus (IAV) released from individually infected cells encapsulated in drops. This method utilizes drop-based microfluidics to encapsulate infected cells within picoliter sized drops, thereby ensuring the released virus is contained within each drop. Single cell burst size distributions of IAV H1N1 and H3N2 are measured from $\approx 10^4$ infected human alveolar epithelial (A549) cells. The burst size, or amount of released virus, was found to be highly heterogeneous, spanning four orders of magnitude. Our method is the first to measure IAV burst size using a high-throughput drop-based assay and will allow for future work in investigating the heterogeneity of IAV and other viral infections. The journal article is titled "*Drop-Based RT-qPCR Reveals Highly Variable Influenza A Viral Burst Size from Single Cells*" and is being prepared for submission to the peer-reviewed journal PNAS.

Appendices A-D provide supplemental information for the manuscripts in Chapters 3-6. Appendices E-J contain additional work completed during this PhD that do not fit into the manuscripts presented in this thesis. Additional work contained in the appendices include: image

analysis work done for the publication "*DropSOAC: Stabilizing Microfluidic Drops for Time-Lapse Quantification of Single-Cell Bacterial Physiology*" by Pratt et al. and published in the peer reviewed journal Frontiers of Microbiology, Volume 10, Article 2112 (Appendix E); an image analysis script written in MATLAB for measuring drop diameters and drop fluorescence across multiple image channels (Appendix F); a statistics-based model written in MATLAB for the loading of cells and virus over multiple passages with the Evolution Chip (Appendix G); a script written in MATLAB for counting fluorescent particles contained in drops from raw time trace data collected from our high speed drop detection platform (Appendix H); a MATLAB model for simulating drop detection data (Appendix I); and finally a MATLAB model for predicting the coalescence events of drops (Appendix J).

CHAPTER TWO

LITERATURE REVIEW

Literature Review Overview

Drop-based microfluidics allows biochemical assays to be performed at high-throughput by encapsulating samples in pico- to nanoliter sized drops. By reducing the reaction volume, samples can be processed and measured at kilohertz rates. Adapting biochemical assays for microfluidic drop systems presents an engineering challenge which requires knowledge of the underlying mechanics of drop systems. The better these concepts are understood, the better we can design a drop-based assay to match, or even outperform, the current bulk assay offerings. Generally, there are three important components to consider when designing a drop-based biochemical assay: microfluidic workflow, drop stability, and transport between drops. A biochemical assay which involves all three of these components is PCR, a common laboratory technique which amplifies DNA from an initial template of RNA or DNA. Adapting PCR for drops requires special hardware to quickly thermocycle drops up to temperatures reaching 98°C and depending on the application, provide fluorescence measurement capabilities. Such temperatures require special consideration for maintaining stable drops as common drop surfactants[1] are designed around drops stored at lower, biologically relevant temperatures (e.g. 37 °C). Additionally, many PCR applications require multiple fluorophores to be measured for quantification purposes and remain contained in each drop throughout the thermocycling process. The following sections provide a review of recent studies involving microfluidic PCR applications, drop surfactants, and transport between drops.

Microfluidic PCR

Introduction

With the advent of microfluidics came the promise of improved biological assays through compartmentalization, reducing reagent costs and increasing sample throughput. One of these biological assays to be adapted to microfluidics was polymerase chain reaction (PCR). Since the first example of quantitative PCR (qPCR) in picoliter sized drops,[2] PCR has been used for a range of biological studies on microfluidic devices including a variety of viruses,[2-6] bacterial cells,[7-12] and mammalian cells.[13-18] By adapting PCR to microfluidics, reaction throughput is greatly increased using either flow-based screening of drops or through the parallelization of reactions in microwells or drops. However, adapting a traditional benchtop assay to the microscale has proven difficult. Simple steps such as washing and mixing now require complex device designs[14, 16, 17] while novel microfluidic thermal cyclers have been developed[3, 4, 8, 19] to allow for on-chip PCR analysis. A few of these innovations have led to commercial offerings such as the BioRad QX200 ddPCR system and the Fluidigm Biomark HD single cell qPCR system. Here, an overview of quantitative PCR methods and how they have been adapted to microfluidic systems is presented.

Quantitative PCR Methods

Overview. Quantitative PCR methods rely on thermal cycling to produce copies of target DNA in large enough quantities to be detected with fluorescent probes. If the target of interest is RNA, an initial reverses transcriptase step is required to form complimentary DNA. Thermal cycling involves two steps: first, in the high temperature denaturing step (94-98 °C), DNA is melted to separate the DNA double helix; second, in the low temperature annealing/extension

step (50-65 °C), a primer that has been designed to be complimentary to the target DNA binds to it and creates a template for DNA polymerase (Figure 2.1). A heat-stable DNA polymerase, such as Taq-polymerase, is then used to enzymatically assemble a new DNA strand. This new strand of DNA acts as a template for the next round of thermal cycling, allowing for exponential amplification of the starting DNA. Incorporating a fluorescent probe in the PCR mix can provide quantification through endpoint or continuous cycle imaging/detection of the fluorescence, depending on the methods outlined below. The two primary probe types are SYBR and TaqMan and both result in an increase in fluorescence after each thermal cycle. SYBR dye is non-specific and will intercalate into double stranded DNA while TaqMan probes bind to a specific DNA sequence and are cleaved off during the extension step, thereby releasing a fluorophore.

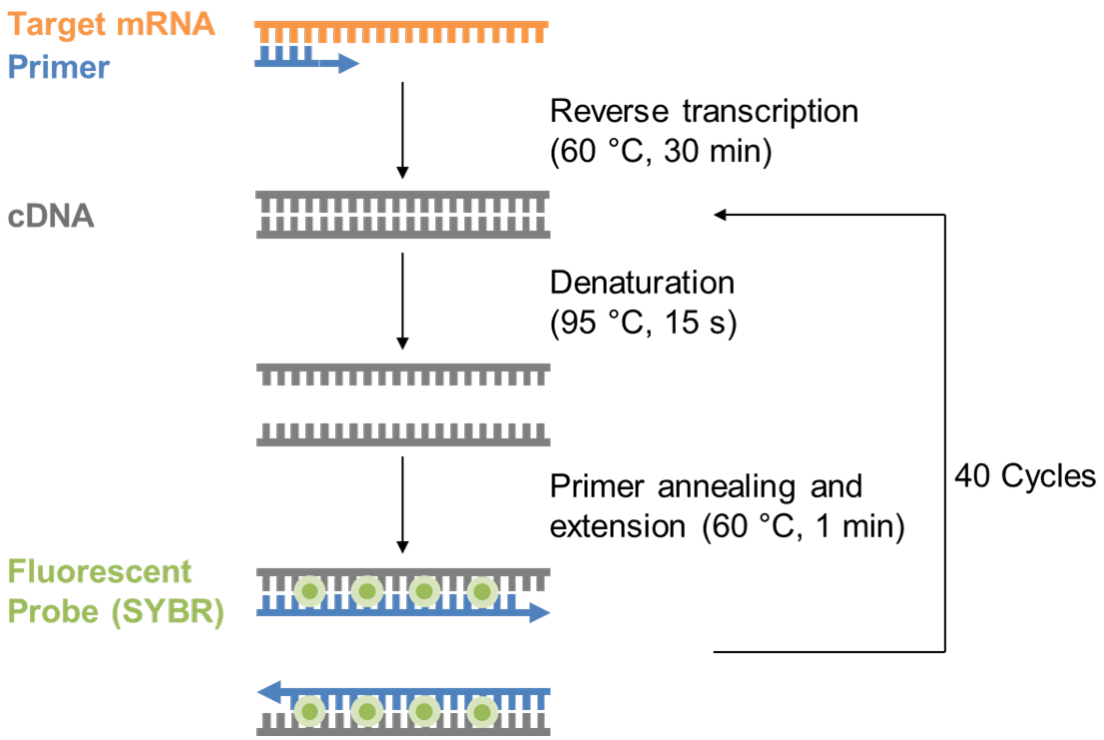


Figure 2.1. PCR amplification of DNA with thermal cycling. RNA requires an additional reverse transcription step to create complimentary DNA (cDNA). A probe such as SYBR will intercalate into double stranded DNA during the extension step and can be measured via fluorescence imaging.

ddPCR. Droplet digital PCR (ddPCR) provides absolute quantification of RNA/DNA without the need for a standard curve by relying on the digital counting of amplifying drops. A dilution series with target RNA/DNA is encapsulated into microscale drops, generally 10-100 μm in diameter, with PCR reagents and a fluorescent probe and then thermal cycled. An end-point measurement of the drop fluorescence is performed either with standard fluorescence microscopy or flow-based detection methods.[20] The counts of bright "positive" drops and dim "negative" drops for each dilution are then fit to a Poisson distribution to calculate the starting concentration of target RNA/DNA. Samples containing the target RNA/DNA are diluted to point in which some drops contain zero RNA/DNA molecules (negative) while the remaining drops contain at least one RNA/DNA molecule (positive). Because of this digital loading, ddPCR provides absolute quantification without the need for a standard curve. As an added benefit, ddPCR is less sensitive to the diffusion of fluorescent probes as it only requires the signal-to-noise ratio (SNR) between positive and negative drops be large enough for a clear distinction.

While the detection of drops for ddPCR is high-throughput at kilohertz rates, sample throughput is relatively slow due to the need for multiple dilutions to be made and detected for a single sample. Multiple dilutions of an unknown sample are required to ensure at least one dilution contains a mixture of positive and negative drops. Additionally, only bulk samples can be analyzed due to the need for a large quantity of drops to be encapsulated from a single sample (i.e. ddPCR cannot be performed on a single drop). For example, $\approx 10^4$ drops, 1 nL in volume, can achieve a dynamic range for absolute quantification spanning from a single copy to ≈100,000 copies.[21] The detection limit of ddPCR is sensitive to background amplification and may limit the ability to detect rare mutants from a background wildtype.[22]

qPCR. Quantitative, or real-time, PCR (qPCR) is based on the principle that PCR amplification is in an exponential growth phase at early thermal cycles before reagents are diminished. This exponential growth phase equates to a reaction efficiency of 100% where at every cycle all DNA is multiplied by a factor of two. By adding a fluorescent probe, a fluorescence threshold can be set in the region of exponential amplification and when a target passes this threshold, a cycle threshold (*Ct*) value is recorded. In this manner, commercial systems using 96-well plate reaction volumes achieve a resolution down to a 1.5-fold change and a dynamic range of ten logs of input template (QuantStudio real time PCR systems, Applied Biosystems). qPCR requires the continuous fluorescence measurement of each well to capture the moment it crosses the threshold. A dilutions series of a known quantity of target RNA/DNA is first required to create a standard curve to relate *Ct* values to RNA/DNA concentration. When *Ct* is plotted against the log of target concentration, the ideal slope is -3.33 cycles per log10(RNA/DNA), relating to a PCR efficiency of 100%. An ideal PCR efficiency is between 90-110%.[23, 24] A PCR efficiency outside of the ideal range will have limited resolution and dynamic range.

Adapting qPCR to microscale wells or drops on a microfluidic device has the potential to provide quantitative measurements of single cells with detection limits down to single copies of RNA/DNA. However, progress on this technology has a few hurdles to overcome. First, developing a device for the continuous imaging/detection of wells or drops requires the fabrication of complex devices with intricate valve systems[16, 17] or fiber optic detection schemes[15, 25] to name a few. However, it may be possible to bypass the need for continuous fluorescence measurements by using PCR kinetics modeling[26] and/or curve fitting[27] to construct

amplification curves from discontinuous fluorescence measurements. By removing the need to track individual wells or drops at every thermal cycle, many more reaction vessels can be imaged/detected. For example, as presented in Chapters 4-6, drops can be pooled from a single cycle and measured off-chip using either epifluorescence microscopy or flow-based fluorescence detection. Second, a benefit of qPCR is that quantification can be done from a single reaction in a well or drop and does not require a large quantity of drops like ddPCR. Because of this, qPCR can be used for single cell measurements. Performing single cell measurements in a well or drop may require additional steps to wash cells[16, 17] and to add PCR reagents.[14, 16, 17, 28] Recent work has implemented these steps using intricate valve systems[16, 17] or the splitting and merging of drops.[14, 28]

Microfluidic PCR Device Design

Overview. Microfluidic PCR device designs can be categorized by how a sample is processed for thermal cycling and fluorescence measurements. These designs include static array, continuous flow, and electrowetting. Static arrays vary from simple to complex in nature and can generally be imaged with a traditional epifluorescence optical path as drops, or wells, and remain static on the thermal cycling platform. Continuous flow designs consist of multiple heating zones whereby drops flow across in a zig-zag like pattern to create thermal cycles and can be done at high-throughput. Electrowetting devices have very low sample throughput but can directly control the reaction volume in the form of a drop, allowing the device to move the drop across thermal cycling and imaging zones via electrowetting. Each of these designs are viable for adapting PCR to a microfluidic platform depending on the following design constraints: sample resolution (static array), throughput (continuous flow), and control (electrowetting).

Static Array. Microfluidic devices employing a static array for thermal cycling and fluorescence measurement are the most diverse. They can perform ddPCR and qPCR in either wells or drops and have been used in a wide range of applications from measuring viral RNA to cellular DNA.[2, 6, 9-11, 16-18, 29] Thermal cycling is generally performed in the same manner across devices with a thermal electric cooler (TEC), allowing for fast temperature changes. Fluorescence measurement methods can range from custom built widefield imaging platforms[11, 16-18] to standard epifluorescence microscopy[2, 6, 9, 10, 29]. Device complexity can also vary, with well-based approaches employing complex valve systems[10, 16, 17] to administer various reagents such as heat lysis buffer or PCR mix in a controlled manner, or simpler drop-based systems[2, 6, 9, 11, 18, 29] where reagents are mixed in bulk and then encapsulated in drops to be placed on the static array. Regardless of the design strategy, static arrays provide the highest resolution (spatial and/or temporal) as the same drops or wells are imaged continuously, usually with a sensitive, high resolution camera. However, their throughput is limited by the areal density of drops and wells on the array and/or the number of field of views (FOV) that can be imaged at one time.

An example of a static array device, as presented in Hatch et al. (2011), used ddPCR and a 1-million drop array to measure chlamydia DNA in 50 pL drops.[11] They were able to achieve a wider dynamic range by using a 100-fold increase in drop count compared to other ddPCR systems. A detection limit of 10 copies/50 µL reaction was achieved with a ceiling of 100,000 copies/50 µL reaction. Imaging of these drops was achieved with a low-cost, high resolution DSLR camera as ddPCR requires only that drops be “on” or “off” and this was achievable with a consumer grade camera. The first application of qPCR on a static array microfluidic device was developed by Beer et al. to measure the DNA virus vaccinia in 70 pL drops.[2] An off-chip valve

system was used to encapsulate PCR reagents and viral DNA into drops and transport them to the thermal cycling chip where they were stored (Figure 2.2). They achieved a detection limit of 1 pfu/drop yet with a PCR efficiency of only 81%. Sample throughput was low at <100 drops per run, yet the application was promising as a proof of concept. Improvements were made to this concept by White et al. who developed a well-based device to measure miRNA expression in K562 cells with qRT-PCR with fully integrated control of cell lysis and PCR reagent injection.[16] The device contained 300 reaction wells (50 nL) with the ability to split different samples across 6 lanes. They achieved a detection limit of 10 fg/well (single copy amplification) of purified RNA from K562 cells and a PCR efficiency of 101%. The microfluidic device maintained a linear *Ct* curve for two orders of magnitude lower than when ran in bulk. The device was later improved upon by VanInsberghe et al. to allow multiplexing of up to 10 different conditions (i.e. PCR primers and/or probes).[17]

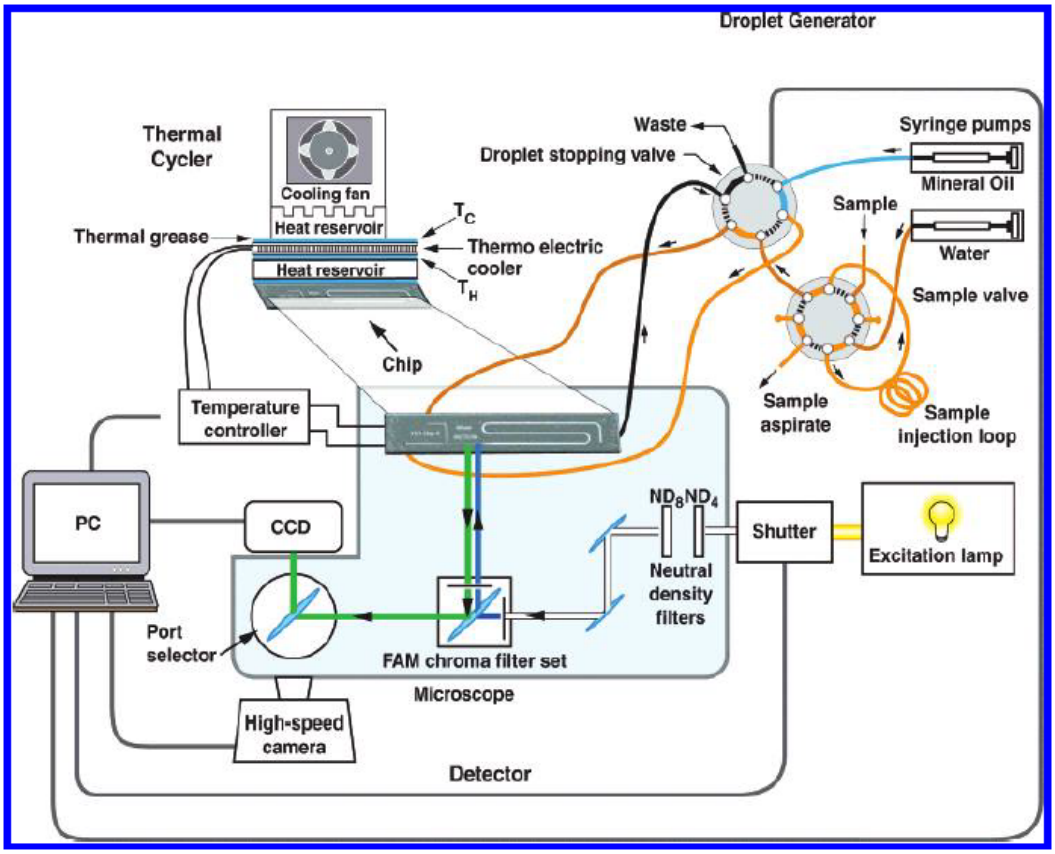


Figure 2.2. Instrument schematic for real-time PCR in picoliter droplets. An integrated droplet generator, thermal cycler, and fluorescence detector are included. Drops are first generated and then stored on-chip where they are kept stationary and thermal cycled with real time fluorescence detection. Reprinted with permission from Beer, N. R.; Hindson, B. J.; Wheeler, E. K.; Hall, S. B.; Rose, K. A.; Kennedy, I. M.; Colston, B. W., "On-Chip, Real-Time, Single-Copy Polymerase Chain Reaction in Picoliter Droplets." *Analytical Chemistry* 2007, 79 (22), 8471-8475.[2] Copyright 2007 American Chemical Society.

Continuous Flow. Continuous flow microfluidic devices were initially used for high-throughput thermal cycling of drops (Figure 2.3) with end-point detection of fluorescence or gel analysis.[3, 19] Instead of relying on a TEC to control thermal cycling, inexpensive resistive heating elements could be placed on a device and the flow of drops back and forth across them would create a thermal cycle.[3, 12, 13, 15, 19, 25, 30] However, while this allows for the continuous thermal cycling of drops and downstream fluorescence detection, the geometry of the device restricts the ability to adjust thermal cycling profiles as the denaturing step and annealing/extension step are

linked by the residence time ratio for those heating zones. If the application requires an endpoint measurement only, like ddPCR, then this limitation can be avoided by simply collecting drops off-chip and thermal cycling them on a benchtop thermal cycler.[14, 21, 31, 32] Continuous flow devices are a good match for ddPCR as the high-throughput nature allows for the fluorescence detection of the large quantity of drops needed for absolute quantification.[21] These systems require custom built equipment for laser induced fluorescence (LIF) detection with photomultiplier tubes (PMT). While PMTs allow for high-speed measurements at kilohertz rates, exposure times to the excitation laser are very low (≈1 ms) due to the fast-moving drops which may lead to a lower SNR when compared to static array methods. This is not necessarily a limitation for ddPCR as commercial units employ this method (e.g. BioRad QX200); however, for qPCR where relative fluorescence measurements between drops is critical, this can drastically reduce throughput. In addition, qPCR requires each drop be continuously tracked cycle to cycle which increases the complexity of the fluorescence detection system.[15, 25, 30] There is potential for curve fitting models[27, 33-35] based on PCR kinetics to assist in linking discontinuous drop fluorescence measurements together and breaking the bandwidth barrier between resolution and throughput. This subject is further discussed in Chapters 4 and 5.

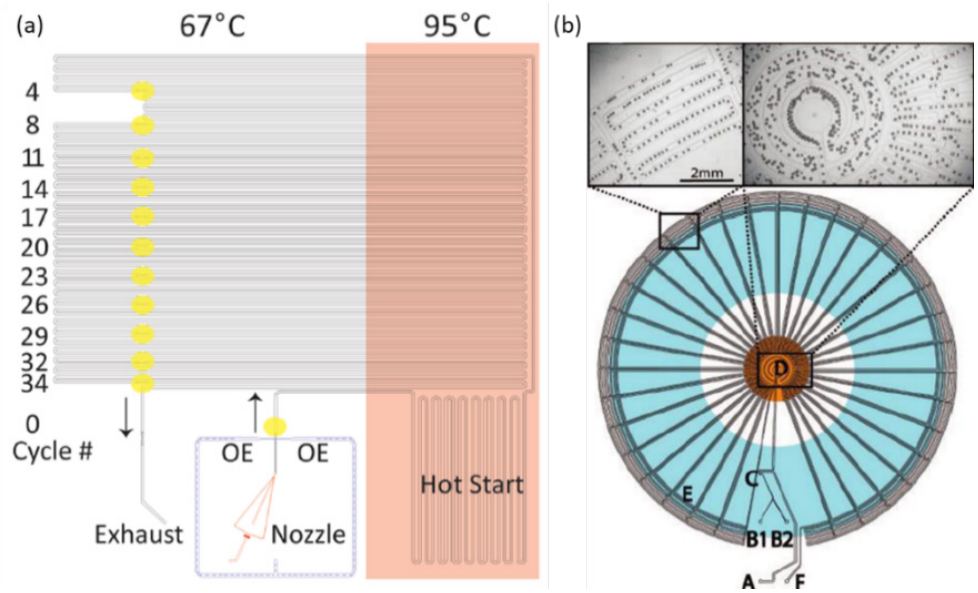


Figure 2.3. Examples of continuous flow thermal cycling devices. (a) Kiss et al. linear design. Pink-shaded regions were heated at 95°C and non-shaded regions were heated at 67°C. The highlighted yellow regions correspond to the interrogation neckdowns with the corresponding cycle numbers shown on the left. Adapted with permission from Kiss, M. M.; Ortoleva-Donnelly, L.; Beer, N. R.; Warner, J.; Bailey, C. G.; Colston, B. W.; Rothberg, J. M.; Link, D. R.; Leamon, J. H., "High-throughput quantitative polymerase chain reaction in picoliter droplets." *Analytical chemistry* 2008, 80 (23), 8975-8981.[3] Copyright 2008 American Chemical Society. (b) Schaerli et al. radial device. The device contains an oil inlet (A) that joins two aqueous inlet channels (B1 and B2) to form droplets at a T-junction (C). The droplets pass through the inner circles in the hot zone (D) for template denaturing and then travel on to the periphery where primer annealing and template extension occur (E). Finally, the droplets exit the device after 34 cycles in the radial device (F). Adapted with permission from Schaerli, Y.; Wootton, R. C.; Robinson, T.; Stein, V.; Dunsby, C.; Neil, M. A.; French, P. M.; DeMello, A. J.; Abell, C.; Hollfelder, F., "Continuous-flow polymerase chain reaction of single-copy DNA in microfluidic microdroplets." *Analytical chemistry* 2008, 81 (1), 302-306.[19] Copyright 2008 American Chemical Society.

Kiss et al., in collaboration with Raindance Technologies (Lexington, MA), presented one of the first applications of ddPCR with a continuous flow design (see Figure 2.3a above). The device contained heating zones for thermal cycling and interrogation neckdown regions at various cycles for fluorescence detection. A full PCR run took 35 minutes and endpoint ddPCR measurements showed the method was sensitive down to one adenovirus copy per 167 drops. While the neckdown regions would have allowed for collecting qPCR data, the drop detection

would not have been continuous cycle to cycle and may explain why they did not explore this capability. Hatch et al. (2014) developed a continuous flow device for qPCR with multi-channel fluorescence detection and the capability to track individual drops (Figure 2.4). Drop encapsulation (0.1 to 10 μL), thermal cycling, and detection were integrated into a single system. Tracking allowed for the formation of amplification curves for each drop but limited the throughput to <10 Hz as drops had to flow serially in the tubing (plug drop flow). They were able to detect a seven orders of magnitude range of DNA concentrations from an environmental sample with a PCR efficiency of 104%. Hindson et al., in collaboration with Bio-Rad Laboratories (Pleasanton, CA), presented one of the first commercial ddPCR systems that achieves continuous, high-throughput detection of 2 million PCR reactions in 1 nL drops with a 96-well plate workflow. Their automated detection system processed 32 wells per hour with the capability to read two colors allowing for multiplexing with TaqMan based assays. The massive partitioning of ddPCR allowed them to detected mutant DNA in a 10^5-fold excess of wildtype background.

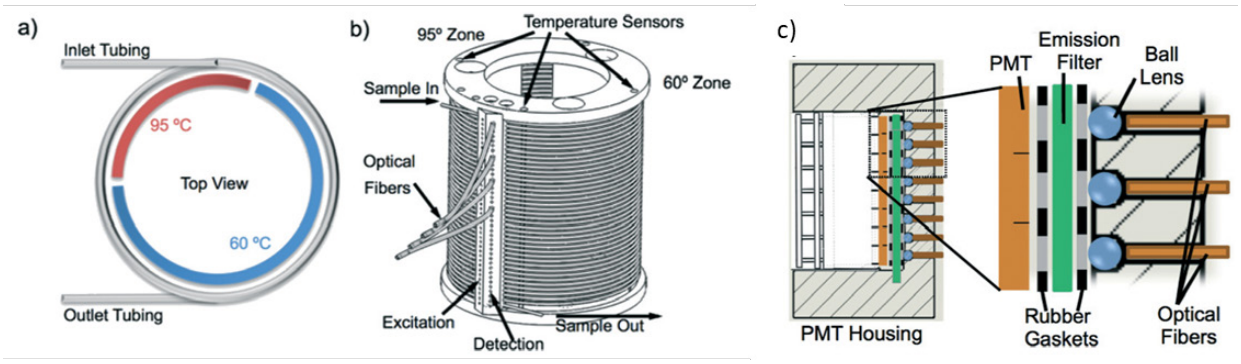


Figure 2.4. Schematic of a continuous flow PCR device depicting: (a) the temperature profile; (b) the two-zone thermocycler, tubing, temperature sensors, optical fiber coupling, and inlet and outlet ports; and (c) schematic of the multichannel LED excitation block. Adapted from Ref. 25 with permission from the Royal Society of Chemistry.[25]

Electrowetting. Electrowetting incorporates design concepts from both static array and continuous flow devices and can be used for ddPCR and qPCR applications.[4, 5, 7, 8] PCR drops suspended in oil remain stationary during each heating step and then are moved via electrowetting with electrodes patterned onto the device to complete the thermal cycle (Figure 2.5). Due to the complexity of this design however, current device throughput Is currently limited to <10 drops per PCR run.[5] Yet with the ability to directly prepare a liquid sample on the device,[8] mix additional reagents,[4, 5] and integrate camera arrays for fluorescence measurements,[7] electrowetting devices have great potential as point-of-care devices requiring very low sample volumes (<10 μL). One application of interest was that done by Prakesh et al. in 2013 and 2015.[4, 5] They developed an electrowetting device to perform qPCR on patient samples containing IAV. Their device incorporated eight individual heating loops, each with its own sample preparation zone. They performed qPCR on eight individual patient samples in parallel with a detection limit of ~3 copies per drop.

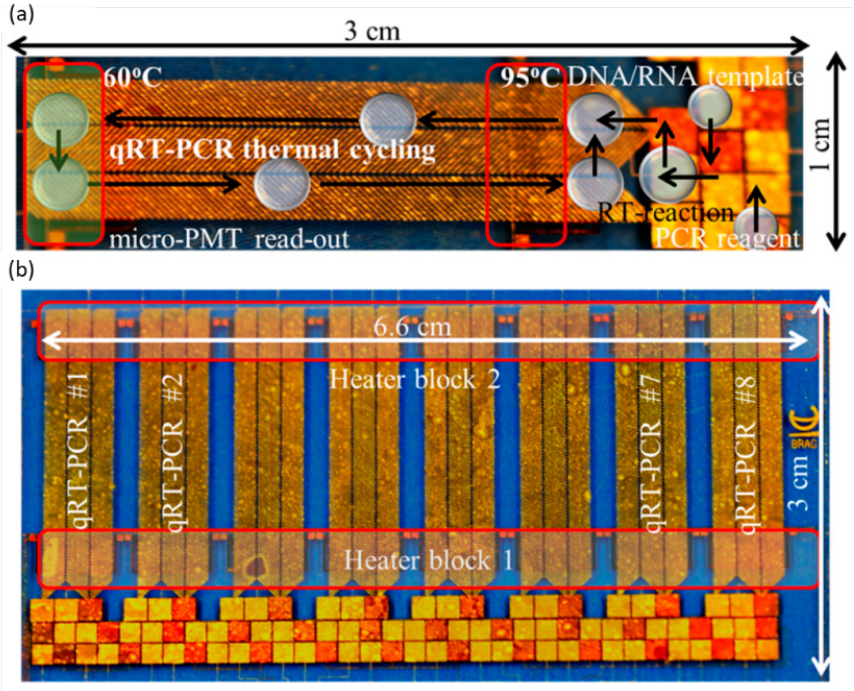


Figure 2.5. Images of an electrowetting RT-qPCR device. It includes a (a) continuous, bi-directional droplet actuation scheme and (b) ability to multiplex up to eight samples in parallel. Adapted from Ref. 5 under the Creative Commons CC BY 4.0 license (https://creativecommons.org/licenses/by/4.0/).[5]

Conclusion

PCR has successfully been implemented at the microfluidic scale with various approaches including static arrays, continuous flow, and electrowetting designs. High throughput bulk sample screening is possible with the implementation of ddPCR technology while qPCR has provided a high-resolution view of single cell and viral measurements in wells and drops, albeit at orders of magnitude lower throughput. This balance of throughput and resolution is a common technological challenge. As imaging technology improves with higher resolution, greater light sensitivity, and increased frame rate, the data bandwidth of microfluidic ddPCR and qPCR applications is expected to increase; thereby meeting or exceeding the accuracy and precision of commercial benchtop units with orders of magnitude increased throughput. In order

to achieve this progress however, the drops used in these qPCR microfluidic devices must remain stable and contain the fluorescent probes or dyes throughout the assay. In the following sections, the progress made towards stabilizing drops with surfactants and limited dye diffusion is discussed.

Drop Surfactants

Introduction

It is necessary to compartmentalize reactants in small volumes to conduct millions of individual reactions for high-throughput biological screening. While this can be done to a certain extent by creating microscale chambers on a microfluidic device, this leads to complex device design. A more robust method is to encapsulate reagents and target biomolecules and/or cells in microscale water-in-oil emulsions. Almost 20 years ago, Thorsen et al. showed this may be possible with the production of monodisperse drops on a microfluidic chip.[36] However, emulsions are complex fluids that exhibit mechanical, rheological, and chemical properties much different than the fluids that create them.[37] At some time scale, drops lose their compartmentalization due to the exchange of chemical species between drops in order to reach chemical equilibrium. This action causes cross-talk between drops which is detrimental to biochemical assays. In addition, ageing of the emulsion leads to coalescence as drops attempt to reduce their interfacial area. Understanding mass transfer and ageing processes of emulsions is important for the progression of drop-based microfluidic technology. Therefore, the selection of oil and surfactant are critical in these applications.

Fluorinated oil is a viable choice as it is hydrophobic and lipophobic, leading to low solubility for biological reagents in the aqueous phase[38, 39] and inhibits molecular diffusion[40].

Other benefits of fluorinated oil include gas permeability of O_2 and CO_2, chemical inertness, and low toxicity/biocompatibility with cells.[1] These oils are readily available and used in a wide range of biological applications such as blood substitutes or breathing liquids.[41-43] Surfactant requirements include mechanical and thermal stability of drops, inertness to biomolecules, and resistance to the transport of biological assay probes. Unfortunately, there are limited commercial options for fluorosurfactants. Options such as perfluorinated polyethers (PFPE) offer long term stabilization but have charged headgroups that interact with oppositely charged biomolecules like DNA, RNA, and proteins.[1] Krytox from DuPont is an example of such an ionic surfactant. Recently, commercial options for fluorosurfactants with non-ionic headgroups are offered by RAN Biotechnologies and Dolomite. While progress has been made in surfactant synthesis during the almost 20 years of drop-based microfluidic technology, there are still gains to be made to provide an ideal stable drop for biological assays. Recent work has shown that this path may not be in the form of traditional block copolymers, but rather from silica-based nano-particles or dendritic oligo-glycerol-based surfactants.[44, 45]

Surfactant Requirements and Limitations

The manipulation of emulsions is an essential characteristic of drop-based systems and surfactant plays a key role.[46] A surfactant is an amphiphilic molecule that has groups with affinities for different immiscible phases. The surfactants basic role is to ensure that drops do not coalesce. Surfactants are constrained to these requirements: drop stability, control of exchange, and biocompatibility.[46] The formation of the interfacial area between the two phases has an unfavorable energy cost and the minimum state is to return to separate phases by reducing the interfacial area through coalescence.[47, 48] The surfactant helps balance this system in a metastable

state.[49, 50] In comparison to bulk systems, interfacial effects now become predominant due to the high surface to volume ratio present in drop-based systems and must be accounted for when adapting a biological assay. The oil-water interface must be biocompatible to facilitate any type of biological screening. Any adsorption to the surface or interaction of the surfactant with biomolecules means the system is no longer biocompatible.

Whether commercially produced or synthesized in the lab, current surfactants for drop-based microfluidics have three key limitations: molecular transport between drops causing cross contamination, incompatibility with adherent mammalian cells, and poor drop stability at high temperatures or salt concentrations.[44] Leakage between drops is detrimental to assays based on fluorescent probes where probe concentration over time is important for quantification of a target biomolecule. This leakage is due to reverse micelles transporting molecules between drops. BSA[51, 52] and sugars[53] added to drops have been shown to improve retention as well as adding hydrophilic groups to small molecules.[54] Current drop-based systems are not suited well to deal with anchorage dependent cells which need a surface to adhere to in order to divide[55] as interfaces with surfactant are not rigid enough for this to occur. The majority of surfactants used in recent drop studies, and unless otherwise stated in this literature review, are based on a block copolymer consisting of a perfluorinated polyether (PFPE) tail and a polyethylene glycol (PEG) headgroup.[1] While these block copolymer surfactants provide good drop stability for aqueous drops at room temperature and biologically relevant incubation temperatures,[1] high temperatures lead to reduced stability due to the decreased solubility of PEG within the surfactant at increased temperatures.[56, 57] This leads to a change in the PEG conformation that negatively affects the surfactant quality. Decreased solubility of PEG at increased temperatures is inconvenient for

applications such as PCR where temperatures reach 95 °C. Additionally, applications with high salt concentrations are affected as PEG solubility decreases with increased salt concentration.[56]

Emulsion Physics

Drop formation of pico- to nano-liter scale drops occurs on the order of milliseconds. Drop stability requires that the surfactant molecules diffuse and bind to the drop interface fast enough before drop collision and coalescence occurs.[1] It is difficult to study these kinetics within the time and length scale of drop formation[58] and there are limited ways to do it (e.g. rotational rheometers or the oscillating droplet method).[59] In order to maintain a stable emulsion that allows for the formation of drops at kilohertz rates, an ideal surfactant formulation must provide a low viscosity while maintaining a high interfacial tension.[37] This combination is important as it minimizes the capillary number at the drop forming junction. The capillary number ($\mathrm{Ca} = \frac{\mu V}{\sigma}$) is defined by the ratio of the viscous drag forces (μ) to surface tension forces (σ) at the interface of two immiscible fluids and is responsible for the formation of drops at a constriction during flow (V, characteristic velocity). Interestingly, the formation of drops in microfluidic devices happens in a transition region for surfactant adsorption between a length scale of 10-100 μm. Above this transition region at the bulk scale, surfactant adsorption is dominated by the diffusion of surfactant molecules to a surface, whereas below it at the microscale, the adsorption is dominated by the kinetics of surfactant adsorption/desorption.[60] Knowledge of the surfactant adsorption kinetics is important as drop collision right after drop formation can result in higher rates of coalescence than expected due to the short time scale limiting proper surfactant adsorption.[58] Furthermore, when handling emulsions it is important to minimize introducing shear, such as during drop re-injection, otherwise coalescence of drops is likely to occur. Coalescence can also

occur when drops are packed closely together and the thin oil film between drops is drained and the emulsion becomes unstable.[61, 62]

The transport of solutes between emulsions is caused by the heterogeneities of their chemical potential in drops, either at the time of encapsulation or as a result of a biochemical reaction (e.g. cell growth). The initiation of mass transfer occurs in emulsions due to the phase partitioning of fluorophores or biomolecules from the continuous to dispersed phase. This is caused by the finite solubility of the dispersed phase in the continuous phase.[63] The mechanism of transport across drops is due to micelle formation when the surfactant concentration is above the critical micelle concentration (CMC).[64] A common result of this transport across drops is Ostwald ripening.[37] Ostwald ripening ages emulsions and causes smaller dilute drops to become even smaller due to the movement of the dispersed phase into larger concentrated drops (Figure 2.6). As the release of solutes is defined by the partition coefficient[63] of solutes between the dispersed and continuous phase, the interfacial properties at the drop surface have shown to be a factor[53, 65-67] in controlling transport. The partition coefficient is defined as the ratio of the solute concentration in the oil phase to the solute concentration in the water phase. In one study by Skhiri et al., the transport of molecules was shown to be a factor of surfactant concentration with the addition of BSA lowering the rate due to an interaction with the surfactant interface.[52] Additionally, it has been shown that transport between drops can be due to a bilayer that forms when drops are in close contact.[68]

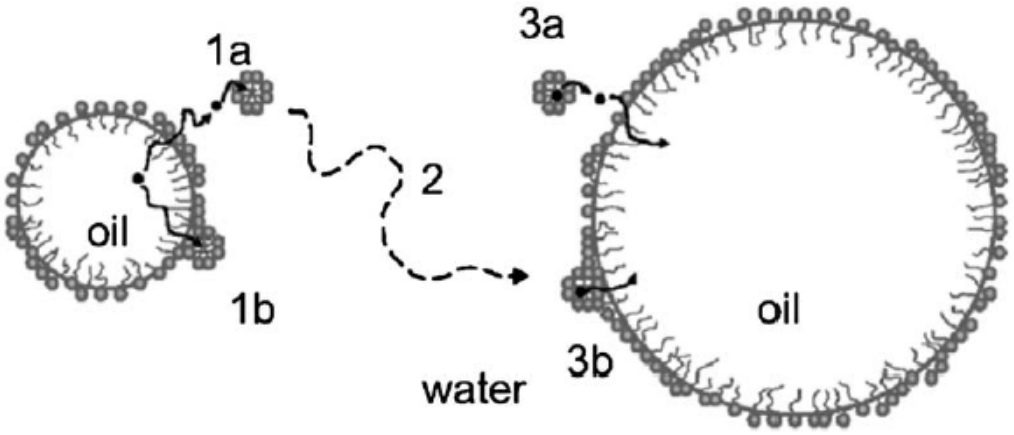


Figure 2.6. Role of surfactant micelles in the transport between drops in the case of Ostwald ripening. Oil molecules solubilized in micelles (1a, 1b) diffuse through the oil (2) and are up taken by another drop (3a, 3b). Reprinted from the Journal of Colloid Interface Science, Vol 343, Ariyaprakai, S. and Dungan, S. R., "Influence of surfactant structure on the contribution of micelles to Ostwald ripening in oil-in-water emulsions," Pages 102-108, Copyright 2010, with permission from Elsevier.[69]

Fluorinated oils such as HFE 7500 and FC-40 are commonly used for the continuous phase of drop-based systems focused on biological assays. Due to the C-F bond, fluorinated oils have low cohesive energy which leads to low solubility of small organic molecules.[37] These weak intermolecular forces also lead to high compressibility which allows gases such as O_2 and CO_2 to have high solubility and diffuse through the oil.[37] This makes the oil ideal for growing cells or performing biological assays in drop-based systems. There is minimal cross-talk between drops due to the low solubility of organic molecules while cells can easily grow due to the diffusion of O_2 and CO_2. In addition, these oils do not swell polydimethylsiloxane (PDMS) like hydrocarbon oils do.[37]

Surfactant Developments

Over ten years ago, Holtze et al. developed a biocompatible surfactant for water in fluorinated oil emulsions suitable for stabilizing drops in many biological assay applications. Their design strategy was focused on tuning a perfluorinated polyether (PFPE) and polyethylene glycol (PEG) block copolymer morphology to have a mixture of triblock (PFPE-PEG-PFPE) and diblock (PFPE-PEG) polymers for best emulsion stability.[70] The outcome of the surfactant performance was largely constrained by the molecular weight (MW) of the surfactant. A low MW surfactant will have increased mobility in the oil phase which allows for fast diffusion to a water-oil interface during drop formation. However, large stresses on drops require a higher MW surfactant to maintain a thick film for stabilization.[1] These stresses include long term incubation where the volume fraction of the emulsion increases as the oil is drained (i.e. creaming) due to the density mismatch of water and fluorinated oil ($\frac{\rho_{oil}}{\rho_{water}} \approx 1.6 - 1.8$), or during drop reinjection, where shear forces are exerted onto an already compressed emulsion. A thick film for stabilizing these stresses may come in the form of large MW PFPE blocks for covering bare patches during creaming and a higher ratio of triblock to diblock copolymers to help surfactant retention during shear.[1] The surfactant CMC can also be tuned by the MW and morphology. Below the CMC, surfactant is dissolved as mobile unimers in the oil phase which easily diffuse to the interface. Above the CMC, surfactant molecules form aggregates, or micelles, and must first dissolve back into unimers before diffusing to the drop interface, which creates a rate limiting step.[1] The CMC is measured experimentally as the surfactant concentration threshold at which the surface tension between the oil and water phases no longer decreases with additional surfactant.

Holtz et al. synthesized surfactants with varying PEG and PFPE MWs and a mixture of triblock and diblock copolymers. Stability was determined by shaking a mixture of water and oil with surfactant and observing which still had a cream layer after 24 hrs. The best surfactant had a PEG MW of 600 g/mol and a PFPE MW of 6000 g/mol. The optimized surfactant was used to form stable drops at 1-30 kHz on a microfluidic device. Drops were then stored tightly packed on a PDMS device and incubated at 37 °C for three days without coalescence. Drops also remained intact after reinjection into another microfluidic device. For biocompatibility, they encapsulated yeast cells and media into drops and incubated overnight. Doubling times were roughly half that observed from bulk growth and may be due to the slower growth rate of densely packed cells prior to encapsulation.[71]

Recently, Etienne et al.[72] performed a more in-depth analysis of the effect of PEG MW of the triblock copolymer using the same surfactant synthesis as presented by Holtz et al.[1] Instead of shaking a vial of water and oil and observing if an emulsion layer is maintained after 24 h,[1] 160 μm diameter drops were formed on a microfluidic device and then subjected to centrifugation and incubation. Additionally, PEG 6000 Da and NaCl solutions were added to drops to test the effect of dispersed phase viscosity and salt concentration on drop stability. Increased viscosity due to the added PEG 6000 Da was found to not affect drop stability while adding NaCl at 0.15 M and 1 M dramatically decreased drop stability during centrifugation and incubation. They did not test other common salts however (e.g. $MgCl_2$ used in PCR). Interestingly, they found an ideal PEG length of 550 Da which is close to the PEG 600 Da that Holtz et al. found to be optimal. The PEG 550 Da surfactant was also found to have the lowest interfacial tension. Low interfacial tension is generally desired as drop stability tends to scale

inversely with interfacial tension. Emulsions want to reduce the interfacial area by coalescing and a surfactant that provides a low interfacial tension would assist in preventing this.[47, 48] PEG length of diblock copolymers was also investigated but found to have little effect on drop stability; however, increased packing density of diblock copolymers was found to improve drop stability when drops contained NaCl. This improvement indicates a mixture of diblock and triblock copolymers is important to provide a more robust surfactant formulation for a wide range of biological assays.

Current surfactants based on PFPE and PEG copolymers have a key limitation for biological assays based on fluorescent probes: cross-talk between drops due to micellular driven solute transport. To overcome this limitation, Pan et al. recently developed a novel application for amphiphilic silica nanoparticles that can stabilize drops in fluorinated oil and prevent leakage between them.[44] The non-toxic silica nanoparticles are presented as an alternative to traditional drop surfactants with the manuscript presenting a simple two-step synthesis. Drops formed with the silica nanoparticles remained stable after incubation at 37 °C, shaking at 100 rpm, and at 95 °C for 20 min. Dye leakage between drops was tested by mixing a population of positive drops containing resorufin, a red dye with a diffusion time scale on the order of hours[52], with negative drops containing only buffer (Figure 2.7). Drops were made with a traditional surfactant and silica nanoparticles (labeled EA-surfactant and F-SiO_2 in Figure 2.7, respectively). After 26 h at 20 °C, all the drops made with traditional surfactant fluoresced red while the drops made with silica nanoparticles did not have any apparent dye leakage. The elimination of micelle formation in the silica system is likely what reduced the transport across drops to a negligible level.[44]

Biocompatibility of the system was shown by growing *E. coli* in drops and comparing the OD of the bulk emulsion to an *E. coli* sample in bulk with little change in OD observed.

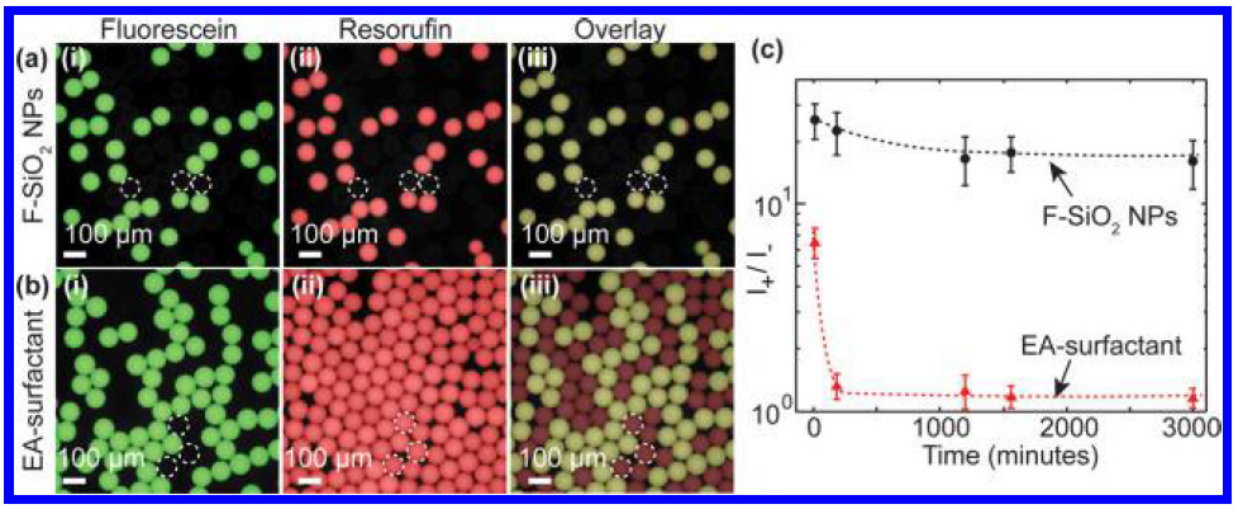


Figure 2.7. Dye leakage experiments with F-SiO_2 NP and EA surfactant stabilized drops. (a) Fluorescence images of positive and negative drops stabilized by F-SiO_2 NPs after mixing for 26 h. The emulsion contained a 1:1 mixture of positive drops containing fluorescein (10 μM) and resorufin (220 μM), and negative drops containing PBS buffer only. (b) Fluorescence images of drops stabilized by EA surfactant after mixing for 26 h. (c) Plots of the time evolution of the ratio of resorufin fluorescence intensity of positive drops (I+) versus that of negative drops (I−), for drops stabilized by F-SiO_2 NPs and EA-surfactants, respectively. Reprinted with permission from Pan, M.; Rosenfeld, L.; Kim, M.; Xu, M.; Lin, E.; Derda, R.; Tang, S. K. Y., "Fluorinated Pickering Emulsions Impede Interfacial Transport and Form Rigid Interface for the Growth of Anchorage-Dependent Cells." *ACS Applied Materials & Interfaces* 2014, 6 (23), 21446-21453.[44] Copyright 2014 American Chemical Society

Conclusion

The progress of drop-based microfluidics is directly linked to the improvements in surfactant formulation and synthesis.[37] As commercial options for surfactants are few or expensive, many researchers resort to lab synthesized surfactants which makes comparisons between drop-based systems very difficult. To fully adapt standard biological assays to drop-based systems there are improvements to be had in the areas of solute cross-talk and drop stability at high temperatures or salt concentrations. This may require a deviation from the

traditional copolymer-based surfactants to emerging technologies like the silica nanoparticles presented above. Improving surfactant technology to meet the needs of biological assays will eventually lead to standardizations in the field as more commercial options become available. In the next section, the dynamics of small molecule transport between drops in relation to biological assays is discussed.

Transport Between Drops

Emulsion drops provide an ideal microenvironment for the parallelization and high-throughput screening of biochemical reactions as they require minimal sample and reagent volume. Three important components in a drop-based biochemical assay are stability against coalescence, biocompatibility, and retention of reagents. These properties are primarily controlled by the surfactant in the continuous oil phase and require optimization for the assay of choice.[46, 49] As most biochemical assays use a reporter dye, quantitative measurements can be altered by dye cross-talk between drops which affects the sensitivity and specificity of the assay. Ideally, the signal-to-noise ratio (SNR) of the reporter dye will increase over time until the reaction ends and/or the signal is saturated. If a drop is unable to retain the reporter dye, the SNR is expected to decrease over time. For applications relying on a digital response like droplet digital PCR (ddPCR), cross-talk between drops would make it difficult to distinguish between "positive" and "negative" drops.

It has been shown in the literature that drop emulsions do not always retain fluorophores within the dispersed aqueous phase and that the mechanism by which they are partitioned into the continuous oil phase is not entirely known. As emulsions stabilized by surfactant are systems intrinsically out of equilibrium, coalescence and solute transport drive these systems to

equilibrium.[64] Physical factors such as surfactant composition around the droplet and chemical factors such as the hydrophilicity of the fluorophore contribute to the transport across drops. The mechanism for the transport between drops is still not fully understood. There are three postulated mechanisms for dye diffusion: 1) direct partitioning of the dye in the continuous phase;[51] 2) transport of the dye in vesicles or micelles formed by surfactant molecules present in the continuous phase;[51, 52, 64] 3) transport of the dye by aqueous drops that spontaneously form at liquid-liquid interfaces.[73-77] In this brief review, we will cover model and experimental data that aim to investigate these proposed mechanisms in drop systems utilizing fluorinated oil and block copolymer surfactants with either a PEG or Jeffamine headgroup.

In order to determine optimal drop properties for maintaining a high SNR throughout the course of a biochemical reaction, Chen et al. proposed a model for the diffusion of fluorophores between drops containing an enzymatic reaction based on Michaelis-Menten kinetics.[78] A schematic of the model is shown in Figure 2.8. Based on their findings, they concluded diffusion is rate limited by the permeability of the drop interface (k_{perm}) and the rate of transport by micelles or direct oil partitioning had little effect on their results (Figure 2.9a). In addition, SNR is maximized with fast reactions in small drops and requires quick interrogation else the SNR will decrease over time (Figure 2.9b and 2.9c). However, a key factor in the determination that drop permeability was the rate limiting step for diffusion assumed that micellular transport was much faster than transport through the drop interface. The authors made this assumption based on the Stokes-Einstein relation for calculating a diffusion coefficient for a particle the size of a micelle and not experimental data. Both Skhiri and Gruner et al. later observed the transport of fluorophores was rate limited by the formation and transport of reverse micelles from

experimental data.[52, 64] They both came to this conclusion as they observed a decrease in retention time of dye in drops with an increase in surfactant concentration in the oil above the CMC. Above the CMC, we expect free surfactant molecules to spontaneously form reverse micelles which can be used for transport between drops. These micelles behave as nanocontainers that effectively increase the solubility of dye in the continuous oil phase. Gruner et al. additionally backed up this observation with modelling to prove the time scales matched micelle transport as the rate limiting step. Skhiri also observed an increase in dye retention in drops with the addition of bovine serum albumin (BSA) to the aqueous phase (also observed by Courtois et al.)[51]. The current hypothesis is BSA decreases the partition coefficient of dye in the continuous oil phase, possibly by some binding mechanism to the fluorophore itself. Their respective results are shown in Figure 2.10. It should be noted that these experiments are using hydrophilic dyes such as fluorescein or resorufin that have time scales of diffusion in days to hours while hydrophobic dyes such as rhodamine will completely leave drops within minutes. Janiesch et al. found that only hydrophilic dyes with a low distribution coefficient (LogD < -4) were retained in drops, with some requiring low pH media having an increased effect.[79] This finding further indicates that the partitioning of fluorophores into the continuous oil phase is the dominating factor for transport and any additives, such as BSA, are required to stable biochemical assays.

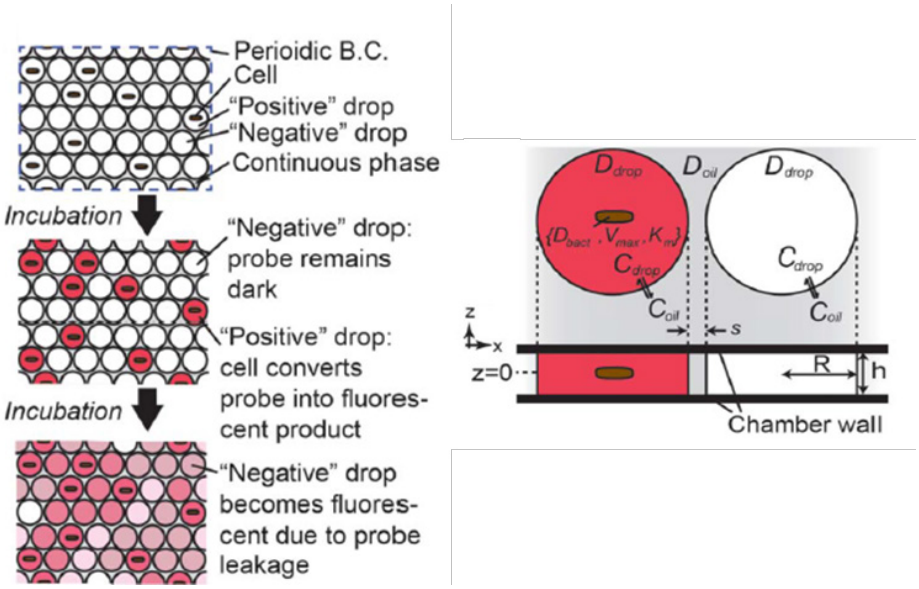


Figure 2.8. Dye diffusion model schematic. The dye diffusion model consists of a 2D array of drops immersed in a continuous oil phase. Positive drops containing cells convert a probe from an initial dark state to a positive fluorescent state. The probe can diffuse into neighboring negative drops. Adapted from Ref. 78 with permission from the Royal Society of Chemistry.[78]

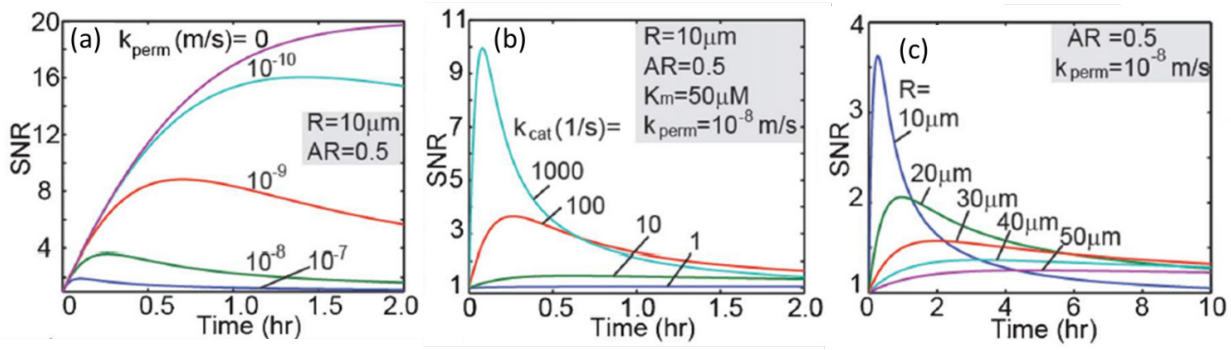


Figure 2.9. Temporal evolution of the signal-to-noise ratio (SNR) while varying one parameter at a time: (a) permeability coefficient, k_{perm}; (b) enzyme turnover rate, k_{cat}; (c) droplet radius, R. Adapted from Ref. 78 with permission from the Royal Society of Chemistry.[78]

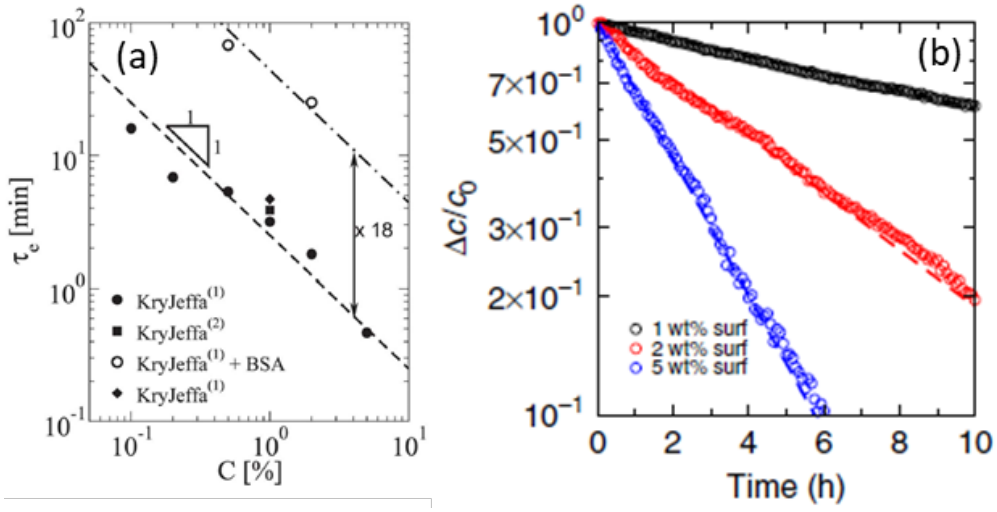


Figure 2.10. Diffusion time scales in drops. (a) Time until dye has equilibrated in the drop system, τ_e, as a function of surfactant concentration, C (w/w), with 10 mM initial resorufin concentration. The open circle corresponds to drops that included Bovine Serum Albumin. Adapted from Ref. 52 with permission from the Royal Society of Chemistry.[52] (b) Variation of resorufin transport rate as a function of surfactant concentration for 15 µm diameter drops. Adapted from Ref. 64 under the Creative Commons CC BY 4.0 license (https://creativecommons.org/licenses/by/4.0/).[64]

There is strong evidence in the literature suggesting micelle driven transport is the mechanism, and rate limiting step, for transport between drops. Yet, there is still debate towards the formation of these micelles if they are formed due to free surfactant molecules in the continuous oil phase or the spontaneous formation of aqueous drops at the liquid-liquid interface. Based on the work presented so far, we may expect the former as all experiments were done above the CMC. However, surfactant concentration does not necessarily need to be above the CMC to form monodisperse drops.[1] Recently in 2018, Etienne et al. investigated how hydrophilic reagents are transported across drops and observed that even well below the CMC there was diffusion in the system. In Figure 2.11, the half-life of dye retention has a similar trend above and below the CMC of the surfactant being used, indicating there may be a different mechanism for the micelle formation. Etienne et al. concluded the transport of reagents is

primarily caused by the spontaneous formation of aqueous drops at the liquid-liquid interface with diameters on the order of 100 nm. This estimate was on par with particle size estimates for micelles from Gruner et al. The difference from traditional reverse micelle, or vesicle, formation is this is a thermodynamic phenomenon and not the self-assembly of surfactant molecules. They argue that spontaneous formation of aqueous drops at the liquid-liquid interface is controlled by the interfacial tension. Since the formation of these drops is energetically expensive, we would expect more drops to form at lower interfacial tensions (high surfactant concentrations) and less drops at higher interfacial tension (low surfactant concentrations). This hypothesis matches well with the data as higher surfactant concentration leads to a higher rate of diffusion due to this small drop formation.

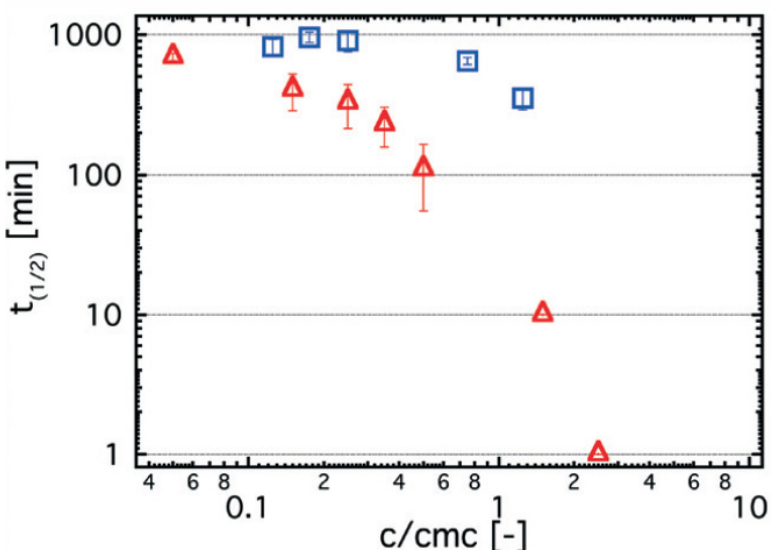


Figure 2.11. Effect of CMC on diffusion between drops. Time until 50% of fluorescein is released, $t_{1/2}$, as a function of the concentration of FSH2-Jeffamine900 (△) and FSH-Jeffamine1000 (□). The surfactant concentrations are normalized by their respective CMCs. Adapted from Ref. 73 with permission from the Royal Society of Chemistry.[73]

Returning to the postulated mechanisms for diffusion, literature has shown the direct partitioning of fluorophores into the continuous oil phase is only a valid mechanism for

hydrophobic fluorophores and leads to retention half-lives in the scale of minutes in drops. For the last two mechanisms, there is a valid argument for both the self-assembly of micelles and the spontaneous formation of aqueous drops at the liquid-liquid interface. Looking at the data in Figure 2.11, while limited for concentrations above the CMC, a distinction could be made for a region where transport is dominated by the formation of aqueous drops below the CMC and then transitions to transport dominated by the self-assembly of reverse micelles above the CMC.

Conclusion

If we revisit the three important components in a drop-based biochemical assay: stability against coalescence, biocompatibility, and retention of reagents; we must be cognizant of the links between each parameter and how they might affect each other when optimizing a drop-based assay. For example, based on the data presented here we could create an optimal emulsion well below the CMC with maximal dye retention, but we would likely have a high degree of coalescence as Janiesch et al. observed when they approached the CMC of their surfactant.[79] From our own data presented in Chapter 4,[80] we have observed BSA improving dye retention while at the same time causing increased coalescence (such coalescence with BSA has been previously observed[1]). Optimization and additive screening were necessary to reduce this drop coalescence, requiring the addition of Tween 20 as an additional surfactant to the aqueous phase. In the end, adapting biochemical assays into microfluidic drops presents an engineering challenge and may require an iterative approach to find the optimal combination of surfactant and experimental conditions which provide stable drops and prevent transport between drops.

CHAPTER 3

RAPID PARALLEL GENERATION OF A FLUORESCENTLY BARCODED DROP LIBRARY FROM A MICROTITER PLATE USING THE PRESSURE COOKER CHIP

Contribution of Authors and Co-Authors

Manuscript in Chapter 3

Author: Geoffrey K. Zath

Contributions: G.K.Z. designed research, performed research, analyzed data, and wrote the manuscript

Co-Author: Ralph A. Sperling

Contributions: R.A.S. designed research, performed research, analyzed data, and wrote the manuscript

Co-Author: Dimitri A. Bikos

Contributions: D.A.B. wrote the manuscript

Co-Author: Carter W. Hoffman

Contributions: C.W.H. performed research and wrote the manuscript

Co-Author: Reha Abbasi

Contributions: R.A performed research

Co-Author: Adam R. Abate

Contributions: A.R.A designed research

Co-Author: David A. Weitz

Contributions: D.A.W. designed research

Contribution of Authors and Co-Authors Continued

Co-Author: Connie B. Chang

Contributions: C.B.C. designed research and wrote the manuscript

Manuscript Information

Geoffrey K. Zath, Ralph A. Sperling, Dimitri A. Bikos, Carter W. Hoffman, Reha Abbasi, Adam R. Abate, David A. Weitz, Connie B. Chang

Lab on a Chip

Status of Manuscript:
_X__ Prepared for submission to a peer-reviewed journal
____ Officially submitted to a peer-reviewed journal
____ Accepted by a peer-reviewed journal
____ Published in a peer-reviewed journal

Royal Society of Chemistry

Abstract

In drop-based microfluidics, an aqueous sample is partitioned into drops using individual pump sources that drive water and oil into a drop-making device. Parallelization of drop-making devices is necessary to achieve high-throughput screening of multiple experimental conditions, especially in time-sensitive studies. Here, we present the Pressure Cooker Chip (PCC), a microfluidic chip designed to generate 50-μm diameter drops of up to 96 different conditions in parallel by interfacing individual drop makers with a standard microtiter 384-well plate. The PCC is used to generate two types of optically barcoded drop libraries consisting of two-color fluorescent particle combinations: a library of 24 microbead barcodes and a library of 192 quantum dot barcodes. Barcoded combinations in the drop libraries are rapidly screened within a microfluidic device using laser-induced fluorescence. The barcoded populations in the fluorescence drop data are identified using DBSCAN data clustering. Signal analysis reveals that particle size defines the dominant noise present in the fluorescence intensity distributions of the barcoded drop populations, arising from Poisson loading for microbeads and shot noise for quantum dots. A barcoded population from a drop library was isolated using fluorescence-activated drop sorting, enabling downstream analysis of drop contents. The PCC can improve multiplexed high-throughput assays by enabling simultaneous encapsulation of barcoded samples stored in a well plate and reducing sample preparation time.

Introduction

Drop-based microfluidics is a technology that reduces assay times and increases sample throughput by rapidly creating and analyzing picoliter-sized drops.[81, 82] Drop-based microfluidics has been recently applied towards combinatorial drug discovery,[83] massively multiplexed nucleic acid detection,[84] and antibiotic susceptibility screening.[85] In these assays, 10^3 to 10^6 drops are tracked by a unique identifier in each drop, called a "barcode". This is commonly achieved using one of two barcode types: DNA barcodes can be introduced to tag drop contents as part of a next generation sequencing pipeline;[86-89] or fluorescent dyes and particles can be used to label drops for fluorescence-based assays, such as enzyme activity or dose-response screening.[83-85, 90-94] DNA barcoding can provide upwards of 10^7 unique labels to enable large-scale single cell transcriptomics, but requires breaking the drop emulsion for sequencing purposes.[86-89] Fluorescent labeling allows the barcode and fluorescent assay output to be measured simultaneously without breaking the drops. The resulting collections of either DNA or fluorescent barcodes in drops, known as "libraries", enable multiplexed or combinatorial readouts of the unique components encapsulated within the drops.[90-93]

A typical method for creating a drop library is to emulsify each barcoded sample one at a time using a single drop making device and subsequently pool the samples together. This process is labor- and time-intensive when using a single drop making device for large numbers of barcodes. Individual microfluidic drop makers can be run in parallel, yet this necessitates multiple pump sources to emulsify each sample. Alternatively, liquid handling machines or autosamplers can be programmed to sequentially load individual samples from a microtiter plate into a microfluidic device;[94-97] however, these technologies can be costly and do not enable the

simultaneous creation of barcodes, which may be necessary for time-sensitive experiments. For example, when screening rapid enzymatic reactions, all samples must be emulsified and processed in parallel to accurately capture time-sensitive kinetics needed for performing comparative studies.[98, 99] Thus, microfluidic devices built with multiple drop makers have been designed to interface with wells on standard microtiter plates to perform parallel encapsulation using vacuum[100] or positive pressure.[87, 88] Prior work from our group used such a device to encapsulate DNA barcodes to perform single cell chromatin profiling.[87, 88] However, the fabrication of this device was not described in detail, nor was the device used to create fluorescently barcoded libraries. Extending the utility of this device for fluorescent barcoding would enable multiplexed assaying in which a barcoded signal is simultaneously measured with an assay output. Fluorescent barcodes in drops also enables sample isolation using fluorescence-activated drop sorting.[20, 101]

Here, we detail the fabrication of the microfluidic device comprised of 96 drop makers called the Pressure Cooker Chip (PCC) that directly interfaces with 96 wells of a standard 384-well microtiter plate. The PCC is housed within a commercial pressure cooker and pressurized air is used to induce parallelized drop formation within the 96 drop makers on the device. Parallelization enables rapid creation of drop libraries at a drop throughput of ≈300 kHz, approximately two orders of magnitude larger compared to serial drop generation with a single drop making device, creating a total of $\approx 3.6 \times 10^7$ drops in 2 min. The diameter of drops produced from the PCC is described using a simple drop scaling law, allowing for fine tuning of drop diameters ranging from ≈50-90 μm. The PCC is used to create two types of optically barcoded drop libraries using two-color combinations of either microbeads or quantum dots

(QDs). A quarter of the 96-drop makers on the PCC was used to create a drop library consisting of 24 fluorescent microbead combinations. The PCC was also used twice to create a drop library consisting of 192 QD combinations. Fluorescence from each barcoded drop is measured at high-speed using a flow-based detection method[20] to create a two-color scatter plot for each type of barcode library. A data clustering method, density-based spatial clustering of applications with noise (DBSCAN),[102] was used to identify uniquely barcoded concentrations and minimize the signal overlap between the combinations. The dominant sources of noise influencing the fluorescence signal overlap between barcode populations arise from Poisson loading for drops containing fluorescent microbeads ≈1 μm in diameter and shot noise of the photodetector for drops containing QDs ≈10 nm in diameter. Finally, we demonstrate the utility of the PCC by sorting and isolating a single fluorescently barcoded sample from a drop library of 24 different barcode combinations.[20, 101] The ability to sort a specific barcoded sample from a drop library can enable further analysis of drop content using downstream techniques such as PCR amplification and sequencing.[103-105] Drop libraries created with the PCC can help to streamline current multiplexed assays, such as combinatorial drug screening[83] or high-throughput assaying of protease activity,[92] by enabling simultaneous encapsulation of barcoded samples stored in a well plate.

Materials and Methods

PCC Design

The PCC was fabricated from three separate 5-mm thick layers of polydimethylsiloxane (PDMS) plasma bonded on top of one another to form a 3-dimensional network of channels. The top layer of the device (Fig. 3.1a, i) is comprised of a narrow strip of PDMS containing two long channels that function as a common oil inlet and drop outlet for all three layers. Oil inlet and drop outlet channels run perpendicular to the channels in the remaining two PDMS layers, thereby allowing oil and drops to flow throughout the device from a single inlet and outlet, respectively. The oil inlet channel (Fig. 3.1a, i, blue) and drop outlet channel (Fig. 3.1a, i, yellow) are connected to the rest of the device through a total of nine via holes punched in the middle layer (Fig. 3.1a, ii), five for oil distribution and four for drop collection, providing a pathway for fluids from the top layer through to the bottom layer (Fig. 3.1a, dashed black lines). The middle layer contains oil distribution and drop collection channels that pass the oil phase to the drop makers and collect produced drops. The bottom layer (Fig. 3.1a, iii) contains 96 drop makers (Fig. 3.1b), each connected to oil distribution and drop collection channels. Drop maker inlet holes are spaced 4.5 mm apart to match the standard pitch of a 384-well microtiter plate, enabling the PCC to interface directly to ¼ of a 384-well microtiter plate.

PCC Fabrication

Each of the PDMS layers i – iii (Fig. 3.1a) was cast from a unique master mold and bonded following standard techniques in soft lithography (see Appendix A, *PCC Fabrication* for details).[20] Short lengths (22.5 mm) of SAE 304 stainless-steel capillary tubes (0.71 mm OD, 0.41 mm ID, Vita Needle) were fitted into the sample inlet holes of the device to provide a path for

fluids from each microtiter plate well to the sample inlet of each drop maker (Fig. 3.1b). For encapsulating barcoded samples, the device was positioned above ¼ of a standard 384-well microtiter plate such that each of the stainless-steel inlet capillaries nearly extends to the bottom of a different well (Fig. 3.1c).

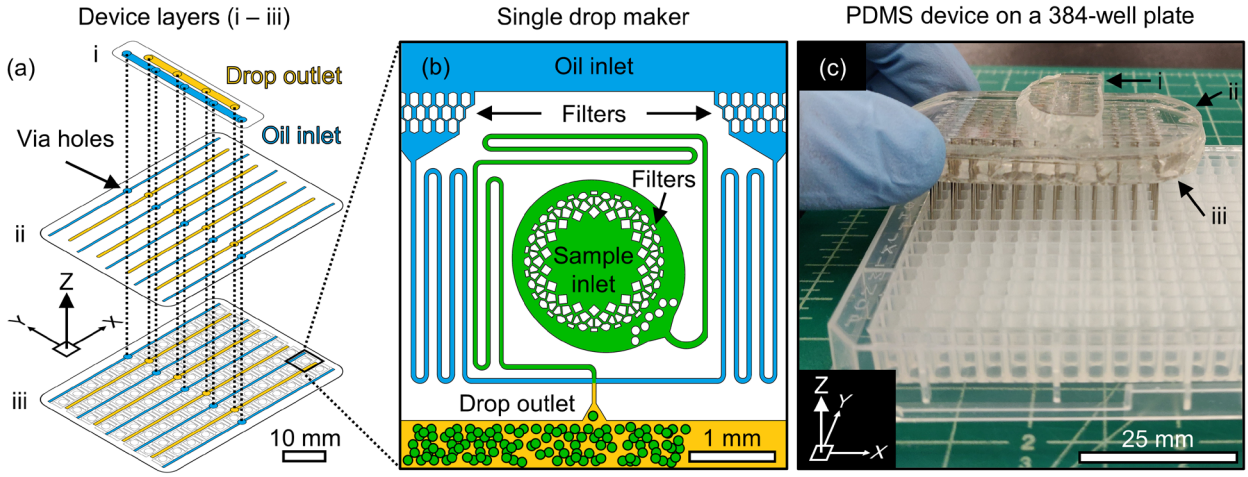


Fig. 3.1. PCC design and assembly. (a) The PCC was assembled from three layers: (i) a top layer containing oil distribution (blue) and drop collection (yellow) channels connected to a single inlet and outlet, respectively; (ii) a middle layer which reduces fluidic resistance by providing additional height to the oil and drop collection distribution channels on the bottom layer; and (iii) a bottom layer which contains an array of 96 drop makers (eight rows of twelve drop makers) with channels for oil distribution (five rows, blue) and drop collection (four rows, yellow). (b) Detailed view of one of the 96 drop makers positioned on the bottom layer. Colors are used to distinguish oil inlet (blue), aqueous sample inlet (green), and drop outlet (yellow) channels. (c) Image of a completed device interfaced with ¼ of a 384-well plate. Each layer (i – iii) of the fully assembled device from part (a) is indicated using black arrows. Stainless steel sample inlet capillary tubes are visible extending into the microtiter plate wells below.

Pressure Chamber

The barcoded samples contained in the wells of the microtiter plate were simultaneously driven into each of the 96 drop makers of the PCC under the uniform pressure within the sealed aluminum interior chamber of a 6-quart pressure cooker (Fig. 3.2a). Compressed house air (≈60 psig) supplied both the oil reservoir pressure P_{oil} and chamber pressure P_{water}, both adjusted from 0-15 psig using manual regulators (McMaster-Carr 6745K32 0-25 psi) and analog gauges

(McMaster-Carr 3850K2 0-15 psi). The oil reservoir was comprised of a pressure-rated glass bottle (Sigma Duran Z674397) and a cap fitted with ports for compressed air and oil inlet tubing. Custom drilled ports in the pressure chamber allowed the passage of oil inlet tubing and drop outlet tubing (Fig. 3.2a, Side view). The ports were sealed with silicone sealant (DAP Kwik Seal Plus). A viewport was created using a 1.5 mm-thick transparent polycarbonate sheet that was affixed and sealed to a fabricated opening in the pressure chamber lid, allowing device operation to be monitored or recorded (Fig. 3.2a, Top view). A strip of white LEDs (Ledmo SMD 2835) was mounted to the inside of the chamber to provide illumination.

Drop Encapsulation

Barcoded samples were pipetted into individual wells of a 384-well microtiter plate and then placed into the pressure chamber apparatus. The PCC was connected to the oil inlet and drop outlet tubing and positioned with the inlet capillaries extending into the wells of the microtiter plate containing barcoded samples (Fig. 3.2b). An oil reservoir was pressurized by house air and was regulated at pressure P_{oil} to control the oil flowrate. The oil reservoir contained Novec 7500 fluorinated oil (3M) with 1.5% w/w of a Krytox-PEG surfactant that was synthesized in-house following a previously published protocol incorporating Jeffamine ED900 (Huntsman) as the hydrophilic portion of the PTFE-PEG-PTFE triblock perfluorosurfactant.[1] The water flowrate was controlled by a second regulator which adjusted P_{water} within the chamber, driving barcoded samples from each microtiter plate well into the PCC to be encapsulated into drops. Barcoded drops passed through the wall of the pressure chamber before reaching a collection tube to form a library of drops, each indexed to a unique sample well. Drop

collection continued for 2-3 min, or until air bubbles were observed in the outlet tubing, indicating sample wells were empty.

A detailed schematic summarizing barcoded drop encapsulation within the PCC is presented in Fig. 3.2c. Barcoding is represented by a unique combination of green and red fluorescent microbead concentrations in each well (Fig. 3.2c). Pressurization of the chamber pushes the fluid from these wells into the bottom PCC layer (Fig. 3.2c, iii) where drops are formed at individual drop makers and collected in shared drop outlet channels formed from the union of channels in the middle and bottom layer (Fig. 3.2c, ii and iii, yellow). These shared channels are connected to a perpendicular collection channel on the top layer (Fig. 3.2c, i) through via holes where drops subsequently flow and are collected in a common drop outlet. The flow of oil is the reverse of the flow of drops; a common oil inlet is distributed in the top layer (Fig. 3.2c, i) to perpendicular channels (Fig. 3.2c, ii and iii, blue) through via holes until oil reaches the drop makers (Fig. 3.2c, iii).

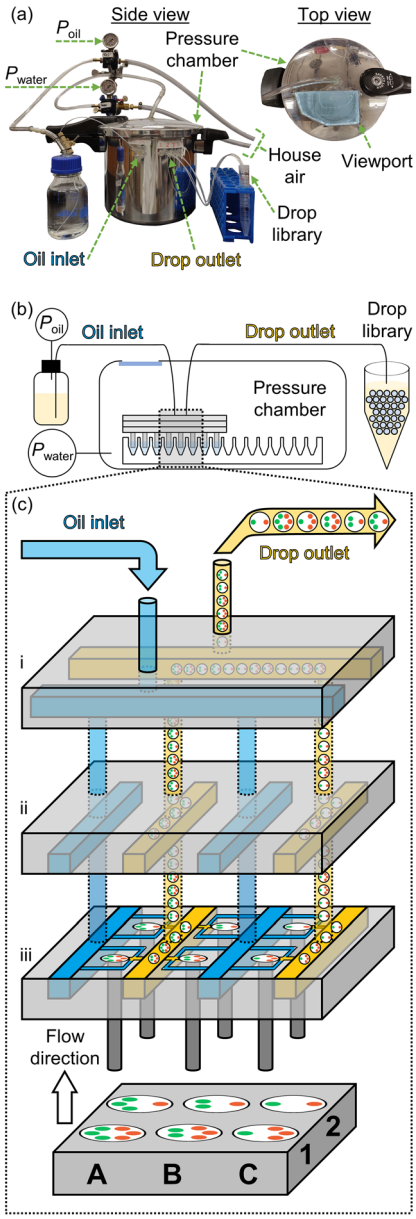


Fig. 3.2. PCC operation and barcoded drop library production. (a) Side view and top view profiles of the PCC apparatus and components. (b) PCC operation schematic for the encapsulation of 96 wells from a 384-well microtiter plate. Pressure P_{oil} is applied to an external oil reservoir to provide oil to the device within the pressure chamber while a second pressure P_{water} applied to the chamber pushes fluid from sample wells into the microfluidic device. Barcoded drops travel through tubing past a sealed opening in the wall of the chamber for collection in a drop library. (c) Detailed schematic of the internal channels and flows within the PCC device. Samples in wells (indexed A – C and 1 – 2) barcoded with different concentrations of green and red microbeads are encapsulated in layer (iii), collected in large drop channels (yellow) formed from both layers (ii) and (iii) where they are transported to perpendicular drop collection channels in layer (i). The barcoded drops flow out of the device in a shared drop outlet.

Drop Measurements

To characterize drop formation, the PCC was placed on a petri dish filled with 10 mL of filtered DI water (0.2 μm filter) within the pressure chamber and the oil reservoir was filled with 100 mL of Novec 7500 (3M) oil with surfactant[1] added at 1.5% w/w. Drops were collected across a range of water P_{water} and oil P_{oil} inlet pressure combinations (2-3, 2-6, 2-12, 4-3, 6-3, 6-6, 6-12, 8-9, and 8-12 psig, where combinations are denoted as P_{water} - P_{oil}). Approximately 10 μL of drops were placed on an 8-well Teflon printed slide (Electron Microscopy Sciences, Cat. #63422-06) and imaged under an inverted brightfield microscope (Nikon TE2000). The height of the Telfon well was estimated to be >50 μm, likely closer to 100 μm, as drops 52.5 - 91.9 μm in diameter regularly formed a bilayer during imaging. A custom image processing script in MATLAB (R2019a) was used to measure drop diameter D_{drop}. To convert the water and oil pressure ratios P_{water}/P_{oil} to volumetric flowrate ratios Q_{water}/Q_{oil}, we measured the volumes V of the oil and water phases after t = 0.5-2.5 min of collection for each water and oil pressure condition. In this case, surfactant was not added to the oil phase to allow for drop coalescence and phase separation of oil and water. The volumetric flowrates of each phase were calculated using $Q_i = \frac{V}{t}$ and plotted as Q_{water}/Q_{oil} versus P_{water}/P_{oil} (Fig. A.1).

Real-time drop formation within the PCC was visualized through the viewport on the pressure cooker using a high-speed camera (Phantom VEO 710L, Vision Research) attached to a tube lens (Model CFM, ISCO-OPTIC) mounted with a 10× objective (NA 0.25). The underside of the PCC was illuminated by a liquid light guide routed through the side of the pressure cooker and attached to an LED light source (SugarCUBE, Ushio America).

Fluorescent Microbead Barcodes

Microbead barcodes consisted of unique two-color combinations of ≈1 μm diameter green and red microbeads (Thermo Scientific Fluoro-Max G0100 ex. 468 / em. 508 nm and R0100 ex. 542 / em. 612 nm). Green and red microbead (stock of 1% solids, $\approx 2.5 \times 10^7$ microbeads/μL) barcode labels were made from five dilutions in water (5.1×10^5, 1.3×10^6, 2.3×10^6, 3.6×10^6, 5.1×10^6 beads/μL). The five dilutions of each microbead color were mixed equally in a combinatorial manner to create a total of 24 barcode labels. The concentration combinations are detailed in Table A.1. Four concentrations of blue microbeads (Thermo Scientific Fluoro-Max B0100 ex. 412 / em. 473 nm, 5.1×10^5, 1.3×10^6, 2.3×10^6, 3.6×10^6 microbeads/μL from a stock of 1% solids, $\approx 2.5 \times 10^7$ microbeads/μL) were randomly spread across 24 microbead-barcoded wells and used as a mock assay signal. For microbead barcoded drop experiments, the oil pressure was set to 3 psig (P_{oil}) and the chamber pressure was set to 2 psig (P_{water}). For the purpose of collecting 24 samples instead of 96, a modification to the PCC was made to allow drop outlet tubing to be directly connected to the drop collection channels of the second layer of the device. This modification provided separate collection from each quadrant of drop makers on the device where each quadrant is comprised of 24 drop makers. A confocal image of the microbead barcoded drops captured in a drop array device[71] is shown in Fig. A.2. The drop library was collected and re-injected into a secondary device for use with a custom drop fluorescence detection system to detect the maximum fluorescence of each drop (See Appendix A *Barcoded drop detection* and Fig. A.4 for details).[20] Photomultiplier tube (PMT) gain was set to 0.32 V for microbead barcoded drop detection.

Quantum Dot Barcodes

QDs of two colors (Thermo Scientific QD625 and QD705) were used as barcode labels by preparing 12 QD625 (1.15×10^4, 9.68×10^3, 8.00×10^3, 6.48×10^3, 5.12×10^3, 3.92×10^3, 2.88×10^3, 2.00×10^3, 1.28×10^3, 7.20×10^2, 3.20×10^2, 8.00×10^1 pM) and 16 QD705 (1.02×10^4, 9.00×10^3, 7.84×10^3, 6.76×10^3, 5.76×10^3, 4.84×10^3, 4.00×10^3, 3.24×10^3, 2.56×3, 1.96×10^3, 1.44×10^3, 1.00×10^3, 6.40×10^2, 3.60×10^2, 1.60×10^2, 4.00×10^1 pM) dilutions in water. The 12 and 16 dilutions were mixed equally in a combinatorial manner to create a total of 192 barcode labels. The concentration combinations are detailed in Table A.2. For drops containing QD barcodes, the oil pressure (P_{oil}) was set to 8 psig while the chamber pressure (P_{water}) was set to 5 psig. The PCC was operated twice to create 192 barcodes (96×2). PMT gain was set to 0.45 V for QD barcoded drop detection.

Two Channel Fluorescence Activated Drop Sorting

Barcoded drops were injected into a microfluidic drop sorting device[20] at a flowrate of 40 µL/h and spacer oil (Novec 7500) without surfactant was injected at a flowrate of 800 µL/h. A sorting electrode driven by a high voltage amplifier (Trek Model 2220-CE) and controlled by a custom LabVIEW program was used to pull drops into a collection channel. The sorting electrode provided a 400 µs pulse of a 25 kHz, 400 V square wave signal when the drop fluorescence signal fell within the threshold values set for a specific barcode (1 – 1.2 V green channel, 0.15 – 0.25 V red channel).

Results and Discussion

Drop Formation Characterization

Drops were generated with the PCC under a range of pressures for P_{water} and P_{oil} to identify combinations that produce monodisperse drops. D_{drop} and monodispersity, as quantified by the coefficient of variation (CV) of D_{drop}, were measured at each pressure combination (Fig. 3.3a). To observe drop formation across the range of pressures tested, high speed videos of drop formation in the PCC were captured at four extreme water and oil pressure combinations. The four combinations are labeled with corresponding symbols in Fig. 3.3a-c: high water pressure (■, P_{water} = 6 psig and P_{oil} = 3 psig), low combined pressure (▼, P_{water} = 2 psig and P_{oil} = 3 psig), high combined pressure (▲, P_{water} = 8 psig and P_{oil} = 12 psig) and high oil pressure (♦, P_{water} = 2 psig and P_{oil} = 12 psig). Representative images of Videos A.1a-d are presented in Fig. 3.3b. At high water pressure (■), the greater water volume fraction led to each drop filling the full length of the exit channel and partially extending into the collection channel before drop break-up occurred, a phenomenon not seen with the other three combinations. As drop formation is no longer fully constrained by the flow focusing junction, this extension of the drop into the collection channel may explain the greater polydispersity at this condition, where D_{drop} = 83.9 ± 12.5 μm. At low and high combined pressure conditions (▼, ▲, both at P_{water}/P_{oil} = 0.67), drop formation occurred within the exit channel, creating smaller, more monodisperse drops at the high pressure condition (▲, D_{drop} = 56.2 ± 2.6 μm) than the low pressure condition (▼, D_{drop} = 68.8 ± 5.0 μm). Drop monodispersity did not improve with a higher oil volume fraction (♦ CV = 6.0%) when compared to the high combined pressure condition (▲, CV = 4.6%). As the oil volume fraction was increased, drop formation was limited by the 50 μm width of the exit

channel, a characteristic of drop formation in the dripping regime.[106, 107] The dripping regime forms highly monodisperse drops, whose diameters are largely determined by the flowrates and the width of the flow focusing junction.[106, 108, 109] For all the conditions observed, drop break-up occurred at the flow focusing junction which indicates that drop formation was in the dripping regime.[106, 108]

The size of drops formed in the dripping regime can be described by a drop scaling law[110], thereby providing a predictive drop formation model for the PCC. A drop scaling law[110] developed for T-junction geometries, and shown to be applicable for flow focusing geometries[111], is fit to the data and defined as:

$$\frac{L_{drop}}{w_{channel}} = 1 + \alpha \frac{Q_{water}}{Q_{oil}} \qquad \text{(Eq. 3.1)}$$

where L_{drop} is defined as the length of a drop in the channel measured end to end, $w_{channel}$ is the width of the channel (50 μm), Q_{water}/Q_{oil} is the volumetric flowrate ratio, and α is a geometric constant of order 1. To apply the scaling law to our data, pressure ratios are converted to flowrate ratios using a standard curve (Fig. A.1). L_{drop} from Eq. 3.1 is converted to drop volume V_{drop} by approximating the shape of the drop as a capsule geometry when drops are elongated within the microfluidic channel (see Appendix A, *PCC Drop Formation Characterization* for details). A best fit of the drop scaling law with V_{drop} plotted as a function of Q_{water}/Q_{oil} is presented as a dotted line in Fig. 3.3c with $\alpha = 1.70$ and an $R^2 = 0.793$.[110] Drops produced using the PCC can be adjusted by tuning the pressures applied to the oil and aqueous phases, thereby adjusting Q_{water}/Q_{oil} and enabling the generation of drops within a desired range of diameters (≈50-90 μm).

Drop monodispersity improved from a CV of 14.9% to 4.6% as Q_{water}/Q_{oil} was decreased from 2 to 0.17 (Fig. 3.3c). When $Q_{water}/Q_{oil} < 1$, further reductions in Q_{water}/Q_{oil} have diminishing effects on V_{drop}. In this case, the minimum drop volume (65 pL, correlating to D_{drop} = 50 μm) is reached as $Q_{water}/Q_{oil} \rightarrow 0$ due to the 50 μm width of the drop channel ($L_{drop} \approx w_{channel}$ according to Eq. 3.1). Interestingly, despite the low and high combined pressure conditions having the same pressure ratio and similar measured flowrate ratios (Q_{water}/Q_{oil} = 0.43 or 0.53, respectively), they produced drops with different V_{drop}, from 173 ± 37 pL to 94 ± 13 pL. The difference in V_{drop} for similar Q_{water}/Q_{oil} at higher oil flowrates may be attributed to an increased oil phase capillary number *Ca* which represents the ratio of the viscous drag to surface tension forces acting on a drop. A higher oil phase *Ca* corresponds to increased drag at the drop formation junction which leads to faster break-up, resulting in a decreased V_{drop}.[106, 111]

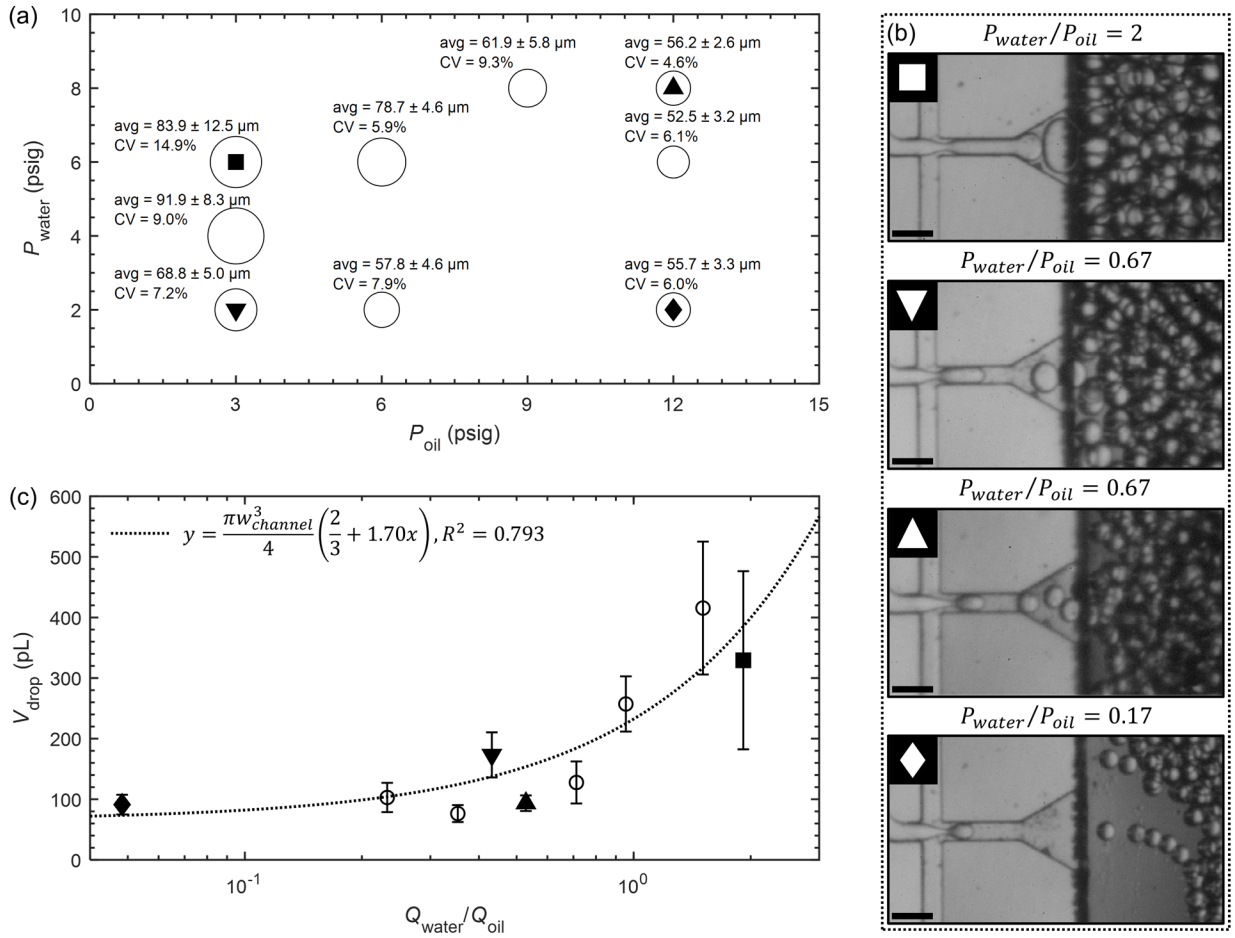


Fig. 3.3. Characterization of drop sizes produced by the PCC. (a) Drop diameter average, standard deviation, and CV at various water pressures P_{water} and oil pressures P_{oil}. For additional visualization, the relative size of each open circle corresponds to the relative mean drop diameter measured. Solid shapes indicate conditions used for high-speed image capture in (b). (b) High-speed image capture of drop formation, ordered by descending D_{drop}, for high water pressure (■, P_{water} = 6 psig and P_{oil} = 3 psig, P_{water}/P_{oil} = 2), low combined pressure (▼, P_{water} = 2 psig and P_{oil} = 3 psig, P_{water}/P_{oil} = 0.67), high combined pressure (▲, P_{water} = 8 and P_{oil} = 12 psig, P_{water}/P_{oil} = 0.67), and high oil pressure (♦, P_{water} = 2 psig and P_{oil} = 12 psig, P_{water}/P_{oil} = 0.17) conditions. Scale bars = 100 µm. (c) Corresponding drop volumes V_{drop} versus the volumetric flowrate ratio Q_{water}/Q_{oil}. V_{drop} scales with Q_{water}/Q_{oil} following a drop scaling law (dotted black line).[110] Error bars represent one standard deviation from the mean.

Signal Discrimination in Barcoded Drop Libraries

The PCC was used to create two types of fluorescently barcoded drop libraries consisting of two-color combinations of either microbeads or QDs. The libraries were prepared by mixing

different ratios of each color to form distinct combinations on a microtiter plate (Materials and Methods). The polystyrene microbead drop library was comprised of 24 barcodes made from ratios of green and red fluorescent polystyrene microbeads while the QD drop library was comprised of 192 barcodes made from ratios of 625 nm and 705 nm QDs. The PCC was used to simultaneously encapsulate all the contents of the plate in 2 min, creating $\approx 3.75 \times 10^5$ drops (D_{drop} = 50 μm) per barcode. Barcoded drops are reinjected into a microfluidic device for analysis using a custom-built detection system[20] that measures drop fluorescence as the drops flow past a laser. Measurements are taken at 300 Hz and $\approx 1.8 \times 10^4$ drops can be read in 1 min.

Contributions from spectral crosstalk and sources of noise limit the number of barcodes that can be identified after library reinjection. The narrow emission spectra of QDs enables fluorescence signal distributions that are more tightly spaced with smaller coefficients of variation than possible using fluorescent microbeads. This can be observed in the raw data of the 24 microbead fluorescence intensities (Fig. 3.4a) compared to the 192 QD fluorescence intensities (Fig. 3.4b). Furthermore, due to the wide emission spectra of the microbeads, the emission spectrum of the green microbeads overlaps with the red microbeads. This causes barcodes with high green intensity to appear more red, skewing the data to the upper right (Fig. 3.4a). We applied a clustering algorithm, Density-Based Spatial Clustering of Applications with Noise (DBSCAN), to identify and separate "clusters" of specific barcoded drops within the libraries.[102] DBSCAN assigns densely packed data points to clusters and outlier data points in low-density regions are marked as noise. When the data is graphed on a linear plot, DBCAN was able to group 70% of the 1.31×10^4 drops containing microbeads into 24 clusters (Fig. 3.4a, blue dots) and 30% as noise (Fig. 3.4a, black dots), with a mean of 399 ± 201 drops per barcode (CV

= 50.4%). However, DBSCAN was not able to completely identify clusters in the QD raw data (Fig. 3.4b, blue dots). Of the clusters identified, DBSCAN grouped 76% of the 1.27×10^5 drops containing QDs with a range of 15 to 6,033 drops per barcode (mean of 508 ± 478 drops and CV = 94.1%). A significant number of clusters were mislabeled as noise (Fig. 3.4b, upper right black dots) due to the large variability in cluster density.

To better distinguish between barcode clusters to inform rescaling of the raw data, we identify two major sources of variation in our data, both of which are a direct consequence of particle size: *Poisson loading* for microbeads and *shot noise* for QDs. The loading of ≈1-μm diameter fluorescent microbeads into drops is dependent upon Poisson statistics. The fluorescence signal obtained from drops containing microbeads follows a Poisson distribution due to the discrete nature of particle loading in drops.[20] The Poisson distribution is described by the equation:

$$P = \frac{\lambda^k e^{-\lambda}}{k!} \qquad \text{(Eq. 3.2)}$$

where P is the probability distribution of drops that contain k number of particles with a mean number of particles per drop λ. Variability inherent to Poisson loading[20] is represented by the standard deviation of the number of particles in drops $\sigma_{\text{particle}} = \lambda^{1/2}$. We plot a representative subset of five red microbead barcodes (Fig. 3.4c, black dots) corresponding to the clusters in Fig. 3.4a (dashed red boxes). The subset is compared to estimated Poisson distributions centered around the microbead loading concentrations λ = 33, 83, 149, 232, and 333 beads/drop where λ is converted to voltage using an experimentally-verified linear standard curve relating PMT intensity (V) to microbead concentration (beads/drop, λ) (Fig. A.6a). The probability of

microbead distributions (Fig. 3.4c, dashed red line) closely tracks the PMT voltage measurements of the red microbead data (Fig. 3.4c, black dots) with $R^2 = 0.931$.

When the particle size is far below the objective resolution, for example in the case of QDs that are ≈10 nm diameter, the variability in drop fluorescence is no longer a function of the number of discrete particles in drops, but is instead governed by the shot noise of the PMT. Shot noise is inherent to counting photons with a PMT and contributes to the fluorescence signal in low light environments such as high-speed detection of drop fluorescence.[112, 113] We plot the signal distributions of a 12 QD625 barcode subset of the QD barcoded library (Fig. 3.4d, black dots) corresponding to the clusters outlined in Fig 4b (dashed green boxes). The Schottky equation approximates shot noise[113, 114] in which the standard deviation of the PMT voltage σ_{shot} is proportional to the square root of the mean PMT voltage $\mu_{intensity}$ (see Appendix A, *Schottky Equation* for details). The subset of QD data is compared to normal distributions defined by $\mu_{intensity}$ and σ_{shot} for each QD barcode. The value of $\mu_{intensity}$ is determined by an experimentally-verified linear standard curve relating PMT intensity (V) to QD concentration (nM) (Fig. A.6b, Eq. A.1). The probability of QD distributions (Fig 4d, dashed green line) closely tracks the PMT voltage measurements of the QD625 data (Fig 4d, black dots) with $R^2 = 0.852$.

To demonstrate that the remainder of the experimental microbead and QD barcode data follow either Poisson loading or shot noise, barcode clusters are manually grouped and compared to theoretical estimates of $\sigma_{particle}$ (Fig. 3.4c-d, inset, dashed red line) and σ_{shot} (Fig. 3.4c-d, inset, dotted green line, see Appendix A, *Calculation of Noise* for details). Drop library fluorescence data are manually grouped by drawing lines around each cluster by eye (Fig. A.5) to isolate individual barcode signal populations for each PMT channel. The mean $\mu_{barcode}$ and standard

deviation σ_{barcode} of the manually-segmented 24 microbead and 192 QD signal distributions are calculated for each PMT channel, yielding 48 and 384 values of μ_{barcode} and σ_{barcode}. The σ_{barcode} is plotted against $\mu_{\text{barcode}}^{1/2}$ for each grouped microbead and QD barcode population (Fig. 3.4c-d, inset, black dots). The experimental σ_{barcode} of the microbeads closely follows the theoretical estimate of particle loading noise σ_{particle} (Fig. 3.4c, inset, dashed red line). The σ_{barcode} is approximately an order of magnitude greater than the theoretical estimate of shot noise σ_{shot} (Fig. 3.4c, inset, dotted green line). Therefore, across all drops, the discrimination of microbead barcode signals is limited by particle loading noise as the dominant source of variation. By contrast, the experimental σ_{barcode} of the QDs closely follows the theoretical estimate of shot noise σ_{shot} (Fig. 3.4d, inset, dotted green line) and is approximately an order of magnitude greater than the estimate of particle loading noise σ_{particle} (Fig. 3.4d, inset, dashed red line), indicating the data is shot noise-limited. The narrow emission spectrum of the QDs results in a 1-2 log decrease of σ_{shot} compared to σ_{particle}. This enables an 8× increase in unique barcodes concentrations obtained with QDs compared to microbeads (192 versus 24).

As signal variation depends upon Poisson loading for microbeads ($\sigma_{\text{particle}} \propto \lambda^{1/2}$) and shot noise for QDs ($\sigma_{\text{shot}} \propto \mu^{1/2}$), scaling the intensity data for both barcode libraries by a square root function linearizes the noise. This scaling spaces each barcode grouping as shown in Fig. 3.4e-f. When DBSCAN is applied to the scaled data, the increased spacing allows for improved clustering of each barcode compared to the unscaled raw data (Fig. 3.4a-b). Of the 1.31×10^4 microbead barcoded drops detected, DBSCAN was able to group 74.8% of the data into 24 clusters (Fig. 3.4e, blue dots) and identify 25.2% as noise (Fig. 3.4e, black dots) with a mean of 408 ± 62 drops per barcode (CV = 15.2%). The CV of clustered square root scaled data

is greatly reduced from 50.4% with the linearly scaled data (Fig. 3.4a) to 15.2% with the square root scaled data (Fig. 3.4e). Additionally, a square root scaling of the QD data allows DBSCAN to correctly identify 188 out of the 192 of barcoded drop populations where the missing four populations are due to two clogged drop makers on the PCC and are indicated by the yellow ovals (Fig. 3.4f). Of the 1.27×10^5 QD barcoded drops detected, DBSCAN was able to group 85.4% of data into 188 clusters (Fig. 3.4f, blue dots) and identify 14.6% as noise (Fig. 3.4f, black dots) with a mean barcode cluster size of 576 ± 88 drops (CV = 15.3%). Once again, the CV is greatly reduced from 94.1% with the linearly-scaled quantum dot data to 15.5% with the square root-scaled data.

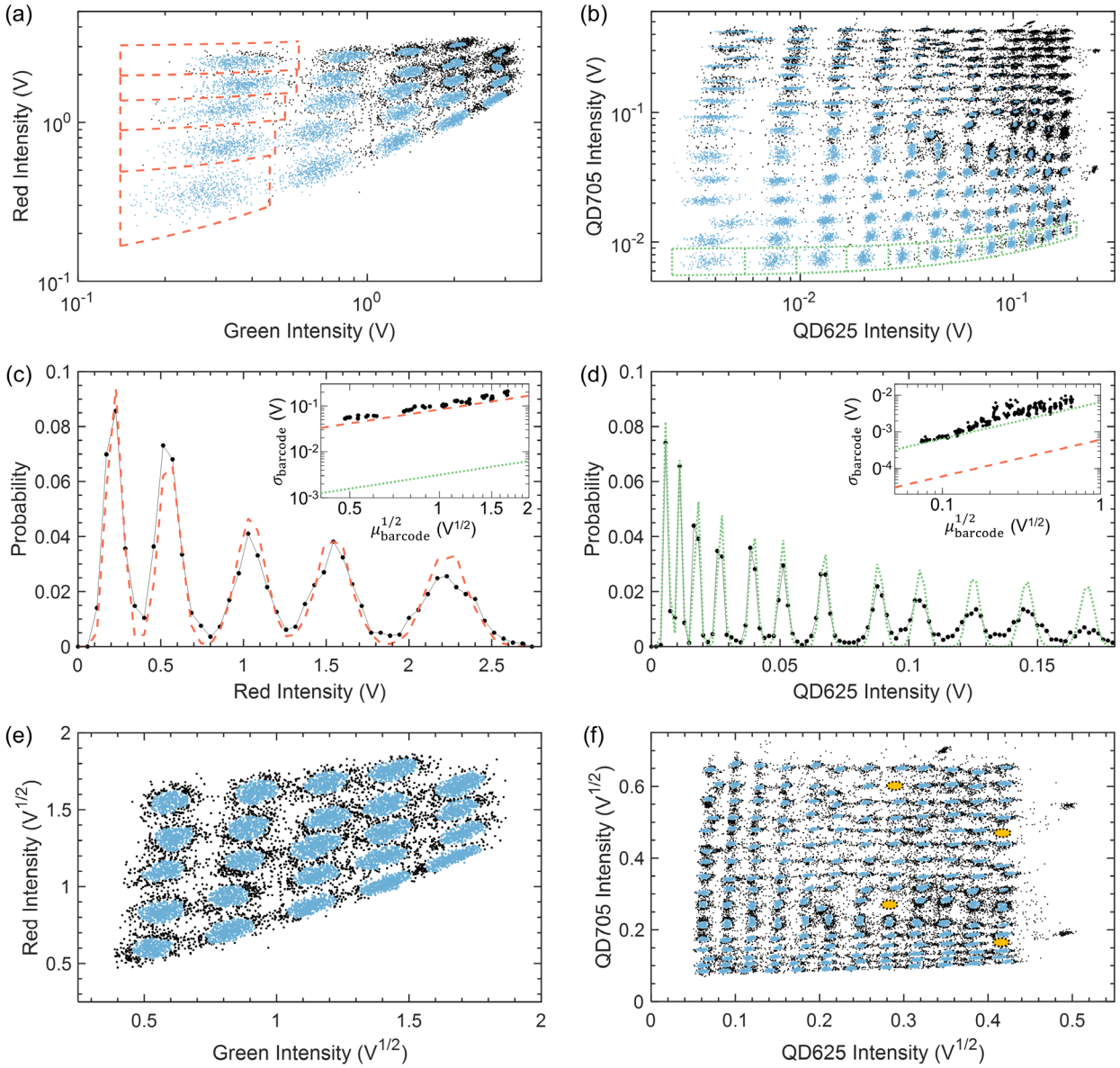


Fig. 3.4. Analysis of microbead and QD barcoded drop libraries. Scatter plots of (a) microbead and (b) QD fluorescence intensity in the drop library. Clusters identified by DBSCAN are indicated in blue while noise is in black. Probability distributions of (c) five red microbead barcoded drop populations (black dots) plotted against the particle loading noise estimate (dashed red line, $R^2 = 0.931$) and (d) twelve QD625 barcoded drop populations (black dots) plotted against the shot noise estimate (dotted green line, $R^2 = 0.852$). Solid black lines guide the eye for the measured microbead and QD625 data. Inset (c-d): standard deviations of each barcode σ_{barcode} (black dots) plotted against $\mu_{\text{barcode}}^{1/2}$ with estimates for σ_{particle} (dashed red line) and σ_{shot} (dotted green line). Scatter plots of (e) microbead and (f) QD drop library data scaled by $V^{1/2}$. Clusters identified by DBSCAN are indicated in blue while noise is in black. Missing clusters in (f) are due to two clogged channels in the PCC and are indicated by dotted yellow ovals.

Sample Isolation Using Fluorescence-Activated Drop Sorting

To demonstrate the utility of the PCC, fluorescence-activated drop sorting[20, 101] was performed to isolate drops of a single barcode population within a drop library of 24 green and red microbead combinations spiked with four concentrations of blue microbeads. We verify that the desired green and red barcode combination was isolated by detecting a single concentration of the blue microbeads. A barcode from the drop library was chosen by designating a box with upper and lower fluorescence intensity bounds in the green and red fluorescence channels (Fig. 3.5a, red box). Recovery of the desired barcode population is confirmed by performing flow-based fluorescence detection on the sorted drops, yielding an isolated barcode cluster with intensity bounds close to those originally chosen in the green and red channels (Fig. 3.5b). However, there is an observed shift in fluorescence signal distribution from pre- to post-sort (Fig. 3.5a-b) where the post-sort data has shifted by ≈0.2 V along the *x*-axis. This shift is likely caused by run-to-run variation arising from the positioning of the laser in the device channel or by partial photobleaching of the microbeads. Post-processing of the sorted drop data using DBSCAN provides a clear distinction between the target barcode population (Fig. 3.5b, red dots) and the outlier data points (Fig. 3.5b, open black circles). The outlier points comprise 7.5% of the drop data.

The four populations of blue microbead-barcoded drops were detected in the pre-sort drop library (Fig. 3.5c). Fluorescence detection of the sorted drops yielded a single blue microbead population with few outliers (Fig. 3.5d), matching the highest blue microbead concentration (Fig. 3.5c, arrow). DBSCAN clustering of corresponding green and red fluorescence identifies these outliers (Fig. 3.5d, black bars) and the target sorted population (Fig. 3.5d, red bars). The outliers comprise 5.9% of the sorted population, in close agreement with the

data corresponding to the green and red barcoded drops (Fig. 3.5b). These results demonstrate the ability to isolate a single barcoded population from a drop library created using the PCC, critical for performing downstream assays.

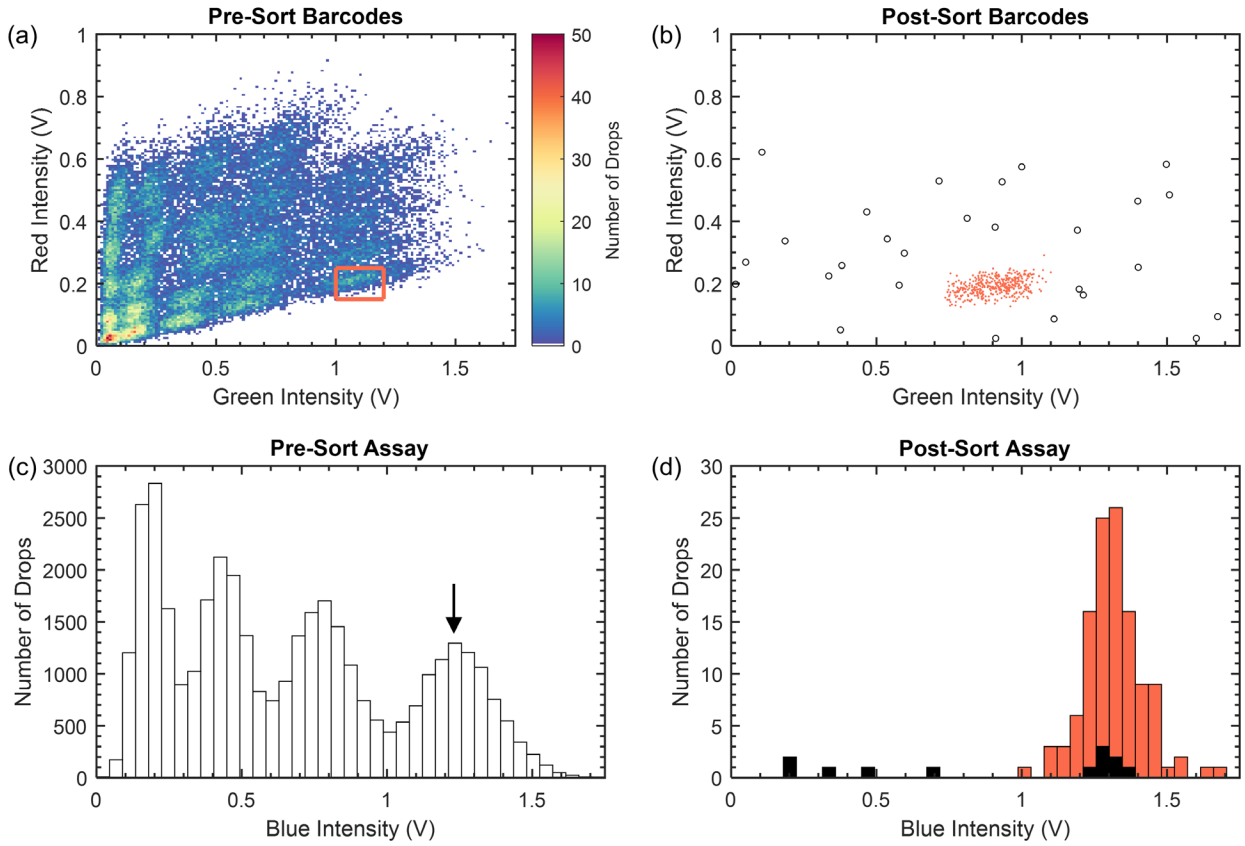


Fig. 3.5. Fluorescence activated drop sorting of a microbead-barcoded drop library (a) Fluorescence intensity of barcoded drops before sorting. The sorted region is indicated by the red box. (b) Fluorescence intensity of barcoded drops after sorting. DBSCAN is used to separate the outlier data points (open black circles) from the target barcode population (red dots). (c) Distribution of four concentrations of blue microbead drops within the drop library. (d) Distribution of blue microbeads in the sorted barcoded drop population shows a single peak corresponding to the largest concentration of blue microbeads. DBSCAN is used to separate the outliers (black bars) from the target sorted population (red bars).

Conclusion

Rapid generation of a fluorescently barcoded drop library is demonstrated with the PCC and is the first reusable device to our knowledge that interfaces directly with a 384-well microtiter plate, eliminating the need for multiple pump sources or liquid handling systems when performing simultaneous sample encapsulation. Previous work achieved parallel encapsulation from a microtiter plate, but required permanently attaching drop making devices to each well and was limited to 24 wells at a time.[100] Drop formation in the PCC is described by a drop scaling law which provides a method for tuning the size of drops produced.

The PCC was used to create barcoded drop libraries containing fluorescent microbeads and QDs. The libraries are screened using a drop-based fluorescence detection method and barcode populations are identified using data clustering (DBSCAN). The signal variation of the barcodes is dependent upon Poisson loading for microbeads and shot noise for QDs. QDs resulted in narrow barcode signal distributions, which allowed more discrete barcode combinations to be measured compared to microbeads, within the same dynamic range of the detection system. Upon optimization with a third color with 16 unique labels, QDs could easily barcode up to eight 384-well microtiter plates, or 3,072 barcodes ($12 \times 16 \times 16$).

Drop libraries barcoded with fluorescence-based barcodes have recently reached a label count of 1,050 unique combinations with the use of four dye colors.[84] Lanthanide nanophosphors are capable of creating up to 1,023 unique labels with a six color combination, but have yet to be used in drop libraries.[115] However, using a large number of barcode colors may not be advantageous, as the overlap of emission spectra between the fluorescent reporters can limit the practical number of colors that can be used in an assay.[116, 117] Simply reducing the number of

barcode colors to one or two and varying their concentrations can greatly expand the range of usable reporters. Previous examples of drop libraries using one or two fluorescence dye colors have realized up to eight[90] or sixteen[91] unique labels. Using the PCC, we achieved a total of 188 discrete barcodes with two-color combinations of QDs. To our knowledge, this is the largest two-color fluorescent barcode combination in drops to date.

The PCC enables the generation of up to 96 different drop conditions in parallel by interfacing individual drop makers with a standard microtiter well plate. This single microfluidic device was reused here to rapidly generate up to 192 unique optical barcodes in a drop library. Finally, we show that barcoded populations with minor signal overlap can be sorted from a drop library with minimal error, thereby enabling downstream analysis of a specific sample population. We envision that the PCC will further advance current multiplexed assays, such as combinatorial drug screening,[83, 90] DNA microarray analysis,[91] or screening of enzyme activity[92] by reducing sample encapsulation time and enabling rapid, parallel generation of a barcoded library from a microtiter plate.

Conflicts of Interest

There are no conflicts to declare.

Acknowledgments

This work was supported by Defense Advanced Research Projects Agency (DARPA) grant W911NF-17-2-0034, National Institutes of Health (NIH) 1R21Al151923, and National Science Foundation (NSF) CAREER DMR-1753352. We thank Rick Uchida and Satoru Ohishi (TOK – Tokio Ohka Kogyo Ltd) for providing a free sample of the TMMF S2030 dry-film photoresist, Joshua Ricouvier, Stan Cotreau for help with machining, and Betsey Pitts for help with confocal imaging. R.A.S. gratefully acknowledges financial support from the German Research Foundation (DFG), grant SP 1282/1-1. G.K.Z. acknowledges financial support from Montana State University Office of the Provost.

CHAPTER 4

SCREENING OF ADDITIVE FORMULATIONS ENABLES OFF-CHIP DROP REVERSE TRANSCRIPTION QUANTITATIVE POLYMERASE CHAIN REACTION OF SINGLE INFLUENZA A VIRUS GENOMES

Contribution of Authors and Co-Authors

Manuscript in Chapter 4

Author: Emma Kate Loveday

Contributions: E.K.L. and G.K.Z. contributed equally to this work, E.K.L. designed research, performed research, analyzed data, and wrote the manuscript

Author: Geoffrey K. Zath

Contributions: E.K.L. and G.K.Z. contributed equally to this work, G.K.Z. designed research, performed research, analyzed data, and wrote the manuscript

Co-Author: Dimitri A. Bikos

Contributions: D.A.B. designed research, performed research, and wrote the manuscript

Co-Author: Zackary J. Jay

Contributions: Z.J.J. performed research

Co-Author: Connie B. Chang

Contributions: C.B.C designed research and wrote the manuscript

Manuscript Information

Emma Kate Loveday, Geoffrey K. Zath, Dimitri A. Bikos, Zackary J. Jay, Connie B. Chang

Analytical Chemistry

Status of Manuscript:
____ Prepared for submission to a peer-reviewed journal
____ Officially submitted to a peer-reviewed journal
____ Accepted by a peer-reviewed journal
__X_ Published in a peer-reviewed journal

American Chemical Society
Volume 93, Issue 10
DOI: 10.1021/acs.analchem.0c03455

Reproduced with permission from:

"Loveday, E. K.; Zath, G. K.; Bikos, D. A.; Jay, Z. J.; Chang, C. B., Screening of Additive Formulations Enables Off-Chip Drop Reverse Transcription Quantitative Polymerase Chain Reaction of Single Influenza A Virus Genomes. *Analytical Chemistry* **2021**"

Copyright 2021 American Chemical Society

You can view the full text of this article at: http://pubs.acs.org/articlesonrequest/AOR-EFA6DTJX7FKBDV4XPGWP

Abstract

The miniaturization of polymerase chain reaction (PCR) using drop-based microfluidics allows for amplification of single nucleic acids in aqueous picoliter-sized drops. Accurate data collection during PCR requires that drops remain stable to coalescence during thermocycling and drop contents are retained. Following systematic testing of known PCR additives, we identified an optimized formulation of 1% w/v Tween-20, 0.8 μg/μl BSA, and 1M betaine in the aqueous phase and 3 wt% (w/w) of PEG-$PFPE_2$ surfactant in the oil phase of 50 μm diameter drops that maintains drop stability and prevents dye transport. This formulation enables a method we call Off-Chip Drop Reverse Transcription quantitative PCR (OCD RT-qPCR) in which drops are thermocycled in a qPCR machine and sampled at various cycle numbers "off-chip", or outside of a microfluidic chip. Construction of qPCR amplification curves from hundreds of individual drops using OCD RT-qPCR and imaged using epifluorescence microscopy correlate with amplification curves of ~300,000 drops thermocycled using a qPCR machine. To demonstrate the utility of OCD RT-qPCR, influenza A virus (IAV) RNA was detected down to a single viral genome copy per drop, or 0.320 cpd. This work was extended to perform multiplexed detection of IAV M gene RNA and cellular β-actin DNA in drops, and direct amplification of IAV genomes from infected cells without a separate RNA extraction step. The optimized additive formulation and OCD-qPCR method allows for drop-based RT-qPCR without complex devices and demonstrates the ability to quantify individual or rare nucleic acid species within drops with minimal processing.

Introduction

Presymptomatic individuals or those with early viral infections as in the COVID-19 pandemic may not have obvious clinical symptoms.[118, 119] To determine positive confirmation of disease and viral loads in patient samples,[120-122] polymerase chain reaction (PCR) is commonly used to amplify small segments of viral RNA or DNA.[123, 124] The application of PCR has been expanded using drop-based microfluidics, a method that increases the speed, sensitivity, and throughput of nucleic acid detection by reducing experimental volumes into aqueous microdrops separated by an immiscible oil phase and stabilized by surfactants.[31, 125-128]

Two methods of performing PCR in drops include droplet digital PCR (ddPCR)[125, 129] and drop-based quantitative PCR (qPCR).[30, 126, 127, 130] The ddPCR method quantifies nucleic acids via limiting dilution, in which samples containing nucleic acids and PCR reagents are diluted to the extent where each drop contains either zero or at least one template. A PCR endpoint analysis that quantifies the number of fluorescent drops that contain a nucleic acid and dim empty drops are used to calculate the starting sample concentration through Poisson statistics.[131] Currently, the majority of ddPCR applications use proprietary reagent mixtures for producing stable drops and a commercial device to detect drop fluorescence.[125] Similarly, drop-based qPCR assays combine samples with PCR reagents to form picoliter-sized drops; however, limiting dilution is not required. Instead, fluorescent probes are released during nucleic acid amplification as thermocycling proceeds. Fluorescence intensities are converted to concentrations using a calibration curve generated from the cycle thresholds (C_t) of known starting nucleic acid concentrations.[126, 130]

The production of stable aqueous drops for PCR is routinely achieved using biocompatible perfluorinated surfactants suspended in fluorinated oils. A commonly used perfluorinated surfactant is the tri-block copolymer PEG-PFPE$_2$. The PEG group extends into the aqueous drop, making the surfactant biocompatible.[1] However, drops made with PEG-PFPE$_2$ have been shown to destabilize during PCR thermocycling where temperatures cycle between 60 and 95 °C.[45, 72] Additionally, the transport of fluorophores into the surrounding oil or neighboring drops has been shown to occur at time scales relevant to thermocycling.[78, 132, 133] As drop-based qPCR assays rely on the detection of qPCR probes and reference dyes, drop stability and dye retention are critical for the detection and precise quantification of genomic content in drops.

Approaches for maintaining drop stability and dye retention in droplet PCR assays include utilizing high surfactant concentrations (2-5 wt%),[14, 45, 134] small drop sizes (typically <40 μm diameter), and/or incorporating additives. Common additives include polyethylene glycol (PEG), Tween-20, bovine serum albumin (BSA), and betaine. Yet systematic testing of these additives is critically lacking to determine how they improve drop stability and limit transport of small molecules. Though complicated microfluidic chips have been engineered to prevent transport between drops and coalescence by keeping drops completely separated,[135, 136] increasing the stability of drop interfaces using additives can enable thermocycling of a large collection of drops in a tube and subsequent downstream analysis. This would allow for stabilized drops to be sampled at various cycle numbers and analyzed “off-chip”, or outside of a microfluidic chip using common imaging techniques. In addition, while drops are routinely thermocycled[137, 138] and endpoint analysis is usually implemented,[14, 28] sampling of drops

undergoing qPCR has never been performed and correlated to real-time amplification curves. This can allow for nucleic acid quantification in drops, without performing limiting dilution as in ddPCR, and without the need for specialized microfluidic devices that perform qPCR on chip.[126, 130] The correlation of drop fluorescence intensities with qPCR amplification curves would validate future work in miniaturizing qPCR and yielding quantitative template numbers at the droplet level, simply by using a basic PCR thermocycler and a fluorescent microscope common in most laboratories and bypassing the need for extensive engineering expertise.

Here, we screen additive formulations of polyethylene glycol (PEG), Tween-20, bovine serum albumin (BSA), and betaine for their ability to stabilize 50 μm diameter drops during RT-qPCR thermocycling. An additive combination of 1% w/v Tween-20, 0.8 μg/μl BSA, and 1 M betaine in the aqueous phase and 3 wt% (w/w) of PEG-$PFPE_2$ surfactant in the oil phase provided stable drops and dye retention during droplet thermocycling. This result enables a method we call Off-Chip Drop Reverse Transcription quantitative PCR (OCD RT-qPCR). In this method, drops containing unique qPCR additive formulations are created using a microfluidic drop maker, placed in several tubes within a standard qPCR machine, thermocycled, and stopped at various cycle numbers (Figure 4.1). Drops are sampled "off-chip" at various cycle numbers and the fluorescence intensities obtained from sampled drops using epifluorescence microscopy are used to create PCR amplification curves that closely follow real-time amplification curves obtained using the standard qPCR machine. To our knowledge, this correlation between a sample of individual drops at various cycle numbers and a bulk measurement has never been systematically demonstrated.

To demonstrate the utility of OCD RT-qPCR for use in studying single cell infections within drops, we thermocycled drops containing low (10^1 cpd) and high (10^4 cpd) viral RNA concentrations. For both of these RNA concentrations, the qPCR amplification curves generated from epifluorescence measurements of sampled drops using OCD RT-qPCR correlate with qPCR amplification curves generated from measurements of thermocycled drops using a standard qPCR machine. We extend our findings to perform multiplexed detection of two target genomes, the IAV M gene and cellular β-actin. Finally, we demonstrate the ability to perform direct amplification of IAV genomes from infected cells without a separate RNA extraction and quantify IAV down to a single viral genome per drop. Our work can be extended to sampling of drops undergoing PCR thermocycling for the analysis of RNA and DNA nucleic acids of interest and for performing highly quantitative studies of other viruses. Furthermore, our ability to detect viral genomes without nucleic acid extraction is a powerful application of this technology that could be extended to other drop-based qPCR diagnostic approaches and for the study of viral infection at a single cell level.

Experimental Section

Virus Strains and Cell Lines

IAV A/California/07/2009 (H1N1) stocks were propagated on Madin-Darby canine kidney (MDCK) cells in DMEM media supplemented with 10% FBS and 1× penicillin/streptomycin. All experimental infections were performed on human alveolar epithelial A549 cells propagated in Hams F-12 media supplemented with 10% FBS and 1× Pen/Strep.

PCR Sequences and Reaction Concentrations

All primer and probe sequences utilized in this study have been previously published. The sequences of qPCR amplification primers for the IAV Matrix gene (M gene) were designed for use by the CDC: M gene forward primer 5′-GACCRATCCTGTCACCTCTGAC-3′, M gene reverse primer 5′-AGGGCATTCTGGACAAATCGTCTA-3′.[139] The sequence of the M gene TaqMan probe was: 5′-/FAM/TGCAGTCCTCGCTCACTGGGCACG/BHQ1/-3′. For the multiplexing assay, the primers targeting the β-actin plasmid (pCAG-mGFP-Actin, Addgene #21948) were: β-actin forward primer 5'-GTGTGGATCGGCGGCTCCATC-3', β-actin reverse primer 5'-GACTCGTCATACTCCTGCTTG-3' and β-actin TaqMan probe 5'-/Cy5/ACCTTCCAGCAGATGTGGATC/BHQ2/-3'.[140] Samples were amplified using SuperScript III Platinum One-Step qRT-PCR kit (Invitrogen 11732-020) with a final reaction volume of 25 µL. SUPERase RNase Inhibitor was added at 0.32 U/µL (Invitrogen AM2694). Tested additives were added at the following concentrations: 1.0% w/v Tween-20, 0.8 µg/µL BSA, 2.5% w/v PEG-6K, and 1.0 M betaine. Thermocycling was performed in a real-time qPCR machine (QuantStudio 3, Applied Biosystems): 1 cycle for 30 min at 60 °C, 1 cycle for 2 min at 95 °C, and 40 cycles between 15 s at 95 °C and 1 min at 60 °C.

In Vitro Transcribed RNA

Standard curves were generated using serial dilutions of *in vitro* transcribed IAV M gene.[141] To generate the *in vitro* transcribed RNA, a gBlock containing a T7 promoter (underlined), forward and reverse primer sites (italicized), and probe sequence (bold) for the M gene was ordered from IDT: 5′-GTCTAATACGACTCACTATAG *GACCAATCCTGTCACCTCTGAC***TGCAGTCCTCGCTCACTGGGCACG**TGCTTCATCGC GAACTGCTTCGCGGATGCCATCGTCATGGCCACGAGGATATGTAAGAGT*TAGACGAT TTGTCCAGAATGCCCT*-3′. The M gene was transcribed *in vitro* using a MEGAscript T7 RNA Synthesis Kit (Ambion, AM1333) following the manufacturer's instructions that includes a DNAse step prior to being purified over a GE Illustra Sephadex G-50 NICK column. RNA concentration was quantified using a NanoDrop spectrophotometer to determine the copy number per µL. The corresponding concentration in cpd is calculated by multiplying the copies/µL value by the volume of a 50 µm diameter drop (6.54×10^{-5} µL/drop).

Drop Encapsulation

Flow-focusing drop making devices were used to make 50 µm diameter drops for the drop stability and PCR dilution experiments and 100 µm diameter drops for infected supernatant experiments. The continuous phase consisted of a 3 wt% (w/w) solution of PEG-$PFPE_2$-based surfactant (RAN Biotechnologies, 008-FluoroSurfactant) in fluorinated HFE-7500 oil (3M). The dispersed and continuous phases were loaded in 1-mL syringes and injected into the drop making microfluidic devices at a flow rate of 800 µL/h and 1600 µL/h, respectively, for 50 µm diameter drops, and 1000 µL/h and 2000 µL/h, respectively, for 100 µm diameter drops (New Era NE-1000 syringe pumps). Drops were collected in 100 µL PCR tubes for 90 s for 50 µm drops and

72s for 100 μm drops, corresponding to a total volume of 60 μL composed of approximately 20 μL of drops and 40 μL of oil. While the microfluidic device was operated at room temperature, the PCR tubes were kept on a cooling block at approximately -20 °C until placed in the qPCR machine.

Imaging of Drops

Thermocycled drops were imaged with a 10× objective. Brightfield and fluorescence images of FAM TaqMan probe for M gene, Cy5 TaqMan probe for β-actin, and ROX reference dye were captured on an inverted epifluorescence microscope (Leica DMi8) with a 10× objective. Three fields of view (FOV) of drops were imaged for each M gene and supernatant dilution. For multiplexed drops, five FOV images of drops were taken.

Analysis of Epifluorescence Images of Drops
During OCD RT-qPCR Thermocycling

FAM fluorescence intensities were normalized as $\Delta R_N/R_{N,0}$, where the qPCR normalized reporter value R_N is defined as $R_N = I_{FAM}/I_{ROX}$, $\Delta R_N = R_N - R_{N,baseline}$, I_i is the respective intensity of FAM or ROX at each cycle, $R_{N,baseline}$ is the average R_N value of the first three cycles, and $R_{N,0}$ is the initial R_N value.

Analysis of Epifluorescence Images of Endpoint OCD RT-qPCR Drops

FAM and Cy5 fluorescence intensities were normalized by the ROX intensity in each drop and denoted as $R_{N,\,FAM}$ and $R_{N,\,Cy5}$. For Poisson estimates, fluorescence thresholds were set with Otsu's method[142] to distinguish positive and negative drops. This method was applied to the image analysis in presented in Figures 4.3E and 4.5D.

Imaging of Multiplexed OCD-qPCR Drops

M gene (2.62×10^5 copies/μL) and β-actin (6.98×10^4 copies/μL) were encapsulated with qPCR mix in 50 □m diameter drops and thermocycled. Drops were imaged using epifluorescence microscopy to quantify fluorescence from the FAM (6-carboxyfluorescein) dye-labeled TaqMan probe for M gene, Cy5 (Cyanine5 NHS ester, ex. 649 nm, 666 em.) dye-labeled TaqMan probe for β-actin, and ROX (6-carboxy-X-rhodamine) reference dye. Five FOV were captured of drops on the epifluorescence microscope for a total of 1127 drops after pooling from all FOV.

Virus Infections

A549 cells were seeded into 6-well plates with 1×10^6 cells per well. The cells were infected with the H1N1 virus at a MOI of 0.1 in infection media consisting of Hams F-12 supplemented with 1 mM HEPES, 1× Pen/Strep and 0.1% BSA. Infection with the H1N1 virus was performed in the presence of 1 μg TPCK-trypsin/ml.[143] Cells were washed with 1× phosphate buffered saline (PBS) and then incubated with virus for 1 h. The inoculum was removed and replaced with fresh infection media and supernatant was collected at 24 hpi. The resulting supernatant, which contains infectious virus released from the cells, was serial diluted in infection media. The diluted supernatant was then added directly to the optimized OCD-qRT-PCR master mix before encapsulation into drops as described above. The drops were thermocycled and three images of each dilution was used to calculate the ratio of "positive" drops, based on FAM fluorescence, to the number of total drops.

Results and Discussion

OCD RT-qPCR

A schematic of the OCD RT-qPCR method is outlined in Figure 4.1A-C. In this method, drops containing our optimized qPCR additive formulation are created using a microfluidic drop maker and placed in a standard qPCR machine (Figure 4.1A). The qPCR machine is stopped at various cycle numbers, at which a tube is removed, and drops are sampled for epifluorescence imaging (Figure 4.1B). Real-time amplification curves are read using the standard qPCR machine over 40 cycles (solid red line, pseudo-continuous, Figure 4.1C) and compared to amplification curves constructed using drops imaged at various cycle numbers (dashed blue line, discontinuous, Figure 4.1C).

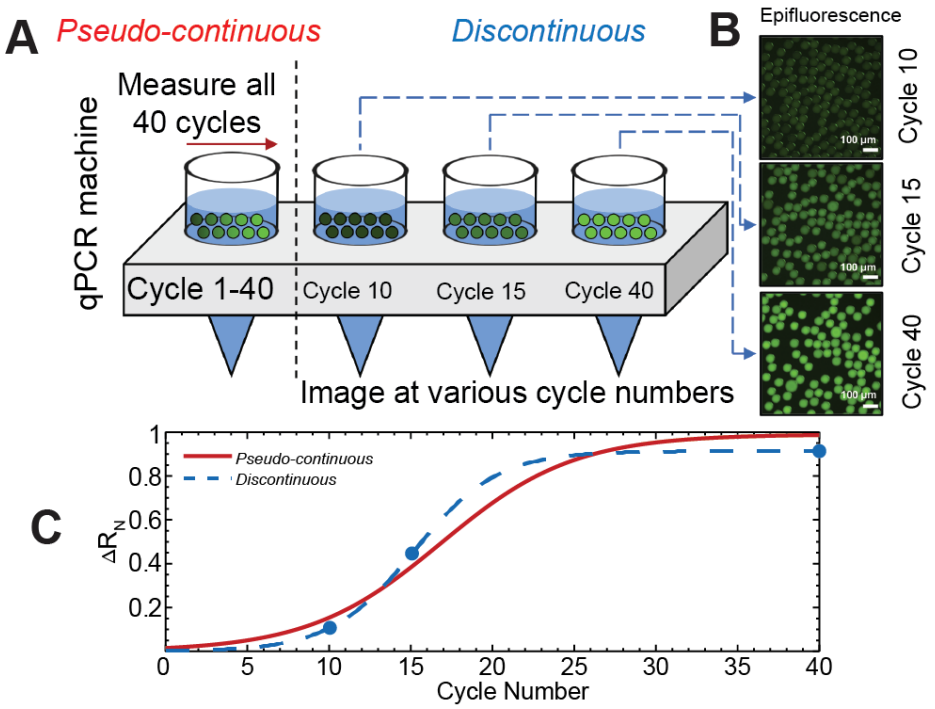


Figure 4.1. Off-Chip Drop Reverse Transcription qPCR (OCD RT-qPCR). (A) Drops containing PCR mix are placed in a standard qPCR machine (B) Fluorescent images of drops are taken at various thermocycles. (C) Real-time amplification curves are read using the standard qPCR machine over 40 cycles (solid red line, pseudo-continuous). Amplification curves are constructed from drops imaged at various cycles (dashed blue line, discontinuous).

Screening Additive Formulations

Though systematic testing of additives, to our knowledge, has never been performed, the additives PEG-6K, BSA, Tween-20, and betaine have been utilized in prior drop PCR assays.[14, 28, 134, 144-147] These additives are thought to enhance reactions and/or the stability of drops under PCR thermocycling. The polyether PEG improves the stability of drops containing high salt content.[72, 148] Additionally, PEG enhances PCR reactions through macromolecular crowding, increasing DNA polymerase activity.[149, 150] The protein BSA has been shown to limit dye diffusion between drops and enhance PCR yields.[133, 151] Tween-20 has been utilized as a co-surfactant for aqueous drops in fluorinated oils[14, 28, 146] to reduce surface tension. Finally, the common PCR enhancer betaine improves PCR amplification of GC rich regions by reducing the formation of nucleic acid secondary structure.[152, 153]

To probe how these PCR additives impact drop stability and dye retention during thermocycling, we measured the effect of Tween-20, BSA, PEG-6K, and betaine individually and in various formulations on the final drop diameter and fluorescence using 3.0 wt% of PEG-$PFPE_2$ as the primary surfactant. All drops contain a TaqMan-based qPCR assay to detect and quantify *in vitro* transcribed M gene IAV RNA. The M gene is highly conserved across different IAV species,[139, 154] making it a frequently used standard target for detection. As a no-additive control, drops were produced from a solution of qPCR mix containing 10^7 copies/μL (≈171 cpd) of M gene. To test additive formulations, the reaction mixture was supplemented with: Tween-20 / PEG-6K; Tween-20 / BSA; and Tween-20 / BSA / betaine. Drops were imaged on an epifluorescence microscope following thermocycling to assess drop stability from drop diameter measurements and retention of the ROX reference dye from fluorescence intensity measurements.

Drops that contained no additives, BSA, PEG-6K, or betaine alone showed evidence of extensive coalescence (Figure 4.2A). Post-thermocycling drop diameters D were compared to initial D_0 with no PCR additives ($D_0 = 61.1\ \mu m \pm 0.8\ \mu m$). Normalized diameters $(D\text{-}D_0)/D_0 \approx 0$ indicate stability. Values of $(D\text{-}D_0)/D_0$ in Figure 4.2B demonstrate that drops containing no additives or only one additive of BSA, PEG-6K, or betaine deviated highly from zero, had a wide distribution of diameters, and produced a large number of outliers indicating coalescence. The addition of Tween-20 alone to the qPCR mix resulted in a narrow distribution of drop diameters with a slight decrease in size ($(D\text{-}D_0)/D_0 = -0.12$, Figure 4.2B, red box). As the addition of Tween-20 prevented coalescence, we tested PEG-6K, BSA, and both BSA and betaine in combination with Tween-20. This resulted in $(D\text{-}D_0)/D_0 < 0$ and lowered coefficients of variation (CV) more effectively than with no additives and with each of the additives alone (Figure 4.2B, *SI Appendix B*, Table B.1). The formulation of Tween-20 / BSA / betaine resulted in $(D\text{-}D_0)/D_0 = -0.04$ with very few outliers, indicating these drops were the most stable to coalescence upon thermocycling (Figure 4.2B, orange box).

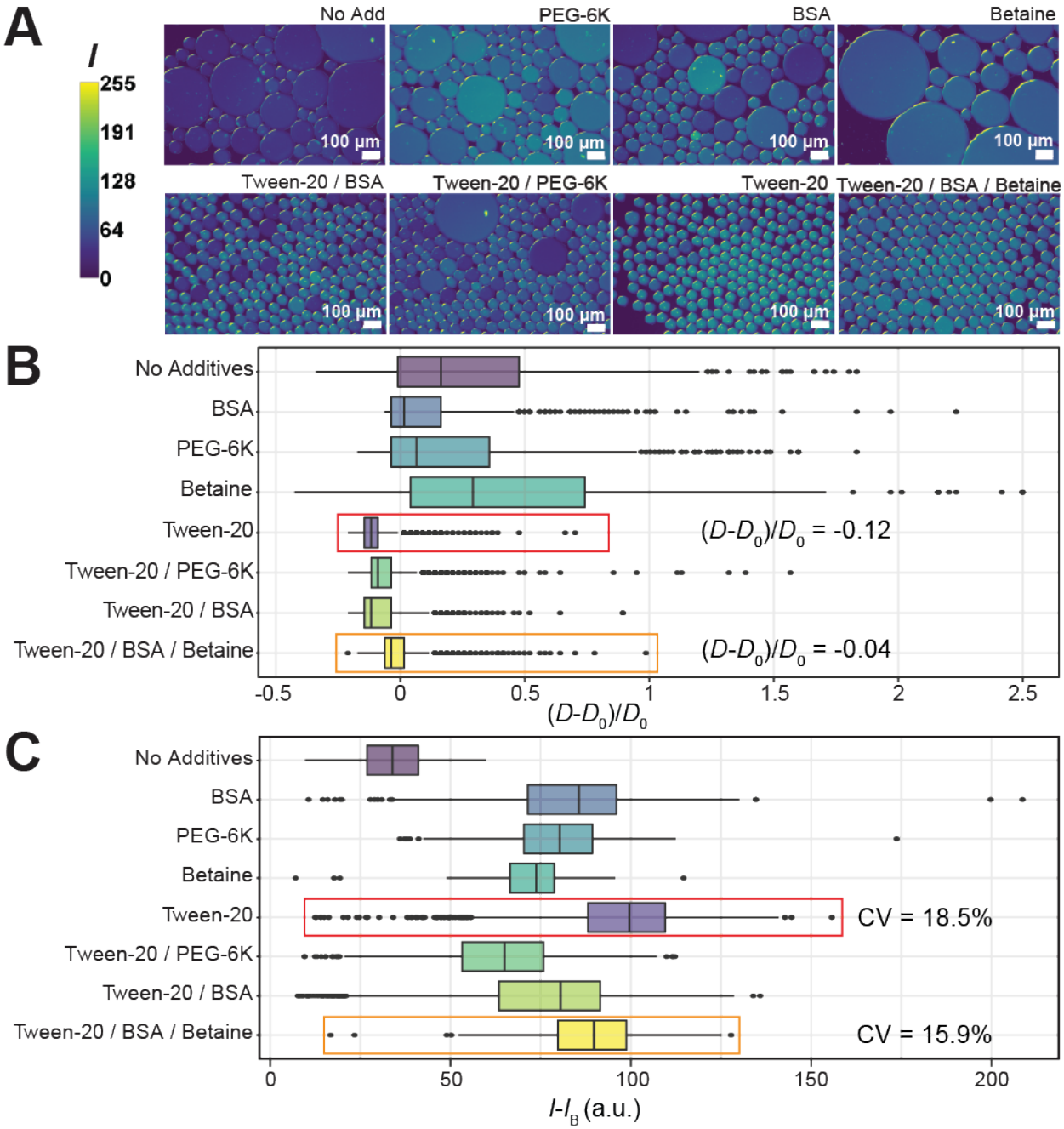


Figure 4.2. Screening of drop additives for PCR. (A) Representative epifluorescence images of drops after thermocycling. Fluorescence intensity I of ROX dye is quantified from 8-bit pixel values and ranges from 0 (low) to 255 (high). (B) Effects of additives on drop size. Boxplots represent values of normalized diameters, $(D\text{-}D_0)/D_0$. (C) Effects of additives on dye retention within drops. Boxplots represent values of normalized mean ROX fluorescence intensity within drops, $I\text{-}I_B$.

We investigated the retention of ROX reference dye within drops after thermocycling. The ROX fluorescence intensity I of each drop was normalized by subtracting the background signal I_B. The value I-I_B of each drop quantified retention of the reference dye (Figure 4.2C). A lower value of I-I_B indicates that ROX diffused out of the drops into the oil and not between neighboring drops. To verify this, we compared I_B for all additive conditions and found that the background fluorescence intensity was highest for the no additive condition (*SI Appendix B*, Figure B.2), indicating that all additives had a positive effect on ROX retention in drops.

A smaller CV of I-I_B within drops indicates less variability in ROX measurements, ideal for normalizing the TaqMan probe signal that increases during qPCR. An ideal additive formulation for dye retention has high I-I_B and small CV (Figure 4.2C). With no additives, there is significant ROX transport out of the drops and I-I_B = 33.6 a.u., the lowest of all eight conditions tested. ROX retention is improved with Tween-20 alone and Tween-20 / BSA / betaine. Tween-20 had the highest I-I_B at 99.6 a.u. (Figure 4.2C, red box) compared to the Tween-20 / BSA / betaine formulation with I-I_B = 89.7 a.u. (Figure 4.2C, orange box). However, the Tween-20 / BSA / betaine formulation resulted in a smaller CV (15.9%) of I-I_B compared to the Tween-20 only condition (18.5%). Based on our results, the additive formulation of Tween-20 / BSA / betaine had the lowest $(D\text{-}D_0)/D_0$ with relatively high overall ROX fluorescence intensity and the lowest CV of fluorescence intensity. Thus, we apply this optimized additive formulation in subsequent experiments. Numbers of drops measured and statistical information from Figures 4.2B and 4.2C can be found in *SI Appendix B*, Table B.1.

Dilution Series Verifies Efficiency of Drops Versus Bulk

To evaluate the reaction efficiency of PCR amplification in drops, we performed a drop dilution series of *in vitro* transcribed RNA compared to conventional bulk dilutions. Standard curves relating cycle threshold (C_t) values to $\log_{10}$ dilutions of M gene RNA concentrations were generated for drop and bulk reactions. Serial dilutions for the bulk reactions ranged from $2.62 \times [10^4$ to $10^9]$ copies/μL. When loaded into 50 μm diameter drops, with a volume of 65 pL, this corresponds with $1.71 \times [10^{-1}$ to $10^4]$ cpd. Amplification curves obtained using qPCR in conventional bulk reactions (Figure 4.3A, solid lines) follow the same trend as in drops (Figure 4.3A, dotted lines).

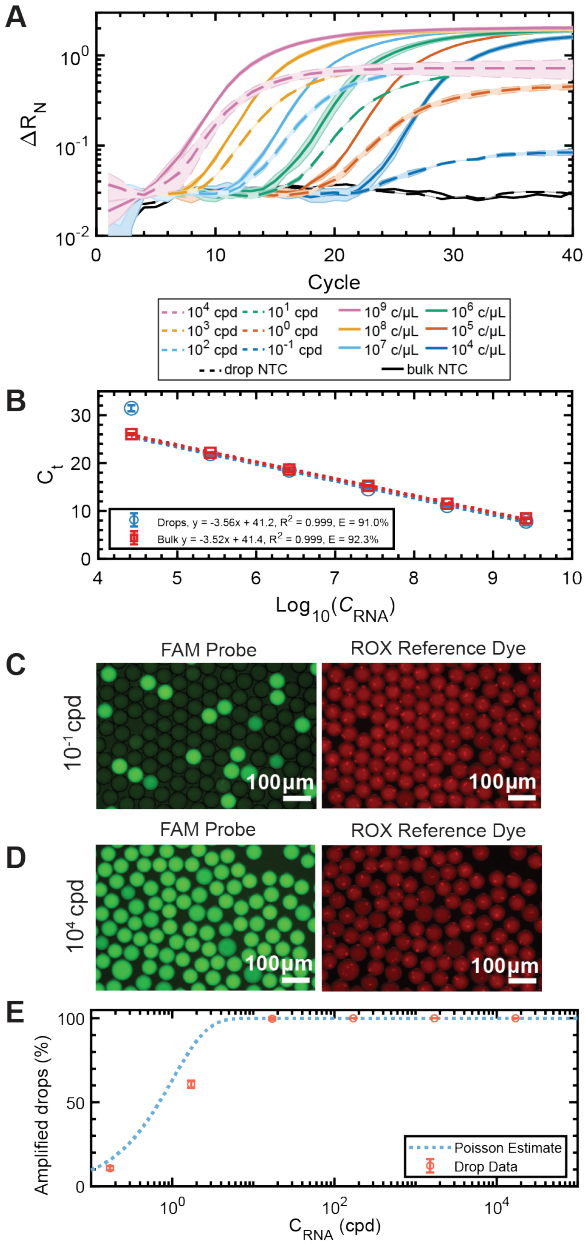


Figure 4.3. Dilution series of *in vitro* transcribed IAV M gene in bulk and in drops. (A) Amplification curves of six 10-fold dilutions of M gene RNA amplified in bulk (solid line) ranging from 2.62 × [10^9 to 10^4] copies/μL and drops (dashed lines) ranging from 1.71 × [10^4 to 10^{-1}] copies per drop (cpd). No template controls (NTC) are included for bulk and drop conditions. (B) C_t standard curves for the bulk (red, y = -3.52x + 41.4, R^2 = 0.999) and drop (blue, y = -3.56x + 41.2, R^2 = 0.999) amplification curves. The PCR efficiency in drops was 91.0% and 92.3% for bulk. Representative epifluorescence images of the FAM (reporter) and ROX (reference) channels of drops containing (C) 10^{-1} cpd and (D) 10^4 cpd after 40 thermocycles. (E) Percentage of amplified drops as a function of RNA concentration C_{RNA}. The total percentage of bright drops (red circles) increases as a function of RNA concentration and closely follows the Poisson estimate with R^2 = 0.929 (blue dotted line).

The C_t values of drops and bulk dilutions were used to generate standard curves. The slopes of the curves yielded an amplification efficiency of 91.0% in drops and 92.3% in bulk (Figure 4.3B). Both fall within typical efficiencies of 90-110%,[155, 156] where 100% indicates all cDNA is multiplied by a factor of two upon completion of every cycle. Reactions with PCR efficiencies outside this range will limit the assay dynamic range and sensitivity. We hypothesize that the lower drop efficiency is due to sequestration of reagents and an earlier exhaustion of reagents compared to bulk. Nonetheless, there is still a notable dynamic range and sensitivity of the assay in drops down to 1 cpd. Below this, at 10^{-1} cpd, the drops overlap with the no template control (NTC); however, this measurement is acquired from drops thermocycled in the qPCR machine. When drops are sampled at endpoint using epifluorescence, bright and dark drops can be resolved at 10^{-1} cpd (Figure 4.3C).

We demonstrate successful implementation of the optimized additive formulation over five orders of magnitude of RNA in drops. Drops from the dilution series in Figure 4.2A were imaged at endpoint. Representative images of the FAM and ROX signals in drops containing 10^{-1} (Figure 4.3C) and 10^{4} (Figure 4.3D) RNA cpd show excellent drop stability and dye retention. The 10^{4} cpd case resulted in all bright drops ($N = 2051$) due to the high concentration of RNA in each drop, while the 10^{-1} cpd case resulted in a combination of bright and dark drops ($N = 2298$) due to not every drop containing template at this limiting dilution of RNA.

We performed endpoint analysis by counting the number of bright (positive) and dim (empty) drops from the endpoint reactions of the dilution series (*SI Appendix B*, Table B.2). Poisson statistics was used to fit the fraction of positive drops from the dilution series images, following eq 4.1:

$$\lambda = -\ln(1 - p) \quad \text{(eq 4.1)}$$

where λ represents the average copy numbers of target RNA (cpd) and p is the fraction of endpoint positive drops.[125] The percentage of amplified drops demonstrated good agreement with Poisson statistics yielding $R^2 = 0.929$ (Figure 4.3E and *SI Appendix B*, Table B.2).

Constructing Amplification Curves Using OCD RT-qPCR

Real-time qPCR amplification curves were constructed from drops using OCD RT-qPCR. Here, we performed a high-resolution investigation of two concentrations of M gene in drops. We compared drops containing low (10^1 cpd) and high (10^4 cpd) viral RNA by sampling drops at various cycle numbers on the qPCR machine and imaging them using epifluorescence microscopy.

The qPCR machine tracks fluorescence amplification at each cycle number without interruption. We amplify RNA within the approximately 300,000 drops contained in a sample tube using qPCR, which we call pseudo-continuous data. Hundreds of drops at intermittent thermocycles were sampled from individual tubes, which we call discontinuous data. This allows construction of discontinuous amplification curves (Figure 4.4A, blue dashed line, Figure 4.4B, red dashed line) that correlate with the real-time pseudo-continuous measurements acquired using the qPCR machine (Figure 4.4A, green solid line and Figure 4.4B, orange solid line).

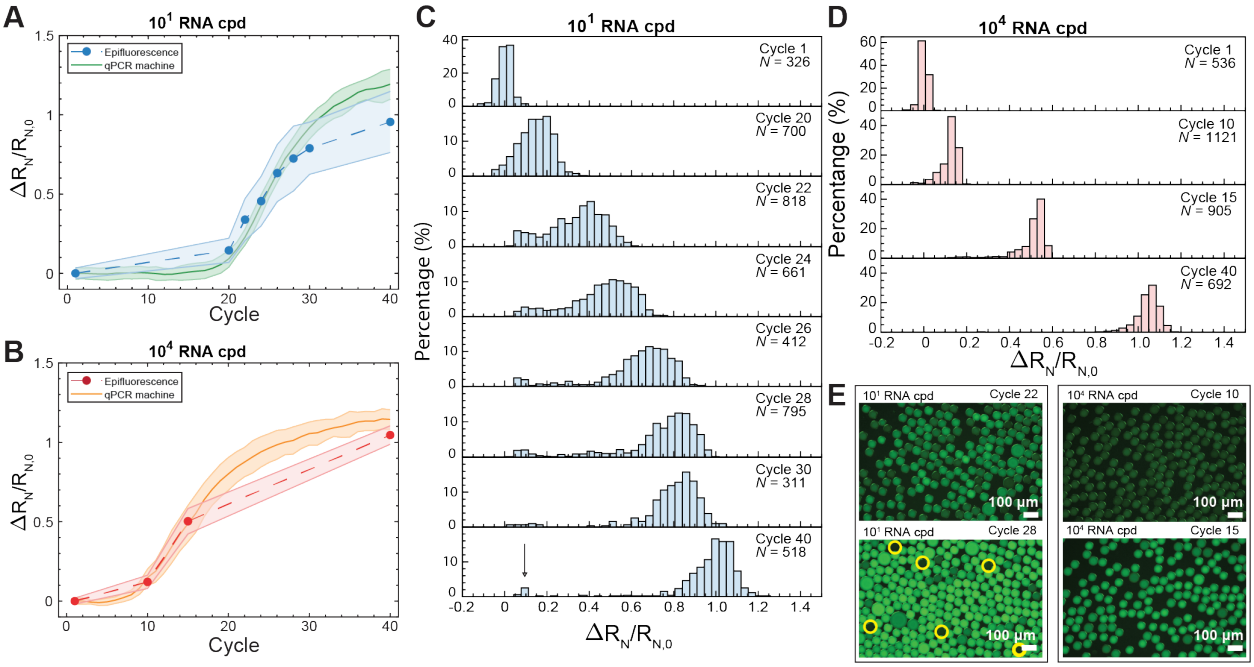


Figure 4.4. OCD RT-qPCR amplification curves compared to standard qPCR curves. Drops containing (A) 1.71×10^1 cpd of M gene RNA (low). The solid green line represents real-time pseudo-continuous fluorescence measurements of drops at each cycle using qPCR. The blue dashed line follows fluorescence measurements of sampled individual drops. Shaded error bars represent one standard deviation. Drops containing (B) 1.71×10^4 cpd of M gene RNA (high). The solid orange line represents pseudo-continuous fluorescence measurements of drops at each cycle using qPCR. The red dashed line follows fluorescence measurements of sampled individual drops. (C) Histograms of individual drop fluorescence values from epifluorescence images for 1.71×10^1 cpd of M gene (low). *N* represents the number of drops measured. The arrow in cycle 40 indicates unamplified drops. (D) Histograms of individual drop fluorescence values from epifluorescence images for 1.71×10^4 cpd of M gene RNA (high). (E) Changes in fluorescence are observed from 1.71×10^1 or 10^4 cpd of M gene RNA at cycles 22 and 28 and cycles 10 and 15, respectively. Yellow circles indicate dark drops containing no template at cycle 28.

Drops from the low RNA loading condition (10^1 cpd) were analyzed across eight cycles (Figure 4.4A). The distributions of drop fluorescence at the various cycle numbers for the low RNA loading condition are presented in Figure 4.4C. As amplification starts to increase exponentially at cycle 20, the distribution of drops shifts to the right as the fluorescence increases. From cycle 20 to 30, we observe that a majority of the drops began to amplify while a

small population does not (Figure 4.4C, arrow, cycle 40), forming a bimodal distribution. We hypothesize that this small population of non-amplifying drops did not contain template RNA, which is confirmed by the presence of dark drops seen under epifluorescence imaging (Figure 4.4E, yellow circles at cycle 28). This would indicate that the 1.71×10^1 cpd loading was an overestimate as empty drops are not expected at this concentration. In comparison, the high RNA loading condition (1.71×10^4 cpd) should result in every drop containing RNA; all drops should amplify in unison without a bimodal distribution. To test this, drops containing 1.71×10^4 RNA cpd were analyzed across four cycles (Figure 4.4B). The distributions of drop fluorescence at each cycle for the high RNA loading condition (Figure 4.4D) show that all drops amplify as expected.

Discrete particles such as RNA are encapsulated into drops following a Poisson distribution.[157] The high RNA loading condition is expected to create a tight distribution while the low RNA loading condition is expected to create a wide distribution. As predicted, the fluorescence intensities of the high RNA loading condition showed tighter distributions at all cycles compared to the low RNA loading condition. Representative images of drops for both low and high RNA loading at early and late cycles provide a visual reference for the distributions in the histograms (Figure 4.4E). OCD RT-qPCR demonstrates that real-time PCR amplification curves can be created from aggregated fluorescence measurements of individual drops that correlate with measurements taken using a standard qPCR machine. This suggests that quantification of nucleic acid concentrations from a large population of drops can be performed without the need for custom qPCR microfluidic devices.[125, 157]

Multiplexed OCD RT-qPCR Drop Detection of Target Genomes

The optimized additive formulation enables endpoint OCD RT-qPCR detection of multiplexed fluorophores within a single sample volume. We perform multiplexed detection of two different nucleic acid targets, a FAM probe for IAV M gene RNA and a Cy5 probe for plasmid-based cellular β-actin DNA. Cellular β-actin DNA is a commonly used eukaryotic "housekeeping" gene for qPCR normalization.[140] Selected M gene and β-actin concentrations were added to the optimized qPCR mix and thermocycled in 50 μm diameter drops. A representative image showing two fluorescence channels of M gene (FAM, Figure 4.5A) and β-actin (Cy5, Figure 4.5B) demonstrates that some drops contain M gene only (Figure 4.5A-B, yellow circle), β-actin only (Figure 4.5A-B, pink circle), and both M gene and β-actin (Figure 4.5A-B, orange circle). Analysis of drops ($N = 1127$) using endpoint OCD RT-qPCR analysis showed that 28.4% of drops contain M gene only, 7.3% of drops contain β-actin only, 2.7% of drops contain both, and 61.7% of drops were empty (Figure 4.5C). Multiplexing of qPCR probes allows measurements of multiple gene targets within a population of drops. Demonstrating that multiplexing is possible off-chip without a decrease in drop stability or preferential loss of one or both reporter probes significantly increases the scope and applicability of OCD RT-qPCR.

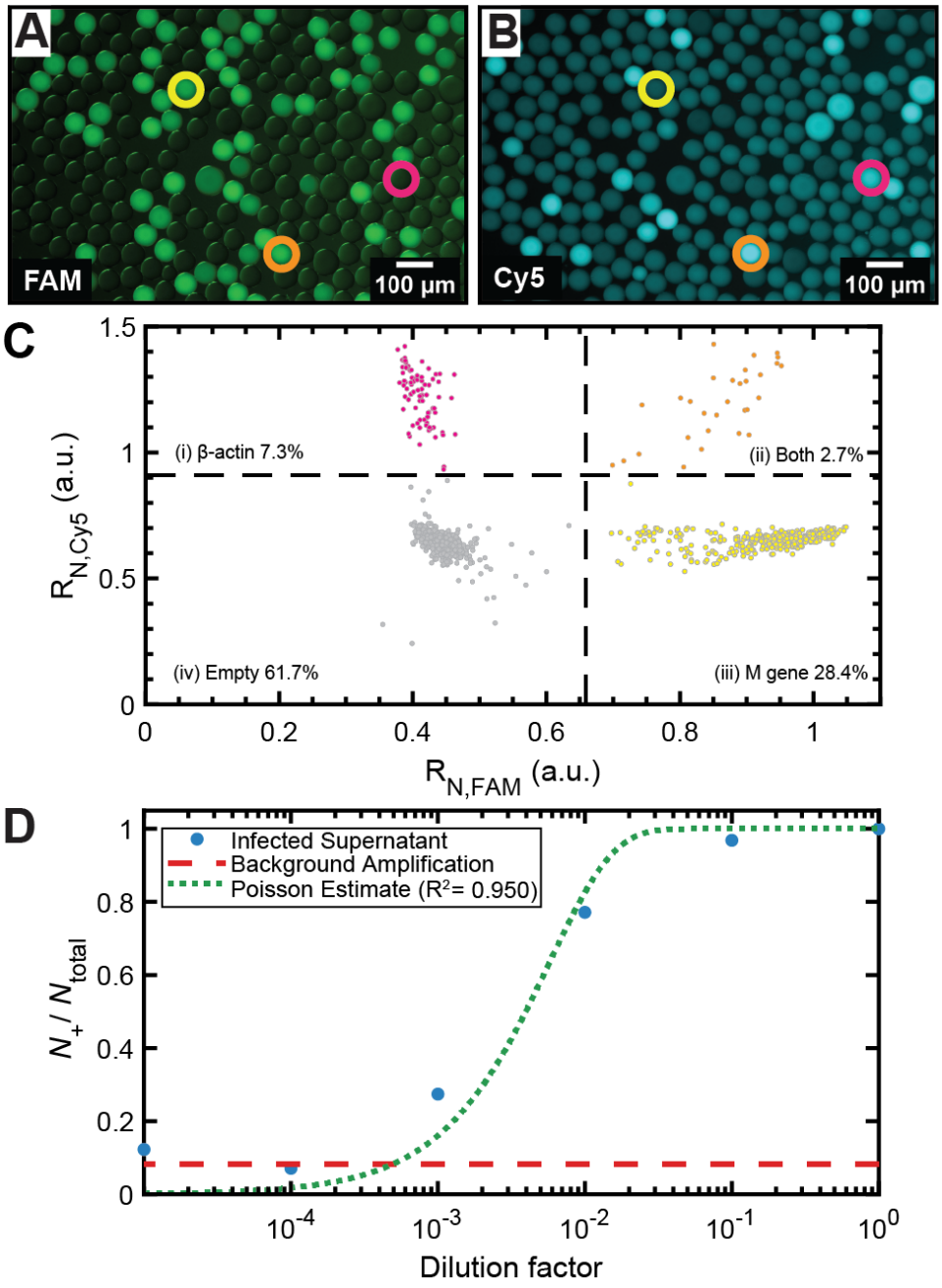


Figure 4.5. Multiplexed endpoint OCD RT-qPCR detection of target genomes. Representative epifluorescence images of drops containing (A) M gene in the FAM channel and (B) β-actin in the Cy5 channel. Circled drops contain M gene only (yellow circle), β-actin only (pink circle), and both M gene and β-actin (orange circle). (C) Image analysis of drops (N = 1127) yields a scatter plot of drops containing only β-actin, both β-actin and M gene, only M gene, and no template. (D) IAV from infected cells analyzed using endpoint OCD RT-qPCR provides N_+/ N_{total} as a function of dilution factor of infected viral supernatant (blue circles). Background amplification level is determined using mock infected cell supernatant (dashed red line). Poisson estimate fit of N_+/ N_{total} values above background, R^2 = 0.950 (dashed green line).

Quantification of Influenza A Virus Genomes from Infected Cells

The optimized additive formulation enabled endpoint OCD RT-qPCR detection of IAV down to a single viral genome per drop. We infected A549 cells, a human alveolar epithelial cell line, with A/California/07/2009 (H1N1) IAV at a 0.1 multiplicity of infection. At 24 h post infection, we prepared six dilutions of supernatant from infected cells (undiluted 10^0 down to 10^{-5} dilution). Supernatant from mock infected cells was included as a control to determine the level of background amplification and viral detection limit. Supernatant solutions were added to the optimized qPCR mix and drops were produced, thermocycled, and imaged. The virus was heat-lysed during the reverse transcription step at 60 °C for 30 min and amplified without an RNA extraction step. This direct PCR method allowed us to quantify viral RNA directly from the supernatant of infected cells. The fraction of positive drops to total drops (N_+/N_{total}) was plotted as a function of the dilution factor (Figure 4.5D, blue circles, *SI Appendix B*, Table B.2). The N_+/N_{total}, also defined as p in eq 4.1**,** can be used to calculate λ, the average cpd. The background amplification level of mock infected supernatant from the measured N_+/N_{total} was determined to be 0.086 cpd (Figure 4.5D, red dashed line, $N_{total} = 208$). Thus, infected supernatant dilutions below 10^{-3} were below the background level and excluded from analysis. A value of $\lambda = 175$ cpd for the uninfected supernatant was calculated based upon a Poisson estimate fit ($R^2 = 0.950$) to the measured N_+/N_{total} of the four infected supernatant dilutions above the background limit of 10^{-3} (Figure 4.5D, green dashed line). The calculated λ corresponds to 3.34×10^6 copies/µL for the undiluted infected supernatant. The standard curve in Figure 4.3B was used to estimate the concentration of the undiluted infected supernatant based upon its measured C_t value. This yielded an estimated starting concentration of 1.96×10^6 copies/µL, in close agreement with 3.34

$\times 10^6$ copies/μL determined from λ. The lowest level of detection at 10^{-3} dilution corresponds to 0.320 cpd ($N_{total} = 208$). Thus, we demonstrate the ability of our optimized endpoint OCD RT-qPCR assay to detect down to single viral genomes encapsulated within drops. Notably, we demonstrate the ability to amplify IAV RNA directly from infected cells.

Conclusion

OCD RT-qPCR is a versatile off-chip method for constructing qPCR amplification curves from individual drops that is enabled by a systematic screening of additive formulations which has been critically lacking and previously unreported. Performing RT-qPCR in picoliter-sized drops offers distinct advantages for speed, sensitivity, and throughput. However, results can be misleading if drops merge or leak. Furthermore, heating cycles are known to destabilize drops. Complex microfluidic devices [135] have been developed to keep drops separated, preventing leakage of contents and coalescence. Yet, these devices are often impractical for many researchers. Other strategies have included replacing liquid drops with hydrogel beads [158] or stabilizing drops using solid particles [159]. These changes can limit downstream options as drops may no longer be easily subdivided by splitting or merged with additional reaction components. Instead, it is more desirable to increase the stability of droplet interfaces while making no irreversible changes to the liquid phase or structure of the droplet itself. We therefore screened a number of PCR additives and established optimal conditions that protect drops during PCR thermocycling. The optimized formulation of Tween-20 / BSA / betaine maintained drop stability and limited dye transport during thermocycling.

Using OCD RT-qPCR, we also demonstrate for the first time that sampled drops imaged using epifluorescence correlates with real-time amplification curves obtained using a standard

qPCR machine. Drop thermocycling and analysis is performed entirely off-chip, or outside of a microfluidic device. Previous drop-based qPCR methods relied on endpoint fluorescence measurements to confirm the presence or absence of specific nucleic acid species[14], or required complex devices to measure drop fluorescence following each thermocycle number[126, 127, 130]. These approaches are either unattainable for laboratories without extensive engineering expertise or fail to provide any quantification of specific nucleic acid species. The OCD RT-qPCR method addresses these pitfalls by demonstrating that fluorescence measurements can be obtained using a standard epifluorescence microscope and sampling drops at various cycles allows for the construction of amplification curves. This combination can be used to quantify specific nucleic acid species of interest within individual drops with high accuracy.

Optimized drop stability can greatly improve single-cell studies, where drops must resist coalescence while containing destabilizing molecules and proteins such as those present in growth media or expressed during cellular metabolism.[160-162] For example, we have confirmed the ability to detect down to a single genome in a drop, or 0.320 cpd, demonstrating the high sensitivity achievable using OCD RT-qPCR. A variety of downstream processing options become available to drops stable enough to be handled for off-chip analysis and eliminates the need for complicated custom microfluidic thermocycling devices.[126, 127] Fluorescence measurements of tens of thousands of drops may be accomplished by replacing epifluorescence microscopy measurements with flow-based drop fluorescence detection.[157] Furthermore, there is potential to measure the viral output of infected single cells using OCD RT-qPCR, significantly increasing the number of cells that can be assayed compared to common serial dilution approaches performed using standard well plates.[163] Importantly, our work establishes the

possibility of directly amplifying viral RNA without the need for RNA extraction, which is advantageous in resource-limited situations such as the COVID-19 pandemic for performing massive testing of SARS-CoV-2.[164]

Acknowledgments

This work was supported by Defense Advanced Research Projects Agency (DARPA) grant W911NF-17-2-0034 and by National Science Foundation (NSF) CAREER Grant 1753352. We thank C. Brooke at the University of Illinois at Urbana-Champaign for providing H1N1 A/California/07/2009 and human alveolar epithelial A549 cells; A. Rynda-Apple at Montana State University for providing MDCK cells.

Supporting Information

Supplemental data tables for drop measurements, additional experimental details for microfluidic device fabrication, PCR mix formulation, image acquisition, and image analysis.

Notes

The authors declare no competing financial interest.

CHAPTER 5

DROP-BASED QPCR ENABLED BY SIGMOIDAL CURVE FITTING USING PCR EFFICIENCY

Contribution of Authors and Co-Authors

Manuscript in Chapter 5

Author: Geoffrey K. Zath

Contributions: G.K.Z. designed research, performed research, analyzed data, and wrote the manuscript

Co-Author: Emma K. Loveday

Contributions: E.K.L. designed research and performed research

Co-Author: Mallory M. Thomas

Contributions: M.M.T. performed research

Co-Author: Connie B. Chang

Contributions: C.B.C. designed research and wrote the manuscript

Manuscript Information

Geoffrey K. Zath, Emma K. Loveday, Mallory M. Thomas, Connie B. Chang

Analytical Chemistry

Status of Manuscript:
_X__ Prepared for submission to a peer-reviewed journal
____ Officially submitted to a peer-reviewed journal
____ Accepted by a peer-reviewed journal
____ Published in a peer-reviewed journal

American Chemical Society

Abstract

Drop-based quantitative polymerase chain reaction (qPCR) applications have been limited in scope when compared droplet digital PCR (ddPCR). This is in part due to the complex microfluidic devices which reproduce the functionality of a qPCR machine in order to collect data suitable for the quantification cycle (*Cq*) method. The *Cq* method requires fluorescence measurements at each thermocycle and has in turn limited the throughput of drop-based qPCR. Alternative qPCR data analysis techniques, such as sigmoidal curve fitting (SCF), do not require all cycles to be measured as information can be extrapolated from the sigmoidal function. We describe a modification to SCF methods called Sigmoidal Curve Fitting using PCR Efficiency (SCFPE). SCFPE provides a more accurate fit to amplification data and allows for novel quantification from a single cycle of fluorescence measurements. Analysis of published qPCR datasets with SCFPE provides a similar linear response to measured samples when compared to the *Cq* method ($R^2 > 0.9640$ and 0.9912, respectively). SCFPE is applied to qPCR data collected from microfluidic drops to quantify single and mixed populations of influenza A virus (IAV) M gene RNA in drops. qPCR drop detection rates of approximately 100 Hz can be achieved with SCFPE analysis. This throughput is a >10-fold increase compared to static imaging or continuous flow drop-based qPCR methods which have been limited to <100 drops per run or a drop throughput of <10 Hz, respectively. The work presented here allows high-throughput drop qPCR to be performed without the need for complicated microfluidic devices.

Introduction

Absolute quantification methods for polymerase chain reaction (PCR) such as droplet digital PCR (ddPCR) and quantitative PCR (qPCR) are routinely used to detect and quantify nucleic acids for clinical diagnostics and academic research.[165, 166] ddPCR utilizes drop-based microfluidics to provide improved precision and sensitivity compared to qPCR.[167] Drop-based microfluidics is a method that increases the speed, sensitivity, and throughput of nucleic acid detection by reducing sample volumes to picoliter drops.[31, 126-128, 167] While ddPCR has become a well-established method with commercial systems available, adapting qPCR to drop-based methods has proven difficult, often requiring complex systems that reproduce the functionality of a qPCR machine such as thermocycling and fluorescence measurements.[30, 126, 127, 130, 168, 169] These complex systems perform the standard data collection and analysis of a benchtop machine.

The standard qPCR data analysis technique used by drop-based qPCR methods for absolute quantification of an unknown template relies on measuring a quantification cycle (*Cq*), referred to here as the *Cq* method. *Cq* is the cycle at which the fluorescence level of an amplifying sample crosses a fluorescence threshold. The fluorescence threshold is set in the exponential region of the amplification curve by the qPCR instrument software. The *Cq* values of each sample are compared to a standard curve made from a known template dilution series to determine starting template concentration. Alternative qPCR data analysis methods that do not rely on measuring *Cq* include pair-wise combinations to determine PCR efficiency[170] or by fitting a pre-defined model to measured amplification data such as linear regression[171, 172] or sigmoidal curve fitting (SCF) methods.[33, 173-175] Linear regression methods fit a linear model to

the exponential region of the amplification curve on a log transformed plot to calculate an initial template concentration. This approach requires highly resolved temporal data in the exponential region for accurate measurements. SCF methods fit a curve to amplification data using a four-parameter sigmoidal function[34] to calculate an initial template concentration. A limitation of SCF methods lies in the fact that sigmoidal curves are symmetric and unable to properly capture the asymmetric shape of the amplification curve. Attempts at improving SCF for fitting to amplification curves have applied user defined cut-offs[173] or an asymmetric term to the fitting function.[174, 175] The shape of the PCR amplification curve becomes asymmetric due to a PCR efficiency of approximately 100% in the exponential phase, relating to an exact doubling of DNA at each cycle, and a low PCR efficiency during the plateau phase as reagents are exhausted. A common factor in the *Cq*, linear regression, and SCF methods is the requirement of collecting fluorescence measurements for the majority of the amplification curve in order to find a *Cq* value or fit a model. In doing so, the cost and complexity of instrumentation is driven up as it must be designed around quickly imaging/detecting all samples in parallel, generally within the final seconds of the annealing phase.

A novel qPCR data analysis technique that can quantify a sample from a single cycle of fluorescence measurements would greatly increase sample throughput by allowing drops to be pooled from a single cycle and measured with flow-based detection methods which can detect drop at rates of approximately 100 Hz,[176] a >10-fold greater throughput than current drop-based qPCR approaches. Current drop-based qPCR approaches rely on the *Cq* method which has led to technical restraints. For instance, static imaging methods rely an array microfluidic device to hold drops while they are thermal cycled and imaged with epifluorescence microscopy.[126, 130]

These methods have been limited to a single field of view as the fluorescence of each drop must be tracked over all thermocycles and has resulted in a sample throughput of <100 reactions per run. Continuous flow methods consist of a coil of tubing around a cylindrical thermocycler in which plugs of fluid are pumped.[30, 168, 169] Fluorescence measurements at each cycle, or coil, are made with a lens array coupled to either photomultiplier tubes (PMT)[168] or high-sensitivity cameras.[30, 169] These continuous flow methods are constrained by the residence time of the flowing drops in the coil of tubing that is required for each thermocycle. Due this constraint, sample throughput is limited to <10 Hz as flowing the drops too fast will shorten the amount of time each drop spends in a heating zone.

We describe a modification to previous SCF methods which accurately fits amplification data by adding a PCR efficiency term into the sigmoidal function and allows the novel quantification of fluorescence measurements made at a single cycle. We call this method Sigmoidal Curve Fitting using PCR Efficiency (SCFPE). In this study, SCFPE is used to quantify Influenza A virus (IAV) M gene RNA, human MYCN gene DNA, and soybean Lectin endogene DNA samples measured on a qPCR machine and provides similar accuracy (<1.7-fold change) and linear response ($R^2 > 0.9640$) as the *Cq* method (<1.9-fold change, $R^2 > 0.9912$). Additionally, SCFPE is applied to our previously published method,[80] where drops are sampled at various thermocycles from a qPCR machine, to provide quantitative measurements of IAV M gene RNA populations in drops collected as a single cycle. The drop populations consist of single and mixed concentrations of M gene RNA are quantified within a 1.5-fold or 2-fold change of the expected template concentration, respectively. SCFPE analysis enables drop qPCR measurements that are made with a 10-fold increase in drop throughput compared to static

imaging and continuous flow drop qPCR methods.[30, 126, 130, 168, 169] By using SCFPE for drop qPCR measurements, complicated microfluidic devices that provide thermocycling and fluorescence measurements for drop-based qPCR are no longer required. Such an approach reduces the required data to quantify samples by a factor of 40 compared to the quantification cycle method. Drop-based qPCR using the SCFPE method provides greater sample throughput and flexibility than current drop-based qPCR techniques.

Experimental Section

PCR Sequences and Reaction Concentrations

The sequences of qPCR amplification primers for the IAV Matrix gene (M gene) were: M gene forward primer 5′-GACCRATCCTGTCACCTCTGAC-3′, M gene reverse primer 5′-AGGGCATTCTGGACAAATCGTCTA-3′.[139] The sequence of the M gene TaqMan probe was: 5′-/FAM/TGCAGTCCTCGCTCACTGGGCACG/BHQ1/-3′. Primers and probes were ordered from Eurofins Operon and were prepared as 100 µM stocks. The working stocks of the primers were 25 µM with a final reaction concentration of 400 nM. The working stock of the probe was 10 µM with a final reaction concentration of 200 nM. Samples were amplified using SuperScript III Platinum One-Step qRT-PCR kit (Invitrogen 11732-020) with a final reaction volume of 25 µL. Each reaction mix contained 0.15 µM ROX reference dye, 2.0 mM $MgSO_4$, 0.32 U/µL SUPERase RNase Inhibitor (Invitrogen AM2694), 1.0% w/v Tween-20 (Calbiochem 655204-100mL), 0.8 µg/µL BSA (Fisher BP675-1), and 1.0 M betaine (Sigma B0300-1VL), and 2.5 µL of RNA or supernatant. Thermocycling was performed in a real-time qPCR machine (QuantStudio 3, Applied Biosystems): 1 cycle for 30 min at 60 °C, 1 cycle for 2 min at 95 °C, and 40 cycles between 15 s at 95 °C and 1 min at 60 °C.

In Vitro Transcribed RNA

Standard curves were generated from five dilutions from a 10-fold dilution series of *in vitro* transcribed IAV M gene (ranging from 2.62 x 10^4 to 2.62 x 10^8 copies/µL) and run in triplicate.[141] To generate the *in vitro* transcribed RNA, a gBlock containing a T7 promoter (underlined), forward and reverse primer sites (italicized), and probe sequence (bold) for the M gene was ordered from IDT: 5′-GTCTAATACGACTCACTATAG *GACCAATCCTGTCACCTCTGAC* **TGCAGTCCTCGCTCACTGGGCACG** TGCTTCATCGCGAACTGCTTCGCGGATGCCATCGTCATGGCCACGAGGATATGTAAG AGT *TAGACGATTTGTCCAGAATGCCCT*-3′. The M gene was transcribed *in vitro* using a MEGAscript T7 RNA Synthesis Kit (Ambion, AM1333) and purified over a GE Illustra Sephadex G-50 NICK column. RNA concentration was quantified using a NanoDrop spectrophotometer to determine the copy number per µL. The corresponding concentration in copies per drop (cpd) cpd was calculated by multiplying the copies/µL value by the volume of a 50 µm diameter drop (6.54×10^{-5} µL/drop).

MYCN and Soybean qPCR Datasets

The human MYCN gene and soybean Lectin endogene DNA datasets were taken from previously published studies on the evaluation of qPCR curve analysis methods[177] and enhanced analysis of real-time PCR data using a variable efficiency model.[178] The MYCN dataset consists of four dilutions from a10-fold dilution series (ranging from 1.88 x 10^0 to 1.88 x 10^3 copies/µL) and uses a SYBR Green Supermix (Bio-Rad). The soybean dataset consists of five dilutions from a 5-fold dilution series (ranging from 6.4 x 10^0 to 4.0 x 10^3 copies/µL) and uses a SYBRgreen mastermix (Diagenode).

Microfluidic Device Fabrication

The 50 μm diameter drop making microfluidic device was fabricated using standard soft lithography methods.[176] Photoresist (Microchem SU-8 3050) was patterned on silicon wafers (University Wafer, ID# 447, test grade) using photolithography. Polydimethylsiloxane (PDMS) (Sylgard 184) was mixed at a 10:1 mass ratio of polymer to cross-linking agent and poured onto the patterned device master molds. Air was purged from the uncured PDMS by placing the filled mold in a vacuum chamber for at least 1 h. The PDMS was cured in an oven at 55 °C for 24 h and then removed from the mold with a scalpel. Ports were punched into the PDMS slabs with a 0.75 mm diameter biopsy punch (EMS Rapid-Core, Electron Microscopy Sciences). The PDMS slab of the drop making device was bonded to 2-in by 3-in glass slides (VWR micro slides, cat. #48382-179) after plasma treatment (Harrick Plasma PDC-001) for 60 s at high power and 400 mTorr oxygen pressure. The device was made hydrophobic by flowing Aquapel (Pittsburgh Glass Works) through the channels, followed by blowing the channels with air filtered through a GVS ABLUO 25 mm 0.2-μm filter (Fisher Scientific) before baking the devices in an oven at 55 °C for 1 h.

Drop Encapsulation

Flow-focusing drop making devices were used to encapsulate M gene RNA in 50 μm diameter drops. The continuous phase consisted of a 3.0 wt% (w/w) solution of PEG-$PFPE_2$-based surfactant (RAN Biotechnologies, 008-FluoroSurfactant) in fluorinated HFE-7500 oil (3M). The dispersed and continuous phases were loaded in 3-mL syringes and injected into the drop making microfluidic devices at flow rates of 800 μL/h and 1600 μL/h, respectively (New Era NE-1000 syringe pumps). Drops were collected in PCR tubes for 1.5 min each for

approximately 20 μL of drops. PCR tubes (Applied Biosystems, MicroAmp Fast 8-tube Strip, 0.1 mL) were stored on a cold block until ready for thermocycling.

Drop Imaging

The qPCR machine was paused at cycles 1, 16, 19, 22, 25, 28, and 40 and three PCR tubes were removed to sample drops. Five fields of view were imaged of the sampled drops on an inverted epifluorescence microscope (Nikon Ti2-E) at 10× magnification (NA 0.3). Brightfield and fluorescence images of the FAM TaqMan probe for M gene (FITC) and ROX reference dye (Texas Red) were captured with a sCMOS (Hamamatsu, ORCA-Flash4.0 v3) camera.

Drop Detection

Thermocycled drops were injected into a microfluidic detection device[176] at a flowrate of 100 μL/h and spacer oil (Novec 7500) without surfactant was injected at a flowrate of 400 μL/h. Up to 10,000 drops were detected at cycles 1, 16, 19, 22, 25, 28, and 40. The drop fluorescence detection system consisted of a custom modified Nikon TiU inverted microscope with two lasers, a set of dichroic mirrors, and two photomultiplier tubes (PMTs, Hamamatsu H10723-20).[176] The beams of the 22 mW, 488 nm laser (Thorlabs MCLS1) and the 25 mW, 561 nm laser (Cobolt Jive) were aligned together and coupled into the backport of the microscope where they were focused to a spot by the 40× objective (NA 0.60). The flowing of drops across the laser spot resulted in fluorescence detection by two PMTs split into two channels using dichroic and bandpass filters, Ch1: 520/40 nm (green) and Ch2: 600/40 nm (red). A field programmable gate array (FPGA, National Instruments NI-7852R) was used to control the PMT gains and record fluorescence measurements using LabVIEW 2015. A custom MATLAB (R2020a) script was

used to process and analyze the drop fluorescence detection data. FAM fluorescence intensities were normalized as ΔR_N, where the qPCR normalized reporter value R_N is defined as $R_N = I_{FAM}/I_{ROX}$, $\Delta R_N = R_N - R_{N,baseline}$, I_i is the respective intensity of FAM or ROX at each cycle, and $R_{N,baseline}$ is the average R_N value of the first cycle.

Amplification Curve Library

An amplification curve library is made with virtual reference amplification curves of the same shape as the reference curve calculated in Eq. 5.7 (see Results and Discussion, *qPCR analysis with SCFPE*). These virtual curves are "extended" to the left and right of the reference curve by substituting $N_{0.5}$ from Eq. 5.7 with $N_{virtual}$. $N_{virtual}$ is the cycle at which the PCR efficiency equals 0.5 for the virtual curve and ranges from 1 to 40. Extension of the reference amplification curve is based on the principles used for the quantification cycle analysis method following Eq. 5.1:

$$Cq = m * \log_{10}(C_{RNA}) + b \quad \text{Eq. 5.1}$$

where Cq is the cycle threshold at which the fluorescence of an amplification curve crosses a fluorescence threshold, C_{RNA} is the concentration of starting template RNA, m is the slope of the Cq versus log10(C_{RNA}) line, and b is the y-intercept of that line. In this case, m is related to the effective PCR amplification efficiency (E_{eff}) at the Cq value measured for each template dilution following Eq. 5.2:

$$m = \frac{1}{log10(E_{eff}+1)} \quad \text{Eq. 5.2}$$

For the quantification cycle analysis method, calculation of E_{eff} requires a dilution series of template to measure m, however, for SCFPE we find that for a single template standard an E_{eff} value can be calculated from the modeled efficiency curve from Eq. 5.5 using a cycle offset of

three as $E_N(N_{0.5}\text{-}3)$ once the fitting parameters have been determined (see Results and Discussion, *qPCR analysis with SCFPE*). This cycle offset of three from $N_{0.5}$ is empirically found to provide a wide dynamic range and high R^2 value for converted M gene data in Figure 5.3B and is used for all fluorescence data conversions in this study (Table C.2). The extension of the virtual reference curves is determined with a scaling factor (f) calculated from Eq. 5.3:

$$f = log10\left(C_{\mathrm{RNA,ref}}\right) - \frac{N_{0.5} - N_{\mathrm{virtual}}}{m} \quad \text{Eq. 5.3}$$

where $C_{\mathrm{RNA,ref}}$ is the single known reference starting template concentration used for the SCFPE analysis. The virtual template concentration ($C_{\mathrm{RNA,virtual}}$) of each curve as a function of N_{virtual} is calculated with Eq. 5.4:

$$C_{RNA,virtual} = 10^{f} \quad \text{Eq. 5.4}$$

The formation of this amplification curve library is represented graphically in Figure 5.2A-B for N_{virtual} ranging from cycle 1 to 40 with 10 and 1000 data points, respectively. The high-resolution amplification curve library from Figure 5.2B is used to create a standard curve relating $C_{\mathrm{RNA,virtual}}$ to the measured normalized fluorescence reporter value (ΔR_N) of a sample at a single cycle (Figure 5.2C). The x-axis of the standard curve is calculated with Eq. 5.3 for a range of N_{virtual} values while keeping $N_{0.5}$ constant. The y-axis of the standard curve is calculated by plugging in the f values calculated from Eq. 5.3 into Eq. 5.4.

SCFPE Drop Analysis

Drop fluorescence measured at intermediate thermocycles was converted to an initial RNA template concentration using SCFPE for single cycle quantification of the M gene drop qPCR data. A reference amplification curve was made from drops containing 1.71 x 10^2 cpd of

M gene RNA. The reference curve was modeled from drops detected at cycles 1, 13, 16, 19, 22, 25, 28, and 40 and used to build an amplification curve library.

Results and Discussion

qPCR Analysis with SCFPE

SCF is unable to properly fit amplification curve data without adding a limit on the number cycles fit[173] or by adding an asymmetric fitting term.[174, 175] The asymmetric nature of qPCR amplification data arises from the decrease in PCR efficiency after each cycle. At early cycles, PCR efficiency is near 100%, relating to an exact doubling of DNA at each cycle, and approaches 0% at later cycles.[178, 179] This relationship leads to a steeper slope at the start of the amplification curve in the exponential region and flatter slope near the plateau phase which SCF is unable to correctly fit.[178] Alternative fitting methods to SCF that correctly fit asymmetric data model the PCR efficiency, rather than the fluorescence data, with a sigmoidal[180] or bilinear[178] model to construct an asymmetric amplification curve. We have chosen an approach similar to the former to model PCR efficiency with a sigmoidal curve; however, rather than using a two-parametric sigmoid function[180], we have modified the four-parametric sigmoid function[173] to model PCR efficiency with Eq. 5.5:

$$E_{\mathrm{N}} = \frac{E_{\mathrm{max}}}{1+e^{\left(\frac{N_{0.5}-N}{k}\right)}} + E_{\mathrm{min}} \qquad \text{Eq. 5.5}$$

where E_{N} is the PCR efficiency at cycle N, E_{max} is the maximum PCR efficiency in the range of 0 to 1, E_{min} is the minimum PCR efficiency in the range of 0 to 1, $N_{0.5}$ is the cycle at which E_{N} equals 0.5, and k is the slope of the curve. Eq. 5.5 is then used to construct an amplification curve consisting of fluorescence data following Eq. 5.6:

$$F_{N+1} = F_N(1 + E_N) \quad \text{Eq. 5.6}$$

where F_{N+1} is the fluorescence value of the amplification curve at cycle N+1, F_N is the fluorescence value of the amplification curve at cycle N. Eq. 5.5 and 5.6 are combined and result in Eq. 5.7:

$$F_{N+1} = F_N\left(1 + \frac{E_{max}}{1+e^{\left(\frac{N_{0.5}-N}{k}\right)}} + E_{min}\right) \quad \text{Eq. 5.7}$$

Eq. 5.7 is fit to the qPCR data iteratively with an initial arbitrary guess for $F_{N,0}$. The fit to Eq. 5.7 is scaled to the measured normalized fluorescence reporter value (ΔR_N) by a calibration factor (CF) calculated in Eq. 5.8 using the measured and modeled fluorescence endpoint ($F_{endpoint}$) values:

$$CF = F_{endpoint,measured}/F_{endpoint,model} \quad \text{Eq. 5.8}$$

A four-parameter fit of Eq. 5.7 (varying E_{max}, E_{min}, $N_{0.5}$, and k) provides an asymmetric function which closely follows the measured fluorescence data collected from a qPCR machine. We call the method of fitting Eq. 5.7 to qPCR data Sigmoidal Curve Fitting using PCR Efficiency (SCFPE). To demonstrate SCFPE, Eq. 5.7 is fit to a qPCR dataset consisting of a dilution series of IAV M gene RNA (2.62×10^4 to 2.62×10^9 copies/µL) and compare it to an SCF fit (Figure 5.1).[173] The SCF method (Figure 5.1A, gray dotted line) does not properly fit the data in the lower ($\Delta R_N < 1$) and upper ($\Delta R_N > 4$) regions of the amplification curves (Figure 5.1, colored data points). The SCFPE method (Figure 5.1B, gray dotted line) more closely fits the amplification curves with an average R^2 of 0.9996. SCFPE captures the asymmetric dynamics of PCR amplification from a starting RNA template and provides a better fit than SCF (see Figure C.1). Here, the fluorescence data is fit to directly, rather than the measured PCR efficiency as done previously in literature.[178, 180] This approach allows for fitting fluorescence data from a

subset of cycles, rather than requiring data from all cycles as is required for calculating, and subsequently fitting to, the PCR efficiency.

SCF methods have been used previously to provide quantification of qPCR data.[33, 173, 174] To demonstrate the ability to quantify qPCR data with SCFPE, we describe to the use of an "amplification curve library" consisting of virtual reference curves that are used to construct a standard curve. This process starts by extending the amplification curve calculated in Eq. 5.6 for all possible starting template concentrations. This extension is presented graphically in Figure 5.2A-B where the SCFPE fit in Figure 5.1B (2.62×10^7 copies/all) is extended to the left and right to build an amplification curve library with 10 and 1000 virtual reference curves (see Amplification curve library in Materials and Methods for details). By cutting a slice vertically through the amplification curve library at a pre-determined measurement cycle (Figure 5.2B, black dotted line), each intersection of this slice with an amplification curve in the library is linked to the baseline subtracted normalized fluorescence reporter value (ΔR_N) and a corresponding starting template concentration (C_{RNA}) of that curve (see Materials and Methods, *Amplification Curve Library* for details). With this information, a standard curve relating C_{RNA} to ΔR_N can be constructed (Figure 5.2C). Due to the nature of qPCR measurements, there will be a minimum and maximum ΔR_N value which can be used with the standard curve (Figure 5.2D, gray region). The minimum value will be limited by the background fluorescence while the maximum value will be at a point at which individual amplification curves can no longer be resolved in the plateau phase. In practice, the valid range applies to the exponential and linear regions of each amplification curve.

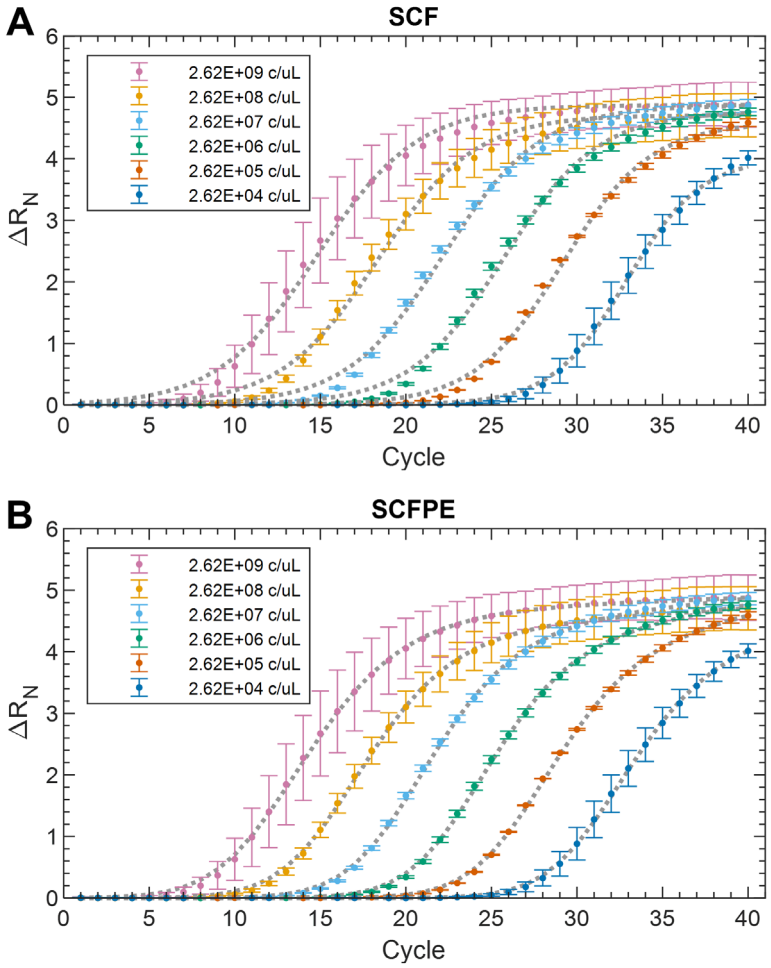


Figure 5.1. (A) SCF and (B) SCFPE methods (dashed gray lines) applied to the M gene dilution series amplification curves (colored datapoints). SCFPE provides a better fit to the data at the lower ($\Delta R_N < 1$) and upper ($\Delta R_N > 4$) regions of the amplification curves. The average R^2 values for SCF and SCFPE are 0.9975 and 0.9996, respectively. Error bars represent one standard deviation. Fitting parameters for SCFPE are provided in Table C.1.

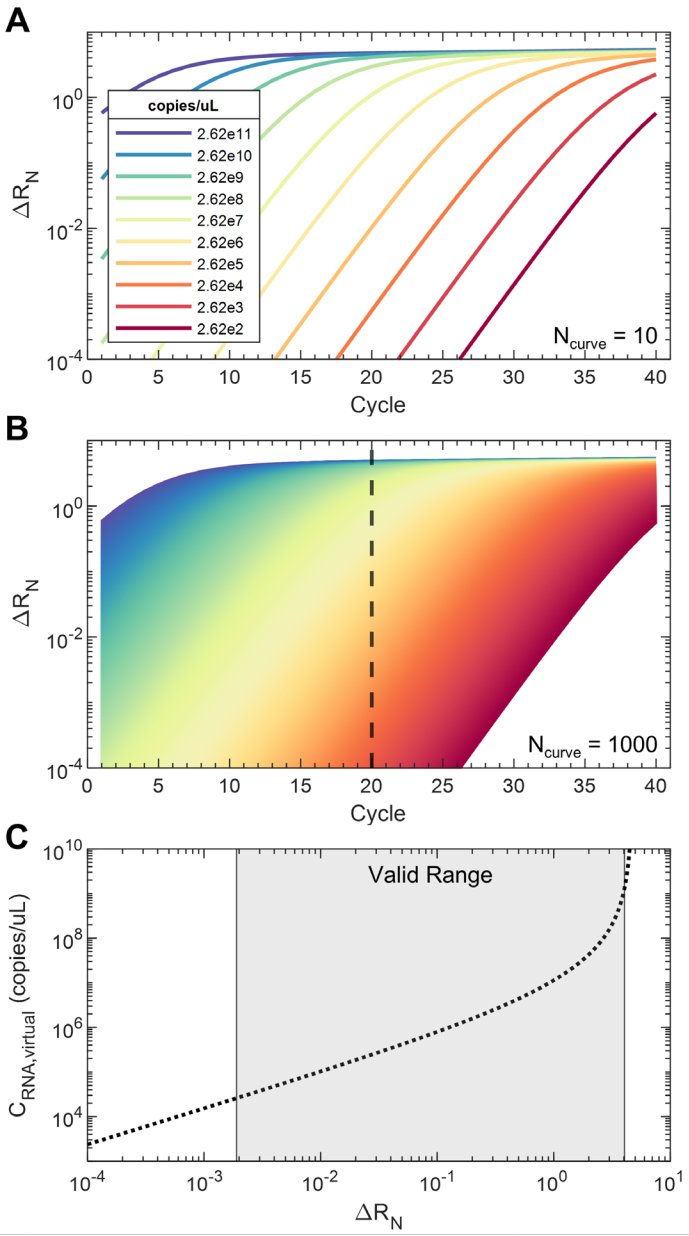


Figure 5.2. Construction of the amplification curve library. The PCR efficiency model fit to the 2.62 x 10^7 copies/µL amplification curve in Figure 5.1 is extended across a spectrum of possible starting template concentrations, creating an amplification curve library with (A) 10 and (B) 1000 virtual reference curves. (C) Standard curve created from a slice of the amplification curve library at cycle 20. The valid range of the standard curve is within the gray region as defined in Table C.3.

Validation of SCFPE with Bulk qPCR Datasets

The SCFPE quantification method is validated against qPCR datasets collected from dilution series of the influenza A virus (IAV) M gene RNA, human MYCN gene DNA,[177] and soybean Lectin endogene DNA[178] and compared to results quantified with the standard *Cq* method. Quantification by calculating a *Cq* value provides a linear response of measured versus expected concentration of RNA or DNA for all datasets (Figure 5.3A, $R^2 > 0.9912$). The measured data falls within a 2-fold change (dotted line) of expected (dashed line) with a max fold change error of 1.9. To quantify the qPCR data with SCFPE, an amplification curve library is built from a single reference curve, as described in Figure 5.2, and a subsequent standard curve is constructed at a single intermediate cycle. The intermediate cycles chosen for the M gene, MYCN, and soybean datasets are cycles 20, 27, and 29, respectively. Quantification of the qPCR datasets with SCFPE provides a similar linear response (Figure 5.3B, $R^2 > 0.9640$) and accuracy as the *Cq* method. While two of the 30 dilutions fall outside a 2-fold change from expected, the other 28 dilutions (93% of the data) are measured accurately with a less than 1.7-fold change error. Additional statistics for conversion of the M gene data at other cycles are provided in Table C.3.

To demonstrate the importance of SCFPE versus SCF, the M gene dataset was analyzed with a reference curve fit with SCF and the result was a non-linear response to the expected value (Figure 5.3B, gray dots, $R^2 = 0.8487$) with many of the data falling outside of the 2-fold change error lines. The comparable performance of the *Cq* and SCFPE methods may be explained by the fact that the two methods share similar assumptions. In the case of the *Cq* method, it is assumed that the PCR efficiency measured at the fluorescence threshold is the same for all samples, regardless of initial template concentration. SCFPE relies on a similar

assumption and assumes that the shape of the PCR efficiency curve is the same for all samples, regardless of initial template concentration. Interestingly, SCFPE closely matches the performance of the quantification cycle method while requiring a fraction of the information. For example compared to the *Cq* method, the SCFPE method analysis of the M gene dataset requires $1/5^{th}$ of the RNA standards to create a standard curve and $1/40^{th}$ of the fluorescence data collected for single cycle quantification of unknown samples. The significant reduction of required information for qPCR analysis positions SCFPE as a good fit to quantify data collected from our previously developed drop-based PCR method which provides high-throughput sampling of drops at various thermocycles.[80]

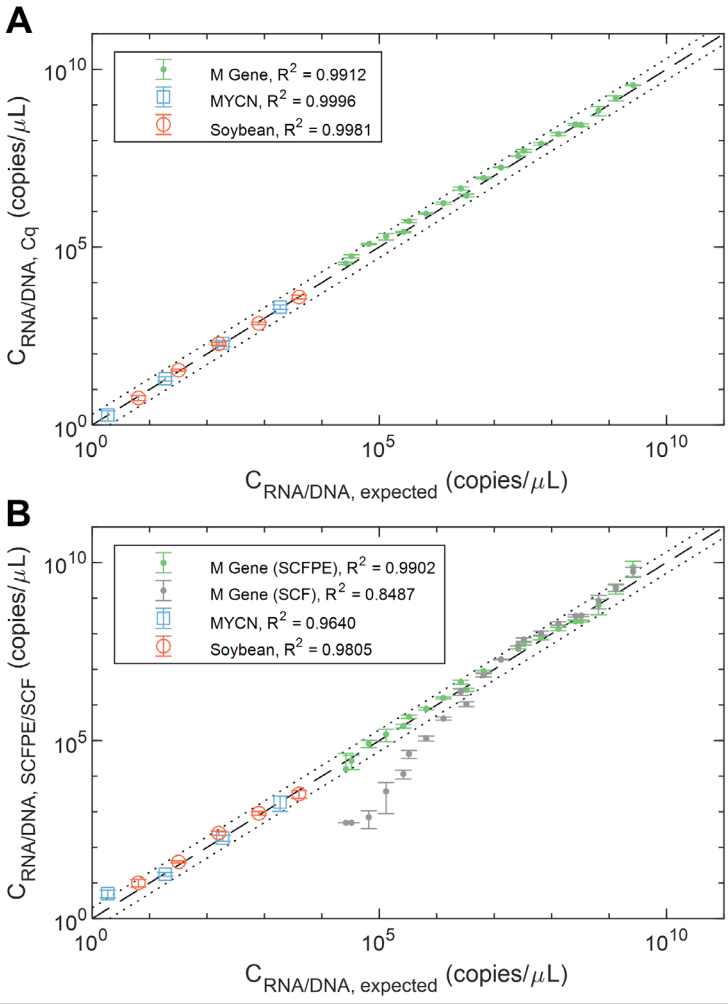


Figure 5.3. Method comparison for bulk M gene (green/gray dot), MYCN gene (blue square), and soybean gene (red circle) qPCR datasets. Conversion with the (A) quantification cycle analysis and (B) SCFPE provides a linear response between the measured and expected RNA or DNA concentration for both methods ($R^2 > 0.9912$ and 0.9640, respectively). Conversion of the M gene dataset with SCF does not provide a linear response across the dilution series ($R^2 = 0.8487$). Error bars represent one standard deviation. For each dilution, there were three, 94, or 18 replicates for the M gene, MYCN, or soybean datasets, respectively.

SCFPE Applied to Drops Collected at Various Thermocycles

SCFPE is applied to drop measurements made with the OCD RT-qPCR method[80] to demonstrate single cycle quantification capabilities in drops at high-throughput. In the OCD RT-qPCR method, drops containing PCR mix and IAV M gene RNA are created using a microfluidic drop maker, collected in PCR tubes, and placed in a qPCR machine. The qPCR

machine is stopped at various cycle numbers, at which a tube is removed, and drops are sampled for epifluorescence imaging and high-throughput drop detection. In this study, an SCFPE reference curve (Figure 5.4A, red dashed line) is created from drops containing IAV M gene RNA (1.71×10^2 cpd) measured at various cycles using high-throughput flow-based detection (Figure 5.4A, black data points). Representative epifluorescence images of the drops show a steady increase in fluorescence across the drops with increasing cycle number (Figure 5.4B). To determine the sources of error in SCFPE drop measurements, an additional sample at 1.71×10^2 cpd is measured across three different days, with one day including measurements from three PCR tubes (Figure 5.4C, each day indicated by various shapes). Measurements across all three days fall within a 1.5-fold change (Figure 5.4C, dotted lines) from the expected value of 1.71×10^2 cpd which is comparable to the error measured from the *Cq* and SCFPE methods analysis of the bulk qPCR datasets. A linear mixed effects (LME) model was fit to the replicate measurements (MATLAB R2020a) with 'cpd' as the response variable, 'cycle number' as the fixed effects, and 'day' and 'PCR tube' as the uncorrelated random effects (see Appendix C, *LME Results* for details). The fixed effect model and 95% confidence intervals are plotted in Figure 5.4C and represented as dashed lines. The minimal error in the drop measurements and the flat response of cpd in relation to the quantification cycle (-1.7 cpd/cycle) demonstrate SCFPE as a viable analysis technique for drop-based qPCR.

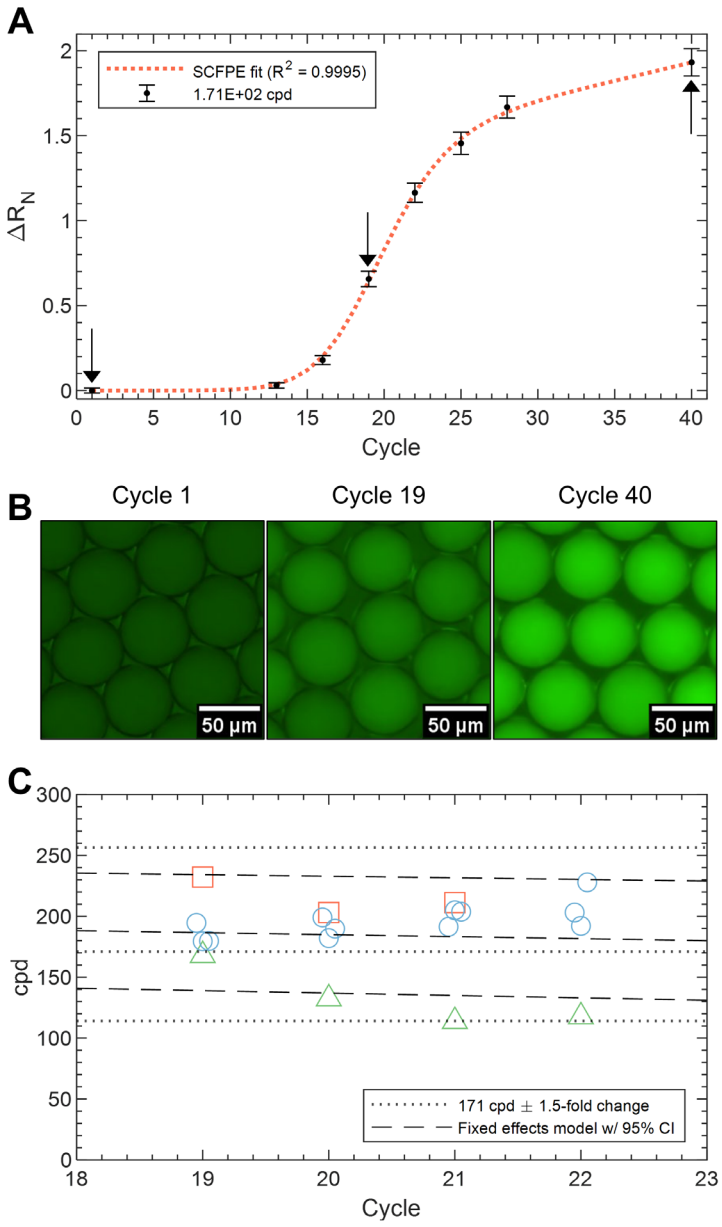


Figure 5.4. SCFPE conversion applied to drop data. (A) SCFPE model built from drop fluorescence measurements made at various thermocycles. (B) Epifluorescence images of 50 µm diameter drops measured at various cycles as indicated by arrows in (A). (C) Conversion of replicate drop measurements. Measurements are made on day one (red squares), day two (green triangles), and day three (blue circles). Day three includes technical replicates measured from three PCR tubes. Data from day one at cycle 22 was removed as an outlier for the LME model analysis. Dotted lines indicate the expected value of 1.71 x 10^2 cpd with upper and lower bounds set as a 1.5-fold change. Dashed lines indicate the fixed effects model with upper and lower bounds set as the 95% confidence intervals.

M Gene Drop Mixture Measured with SCFPE

To demonstrate the ability to resolve more than one concentration of RNA in drops with SCFPE, an equal mixture of three M gene concentrations in drops was prepared. The three populations of drops contained either 1.71 x 10^1 cpd, 1.71 x 10^2 cpd, or 1.71 x 10^3 cpd. A representative epifluorescence image of these drops sampled at cycle 22 is displayed in Figure 5.5A and shows separation in fluorescence intensity between the three M gene populations. Measurements made of this drop population at cycle 22 with a flow-based fluorescence detection method at a rate of approximately 100 Hz (N = 5.9 x 10^3 drops) are converted to cpd values with the SCFPE method (Figure 5.5B). Three distinct distributions are observed that are centered approximately on the expected cpd value. A gaussian mixture model (GMM) is applied to the data to extract the three populations (Figure 5.5B, colored lines). GMM fits of the mixed population are compared to the respective M gene populations measured by themselves (Figure 5.5C). The GMM fits are centered on the individually measured populations to demonstrate that the populations within the mixture are similar to those measured individually (distribution statistics provided in Table C4). Both the low (10^1 cpd) and high (10^3 cpd) examples have similar distributions between the mixed and individual measurements while the 10^2 cpd GMM fit (Figure 5.5C, green dashed line) has a wider distribution than the individual measurement and is likely due to run-to-run variation as was observed in Figure 5.4C. The difference between the population means of the single M gene and mixed M gene samples falls within a <1.9-fold measurement error which is similar to the error observed with the bulk qPCR datasets in Figure 5.3. The <1.9-fold error between the GMM fits and individual samples demonstrates that GMM can be used to accurately extract populations of interest from SCFPE drop-based qPCR data.

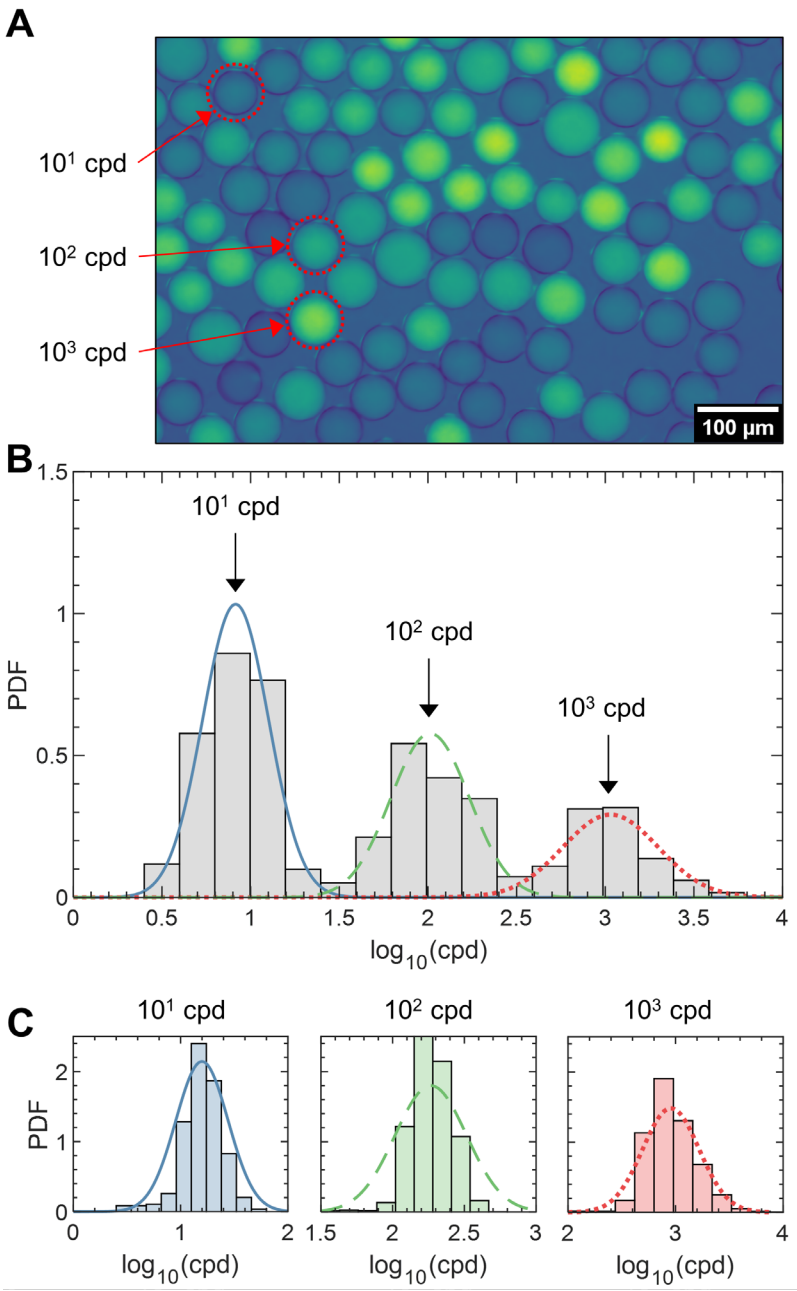


Figure 5.5. Mixed and individual M gene drop populations. (A) Epifluorescence image of the M gene drop mixture at cycle 22 containing either 1.71 x 10^1, 1.71 x 10^2, or 1.71 x 10^3 cpd. (B) Conversion of drop fluorescence measurements of the M gene mixture to cpd using the SCFPE method (N = 5.9 x 10^3 drops). A Gaussian Mixture Model (GMM) is fit to the data to extract the estimated individual distributions of each M gene concentration as indicated by the colored lines. (C) Individual measurements of 1.71 x 10^1 cpd (N = 1.0 x 10^3 drops), 1.71 x 10^2 cpd (N = 2.2 x 10^3 drops), and 1.71 x 10^3 cpd (N = 7.9 x 10^3 drops) M gene drop populations from independent experiments with the respective GMM fit from (B) centered and overlaid on the histogram.

Conclusion

SCFPE is a novel curve fitting approach for qPCR amplification curve data that provides a more accurate fit than SCF methods. The improved accuracy is obtained by incorporating the effect of PCR efficiency into the sigmoidal function which provides an asymmetric fit to each amplification curve. Novel analysis of qPCR data can be performed with SCPFE from a single cycle of fluorescence data collected in the exponential to linear region of the amplification curve, reducing the amount of information required for sample measurements. Even with the reduced information, we show that SCFPE quantifies published qPCR datasets and our own qPCR datasets with similar accuracy when compared to the standard *Cq* method. The single cycle quantification of SCPFE allows measurements made with our OCD RT-qPCR method to be quantified.[80] We demonstrate the ability of SCPFE to accurately resolve single and mixed populations of IAV M gene in drops, thereby validating the novel drop-based qPCR approach which detects drops at approximately 100 Hz. This novel approach simplifies the operations and increases the drop throughput of static imaging[126, 130] or flow-based[30, 168, 169] systems which have been limited to <100 drops per run or <10 Hz, respectively. The work presented here will allow high-throughput single cell studies to be performed with traditional qPCR accuracy and the speed of drop-based microfluidics by building upon previous drop PCR work where PCR mix was directly injected into drops containing single mammalian cells and thermocyled.[181, 182] Doing so will enable new questions related to single cell population diversity to be answered with qPCR measurements of these drops that were previously unobtainable.

Acknowledgments

This work was supported by Defense Advanced Research Projects Agency (DARPA) grant W911NF-17-2-0034 and by National Science Foundation (NSF) CAREER Grant 1753352.

Supporting Information

Supplemental data tables for drop measurements and LME results.

Notes

The authors declare no competing financial interest.

CHAPTER 6

DROP-BASED RT-QPCR REVEALS HIGHLY VARIABLE INFLUENZA A VIRAL BURST SIZE FROM SINGLE CELLS

Contribution of Authors and Co-Authors

Manuscript in Chapter 6

Author: Geoffrey K. Zath

Contributions: G.K.Z. designed research, performed research, analyzed data, and wrote the manuscript

Co-Author: Mallory M. Thomas

Contributions: M.M.T. designed research, performed research, and wrote the manuscript

Co-Author: Emma K. Loveday

Contributions: E.K.L. designed research, performed research, and wrote the manuscript

Co-Author: Dimitri A. Bikos

Contributions: D.A.B. designed research, performed research, and wrote the manuscript

Co-Author: Connie B. Chang

Contributions: C.B.C. designed research and wrote the manuscript

Manuscript Information

Geoffrey K. Zath, Mallory M. Thomas, Emma K. Loveday, Dimitri A. Bikos, Connie B. Chang

Proceedings of the National Academy of Sciences (PNAS)

Status of Manuscript:
__X_ Prepared for submission to a peer-reviewed journal
____ Officially submitted to a peer-reviewed journal
____ Accepted by a peer-reviewed journal
____ Published in a peer-reviewed journal

United States National Academy of Sciences

Abstract

Viral infection is a complex process that involves highly diverse and dynamic viral populations interacting with a heterogeneous population of host cells. A better understanding of viral diversity at the single cell level would provide greater insight into how heterogeneity of infection affects population-level dynamics. Investigating virus and host cell dynamics is typically performed using bulk culture or intracellular measurements and may not fully capture the cell-to-cell differences in virus production. Thus, there is a need for high-throughput quantification of the extracellular viral output, or burst size, from single cells to elucidate individual host-cell dynamics. Here, we have developed a novel drop-based reverse transcriptase quantitative polymerase chain reaction (RT-qPCR) method to measure the amount of influenza A virus (IAV) viral RNA (vRNA) produced from cells infected with a single virion. This method utilizes drop-based microfluidics to encapsulate infected cells within picoliter sized drops, thereby ensuring the released virus is contained. Single cell burst size distributions of IAV H1N1 and H3N2 are measured from $\approx 10^4$ infected human alveolar epithelial (A549) cells. The burst size was found to be highly heterogeneous, spanning four orders of magnitude. Our method is the first to measure IAV burst size using a high-throughput drop-based assay and will allow for future work in investigating the heterogeneity of IAV and other viral infections.

Significance Statement

Influenza A virus (IAV) infection is a complex process involving diverse virus and cell populations. A better understanding of the virus released from a single cell, or burst size, is important for IAV infection models. Performing burst size measurements using reverse transcription quantitative polymerase chain reaction (RT-qPCR) in microdrops offers distinct advantages in sample isolation and throughput compared to traditional techniques. However, typical drop-based RT-qPCR methods require the construction of complex microfluidic devices to mimic the functionality of a standard benchtop instrument. Here, a novel drop-based RT-qPCR method measures burst size from single cells at high-throughput, without the need for a complex device.

Introduction

Influenza A virus (IAV) is notorious for causing seasonal epidemics and sporadic worldwide pandemics. On an annual basis, 3-5 million cases of severe illness and ≈500,000 deaths are reported worldwide.[183] Due to the persistence of IAV infections, flu vaccines are administered yearly. These vaccines rely on forecasting models to predict the most prevalent circulating strains. The predictive models are based upon the observation of current circulating IAV strains and result in vaccine efficacies of 35-50%.[184] Low efficacy is partly due to IAV being a rapidly evolving RNA virus. IAV populations exist as an extremely heterogeneous collection of particles with diverse genotypes and phenotypes.[185] Therefore, viral infection result in a complex process that involves highly diverse and dynamic viral populations interacting with a heterogeneous population of host cells. This inherent heterogeneity is not adequately accounted

for by traditional cell culture systems and virological methods. Thus, high-resolution examination into the heterogeneity and stochasticity of viral production of IAV at the single-cell level is necessary.

Understanding how IAV interacts with its host cells is typically performed using tissue culture systems or with animal models. These traditional methods measure population averages from infected cell cultures. However, individual cells exist as a heterogeneous population, resulting in cell-to-cell differences in virus production. Recent studies have utilized reverse transcription quantitative polymerase chain reaction (RT-qPCR),[186-188] RNA sequencing,[188-190] fluorescence activated cell sorting (FACS),[186, 191] or flow cytometry[192] to elucidate the distribution of virus production at the single cell level. These methods have shown the *intracellular* production of virus to be highly heterogeneous.[186-190, 192] Plaque assays of cells isolated by serial dilution in a microtiter plate[187, 188] or FACS[191] provide a measure of *extracellular* release of infectious virus from cells. However, plaque assays only measure infectious virus which does not provide a true measure of all the viral particles released, or "burst size",[193] from a cell. Viral burst size is an important parameter for the modeling of viral dynamics,[194, 195] including IAV immune responses.[196] Additionally, single cell studies are typically limited to $\approx 10^2$ cells[186-188, 190, 191] which may not provide a true measure of the population heterogeneity. While the number of cells analyzed for *intracellular* viral content has recently reached $>10^3$ cells,[189] there is still a need for high-throughput analysis of single cells to measure the *extracellular* burst size.

Drop-based microfluidics is a powerful technology for the study of IAV with single cell resolution. Individually infected cells are compartmentalized in aqueous microdroplets that are

picoliters in volume, separated by immiscible oil. The drops are a thousand-fold decrease in volume compared to microliter wells and can be generated at rates of ≈1 kHz. This allows 10^3-10^6 single cells to be assayed from a single tube containing 1 mL of drops. By encapsulating an infected cell in a drop, the viral progeny from that cell are contained within that drop. The viral progeny of the infected cell can be isolated by splitting off a portion of the drop,[197] thereby providing a sample volume containing extracellular infectious and non-infections particles. By measuring the isolated sample with drop-based RT-qPCR, the burst size of IAV can be determined from thousands of individually infected cells. Prior work using drop-based RT-qPCR has relied on complex devices for thermocycling drops and measuring fluorescence.[5, 15, 25, 30, 126] Additionally, the technology has been limited to assaying a bulk sample which is encapsulated into a drop, rather than assaying a sample already in a drop, such as viral progeny. Recent work from our group[80] has demonstrated that real-time amplification curves, a requirement for qPCR analysis, can be constructed from drops sampled at various cycles, eliminating the need for a complicated microfluidic device. This work has laid the groundwork for developing a novel drop-based RT-qPCR method for measuring the burst size from drops containing individually infected cells.

Here, a novel drop-based qPCR method was developed to characterize the single cell burst size of IAV H1N1 and H3N2 from ≈10^4 infected human alveolar epithelial (A549) cells. The extracellular viral output from single cells was found to be highly heterogeneous, spanning four orders of magnitude, and is consistent with similar intracellular studies of IAV.[187, 190] Cellular β-actin was measured to filter out drops containing lysed cells which may have released intracellular viral RNA (vRNA). To achieve these measurements, infected drops were processed

on a microfluidic chip which splits a portion of the drop and merges it with an RT-qPCR mix.[197] The merged drops were thermocycled using a standard qPCR machine and sampled at different cycles to measure drop fluorescence with a flow-based detection method. A novel qPCR analysis technique based on the mapping of amplification curves enabled quantification of the fluorescence measurements made at each cycle. Our method is the first to measure IAV burst size at the single cell level using a high-throughput, multiplexed drop-based assay. The work presented here will allow for future work in investigating the heterogeneity of not only IAV production, but other viruses such as HIV or SARS-CoV-2, in order to better understand and predict their emergent behavior.

Results

Single Cell RT-qPCR Using Drop-Based Microfluidics

A549 cells are prepared for single cell drop experiments with an initial infection of IAV H3N2 or H1N1 at an MOI of 0.1 in 6-well plates (Figure 6.1A). The cells are then washed, resuspended in media, and either re-plated (bulk sample) or encapsulated in 100 μm diameter drops and incubated for 18 h. After 18 hours post infection (hpi), the supernatants of the bulk and broken drop samples are measured with bulk RT-qPCR while the remaining drops are prepared for drop based RT-qPCR (Figure 6.1B). H3N2 and H1N1 infections are verified with bulk RT-qPCR (Figure 6.1C) for the bulk and broken drop samples at 0 and 18 hpi. For both strains, the bulk and broken drop samples at 18 hpi are significantly different when measured with a two-sample Student's t-test ($p << 0.05$). Virus production in drops is 10.9× or 2.4× greater than bulk for the H3N2 or H1N1 infections, respectively. On average, H3N2 production in drops is 5.0× greater than H1N1 ($p << 0.5$).

To investigate virus production between H3N2 and H1N1 at a single level, incubated drops are processed on a split-and-merge microfluidic chip[182] which prepares the drops for drop-based RT-qPCR (Figure 6.1D). On the split-and-merge chip (Figure 6.1E), drops (i) are split into a waste drop (ii) and smaller split drop (iii) at a 1:8 split ratio. The split drop (iii) is merged with RT-qPCR mix (iv) that has been optimized for improved drop stability and dye retention during thermocycling.[80] The merged drops (v) are collected in qPCR tubes and subsequently thermocycled on a qPCR machine (Figure 6.1F). The qPCR machine is paused at various thermocycles, following our previously developed protocol,[80] and the fluorescence of each drop is measured using flow-based fluorescence detection (Figure 6.1G).[176] An example of the Taqman probe fluorescence increasing in drops with each cycle detected (Figure 6.1H).

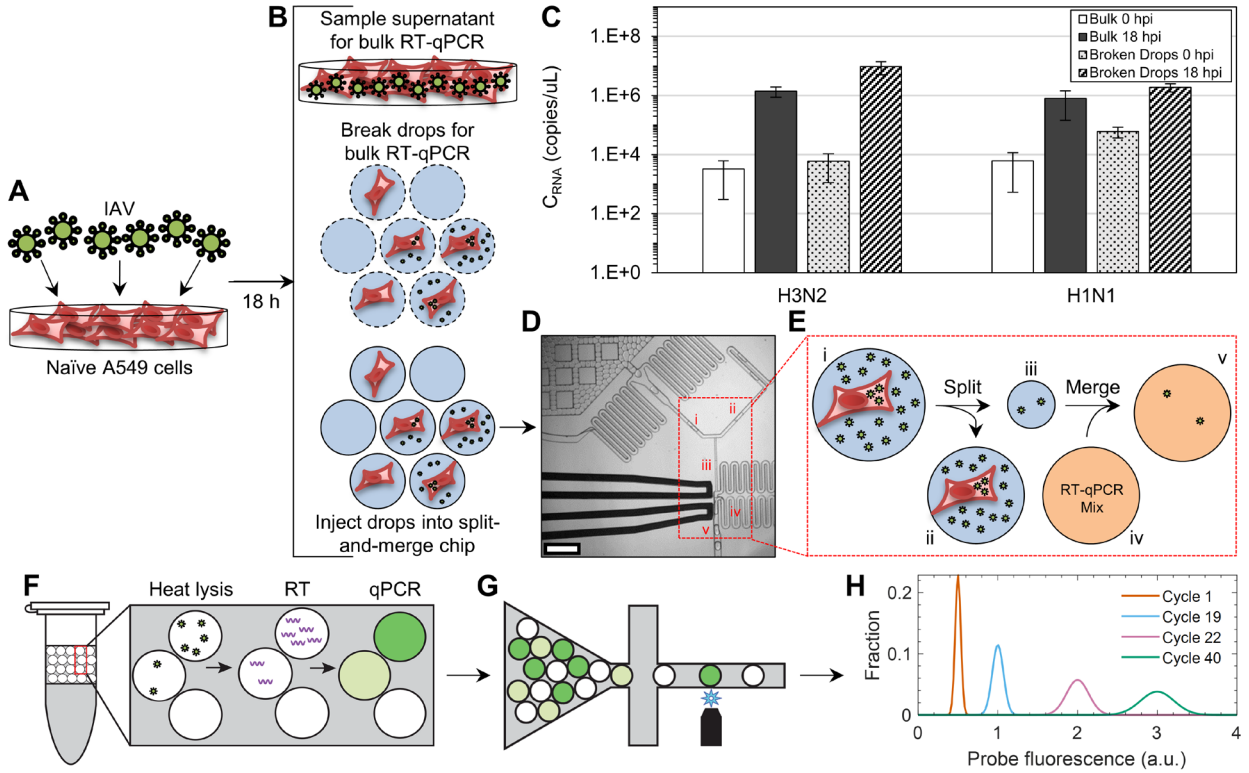


Figure 6.1. Workflow for RT-qPCR of IAV from single cells. (A) Plated naïve A549 cells are infected with IAV prior to being incubated for 18 h in a 6-well plate (bulk sample) or 100 µm diameter drops. (B) After 18 hpi, the supernatant of the infected cells is sampled from the 6-well plates or from broken drops for bulk RT-qPCR. For drop-based RT-qPCR, drops are injected into the split-and-merge chip for processing. (C) Bulk RT-qPCR results of the bulk and broken drop sampling for the H3N2 and H1N1 infected cells. Each bar represents the pooled data from each respective replicate. Error bars represent one standard deviation. (D) Micrograph of the split-and-merge chip in operation. Scale bar represents 500 µm. (E) The infected drop (i) is split into a waste drop (ii) and a split drop (iii). The split drop is merged with RT-qPCR mix (iv). The merged drop (v) is collected in a qPCR tube off-chip and stored on a cold block. (F) Drops are thermocycled in qPCR tubes off-chip and sampled at various cycles. IAV is heat lysed during the RT step, thereby releasing genomic RNA. (G) The fluorescence of drops collected at various thermocycles are measured via flow-based fluorescence detection. (H) Representative data shows the probe fluorescence measured in drops increases with each cycle.

Novel qPCR Analysis Using Amplification Curve Mapping

To demonstrate the ability to quantify the amount of RNA contained within a drop, three populations of M gene RNA corresponding to 1.71×10^1, 1.71×10^2, or 1.71×10^3 copies per drop (cpd) are encapsulated in 50 µm diameter drops across three independent experiments.

Examples of the normalized reporter fluorescence (ΔR_N) of these drops detected at cycles 1, 19, 22, and 40 are shown in Figure 6.2A. By cycle 19, there are three distinct populations with fluorescence increasing with the higher concentration of RNA as expected. However, the fluorescence value alone does not provide a quantitative measurement for the contents of the drop and requires additional processing as is typical for qPCR data. In this case, rather than employ the standard *Cq* or *Ct* method of analysis for qPCR data, we use a novel qPCR analysis technique which creates a map, or library, of amplification curves from a single reference curve.

The novel qPCR analysis technique provides quantification of a sample when measured at a single cycle and is highlighted in Figure 6.2B-G. First, a reference curve (solid black line, Figure 6.2B-D) is constructed from a known sample, in this case 1.71×10^2 cpd, using a sigmoidal curve that has been modified to take into account the changing PCR efficiency throughout the reaction (see Appendix D, *Sigmoidal Curve Fitting Using PCR Efficiency* for details). By comparing the three population of M gene RNA data to the reference curve, we observe that the 1.71×10^3 cpd (green dots, Figure 6.2B) and 1.71×10^1 cpd (red dots, Figure 6.2D) data are separated by approximately three cycles on the x-axis as expected. The 1.71×10^3 cpd (blue dots, Figure 6.2C) data fall on the same line as the reference curve as expected, showing consistency between the two samples detected here.

Amplification curve mapping is demonstrated with the 1.71×10^3 cpd sample in Figure 6.2E. Virtual amplification curves (N = 10 and 1000) are extended from the reference curve (multi-colored lines, Figure 6.2E-F) and represent different concentrations of RNA (see Appendix D, *Amplification Curve Library* for details). A standard curve relating ΔR_N to cpd can be created by taking a slice through the library (black dotted line, Figure 6.2E-F) at a single cycle

and recording the ΔR_N at each intersection point with the virtual amplification curves. As each virtual curve has a starting template concentration associated with it, this process results in the standard curve in Figure 6.2G. The usable range of the standard curve (gray shaded area, Figure 6.2G) is defined by ΔR_N of the reference curve. The range has a maximum at $\mu - 3 \times \sigma$ of the reference curve cycle 40 fluorescence and the minimum is set at the 99.5th percentile of cycle 1 fluorescence. The minimum and maximum are represented by red dots in Figure 6.2F-G.

At one cycle, the amplification curve mapping technique can accurately convert the fluorescence of three RNA drop populations to cpd (Figure 6.2H-I) with an average absolute percent difference of 32% ± 16% from the expected mean value. One approach to quantify the heterogeneity of the measured populations is with the Gini coefficient (G). G is traditionally used to measure income inequality,[198] but has also been used to describe the extreme heterogeneity of IAV infection in single cells.[190] $G = 0$ describes a perfectly uniform distribution while $G = 1$ describes a completely skewed distribution. In this case, $G < 0.298$ describes a homogeneous distribution of measured RNA in drops. This is represented graphically in Figure 6.2J where a homogeneous distribution has a curve close to the diagonal (dashed black line, Figure 6.2J). By contrast, a heterogenous distribution will have a sharp curve with $G \rightarrow 1$.

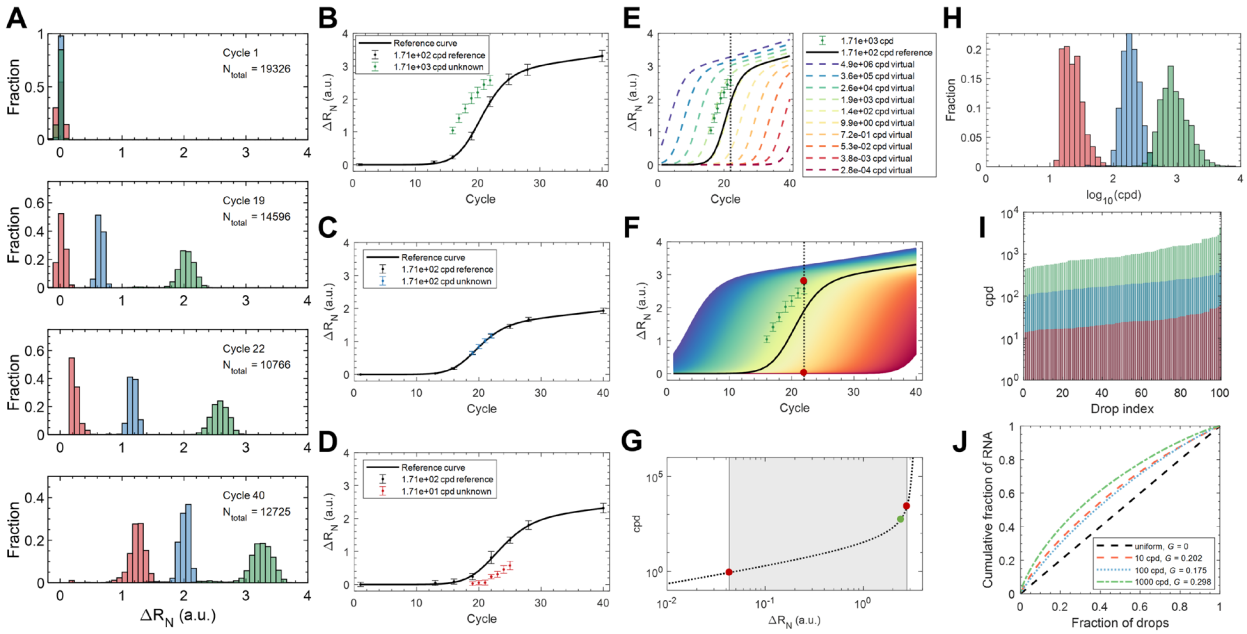


Figure 6.2. Homogeneous distributions of RNA measured with drop-based RT-qPCR analysis using amplification curve mapping. (A) Histograms of normalized fluorescence measurements ΔR_N taken at increasing RT-qPCR cycles. Drops contained M gene RNA at 1.71 x 10^1 (red), 1.71 x 10^2 (blue), or 1.71 x 10^3 (green) cpd. Average ΔR_N of the homogeneous distributions measured between cycles 15-25 (B) 1.71 × 10^3 (solid green circles), (C) 1.71 × 10^2 (solid blue circles), and (D) 1.71 × 10^3 (solid red circles) cpd. Each set of data is plotted against the respective 1.71 × 10^2 cpd reference data (solid black circles) fit using the SCFPE method (solid black line). Error bars represent one standard deviation. Construction and interpretation of amplification curve libraries built from a 1.71 x 10^2 cpd reference curve extended across a spectrum of (E) 10 and (F) 1000 virtual reference curves. The ΔR_N data for drops containing 1.71 x 10^3 cpd (solid green circles) are mapped onto each library. A slice of the amplification curve library at cycle 22 (black dashed line) is used to construct a (G) standard curve relating ΔR_N to cpd. The usable range (gray shaded area) for drop measurements is defined by ΔR_N of the reference curve. The range has a maximum at $\mu - 3 \times \sigma$ of the reference curve cycle 40 fluorescence and the minimum is set at the 99.5 percentile of cycle 1 fluorescence. The minimum and maximum are represented by red dots on (F) and (G). (H) ΔR_N of each M gene distribution from cycle 22 converted to cpd using the respective standard curve. (I) The 1.71 x 10^1 (red), 1.71 x 10^2 (blue), or 1.71 x 10^3 (green) cpd populations in drops as measured at cycle 22 arranged in order of increasing RNA per drop. A random subset (N = 100) is chosen for each population. (J) Cumulative fraction of drops containing 1.71 × 10^1 (dashed red line), 1.71 × 10^2 (dotted blue line), and 1.71 × 10^3 (dash-dotted green line) cpd from (I) with the corresponding *G*. $G = 0$ indicates a perfectly uniform distribution of RNA across drops (dashed black line).

Heterogeneous Population of IAV RNA in Drops

To represent a heterogenous population of RNA in drops, three populations of M gene RNA are encapsulated in 50 μm diameter drops (1.71×10^1, 1.71×10^2, or 1.71×10^3 cpd) and mixed together in a single experiment (Figure 6.3A). The three populations of drops can be seen in an epifluorescence image taken at cycle 22 (Figure 6.3B). Flow-based detection of the drops at cycles 19, 20, 21, 22 reveals four peaks rather than the expected three (Figure 6.3C). The fourth peak (red arrows, Figure 6.3C) appears between what is likely the 1.71×10^2 and 1.71×10^3 cpd peaks. It may be due to coalesced drops and/or diffusion between drops during thermocycling, however, we have shown previously that these effects are minimal for 50 μm diameter drops with an optimized PCR mix.[80] We speculate that the fourth peak here is due to variability in the PCR reaction from improper mixing of the master mix prior to encapsulation and is likely a bimodal distribution from the 1.71×10^2 cpd condition. Because PCR is being carried out in a 65 pL volume, the effect of improper mixing may be more apparent than when performed in a standard qPCR tube (25 μL). Interestingly, when the ΔR_N values are converted to cpd using the amplification curve mapping method (Figure 6.3D), the prominence of the fourth peak is lessened at later cycles.

A randomly chosen subset of the cpd data (N = 100) from cycle 22 is highlighted in Figure 6.3E. Instead of a relatively flat increase in RNA compared to the drop index as seen in Figure 6.2I, the heterogenous population has three distinct “steps” related to the three concentrations of RNA in the mixture. As expected, the cumulative fraction of RNA in drops at cycle 22 for the mixture of all three RNA concentrations has a sharp curve (Figure 6.2F, G = 0.786), indicating a highly heterogenous distribution of RNA across drops compared to the single populations (G <0.298). Here, we have defined what an expected homogeneous and

heterogenous population of RNA in drops may look like and provided a baseline for describing IAV burst size measurements.

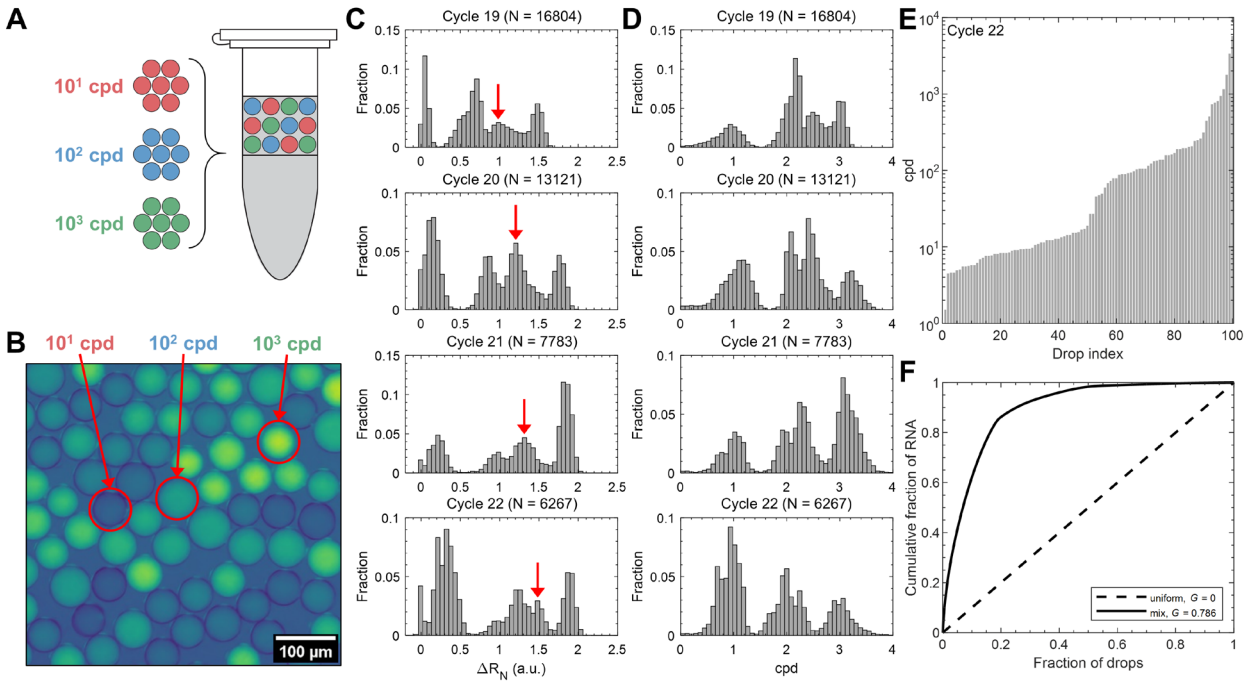


Figure 6.3. Heterogeneous distributions of IAV M gene RNA in drops. (A) Heterogeneous distributions are creating by collecting equal volumes of 50 µm diameter drops containing either 1.71×10^1, 1.71×10^2, or 1.71×10^3 cpd. (B) Epifluorescence image of drops from part (A) at cycle 22. (C) Normalized fluorescence ΔR_N of the M gene FAM probe collected using flow-based detection at cycles 19, 20, 21, and 22. An unexpected fourth peak is indicated with a red arrow. (D) Result of converting ΔR_N to cpd using the amplification curve mapping method. (E) Concentration of M gene RNA in each drop as measured at cycle 22 and arranged in order of increasing RNA. (F) Cumulative fraction of RNA in drops at cycle 22 from (E) with the corresponding *G*.

Single Cell IAV Production Measured with Drop-Based RT-qPCR

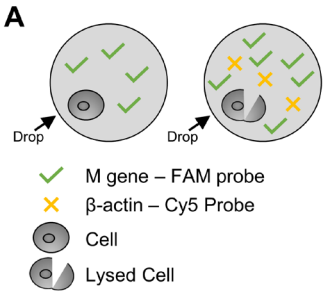
To ascertain the distribution of extracellular IAV vRNA at the single cell level, three replicates of single cell IAV burst size experiments are conducted for H3N2 and H1N1 at an MOI of 0.1 following the workflow presented in Figure 6.1. The loading of cells in drops is measured during each replicate experiment to ensure the majority of drops contain single cells.

Based on these measurements, we expect that of the drops containing cells, ≈86% contain single cells while the remaining contain two or more cells (Figure D.1). A Taqman probe for cellular β-actin is included in the drop RT-qPCR mix, along with the IAV M gene probe, to identify drops containing cells which may have released intracellular vRNA due to lysis (Figure 6.4A). Our results show that β-actin levels are linearly correlated with the concentration of cells in suspension when sampled for bulk RT-qPCR (Figure D.2, $R^2 = 0.995$). Therefore, a high level of β-actin in a drop indicates a cell was present. We use one of two thresholds to ensure drops containing lysed cells are removed from the data. The threshold is set at either the top 12.5% of drops containing β-actin, corresponding to the split-and-merge chip split ratio, or above a β-actin concentration of 2×10^3 cpd, corresponding to the slope of Figure D.2 ($\approx 2 \times 10^3$ β-actin copies per cell). The threshold which removes the most drops is chosen to ensure as many lysed cells are removed as possible.

Experimental measurements and burst size statistics for each replicate of H3N2 and H1N1 are provided in Figure 6.4B. Here, a breakdown between each replicate reveals a wide range of average H3N2 burst size (3.8×10^2 to 1.6×10^3 copies/cell) compared to the narrow range of average H1N1 burst size (4.8×10^2 to 4.9×10^2 copies/cell). Interestingly, a narrow range of average burst size measurements for H1N1 does not result in a consistent G (0.520 to 0.623) which indicates the distributions of each replicate have a different shape. This is further illustrated with the H3N2 replicates where a wide range of burst size results in an even greater range of G (0.518 to 0.724) compared to H1N1 replicates. We observe similar trends when the replicate data is pooled; H3N2 has a ≈2× greater burst size than H1N1 and a more heterogenous distribution ($G_{H3N2} = 0.705$ versus $G_{H1N1} = 0.586$).

A random subset of β-actin filtered M gene data (N =100) for the H3N2 and H1N1 replicates are presented in Figure 6.4C-E and Figure 6.4F-H, respectively. Figure D.3 indicates that many of the drops filtered by high β-actin levels also contained high levels of vRNA. To provide a comparative view of the H3N2 and H1N1 replicates, the average cumulative fractions of drops containing vRNA for each replicate are plotted in Figure 6.4I. In both cases, the distributions of extracellular vRNA for H3N2 and H1N1 measured by drop-based RT-qPCR are heterogenous with a mean G of 0.608 ± 0.106 and 0.581 ± 0.054, respectively. These values fall between the distributions of the homo- and heterogenous distributions presented in Figures 6.2 and 6.3. The relative heterogeneity of H3N2 is highly varied between replicates as indicated by the blue shaded region on Figure 6.4I which represent one standard deviation from the mean. In contrast, the H1N1 replicates are more consistent with a narrower red shaded region on Figure 6.4I. By pooling the replicate data, a more complete picture is drawn of the burst size distributions from the thousands of cells assayed (Figure 6.4J-K). The pooled H3N2 distribution is markedly more heterogenous (Figure 6.4L) than the pooled H1N1 distribution with G_{H3N2} = 0.705 compared to G_{H1N1} = 0.586.

A



B

Strain	Replicate	Drops	Filtered drops	Avg burst size (copies/cell)	Burst size IQR (copies/cell)	Gini coefficient
H3N2	1	4524	3955	1.6×10^3	1.1×10^2 to 1.6×10^3	0.724
H3N2	2	4288	3751	6.3×10^2	1.1×10^2 to 8.1×10^2	0.581
H3N2	3	2193	1914	3.8×10^2	5.3×10^1 to 5.8×10^2	0.518
H3N2	**Pooled**	**11005**	**9620**	**1.0×10^3**	**9.3×10^1 to 8.9×10^2**	**0.705**
H1N1	1	2141	1873	4.9×10^2	6.3×10^1 to 6.9×10^2	0.623
H1N1	2	2840	1932	4.8×10^2	1.1×10^2 to 6.8×10^2	0.520
H1N1	3	2036	1780	4.8×10^2	9.9×10^1 to 5.0×10^2	0.601
H1N1	**Pooled**	**7017**	**5585**	**4.8×10^2**	**8.8×10^1 to 6.3×10^2**	**0.586**

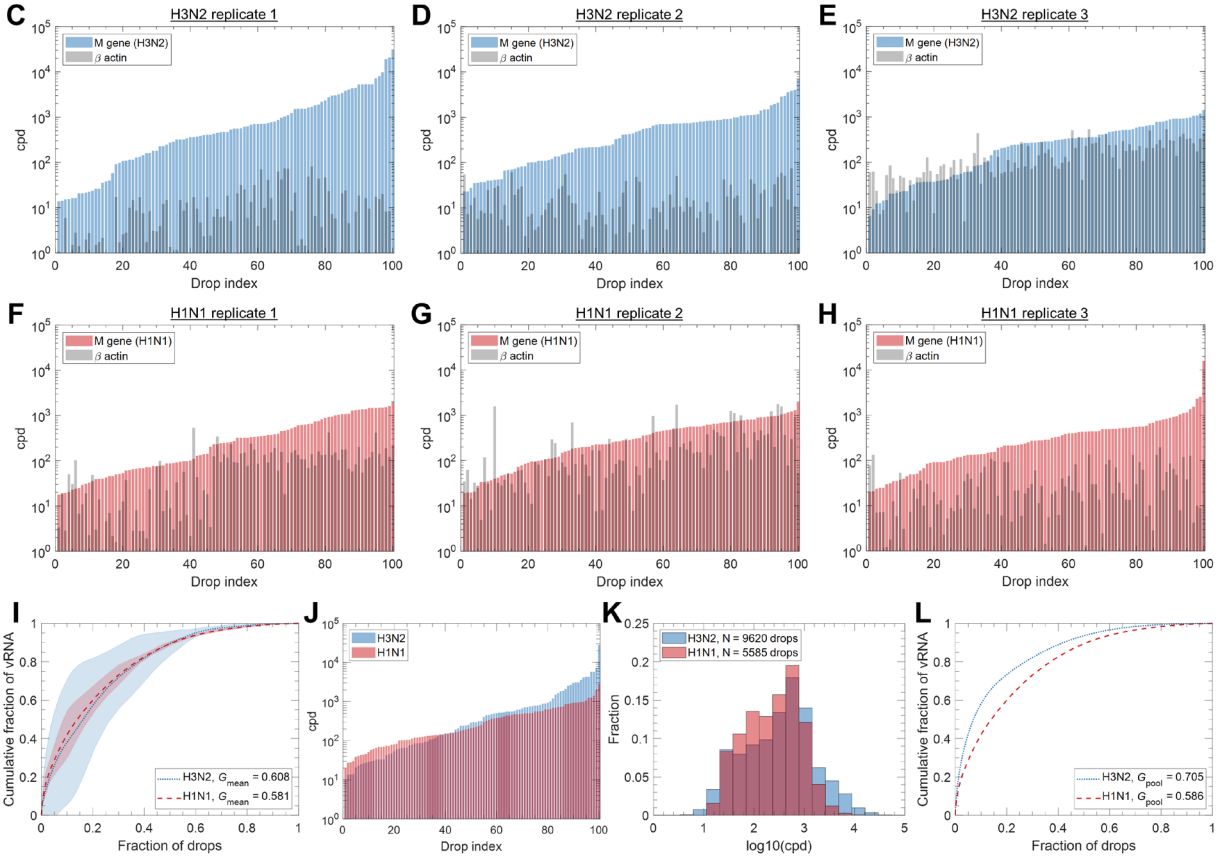


Figure 6.4. Single cell burst size measured with drop-based RT-qPCR for H3N2 and H1N1. (A) A β-actin probe (yellow X) is added to the PCR mix to identify drops containing lysed cells which have released intracellular vRNA (green check mark). (B) Additional experimental measurements and burst size statistics for each replicate of H3N2 and H1N1. The interquartile range (IQR) is bounded by the 25th and 75th percentile of the burst size data. A subset (N = 100 drops) of (C-E) H3N2 (blue) and (F-H) H1N1 (red) arranged in order of increasing cpd. The equivalent β-actin in each drop is represented as a gray bar. Drops containing high β-actin are filtered out. (I) Average cumulative fraction of vRNA in drops of the H3N2 (blue dotted line) and H1N1 (red dashed line) replicates with the corresponding mean *G*. Shaded regions represent one standard deviation from the mean. (J) A subset (N = 100 drops) of pooled data for H3N2 (blue) and H1N1 (red) replicates. (K) Histogram of all pooled data for H3N2 (blue) and H1N1 (red) replicates. (L) Cumulative fraction of vRNA in drops for the pooled data of H3N2 (blue dotted line) and H1N1 (red dashed line) replicates with the corresponding pooled *G*.

Discussion

Here, high-throughput single cell level measurements of IAV burst size is enabled by a novel drop-based RT-qPCR method. This approach for drop-based RT-qPCR removes the need for a complicated microfluidic device for thermocycling and fluorescence detection. Instead of requiring a complex device, the amplification curve mapping data analysis technique can quantify the fluorescence of drops sampled at various cycles from a benchtop thermocycler. To demonstrate our method, we show that it can be used to accurately measure homo- and heterogeneous populations of IAV M gene in drops. It is then used to measure IAV burst size from single cells infected with H3N2 or H1N1. The infected cells are encapsulated in 100 μm diameter drops, incubated, and processed for drop-based RT-qPCR at high-throughput with a split-and-merge chip.

While much is known about *intracellular* RNA in single cells infected with IAV,[187-190] measurements of *extracellular* RNA (i.e. burst size) at the scale presented here have not been reported. Previous measurements of IAV burst size are estimated to be between 10^3-10^4 virions/cell from bulk assays.[199, 200] The distributions of H3N2 ($G = 0.608 \pm 0.106$) and H1N1 ($G = 0.581 \pm 0.054$) extracellular RNA measured here by drop-based RT-qPCR are highly heterogenous, an observation that is consistent with previous measurements of viral gene expression between the two strains.[189] However, the distributions are not *extremely* heterogenous as previously reported for intracellular RNA of H1N1 as measured by single cell RNA sequencing ($G = 0.64$ to 0.81).[190] Additionally, the range of extracellular RNA measured in the drop experiments ($\approx 10^1$ to $\approx 10^4$ cpd) is narrower and orders of magnitude lower than previously reported for single cell intracellular RNA of H1N1 as measured by RT-qPCR.[187] These

differences may be attributed to that fact that the production of viral particles is proportional to the level of the least-abundant genome segment in the cell.[187] Therefore, it is expected that the amount of intracellular RNA would be greater than the extracellular RNA because the production of virus is constrained by viral genome production within a cell.

The high-throughput measurement of single cell IAV burst size presented here is to our knowledge to first of its kind. Within a single experiment, $>10^3$ cells can be analyzed, thereby quickly providing insight into the heterogenous release of virus. This may be a critical step in understanding novel viruses such as the recent pandemic caused by SARS-CoV-2. We foresee this method to be used for future studies investigating the heterogeneity of virus production to better understand the dynamics of infection and inform single cell infection models.

Materials and Methods

Virus Strains and Cell Lines

IAV A/California/07/2009 (H1N1) or A/Perth/16/2009 (H3N2) stocks were propagated on Madin-Darby canine kidney (MDCK) cells in DMEM media supplemented with 10% FBS and 1× penicillin/streptomycin. All experimental infections were performed on human alveolar epithelial A549 cells propagated in Hams F-12 growth media supplemented with 10% FBS and 1× Pen/Strep.

Bulk Virus Infection

A549 cells were seeded onto 6-well plates with 1×10^6 cells per well and allowed to incubate at 37 °C for 24 h The cells were washed twice with 1X PBS and then infected with either H1N1 or H3N2 at a MOI of 0.1 suspended in infection media for 1 h. The infection media

consisted of Hams F-12 supplemented with 5-mM HEPES, 1× Pen/Strep and 0.2% BSA. Infection with either the H1N1 or H3N2 virus was performed in the presence of 1 μg TPCK-trypsin/ml.[201] After 1 h, the virus inoculum was removed and fresh infection media was added before an additional 1 h incubation period at 37 °C. Following the second incubation period, infected cells were collected by incubating with 0.25% Trypsin + 1X EDTA and pooled. The pooled cells were centrifuged at 500 g for 5 min, washed in 1X PBS, and spun down again. Washed infected cells were resuspended in infection media to a final concentration of 2 x 10^6 cells/mL and either encapsulated in drops or replated at a concentration of 1 x 10^6 cells per well.

PCR Sequences and Reaction Concentrations

The sequences of qPCR amplification primers for the IAV Matrix gene (M gene) were designed for use by the CDC: M gene forward primer 5′-GACCRATCCTGTCACCTCTGAC-3′, M gene reverse primer 5′-AGGGCATTCTGGACAAATCGTCTA-3′.[139] The sequence of the M gene TaqMan probe was: 5′-/FAM/TGCAGTCCTCGCTCACTGGGCACG/BHQ1/-3′. The primers targeting the β-actin plasmid (pCAG-mGFP-Actin, Addgene #21948) were: β-actin forward primer 5'-GTGTGGATCGGCGGCTCCATC-3', β-actin reverse primer 5'-GACTCGTCATACTCCTGCTTG-3' and β-actin TaqMan probe 5'-/Cy5/ACCTTCCAGCAGATGTGGATC/BHQ2/-3'.[140] Primers and probes were ordered from Eurofins Operon and were prepared as 100 μM stocks. The working stocks of the primers were 25 μM with a final reaction concentration of 400 nM. The working stock of the probe was 10 μM with a final reaction concentration of 200 nM. Samples were amplified using SuperScript III Platinum One-Step qRT-PCR kit (Invitrogen 11732-020) at a dilution of 1 μL of enzyme mix per 25 μL reaction volume. Each reaction mix contained 0.05 μM ROX reference dye, 2.0 mM

$MgSO_4$, 0.32 U/µL SUPERase RNase Inhibitor (Invitrogen AM2694), 1.0% w/v Tween-20 (Calbiochem 655204-100mL), 0.8 µg/µL BSA (Fisher BP675-1), and 1.0 M betaine (Sigma B0300-1VL). For the in-drop reaction mix, 0.15 µM ROX reference dye was used. Thermocycling was performed using a qPCR machine (QuantStudio 7, Applied Biosystems): 1 cycle for 30 min at 60 °C, 1 cycle for 2 min at 95 °C, and 40 cycles between 15 s at 95 °C and 1 min at 60 °C.

In Vitro Transcribed RNA

Standard curves were generated using serial dilutions of *in vitro* transcribed IAV M gene.[141] To generate the *in vitro* transcribed RNA, a gBlock containing a T7 promoter (underlined), forward and reverse primer sites (italicized), and probe sequence (bold) for the M gene was ordered from IDT: 5′-GTCTAATACGACTCACTATAG *GACCAATCCTGTCACCTCTGAC* **TGCAGTCCTCGCTCACTGGGCACG** TGCTTCATCGCGAACTGCTTCGCGGATGCCATCGTCATGGCCACGAGGATATGTAAG AGT *TAGACGATTTGTCCAGAATGCCCT*-3′. The M gene was transcribed *in vitro* using a MEGAscript T7 RNA Synthesis Kit (Ambion, AM1333) and purified over a GE Illustra Sephadex G-50 NICK column. RNA concentration was quantified using a NanoDrop spectrophotometer to determine the copy number per µL. The corresponding concentration in cpd was calculated by multiplying the copies/µL value by the volume of a 50 µm or 100 µm diameter drop (6.54×10^{-5} or 5.24×10^{-4} µL/drop).

Sample Preparation for Bulk qPCR

Bulk infections were prepared for bulk RT-qPCR by collecting both the supernatant and cellular monolayer from each well. The 0 hpi bulk samples were frozen overnight at -80 °C

while the 24 hpi bulk samples were taken straight from the incubator. Preparation of drop infections for bulk RT-qPCR involved freezing a 300ul sample of drops at -80 °C for 30 min and collecting a 200ul sample of the broken drop suspension. Collected bulk and drop infections were centrifuged at 500 g for 5 min and the supernatant was sampled for RT-qPCR.

Microfluidic Device Fabrication

The split-and-merge and drop making (50 μm and 100 μm diameter) microfluidic devices were fabricated using standard soft lithography methods.[176] Photoresist (Microchem SU-8 3050) was patterned on silicon wafers (University Wafer, ID# 447, test grade) using photolithography. Polydimethylsiloxane (PDMS) (Sylgard 184) mixed at a 10:1 mass ratio of polymer to cross-linking agent was poured onto the patterned device master molds. Air was purged from the uncured PDMS by placing the filled mold in a vacuum chamber for at least 1 h. The PDMS was cured in an oven at 55 °C for 24 h and then removed from the mold with a scalpel. Ports were punched into the PDMS slabs with a 0.75 mm diameter biopsy punch (EMS Rapid-Core, Electron Microscopy Sciences). The PDMS slabs of the split-and-merge devices were bonded to each other after plasma treatment (Harrick Plasma PDC-001) for 30 s at medium power and 700 mTorr oxygen pressure. The bonded PDMS slabs of the split-and-merge device and PDMS slab of the drop making device were bonded to 2-in by 3-in glass slides (VWR micro slides, cat. #48382-179) after plasma treatment for 60 s at high power and 400 mTorr oxygen pressure. Microelectrodes were added to the split-and-merge device by injecting molten solder (Indium Corporation of America, cat. #53307) into the electrode channels on the device and terminated with a pin terminal (Phoenix Contact, cat. #1945151). Both devices were made hydrophobic by flowing Aquapel (Pittsburgh Glass Works) through the channels, followed by blowing the

channels with air filtered through a 0.2-μm filter (GVS ABLUO 25 mm, Fisher Scientific) before baking the devices in an oven at 55 °C for 1 h.

Drop Encapsulation

Flow-focusing drop making devices were used to make 50 μm or 100 μm diameter drops. For drops being incubated, the continuous phase consisted of a 1.5 wt% (w/w) solution of PEG-$PFPE_2$-based surfactant (RAN Biotechnologies, 008-FluoroSurfactant) in fluorinated HFE-7500 oil (3M). For drops undergoing PCR, the continuous phase consisted of 3.0 wt% (w/w) surfactant. The dispersed and continuous phases were loaded in 3-mL syringes and injected into the drop making microfluidic devices at flow rates of 800 μL/h and 1600 μL/h or 1000 μL/h and 3000 μL/h (New Era NE-1000 syringe pumps) for 50 μm or 100 μm diameter drops, respectively. Infected and mock infected cell encapsulation occurred in a biosafety cabinet which had been previously UV treated overnight to maintain a sterile environment. Drops containing cells were collected in 5-mL syringes for 30 minutes. Syringes containing cells were capped with a syringe filter and placed in an incubator at 37 °C and 5% CO_2. Drops containing M gene and/or β-actin were stored in a syringe or qPCR tubes and kept on ice.

Drop Processing for RT-qPCR

All supplies used for processing drops were treated with UV in a biosafety cabinet overnight for sterilization. Infected drops were injected into the split and merge device at a flow rate of 500 μL/h and spaced by oil flowing at 2000 μL/h (HFE 7500 with 3.0 wt% RAN surfactant). The injected drops flowed past a split junction where approximately $1/8^{th}$ of the volume was split and sent to the merge junction. A second spacer oil was injected at the merge junction at a flow rate of 500 μL/h (HFE 7500 with 3.0 wt% RAN surfactant). RT-qPCR mix

was injected at a flow rate of 438 μL/h and merged with the split drop at the merge junction. A microelectrode driven by a high voltage amplifier (Trek Model 2220-CE) and controlled by a custom LabVIEW program was used to merge the drops. The microelectrode at the merge junction provided a constant 25 kHz, 200 V square wave signal which destabilized the drop interface to allowing merging with the RT-qPCR mix. Merged drops were collected in PCR tubes for 2.5 min each for approximately 20 μL of drops. PCR tubes were stored on a cold block until ready for thermocycling. Drops containing M gene and β-actin were processed with the split and merge device following the infected drops.

Drop Sampling and Imaging

The qPCR machine was paused and three PCR tubes were removed to sample drops at various cycles. Five fields of view were imaged of the sampled drops on an inverted epifluorescence microscope (Nikon Ti2-E) at 10× magnification (NA 0.3). Brightfield and fluorescence images of the FAM TaqMan probe for M gene (FITC), ROX reference dye (Texas Red), and Cy5 TaqMan probe for β-actin were captured with a sCMOS (Hamamatsu, ORCA-Flash4.0 v3) camera.

Drop Detection

Thermocycled drops were injected into a microfluidic detection device[176] at a flowrate of 200 μL/h and spacer oil (Novec 7500) without surfactant was injected at a flowrate of 800 μL/h. Approximately $\approx 10^3$ drops were detected at each cycle for drops containing M gene and approximately $\approx 10^4$ drops were detected for drops containing cells. The drop fluorescence detection system consisted of a custom modified Nikon TiU inverted microscope with three lasers, a set of dichroic mirrors, and two photomultiplier tubes (PMTs, Hamamatsu H10723-

20).[176] The beams of the 22 mW 488 nm laser (Thorlabs MCLS1), 25 mW 561 nm laser (Cobolt Jive), and 20 mW 642 nm laser (Thorlabs MCLS1) were aligned together and coupled into the backport of the microscope where they were focused to a spot by the 40× objective (NA 0.60). The flowing of drops across the laser spot resulted in fluorescence detection by three PMTs split into three channels using dichroic and bandpass filters, Ch1: 520/40 nm (green), Ch2: 600/40 nm (red), and Ch3: 670/10 nm (far-red). A field programmable gate array (FPGA, National Instruments NI-7852R) was used to control the PMT gains and record fluorescence measurements using LabVIEW 2015. A custom MATLAB (R2020a) script was used to process and analyze the drop fluorescence detection data. FAM and Cy5 fluorescence intensities were normalized as ΔR_N, where the qPCR normalized reporter value R_N is defined as $R_N = (I_{\mathrm{FAM}}\ or\ I_{Cy5})/I_{\mathrm{ROX}}$, $\Delta R_N = R_N - R_{N,\mathrm{baseline}}$, I_i is the respective intensity of FAM / Cy5 / ROX at each cycle, and $R_{N,\mathrm{baseline}}$ is the average R_N value of the first cycle.

Amplification Curve Mapping for Infected Drops Experiments

A reference amplification curve was made from drops containing 1.71×10^2 cpd of M gene and 3.49×10^2 cpd of β-actin after processing on the split-and-merge device. The reference curve was fit using SCFPE (see Appendix D, *Sigmoidal Curve Fitting Using PCR Efficiency* for details) from drops detected at cycles 1, 16, 19, 22, 25, 28, 31, and 40 and used to build an amplification curve library. A standard curve relating initial RNA template concentration to drop fluorescence measured at an intermediate thermocycle was extracted from the amplification curve library at cycles 19, 22, 25, and 28. Infected drops were sampled at cycles 1, 19, 22, 25, 28, and 40. For each burst size replicate, converted cpd data from cycles 19, 22, 25, and 28 were pooled.

Acknowledgements

This work was supported by Defense Advanced Research Projects Agency (DARPA) grant W911NF-17-2-0034 and by National Science Foundation (NSF) CAREER Grant 1753352. We thank Humberto Sanchez for his help developing the protocol for encapsulating infected cells.

CHAPTER 7

CONCLUSIONS AND OUTLOOK

Conclusions

The research presented in this thesis contributes to the understanding of adapting biological assays for drop-based microfluidic applications and is focused on two projects. Chapter 3 discusses the design and characterization of the Pressure Cooker Chip (PCC) for the rapid encapsulation of drop libraries. Chapters 4-6 covers the development of a drop-based reverse transcription quantitative polymerase chain reaction (RT-qPCR) method to measure IAV output from infected cells.

In Chapter 3, rapid generation of fluorescently barcoded drop libraries is demonstrated with the PCC. The PCC interfaces directly with a 384-well microtiter plate and eliminates the need for multiple pump sources or liquid handling systems when performing simultaneous sample encapsulation. We show that drop formation in the PCC is monodisperse (CV = 4.6%) and is described by a drop scaling law.[110] The drop scaling law provides a method for tuning the size of drops produced. Using the PCC, we create drop libraries based on microbead and quantum dot fluorescent barcode labels, achieving a measured total of 188 discrete barcodes with a two-color combination of quantum dots. The 188 discrete barcode combination is to our knowledge the largest two-color fluorescent barcode combination in drops to date. Further optimization of the quantum dot barcodes with a third color would allow multiple 384-well microtiter plates to be barcoded and encapsulated into a drop library. Barcoding multiple microtiter plates would improve current fluorescently barcoded drop library applications such as

drug screening,[83, 90] adapting DNA microarray analysis into drops,[91] or screening protease activity.[92] For example, a greater barcode count would provide more information per assay by increasing the number of testable drug combinations or improving the resolution of dose-response curves. The additional utility of using a drop library is demonstrated by sorting a barcoded drop population with minimal error; thereby enabling downstream analysis of a specific sample population with methods such as PCR and/or sequencing.[103-105] Overall, the PCC provides a streamlined workflow requiring only a single microfluidic device to rapidly generate up to 192 unique samples in a drop library. The PCC will be a useful tool for performing multiplexed assays in fields such as drug screening or molecular biology where a large number of chemical or biochemical reactions must be processed.

In Chapters 4-6, the development and application of a drop-based RT-qPCR method is presented for the purpose of measuring the output of IAV from single cells encapsulated in drops. The study of IAV is important as it causes seasonal epidemics and sporadic worldwide pandemics that have resulted in over 100 million deaths during the past century. A better understanding of IAV diversity at the single cell level would provide greater insight into how heterogeneity of infection affects population-level dynamics.

To adapt RT-qPCR in drops in Chapter 4, we found PCR additives which stabilized drops and limited dye diffusion during thermocycling after systematic tested of many known PCR additives. This is a critical step as results can be misleading if drops merge or leak. Previous solutions include complex microfluidic devices to keep drops separated,[135] replacing liquid drops with hydrogel beads,[158] or stabilizing drops using solid particles.[159] These approaches can limit downstream options as drops may no longer be easily subdivided by splitting or merged with

additional reaction components as we present in Chapter 6. Instead, it is more desirable to improve drops stability and dye retention by modifying the composition of the reaction mix itself. Through the process of PCR additive screening, we developed a method we call Off-Chip Drop Reverse Transcription quantitative (OCD RT-qPCR) in which drops are thermocycled in a qPCR machine and sampled at various cycle numbers "off-chip", or outside of a microfluidic chip. Using OCD RT-qPCR, we demonstrate for the first time that sampled drops imaged using an epifluorescence microscope correlate with real-time amplification curves obtained with a standard qPCR instrument. The correlation between the image data and instrument data indicate quantitative analysis of the drops may be possible using a variation of current qPCR analysis techniques as presented in Chapter 5. Drop thermocycling and analysis is performed entirely off-chip, or outside of a microfluidic device. A variety of downstream processing options become available to drops stable enough to be handled for off-chip analysis and eliminates the need for complicated custom microfluidic thermocycling devices.[126, 127, 130] Furthermore, in Chapter 6 we show that OCD RT-qPCR can be used to measure the viral output of infected single cells.

Chapter 5 describes a novel qPCR data analysis technique that was developed to quantify drop fluorescence data collected with the OCD qRT-PCR method described in Chapter 4. We call this method Sigmoidal Curve Fitting using PCR Efficiency (SCFPE). SCFPE is a novel curve fitting approach for qPCR amplification curve data that provides a more accurate fit than sigmoidal curve fitting (SCF) methods. The improved fit is achieved by modeling the PCR amplification efficiency of the reaction which better fits the asymmetric amplification curve. SCFPE analysis of qPCR data reduces the amount of information required for sample measurement as only a single cycle of fluorescence data in the exponential or linear region of the

PCR amplification curve is needed. We validate SCFPE data analysis by applying it to multiple qPCR datasets and find that it converts fluorescence data with similar accuracy and precision when compared to the standard quantification cycle method. Applying SCFPE analysis to the data collected from our OCD RT-qPCR method provides single cycle quantification of individual drops undergoing PCR. Combining these two methods simplifies the operations of drop-based RT-qPCR and increases drop throughput by at least 10-fold compared to previously published techniques.[30, 126, 130, 168] We demonstrate this ability by accurately measuring single and mixed populations of IAV M gene RNA in drops. The novel drop qPCR methods developed in Chapters 4 and 5 are the first to measure IAV RNA using a high-throughput drop-based assay. These developments enable the screening of single IAV infected cells in drops with traditional qPCR accuracy and the high-throughput of drop-based microfluidics.

Chapter 6 describes the application of OCD RT-qPCR and SCFPE for the purpose of measuring the viral output, or burst size, of IAV from individually infected cells in drops. Human alveolar epithelial (A549) cells infected with either the seasonal 2008 H3N2 or pandemic 2009 H1N1 IAV strains were encapsulated within millions of picoliter sized drops followed by single cell, drop-based RT-qPCR analysis. In order to probe the contents of each drop, a split-and-merge chip was used to split off a portion of each drop and merge it with PCR mix.[182] This created a new drop containing PCR mix and any virions released from a single cell. In this manner we screened $\approx 10^4$ cells to quantify IAV RNA (M gene) and cellular mRNA (β-actin). This is a significant increase in single cell throughput compared to common serial dilution approaches performed using standard 384-well plates.[163, 188] We found that extracellular IAV production is highly heterogeneous as observed previously for intracellular IAV production.[163,

[188-190] Our approach is the first to measure individual host-pathogen dynamics from thousands of IAV infected single cells using this high-throughput, drop-based RT-qPCR assay. The work presented here provides a better understanding of IAV diversity at the single cell level by providing extracellular measurements which have been previously unobtainable. The drop-based RT-qPCR method will be useful for future studies of viruses to better understand and predict their emergent behavior.

Outlook

The two projects presented in this thesis share a common goal of increasing the sample throughput of traditional biological assays by adapting their methodology for use in microfluidic drops. They achieve this goal through either parallelized drop formation or the use of a novel data analysis technique, however, their overlap is not demonstrated. While this demonstration is outside the scope of this thesis, suggestions for future work on combining the PCC and drop-based qPCR are described in this section.

The burst size measurements performed in Chapter 6, while novel, could be expanded to include additional IAV strains, multiplicity of infection (MOI), and/or cell type (e.g. MDCK cells). How these factors impact the output of virions are important questions to answer as they will provide further insight into how viral infection dynamics are affected in complex *in vivo* environments (i.e. the human body) where one or more of these factors may vary greatly. While our novel drop-based RT-qPCR approach provides high-throughput screening of single cells for one infection condition, doing so for multiple factors would be labor and time intensive. The PCC provides a solution in this case where multiple factors such as IAV strain, MOI, and/or cell type can be tested simultaneously and in a combinatorial manner. Each combination can be

barcoded with either microbeads or quantum dots and added to a 384-well microtiter plate for encapsulation with the PCC. The drop library created with the PCC can then be processed with the same workflow presented in Chapter 6, thereby providing massive amounts of information about IAV infection dynamics.

Future burst size experiments may include adding a PCR probe to track the abundance of defective interfering particles (DIPs) within the viral output of a single cell. DIPs are defective in virus replication due to a large deletion in one of their eight viral genomes and interfere with virus replication.[202, 203] The production of DIPs from approximately 200 single infected cells has been shown to be highly variable and may have an impact on IAV production.[188] Our drop-based qPCR approach would improve on this study by the measuring DIP production of tens of thousands of cells, thereby providing further insight into the heterogeneity of DIPs in single infected cells. Lastly, as demonstrated in Chapter 3, sorting of drops allows for a specific population of interest to be collected for downstream analysis. Sorting based on a PCR fluorescent probe[204] would allow drops to be selected based on viral output level (e.g. low, intermediate, or high) and prepared for RNA sequencing analysis. This would be a unique approach of using RNA sequencing to study the extreme heterogeneity of IAV viral infection.[190, 205]

The future work presented here is not strictly limited to IAV infection. For example, the recent COVID-19 pandemic has highlighted the need for a rapid response to emerging viruses such as SARS-CoV-2. The use of multiplexed PCR probes or RNA sequencing to track mutations at the single cell level would be useful in quickly understanding these new viruses. Additionally, the increased sample throughput provided by the PCC may even be used for testing

new antiviral drugs. In the end, the adaption of biological assays for use with drop-based microfluidic technologies will not only lead to improved iterations of these assays, but also to their novel use in academic and medical research.

APPENDICES

APPENDIX A

SUPPLEMENTAL INFORMATION FOR CHAPTER 3: RAPID PARALLEL GENERATION OF A FLUORESCENTLY BARCODED DROP LIBRARY FROM A MICROTITER PLATE USING THE PRESSURE COOKER CHIP

PCC Fabrication

Negative master molds were fabricated upon 3-in diameter silicon wafers (University Wafer, ID# 447, test grade) using UV cross-linked SU-8 photoresist exposed through photomasks printed on high-resolution transparent plastic film (CAD Art, 20k dpi). The top (Fig. 3.1a, i) and middle (Fig. 3.1a, ii) layer negative master molds were made with SU-8 2075 (MicroChem) to create 250 μm tall channels while the bottom layer (Fig. 3.1a, iii) was made with SU-8 3050 (MicroChem) to create 50 μm tall channels. To create the 250 μm tall channels, a first coat of SU-8 2075 was spun at 1000 rpm for 30 s, then softbaked at 100 °C for 60 min, and resulted in a ~200 μm thick layer. The second coat of SU-8 2075 was spun at 3000 rpm for 30 s, then softbaked at 100 °C for 10 min, and resulted in a ~250 thick layer. To create the 50 μm tall channels, SU-8 3050 was spun at 3000 rpm for 30 s, then softbaked at 95 °C for 15 min. For all spin coating conditions, photoresist was initially spun at 500 rpm for 10 s to evenly coat the wafer surface. PDMS prepolymer (Sylgard 184, 10:1 mix ratio of prepolymer to curing agent) was cast onto the negative master molds and cured overnight at 65°C. The cross-linked PDMS devices were cut out using a scalpel. Via holes and sample inlet holes were manually punched using a 0.75 mm ID biopsy punch (Harris Unicore). A larger 1.25 mm ID biopsy punch (Robbins Instruments RBP-12) was used to fit 1/16-in OD tubing (IDEX FEP tubing) to the oil inlet and 0.052-in OD tubing (Scientific Commodities PE/5) to the drop outlet port on the top layer (Fig. 3.1a, i) of the device. Assembly of the PCC began with oxygen plasma treatment (Harrick Plasma PDC-001) of the middle (Fig. 3.1a, ii) and bottom (Fig. 3.1a, iii) PDMS layers for 30 s at medium power and 700 mTorr oxygen pressure. A thin layer of deionized (DI) water was introduced between the plasma-treated surfaces to temporarily prevent the PDMS layers from

bonding during the alignment process, which was accomplished by eye. The aligned layers were immediately baked for ≥1 h in a 65 °C oven to dry the DI water and allow the PDMS layers to bond. The top face of the bonded two-layer device was subjected to oxygen plasma (Fig. 3.1a, i) of the device with the previously mentioned plasma treatment settings. DI water was introduced to prevent bonding while the top layer (Fig. 3.1a, i) was aligned with the previously bonded middle (Fig. 3.1a, ii) and bottom (Fig. 3.1a, iii) layers such that the via holes of the middle layer (Fig. 3.1a, ii) connect with their respective oil inlet and drop outlet channels. Device channels were made hydrophobic by flowing Aquapel (Pittsburgh Glass Works) through the channels of the bonded device, flushing with compressed air, and baking in a 65 °C drying oven for ≥1 h to complete the reaction.

Microbead and Quantum Dot Barcode Label Combinations

Table A.1. Green and red microbead barcode concentration combinations.

#	Green microbeads (beads/μL)	Red microbeads (beads/μL)	#	Green microbeads (beads/μL)	Red microbeads (beads/μL)
1	5.1×10^5	5.1×10^5	13	2.3×10^6	2.3×10^6
2	1.3×10^6	5.1×10^5	14	3.6×10^6	2.3×10^6
3	2.3×10^6	5.1×10^5	15	5.1×10^6	2.3×10^6
4	3.6×10^6	5.1×10^5	16	5.1×10^5	3.6×10^6
5	5.1×10^6	5.1×10^5	17	1.3×10^6	3.6×10^6
6	5.1×10^5	1.3×10^6	18	2.3×10^6	3.6×10^6
7	1.3×10^6	1.3×10^6	19	3.6×10^6	3.6×10^6
8	2.3×10^6	1.3×10^6	20	5.1×10^6	3.6×10^6
9	3.6×10^6	1.3×10^6	21	5.1×10^5	5.1×10^6
10	5.1×10^6	1.3×10^6	22	1.3×10^6	5.1×10^6
11	5.1×10^5	2.3×10^6	23	2.3×10^6	5.1×10^6
12	1.3×10^6	2.3×10^6	24	3.6×10^6	5.1×10^6

Table A.2. QD625 and QD705 quantum dot barcode concentration combinations.

#	QD625 (pM)	QD705 (pM)	#	QD625 (pM)	QD705 (pM)	#	QD625 (pM)	QD705 (pM)	#	QD625 (pM)	QD705 (pM)
1	1.15×10^4	1.02×10^4	49	1.15×10^4	5.76×10^3	97	1.15×10^4	2.56×10^3	145	1.15×10^4	6.40×10^2
2	9.68×10^3	1.02×10^4	50	9.68×10^3	5.76×10^3	98	9.68×10^3	2.56×10^3	146	9.68×10^3	6.40×10^2
3	8.00×10^3	1.02×10^4	51	8.00×10^3	5.76×10^3	99	8.00×10^3	2.56×10^3	147	8.00×10^3	6.40×10^2
4	6.48×10^3	1.02×10^4	52	6.48×10^3	5.76×10^3	100	6.48×10^3	2.56×10^3	148	6.48×10^3	6.40×10^2
5	5.12×10^3	1.02×10^4	53	5.12×10^3	5.76×10^3	101	5.12×10^3	2.56×10^3	149	5.12×10^3	6.40×10^2
6	3.92×10^3	1.02×10^4	54	3.92×10^3	5.76×10^3	102	3.92×10^3	2.56×10^3	150	3.92×10^3	6.40×10^2
7	2.88×10^3	1.02×10^4	55	2.88×10^3	5.76×10^3	103	2.88×10^3	2.56×10^3	151	2.88×10^3	6.40×10^2
8	2.00×10^3	1.02×10^4	56	2.00×10^3	5.76×10^3	104	2.00×10^3	2.56×10^3	152	2.00×10^3	6.40×10^2
9	1.28×10^3	1.02×10^4	57	1.28×10^3	5.76×10^3	105	1.28×10^3	2.56×10^3	153	1.28×10^3	6.40×10^2
10	7.20×10^2	1.02×10^4	58	7.20×10^2	5.76×10^3	106	7.20×10^2	2.56×10^3	154	7.20×10^2	6.40×10^2
11	3.20×10^2	1.02×10^4	59	3.20×10^2	5.76×10^3	107	3.20×10^2	2.56×10^3	155	3.20×10^2	6.40×10^2
12	8.00×10^1	1.02×10^4	60	8.00×10^1	5.76×10^3	108	8.00×10^1	2.56×10^3	156	8.00×10^1	6.40×10^2
13	1.15×10^4	9.00×10^3	61	1.15×10^4	4.84×10^3	109	1.15×10^4	1.96×10^3	157	1.15×10^4	3.60×10^2
14	9.68×10^3	9.00×10^3	62	9.68×10^3	4.84×10^3	110	9.68×10^3	1.96×10^3	158	9.68×10^3	3.60×10^2
15	8.00×10^3	9.00×10^3	63	8.00×10^3	4.84×10^3	111	8.00×10^3	1.96×10^3	159	8.00×10^3	3.60×10^2
16	6.48×10^3	9.00×10^3	64	6.48×10^3	4.84×10^3	112	6.48×10^3	1.96×10^3	160	6.48×10^3	3.60×10^2
17	5.12×10^3	9.00×10^3	65	5.12×10^3	4.84×10^3	113	5.12×10^3	1.96×10^3	161	5.12×10^3	3.60×10^2
18	3.92×10^3	9.00×10^3	66	3.92×10^3	4.84×10^3	114	3.92×10^3	1.96×10^3	162	3.92×10^3	3.60×10^2
19	2.88×10^3	9.00×10^3	67	2.88×10^3	4.84×10^3	115	2.88×10^3	1.96×10^3	163	2.88×10^3	3.60×10^2
20	2.00×10^3	9.00×10^3	68	2.00×10^3	4.84×10^3	116	2.00×10^3	1.96×10^3	164	2.00×10^3	3.60×10^2
21	1.28×10^3	9.00×10^3	69	1.28×10^3	4.84×10^3	117	1.28×10^3	1.96×10^3	165	1.28×10^3	3.60×10^2
22	7.20×10^2	9.00×10^3	70	7.20×10^2	4.84×10^3	118	7.20×10^2	1.96×10^3	166	7.20×10^2	3.60×10^2
23	3.20×10^2	9.00×10^3	71	3.20×10^2	4.84×10^3	119	3.20×10^2	1.96×10^3	167	3.20×10^2	3.60×10^2
24	8.00×10^1	9.00×10^3	72	8.00×10^1	4.84×10^3	120	8.00×10^1	1.96×10^3	168	8.00×10^1	3.60×10^2
25	1.15×10^4	7.84×10^3	73	1.15×10^4	4.00×10^3	121	1.15×10^4	1.44×10^3	169	1.15×10^4	1.60×10^2
26	9.68×10^3	7.84×10^3	74	9.68×10^3	4.00×10^3	122	9.68×10^3	1.44×10^3	170	9.68×10^3	1.60×10^2
27	8.00×10^3	7.84×10^3	75	8.00×10^3	4.00×10^3	123	8.00×10^3	1.44×10^3	171	8.00×10^3	1.60×10^2
28	6.48×10^3	7.84×10^3	76	6.48×10^3	4.00×10^3	124	6.48×10^3	1.44×10^3	172	6.48×10^3	1.60×10^2
29	5.12×10^3	7.84×10^3	77	5.12×10^3	4.00×10^3	125	5.12×10^3	1.44×10^3	173	5.12×10^3	1.60×10^2
30	3.92×10^3	7.84×10^3	78	3.92×10^3	4.00×10^3	126	3.92×10^3	1.44×10^3	174	3.92×10^3	1.60×10^2
31	2.88×10^3	7.84×10^3	79	2.88×10^3	4.00×10^3	127	2.88×10^3	1.44×10^3	175	2.88×10^3	1.60×10^2
32	2.00×10^3	7.84×10^3	80	2.00×10^3	4.00×10^3	128	2.00×10^3	1.44×10^3	176	2.00×10^3	1.60×10^2
33	1.28×10^3	7.84×10^3	81	1.28×10^3	4.00×10^3	129	1.28×10^3	1.44×10^3	177	1.28×10^3	1.60×10^2
34	7.20×10^2	7.84×10^3	82	7.20×10^2	4.00×10^3	130	7.20×10^2	1.44×10^3	178	7.20×10^2	1.60×10^2
35	3.20×10^2	7.84×10^3	83	3.20×10^2	4.00×10^3	131	3.20×10^2	1.44×10^3	179	3.20×10^2	1.60×10^2
36	8.00×10^1	7.84×10^3	84	8.00×10^1	4.00×10^3	132	8.00×10^1	1.44×10^3	180	8.00×10^1	1.60×10^2
37	1.15×10^4	6.76×10^3	85	1.15×10^4	3.24×10^3	133	1.15×10^4	1.00×10^3	181	1.15×10^4	4.00×10^1
38	9.68×10^3	6.76×10^3	86	9.68×10^3	3.24×10^3	134	9.68×10^3	1.00×10^3	182	9.68×10^3	4.00×10^1
39	8.00×10^3	6.76×10^3	87	8.00×10^3	3.24×10^3	135	8.00×10^3	1.00×10^3	183	8.00×10^3	4.00×10^1
40	6.48×10^3	6.76×10^3	88	6.48×10^3	3.24×10^3	136	6.48×10^3	1.00×10^3	184	6.48×10^3	4.00×10^1
41	5.12×10^3	6.76×10^3	89	5.12×10^3	3.24×10^3	137	5.12×10^3	1.00×10^3	185	5.12×10^3	4.00×10^1
42	3.92×10^3	6.76×10^3	90	3.92×10^3	3.24×10^3	138	3.92×10^3	1.00×10^3	186	3.92×10^3	4.00×10^1
43	2.88×10^3	6.76×10^3	91	2.88×10^3	3.24×10^3	139	2.88×10^3	1.00×10^3	187	2.88×10^3	4.00×10^1
44	2.00×10^3	6.76×10^3	92	2.00×10^3	3.24×10^3	140	2.00×10^3	1.00×10^3	188	2.00×10^3	4.00×10^1
45	1.28×10^3	6.76×10^3	93	1.28×10^3	3.24×10^3	141	1.28×10^3	1.00×10^3	189	1.28×10^3	4.00×10^1
46	7.20×10^2	6.76×10^3	94	7.20×10^2	3.24×10^3	142	7.20×10^2	1.00×10^3	190	7.20×10^2	4.00×10^1
47	3.20×10^2	6.76×10^3	95	3.20×10^2	3.24×10^3	143	3.20×10^2	1.00×10^3	191	3.20×10^2	4.00×10^1
48	8.00×10^1	6.76×10^3	96	8.00×10^1	3.24×10^3	144	8.00×10^1	1.00×10^3	192	8.00×10^1	4.00×10^1

PCC Drop Formation Characterization

Reynolds Number Calculation

The Reynolds number was calculated independently for the water and oil phases as $Re = \frac{\rho v d}{\mu}$ where ρ is the fluid density (0.997 g/mL for water and 1.614 g/mL for HFE 7500), v is the fluid velocity (maximum of 0.4 m/s for water and 0.9 m/s for oil), d is the hydraulic diameter ($2w_{channel}$ for a square channel, or 100 μm), and μ is the dynamic viscosity (0.881 mPa·s for water and 1.243 mPa·s for oil). A maximum Reynolds number of 45 was calculated for the water inlet channel and 58 for the oil inlet channel. For low Reynolds number flow ($Re < 60$ for PCC operation), a linear correlation between P and Q is expected based upon the Hagen-Poiseuille relationship ($\Delta P = \frac{8\mu l}{\pi r^4} Q$). We generated a standard curve which verifies that Q_{water}/Q_{oil} is linearly correlated with P_{water}/P_{oil} ($R^2 = 0.916$) (Fig. A.1).

Convert L_{drop} to V_{drop}

To fit the data of V_{drop} as a function of Q_{water}/Q_{oil} in Fig 3.3c, we converted L_{drop} to V_{drop} in the drop with a scaling law,[110] which relates drop length (L_{drop}) to Q_{water}/Q_{oil} (Eq. 3.1). The V_{drop} is converted by approximating a drop in a channel as having a capsule geometry where $V_{drop} = \frac{\pi}{4} w_{channel}^2 (L_{drop} - \frac{1}{3} w_{channel})$.

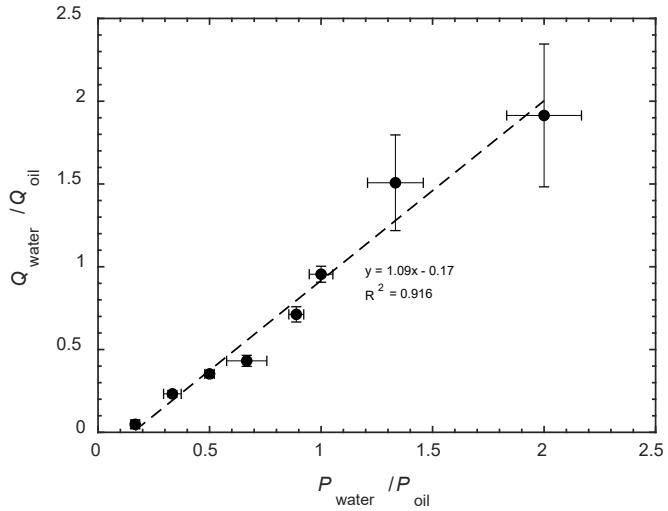
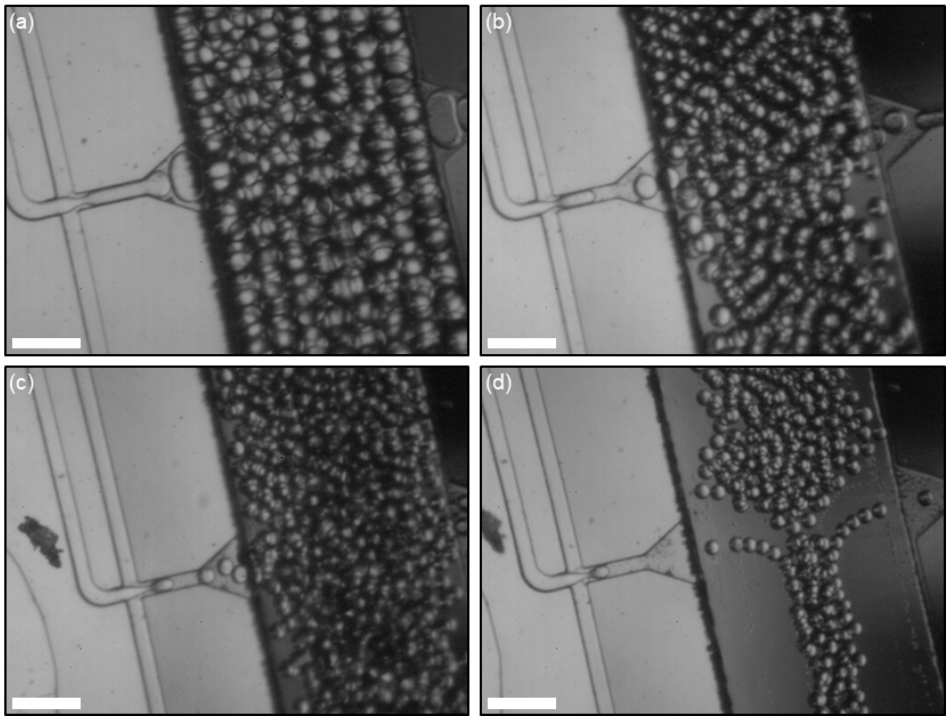


Fig. A.1. Standard curve relating volumetric flowrate ratio to pressure ratio during PCC operation. The relationship between the water/oil pressure ratio (P_{water}/P_{oil}) and water/oil volumetric flowrate ratio (Q_{water}/Q_{oil}) is linear. Error bars on the x-axis represent gauge error and error bars on the y-axis represent one standard deviation of volume measurements.



Video A.1. High speed video capture of drop formation in the PCC ordered by descending D_{drop}, for (a) high water pressure (■, P_{water} = 6 psig and P_{oil} = 3 psig, P_{water}/P_{oil} = 2), (b) low combined pressure (▼, P_{water} = 2 psig and P_{oil} = 3 psig, P_{water}/P_{oil} = 0.67), (c) high combined pressure (▲, P_{water} = 8 and P_{oil} = 12 psig, P_{water}/P_{oil} = 0.67), (d) and high oil pressure (♦, P_{water} = 2 psig and P_{oil} = 12 psig, P_{water}/P_{oil} = 0.17) conditions. Scale bars are 500 μm.

Barcoded Drop Detection

The drop fluorescence detection system for the microbead barcoded drop library consisted of a custom modified Nikon Diaphot 300 inverted microscope with two lasers, a set of dichroic mirrors and photomultiplier tubes (PMTs, Hamamatsu H10723-20).[20] The beams of the 50 mW, 473 nm laser (Suzhou Daheng Optics and Fine Mechanics Co., DHOM-W473-50mW) and the 50 mW, 405 nm laser (Changchun New Industries Optoelectronics Tech Co., MDL-III-405-50mW) were aligned together and coupled into the backport of the microscope where they were focused to a spot by the objective (40×, NA 0.60, Motic). The flowing of drops across the laser spot resulted in fluorescence detection by three PMTs split into three channels using dichroic and bandpass filters, Ch1: 445/40 nm (blue), Ch2: 525/50 nm (green), Ch3: >561 nm (red). A schematic of the drop fluorescence detection system and a detailed optical path representation are provided in Fig. A.4. For bright field illumination, the light from the incandescent bulb was filtered by a 785/62 nm near-infrared (NIR) bandpass filter in order to not interfere with fluorescence detection measurements. A field programmable gate array (FPGA, National Instruments NI-7852R) was used to control the PMT gains and record fluorescence measurements using LabVIEW 2015.

The detection system for quantum dot barcoding consisted of a custom modified microscope, similar to the one described above. The beam of the laser (488 nm, 25 mW, Picarro) was coupled into the backport of the microscope and focused to a spot by the objective (40×, 0.85 NA, Leica). The light was split into three colors for fluorescent detection by using dichroic and bandpass filters for each channel, Ch1: 536/40 nm (green), Ch2: 632/22 nm (red), Ch3: 716/40 nm (far-red), and detected by a PMT for each channel.

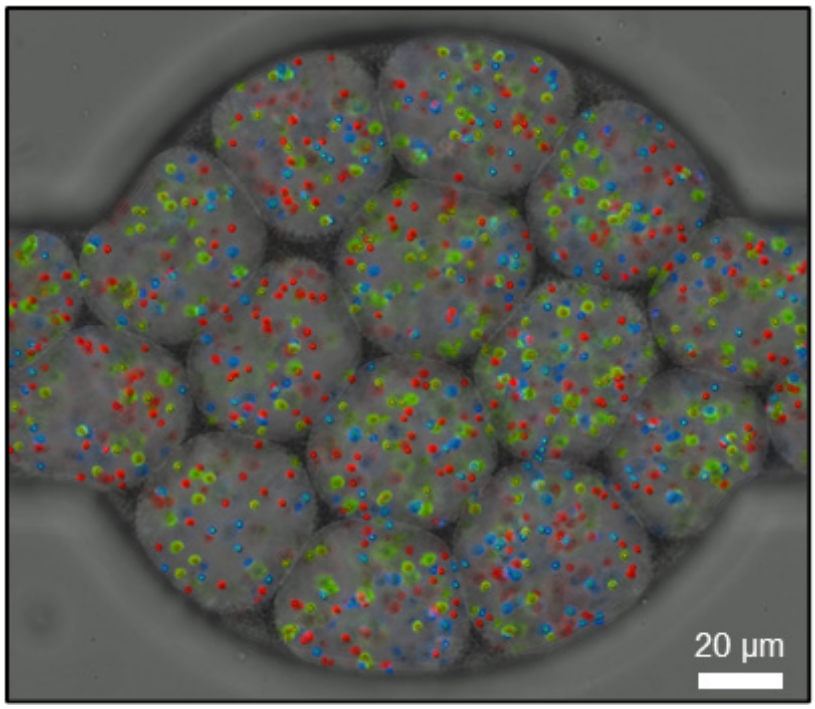


Fig. A.2. Confocal image of fluorescent blue, green, and red microbeads in drops.

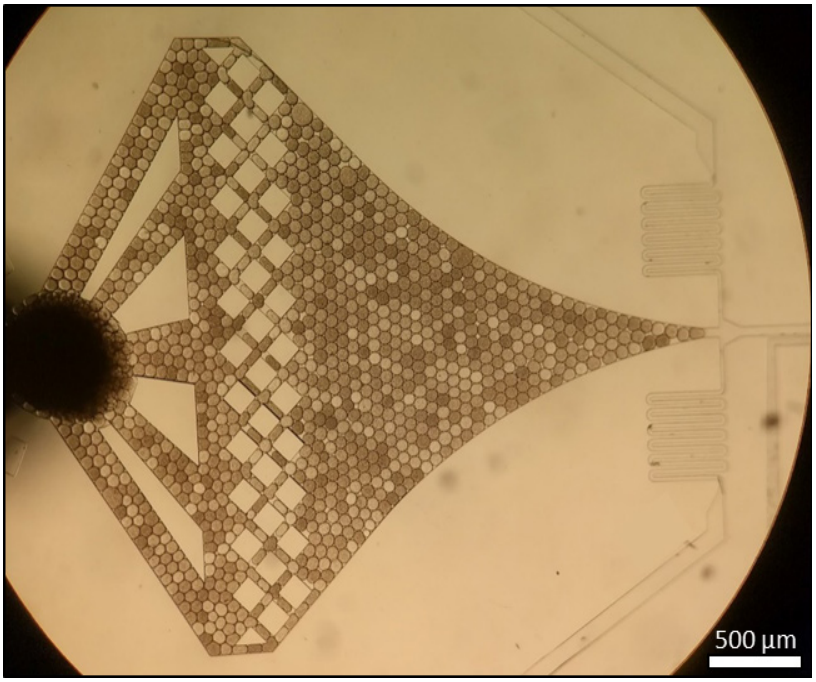
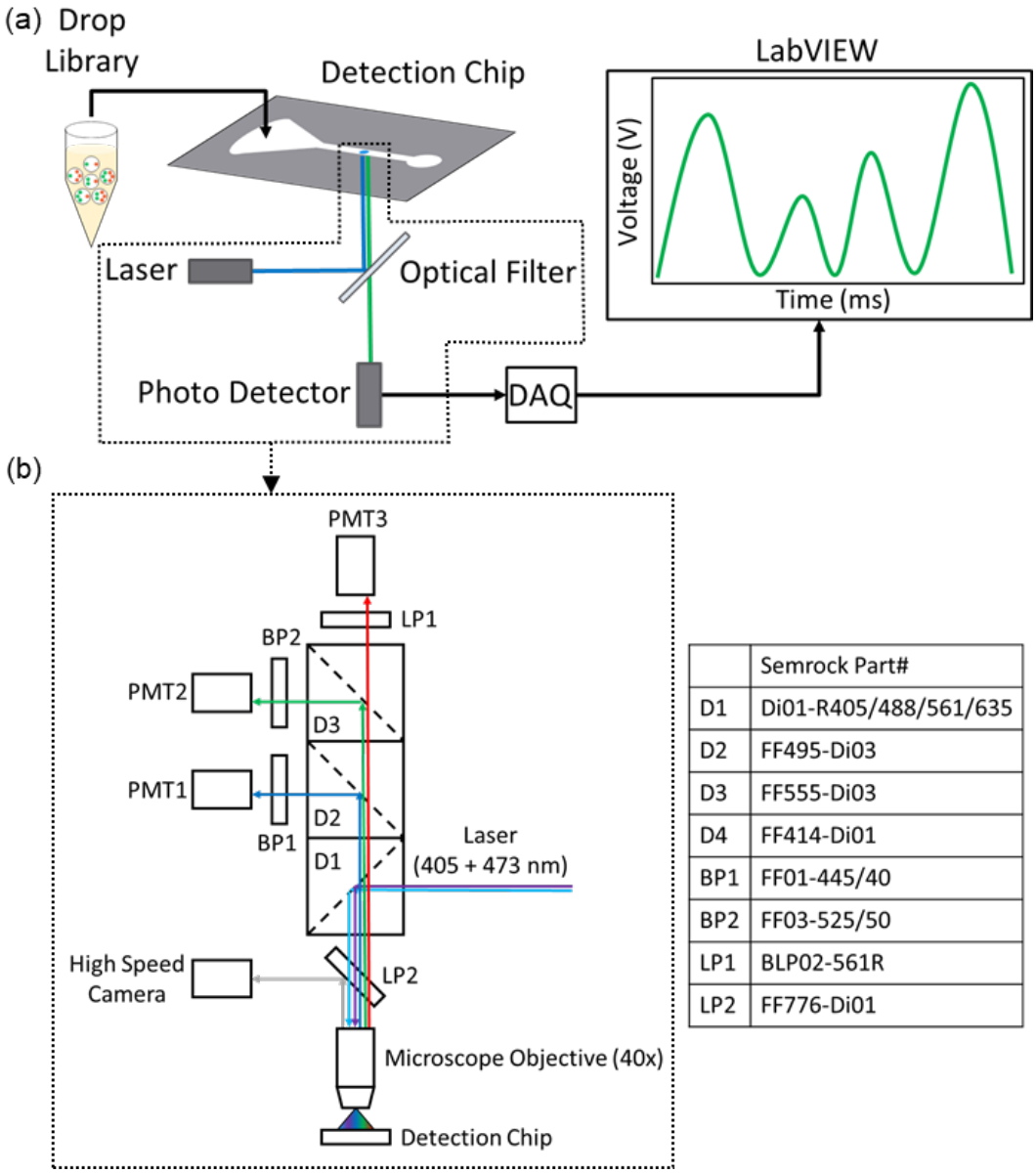


Fig. A.3. Re-injection of barcoded drops into a detection chip. The shading of drops is due to the various microbead concentrations encapsulated in the drops.



	Semrock Part#
D1	Di01-R405/488/561/635
D2	FF495-Di03
D3	FF555-Di03
D4	FF414-Di01
BP1	FF01-445/40
BP2	FF03-525/50
LP1	BLP02-561R
LP2	FF776-Di01

Fig. A.4. (a) Schematic of the drop detection process. Drops from the drop library are reinjected into a detection chip mounted on the stage of a fluorescence detection microscope. The optical filter system allows laser light to be reflected towards the fluorescent barcoded drop while allowing emitted light from the drop to be detected by a photodetector in-line with the drop. The output of the photo detector is collected by a data acquisition device (DAQ) and then processed and recorded in a custom LabVIEW program. (b) Optical path for fluorescent drop detection. Coupled laser light enters the PMT stack and is reflected to the objective by the first dichroic mirror (D1). Emitted fluorescence passes through the first dichroic mirror (D1) and blue light is reflected by the second dichroic (D2), filtered by the first bandpass filter (BP1), and detected by the channel 1 PMT (PMT1). This process is repeated for green light while all red light above a wavelength of 555 nm is collected by PMT3. A 776 nm longpass filter (LP2) allows for transmitted light to be captured by a high-speed camera during fluorescent drop detection.

Discrimination of Discrete Signals in Barcoded Drop Libraries

Drop Library Clustering

The clustering algorithm Density-Based Spatial Clustering of Applications with Noise (DBSCAN) was used to assign each drop detected to a cluster related to a specific barcode in the microbead and quantum dot barcoded drop library.[102] DBSCAN is a density-based clustering method that groups together closely packed data points and marks outliers which lie in low-density regions as noise. Drops containing the same concentration of a fluorescence barcode should emit the same fluorescence signal, while factoring in signal noise, and will therefore create a data cluster that DBSCAN can find and tag with a specific identification code. DBSCAN uses two parameters for clustering, *minPts* defines the minimum number of data to include in a cluster and ε represents the maximum allowable distance between data in a cluster. The DBSCAN function in MATLAB was used for clustering data (introduced in MATLAB R2019a). For microbead barcoding, *minPts* was set to 50 and ε was set to 2.8×10^{-2} while for quantum dot barcoding, *minPts* was set to 25 and ε was set to 1×10^{-4}.

Schottky Equation

The Schottky equation adapted for PMTs with a voltage output,[113, 114] approximates shot noise and is defined here as:

$$\sigma_{\text{shot}} = \sqrt{\mu_{\text{itensity}} C G e \pi f_{3\text{dB}}} \qquad \text{(Eq. A.1)}$$

where σ_{shot} is the standard deviation of the PMT intensity measured in volts, $\mu_{\text{intensity}}$ is the average measured PMT intensity in volts, C is a current to voltage conversion factor, G is the gain of the PMT (unitless), e is the fundamental charge of an electron (1.6×10^{-19} C), $f_{3\text{dB}}$ is the 3 dB point in the PMT frequency distribution and is inversely proportional to the measurement

time of the PMT. Values for C (0.1 V/μA), G across a range of control voltages, and f_{3dB} (200 kHz) are provided in the PMT spec sheet (0.1 V/μA).[206]

Calculation of Noise

The theoretical estimates of $\sigma_{particle}$ ($\sqrt{\lambda}$) are calculated for an arbitrary range of particle loading values (λ) of microbeads and quantum dots in drops. For microbeads, a range of 10^1 to 10^3 microbeads/drop is used. The number of quantum dots are calculated from the molarity, assuming each particle represents a molecule. Therefore, the particle concentration is calculated as the molarity multiplied by the drop volume (65 pl) and Avogadro's number (6.022×10^{23} mol^{-1}). A quantum dot concentration range of 1.3×10^0 to 1.3×10^5 pM is used and corresponds to a particle loading range of 5×10^2 to 5×10^6 QD/drop. For comparison with the barcode data (Fig. 3.4c-d, inset), the estimates of $\sigma_{particle}$ (Fig. 4c-d, inset, dashed red line) are converted from particles/drop to voltage using Fig. A.6a and Fig. A.6c for the microbead and quantum dot cases, respectively. The voltage ranges used for the x-axis are calculated by converting the range of microbead and quantum dot particles per drop to voltages using the respective standard curves in Fig. A.6. The same voltage ranges are then used to calculate σ_{shot} from Eq. A.1 (Fig. 4c-d inset, dotted green line).

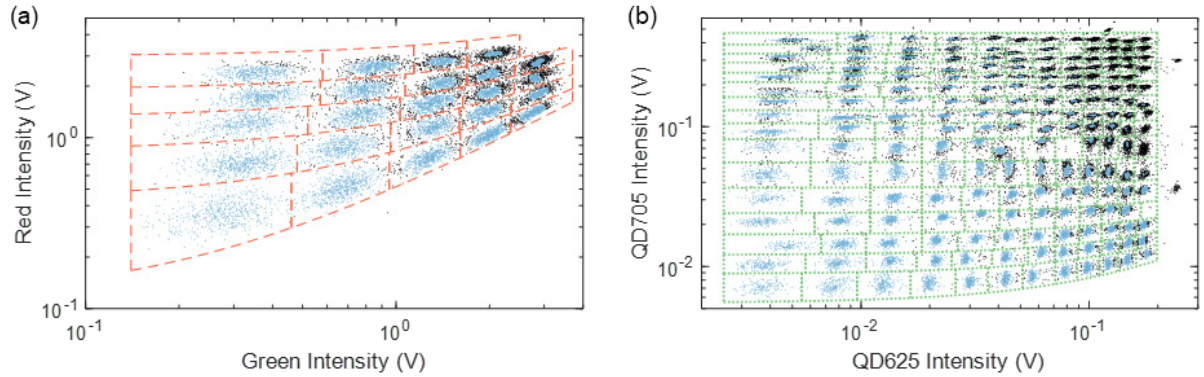


Fig. A.5. Manual segmentation, or grouping, of barcoded drop library data for (a) microbead and (b) quantum dot barcoded drops indicated by dashed red and dotted green lines, respectively.

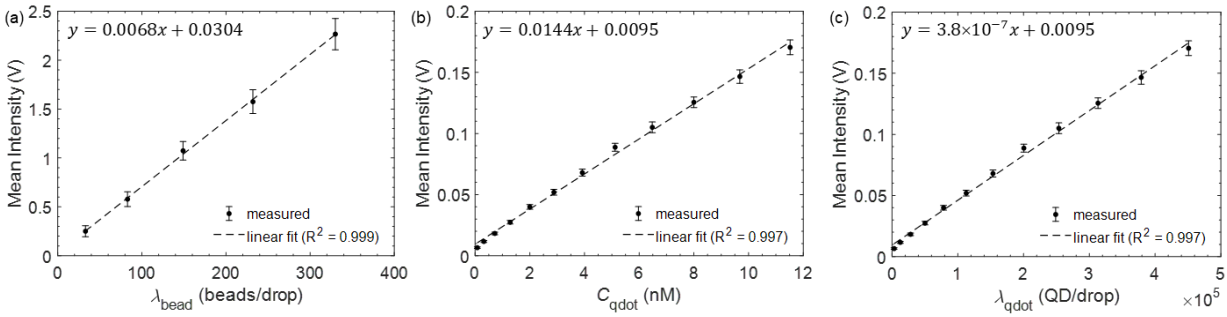


Fig. A.6. Standard curves of the mean fluorescence intensity versus the concentration of (a) microbeads ($C_{\mu bead}$) or (b) quantum dots (C_{qdot}) in drops. Error bars represent one standard deviation.

APPENDIX B

SUPPLEMENTAL INFORMATION FOR CHAPTER 4: SCREENING OF ADDITIVE FORMULATIONS ENABLES OFF-CHIP DROP REVERSE TRANSCRIPTION QUANTITATIVE POLYMERASE CHAIN REACTION OF SINGLE INFLUENZA A VIRUS GENOMES

Table B.1. Supplemental data table for Figures 4.2B and 4.2C.

Additive	$(D-D_0)/D_0$ mean	$(D-D_0)/D_0$ standard deviation	$(D-D_0)/D_0$ median	D CV	$(I-I_B)$ mean	$(I-I_B)$ standard deviation	$(I-I_B)$ median	$(I-I_B)$ CV	N_{drops}
No Additives	0.31	0.43	0.16	33%	33.6	10.4	34.0	30.9%	405
BSA	0.12	0.28	0.01	25%	83.6	20.1	85.7	24.0%	915
PEG-6K	0.25	0.40	0.09	32%	79.2	15.0	80.0	19.0%	622
Betaine	0.46	0.60	0.29	41%	72.6	10.9	73.8	15.1%	270
Tween-20	-0.10	0.08	-0.12	9%	97.0	17.9	99.6	18.5%	1948
Tween-20 / PEG-6K	-0.05	0.14	-0.09	15%	63.9	16.9	65.3	26.4%	1534
Tween-20 / BSA	-0.07	0.11	-0.12	12%	76.2	23.5	80.5	30.8%	1460
Tween-20 / BSA / Betaine	-0.01	0.12	-0.04	12%	88.9	14.1	89.7	15.9%	1155

Table B.2. Supplemental data table for endpoint analysis Figures 4.3E and 4.5D.

M gene copies/drop (cpd)	N_+/N_{total} (measured) (M gene standards)	N_+/N_{total} (Poisson) (M gene standards)	Supernatant dilution factor	N_+/N_{total} (measured) (infected supernatant)	N_+/N_{total} (Poisson) (infected supernatant)
1.7×10^4	1 (N_{total} = 2051)	1.00	10^0	1.00 (N_{total} = 138)	1.00
1.7×10^3	1 (N_{total} = 2100)	1.00	10^{-1}	0.968 (N_{total} = 95)	1.00
1.7×10^2	1 (N_{total} = 1889)	1.00	10^{-2}	0.771 (N_{total} = 280)	0.826
1.7×10^1	0.997 (N_{total} = 2038)	1.00	10^{-3}	0.274 (N_{total} = 208)	0.161
1.7×10^0	0.606 (N_{total} = 2076)	0.819	10^{-4}	0.071 (N_{total} = 141)	0.017
1.7×10^{-1}	0.107 (N_{total} = 2298)	0.157	10^{-5}	0.123 (N_{total} = 155)	0.002
Negative Control	0.000 (N_{total} = 1774)	N/A	Negative Control	0.082 (N_{total} = 208)	N/A

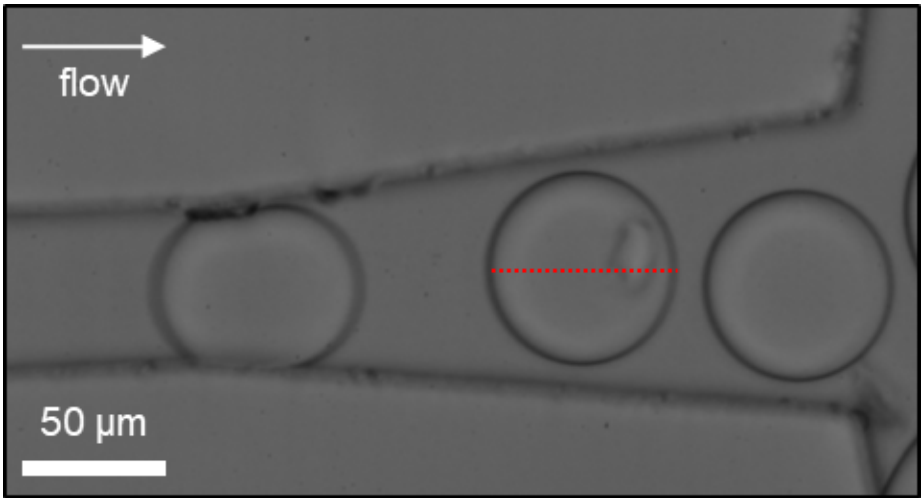


Figure B.1. Drops at the exit of a drop making device. Initial drop diameter (D_0) is measured as indicated by the dotted red line.

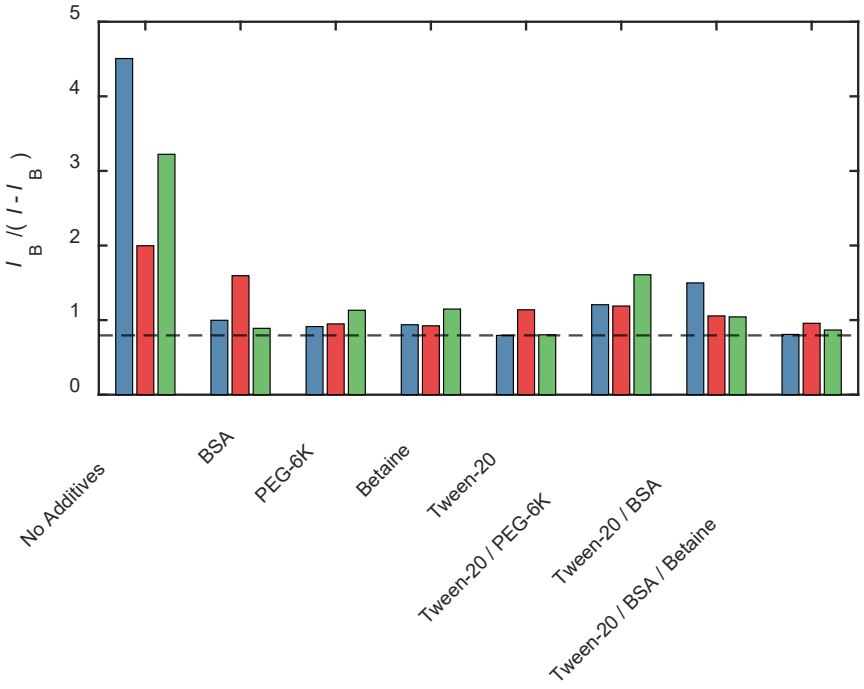


Figure B.2. Mean normalized background fluorescence intensity $\frac{I_B}{I-I_B}$ for each PCR additive condition. Colored bars for each additive represent pooled image data from each qPCR tube sampled. The dashed line indicates that the Tween-20 alone and the Tween-20 / BSA / betaine combination had the lowest normalized background, indicating the best retention of ROX dye in the drops during thermocycling.

Expanded Experimental Details

Microfluidic Device Fabrication

Microfluidic devices for making 50 μm and 100 μm diameter drops were fabricated using standard soft lithographic methods. Photoresist (Microchem SU-8 3050) was patterned on silicon wafers (University Wafer, ID# 447, test grade) using photolithography. Polydimethylsiloxane (PDMS) (Sylgard 184) was mixed at a 10:1 mass ratio of polymer to cross-linking agent and poured onto the patterned device master molds. Air was purged from the uncured PDMS by placing the filled mold in a vacuum chamber for at least 1 h. The PDMS was cured in an oven at 55 °C for 24 h and then removed from the mold with a scalpel. Ports were punched into the PDMS slab with

a 0.75 mm diameter biopsy punch (EMS Rapid-Core, Electron Microscopy Sciences). The PDMS slab was bonded to a 2-in by 3-in glass slide (VWR micro slides, cat. #48382-179) after plasma treatment (Harrick Plasma PDC-001) for 60 s at high power (30 W) and 700 mTorr oxygen pressure. The drop making devices were made hydrophobic by flowing Aquapel (Pittsburgh Glass Works) through the channels, followed by blowing the channels with air filtered through a GVS ABLUO 25 mm 0.2-μm filter (Fisher Scientific) before baking the devices in an oven at 55 °C for 1 h.

PCR Sequences and Reaction Concentrations

Primers and probes were ordered from Eurofins Operon and were prepared as 100 μM stocks. The working stocks of the primers were 25 μM with a final reaction concentration of 400 nM. The working stock of the probe was 10 μM with a final reaction concentration of 200 nM. Each reaction mix contained 0.05 μM ROX reference dye, 2.0 mM $MgSO_4$ and 0.32 U/μL SUPERase RNase Inhibitor (Invitrogen AM2694), and 2.5 μL of RNA or supernatant. Tested additives were added to the qRT-PCR reaction mix at the following concentrations: 1.0% w/v Tween-20 (Calbiochem 655204-100mL), 0.8 μg/μL BSA (Fisher BP675-1), 2.5% w/v PEG-6K (Acros Organics 192280010), and 1.0 M betaine (Sigma B0300-1VL).

Imaging of Drops Containing PCR Additives

20 μL of thermocycled drops were imaged to capture a full field of view (FOV) of drops with a 10× objective. Brightfield and fluorescence images (Texas Red, TXRED ex. 540-580 nm, em. 592-669 nm) of the drops were captured on an inverted epifluorescence microscope (Leica DMi8) with a 10× objective (Leica, NA 0.32). The Leica Application Suite X was used for image acquisition. For each of the eight additive conditions, drops were imaged from three PCR tubes

and three FOV per tube (>100 drops per FOV) were captured. The device used for imaging had a channel height of 50 μm, thereby compressing drops larger than 50 μm in diameter and skewing larger drop diameter measurements. Thus, drop diameters greater than this height were adjusted by estimating the compressed drops as oblate spheroids and then using the oblate spheroid volume to calculate the equivalent sphere diameter using the equation $D_S = \sqrt[3]{D_E^2 h}$ where D_S is the diameter of the equivalent sphere, D_E is the measured diameter of a compressed drop, and h is the channel height of 50 μm.

Analysis of Endpoint Epifluorescence Images of Drops Containing PCR Additives

Drops imaged on the epifluorescence microscope were processed with a custom MATLAB (R2019a) script to measure drop diameter and ROX fluorescence intensity. Diameters D from at least 270 drops per condition were made. ROX fluorescence intensities I were normalized by subtracting the background fluorescence I_B, set as the average pixel value measured from a 100 px^2 background region using Fiji.[207] Normalization of measured D from an initial drop diameter D_0 was performed using the expression $(D\text{-}D_0)/D_0$. The initial D_0 is the average drop diameter measured from drops without PCR additives upon exit from a drop making device (*SI Appendix B*, Figure B.1).

Imaging of Drops During OCD-qPCR Thermocycling

The qPCR machine was paused and one PCR tube was removed to sample drops. Drops were imaged using epifluorescence microscopy to quantify fluorescence from the FAM (6-carboxyfluorescein) dye-labeled TaqMan probe and ROX (6-carboxy-X-rhodamine) reference

dye. Five FOV were captured of drops from each tube at each cycle on the epifluorescence microscope for an average of 650 drops after pooling from all FOV.

Imaging of Multiplexed OCD-qPCR Drops

M gene (2.62×10^5 copies/μL) and β-actin (6.98×10^4 copies/μL) were encapsulated with qPCR mix in 50 μm diameter drops and thermocycled. Drops were imaged using epifluorescence microscopy to quantify fluorescence from the FAM (6-carboxyfluorescein) dye-labeled TaqMan probe for M gene, Cy5 (Cyanine5 NHS ester, ex. 649 nm, 666 em.) dye-labeled TaqMan probe for β-actin, and ROX (6-carboxy-X-rhodamine) reference dye. Five FOV were captured of drops on the epifluorescence microscope for a total of 1127 drops after pooling from all FOV.

APPENDIX C

SUPPLEMENTAL INFORMATION FOR CHAPTER 5: DROP QPCR ENABLED BY SIGMOIDAL CURVE FITTING USING PCR EFFICIENCY

Table C.1. SCFPE fitting parameters for Figure 5.1.

M gene dilution (copies/µL)	E_{min} (unitless)	E_{max} (unitless)	$N_{0.5}$ (cycle)	k (cycle)	R^2 (SCFPE)	R^2 (SCF)
2.62×10^9	0.002	1.000	9.1	3.31	0.9994	0.9965
2.62×10^8	0.003	1.000	13.1	3.03	0.9995	0.9967
2.62×10^7	0.005	1.000	17.1	2.97	0.9996	0.9972
2.62×10^6	0.009	1.000	20.8	2.83	0.9997	0.9976
2.62×10^5	0.010	0.993	24.4	2.90	0.9998	0.9984
2.62×10^4	0.010	1.000	28.9	2.83	0.9997	0.9988

Table C.2. SCFPE cycle offset performance. Minimum and maximum concentrations are defined as the M gene template concentration prior to which converted data falls outside a 2-fold change threshold.

Offset	$C_{RNA, min}$ (copies/µL)	$C_{RNA, max}$ (copies/µL)	Dynamic Range ($\log_{10}$(copies/µL))	R^2
0	3.28×10^6	1.31×10^8	1.60	0.886
-1	3.28×10^6	2.62×10^8	1.90	0.960
-2	2.62×10^4	2.62×10^9	5.00	0.986
-3	2.62×10^4	1.31×10^9	4.70	0.990
-4	3.28×10^4	1.31×10^9	4.60	0.986
-5	6.55×10^4	6.55×10^8	4.00	0.979

Table C.3. SCFPE cycle conversion performance. Minimum and maximum concentrations are defined as the M gene template concentration prior to which converted data falls outside a 2-fold change threshold.

Method	Cycle	$C_{RNA, min}$ (copies/µL)	$C_{RNA, max}$ (copies/µL)	Dynamic Range (log_{10}(copies/µL))	R^2
Cycle threshold analysis	NA	2.62×10^4	2.62×10^9	5.00	0.991
SCFE	17	2.62×10^5	2.62×10^9	4.00	0.812
SCFE	18	1.32×10^5	2.62×10^9	4.30	0.800
SCFE	19	6.55×10^4	2.62×10^9	4.60	0.989
SCFE	20	2.62×10^4	1.31×10^9	4.70	0.990
SCFE	21	2.62×10^4	1.31×10^9	4.70	0.981
SCFE	22	3.28×10^5	6.55×10^8	4.30	0.962
SCFE	23	6.55×10^4	6.55×10^8	4.00	0.938

Table C.4. Comparison of single M gene drop populations to GMM fitted distributions from the mixed M gene drop sample measured at cycle 22.

$C_{RNA\ expected}$ (CPD)	μ_{single} (CPD)	CV (%)	μ_{GMM} (CPD)	CV (%)	% Difference (single vs. GMM)
1.71×10^1	1.58×10^1	15.9	8.23×10^0	20.3	-47.9
1.71×10^2	1.84×10^2	6.1	1.03×10^2	11.0	-44.0
1.71×10^3	9.05×10^2	7.7	1.07×10^3	8.8	18.2

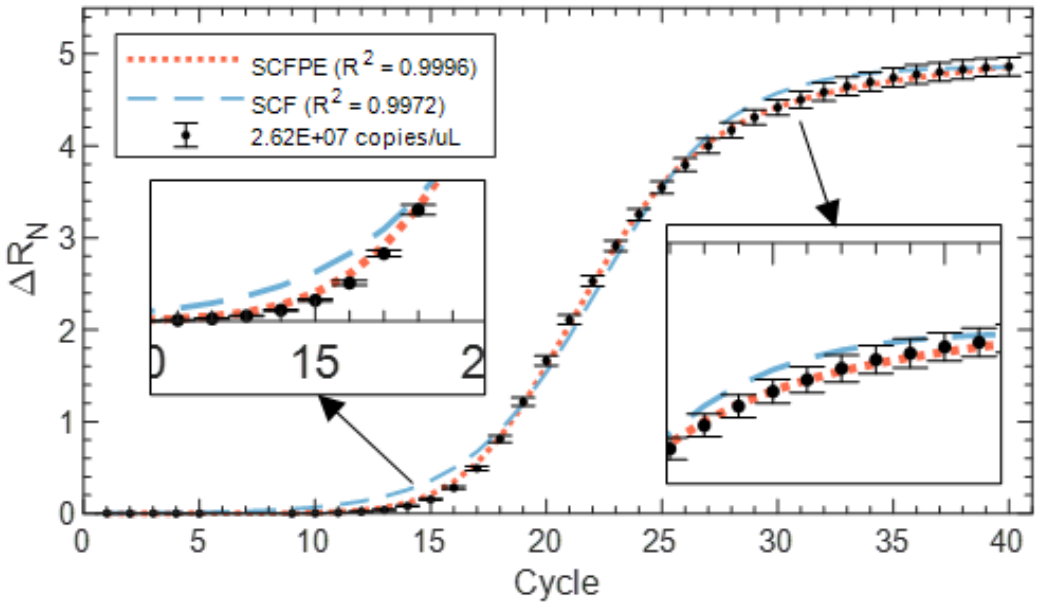


Figure C.1. Close up comparison of SCFPE and SCF fits. SCFPE (red dotted line) and SCF (blue dashed line) fits are compared to bulk qPCR data (black datapoints). The asymmetric nature of SCFPE provides a better fit than SCF at the exponential and plateau phases of the amplification curve. The zoomed in sections highlight this better fit. Error bars represent one standard deviation.

LME Results

The LME results indicate that while the cycle numbers used for measurements do have a significant effect ($p < 0.05$), it is very small (-1.7 cpd/cycle). This is consistent with the cycle number selection of the M gene dilution series dataset used in Figure 5.2B where there was a viable range of approximately four cycles (Table C.3). Additionally, the LME model indicates that the majority of error originates from day-to-day and intra-drop measurements (41.0% and 56.7% of total error, respectively) while the error between replicates is minor (2.3% of total error).

APPENDIX D

SUPPLEMENTAL INFORMATION FOR CHAPTER 6: DROP-BASED RT-QPCR REVEALS HIGHLY VARIABLE INFLUENZA A VIRAL BURST SIZE FROM SINGLE CELLS

Sigmoidal Curve Fitting Using PCR Efficiency (SCFPE)

Sigmoidal curve fitting (SCF) methods are unable to properly fit amplification curve data without adding a limit on the number cycles fit[173] or by adding an asymmetric fitting term.[174, 175] The asymmetric nature of qPCR amplification data arises from the decrease in PCR efficiency after each cycle. At early cycles, PCR efficiency is near 100%, relating to an exact doubling of DNA at each cycle, and approaches 0% at later cycles.[178, 179] This relationship leads to a steeper slope at the start of the amplification curve in the exponential region and a flatter slope near the plateau phase which SCF is unable to correctly fit.[178] Alternative fitting methods to SCF that correctly fit asymmetric data model the PCR efficiency, rather than the fluorescence data, with a sigmoidal[180] or bilinear[178] model to construct an asymmetric amplification curve. We have chosen an approach similar to the former to model PCR efficiency with a sigmoidal curve; however, rather than using a two-parametric sigmoid function[180], we have modified the four-parametric sigmoid function[173] to model PCR efficiency with Eq. D.1:

$$E_{\mathrm{N}} = \frac{E_{\mathrm{max}}}{1+e^{\left(\frac{N_{0.5}-N}{k}\right)}} + E_{\mathrm{min}} \qquad \text{Eq. D.1}$$

where E_{N} is the PCR efficiency at cycle N, E_{max} is the maximum PCR efficiency in the range of 0.9 to 1, E_{min} is the minimum PCR efficiency in the range of 0 to 0.1, $N_{0.5}$ is the cycle at which E_{N} equals 0.5, and k is the slope of the curve. Eq. D.1 is then used to construct an amplification curve consisting of fluorescence data following Eq. D.2:

$$F_{\mathrm{N+1}} = F_{\mathrm{N}}(1 + E_{\mathrm{N}}) \qquad \text{Eq. D.2}$$

where $F_{\mathrm{N+1}}$ is the fluorescence value of the amplification curve at cycle N+1, F_{N} is the fluorescence value of the amplification curve at cycle N. Eq. D.1 and D.2 are combined and result in Eq. D.3:

$$F_{N+1} = F_N\left(1 + \frac{E_{max}}{1+e^{\left(\frac{N_{0.5}-N}{k}\right)}} + E_{min}\right) \quad \text{Eq. D.3}$$

Eq. D.3 is fit to the qPCR data iteratively with an initial arbitrary guess for $F_{N,0}$. The fit to Eq. D.3 is scaled to the measured normalized fluorescence reporter value (ΔR_N) by a calibration factor (CF) calculated in Eq. D.4 using the measured and modeled fluorescence endpoint ($F_{endpoint}$) values:

$$CF = F_{endpoint,measured}/F_{endpoint,model} \quad \text{Eq. D.4}$$

A four-parameter fit of Eq. D.3 (varying E_{max}, E_{min}, $N_{0.5}$, and k) provides an asymmetric function which closely follows the measured fluorescence data collected from a qPCR machine. We call the method of fitting Eq. D.3 to qPCR data sigmoidal curve fitting using PCR efficiency (SCFPE). To demonstrate SCFPE, Eq. D.3 is fit to a qPCR dataset consisting of a dilution series of IAV M gene RNA (2.62 x 10^4 to 2.62 x 10^9 copies/µL) and compared to an SCF fit[173] (Figure D.4). The dilution series was made of five dilutions from a 10-fold dilution series of *in vitro* transcribed IAV M gene (ranging from 2.62 x 10^4 to 2.62 x 10^8 copies/µL) and run in triplicate.[141] The SCF method (Figure D.4A, gray dotted line) does not properly fit the data in the lower ($\Delta R_N < 1$) and upper ($\Delta R_N > 4$) regions of the amplification curves (Figure D.4, colored data points). The SCFPE method (Figure D.4B, gray dotted line) more closely fits the amplification curves with an average R^2 of 0.9996. The SCFPE fitting parameters for the dilution series are provided in Table D.1. SCFPE captures the asymmetric dynamics of PCR amplification from a starting RNA template and provides a better fit than SCF (see Figure D.5). Here, the fluorescence data is fit to directly, rather than the measured PCR efficiency as done previously in literature.[178, 180] This approach allows for fitting fluorescence data from a subset of

cycles, rather than requiring data from all cycles as is required for calculating, and subsequently fitting to, the PCR efficiency.

Amplification Curve Library

An amplification curve library is made with virtual reference amplification curves of the same shape as the reference curve calculated in Eq. D.3 (see Appendix D, *Sigmoidal Curve Fitting Using PCR Efficiency* for details). These virtual curves are "extended" to the left and right of the reference curve by substituting $N_{0.5}$ from Eq. D.3 with $N_{virtual}$. $N_{virtual}$ is the cycle at which the PCR efficiency equals 0.5 for the virtual curve and ranges from 1 to 40. Extension of the reference amplification curve is based on the principles used for the quantification cycle analysis method following Eq. D.5:

$$Cq = m * \log_{10}(C_{\mathrm{RNA}}) + b \qquad \text{Eq. D.5}$$

where Cq is the cycle threshold at which the fluorescence of an amplification curve crosses a fluorescence threshold, C_{RNA} is the concentration of starting template RNA, m is the slope of the Cq versus log10(C_{RNA}) line, and b is the y-intercept of that line. In this case, m is related to the effective PCR amplification efficiency (E_{eff}) at the Cq value measured for each template dilution following Eq. D.6:

$$m = \frac{1}{log10(E_{\mathrm{eff}}+1)} \qquad \text{Eq. D.6}$$

For the quantification cycle analysis method, calculation of E_{eff} requires a dilution series of template to measure m. However, for the amplification curve mapping method we find that for a single template standard an E_{eff} value can be calculated from the modeled efficiency curve from Eq. D.1 using a cycle offset of three as $E_N(N_{0.5}\text{-}3)$ once the fitting parameters have been

determined. This cycle offset of three from $N_{0.5}$ is empirically found to provide a wide dynamic range and high R^2 value for converted M gene data in Figure D.6B and is used for all fluorescence data conversions in this study (Table D.2). The extension of the virtual reference curves is determined with a scaling factor (f) calculated from Eq. D.7:

$$f = log10\left(C_{\mathrm{RNA,ref}}\right) - \frac{N_{0.5} - N_{\mathrm{virtual}}}{m} \quad \text{Eq. D.7}$$

where $C_{\mathrm{RNA,ref}}$ is the single known reference starting template concentration used for the amplification curve mapping analysis. The virtual template concentration ($C_{\mathrm{RNA,virtual}}$) of each curve as a function of N_{virtual} is calculated with Eq D.8:

$$C_{RNA,virtual} = 10^{f} \quad \text{Eq. D.8}$$

The formation of this amplification curve library is represented graphically in Figure 6.2E-F for N_{virtual} ranging from cycle 1 to 40 with 10 and 1000 data points, respectively. The high-resolution amplification curve library from Figure 6.2F is used to create a standard curve relating $C_{\mathrm{RNA,virtual}}$ (copies per drop or cpd) to the measured normalized fluorescence reporter value (ΔR_{N}) of a sample at a single cycle (Figure 6.2G). The x-axis of the standard curve is calculated with Eq. D.7 for a range of N_{virtual} values while keeping $N_{0.5}$ constant. The y-axis of the standard curve is calculated by plugging in the f values calculated from Eq. D.7 into Eq. D.8.

Validation of Amplification Mapping Analysis with Bulk qPCR Datasets

The amplification curve mapping method is validated against qPCR datasets collected from dilution series of the influenza A virus (IAV) M gene RNA, human MYCN gene DNA,[177] and soybean Lectin endogene DNA[178] and compared to results quantified with the standard *Cq* method. Quantification by calculating a *Cq* value provides a linear response of measured versus

expected concentration of RNA or DNA for all datasets (Figure D.6A, $R^2 > 0.9912$). The measured data falls within a 2-fold change (dotted line) of expected (dashed line) with a max fold change error of 1.9. To quantify the qPCR data with amplification curve mapping, an amplification curve library is built from a single reference curve and a subsequent standard curve is constructed at a single intermediate cycle. The intermediate cycles chosen for the M gene, MYCN, and soybean datasets are cycles 20, 27, and 29, respectively. Quantification of the qPCR datasets with SCFPE provides a similar linear response (Figure D.6B, $R^2 > 0.9640$) and accuracy as the *Cq* method. While two of the 30 dilutions fall outside a 2-fold change from expected, the other 28 dilutions (93% of the data) are measured accurately with a <1.7-fold change error. Additional statistics for conversion of the M gene data at other cycles are provided in Table D.3. To demonstrate the importance of SCFPE versus SCF, the M gene dataset was analyzed with a reference curve fit with SCF and the result was a non-linear response to the expected value (Figure D.6B, gray dots, $R^2 = 0.8487$) with many of the data falling outside of the 2-fold change error lines. The comparable performance of the *Cq* and amplification curve mapping methods may be explained by the fact that the two methods share similar assumptions. In the case of the *Cq* method, it is assumed that the PCR efficiency measured at the fluorescence threshold is the same for all samples, regardless of initial template concentration. Amplification curve mapping relies on a similar assumption and assumes that the shape of the PCR efficiency curve is the same for all samples, regardless of initial template concentration. Interestingly, amplification curve mapping closely matches the performance of the quantification cycle method while requiring a fraction of the information. For example compared to the *Cq* method, the mapping method analysis of the M gene dataset requires $1/5^{th}$ of the RNA standards to create a standard

curve and 1/40th of the fluorescence data collected for single cycle quantification of unknown samples.

MYCN and Soybean qPCR Datasets

The human MYCN gene and soybean Lectin endogene DNA datasets were taken from previously published studies on the evaluation of qPCR curve analysis methods[177] and enhanced analysis of real-time PCR data using a variable efficiency model.[178] The MYCN dataset consists of four dilutions from a10-fold dilution series (ranging from 1.88 x 10^0 to 1.88 x 10^3 copies/µL) and uses a SYBR Green Supermix (Bio-Rad). The soybean dataset consists of five dilutions from a 5-fold dilution series (ranging from 6.4 x 10^0 to 4.0 x 10^3 copies/µL) and uses a SYBRgreen mastermix (Diagenode).

Table D.1. SCFPE fitting parameters for Figure D.4.

M gene dilution (copies/µL)	E_{min} (unitless)	E_{max} (unitless)	$N_{0.5}$ (cycle)	k (cycle)	R^2 (SCFPE)	R^2 (SCF)
2.62 x 10^9	0.002	1.000	9.1	3.31	0.9994	0.9965
2.62 x 10^8	0.003	1.000	13.1	3.03	0.9995	0.9967
2.62 x 10^7	0.005	1.000	17.1	2.97	0.9996	0.9972
2.62 x 10^6	0.009	1.000	20.8	2.83	0.9997	0.9976
2.62 x 10^5	0.010	0.993	24.4	2.90	0.9998	0.9984
2.62 x 10^4	0.010	1.000	28.9	2.83	0.9997	0.9988

Table D.2. Amplification curve mapping. Minimum and maximum concentrations are defined as the M gene template concentration prior to which converted data falls outside a 2-fold change threshold.

Offset	$C_{RNA,\ min}$ (copies/µL)	$C_{RNA,\ max}$ (copies/µL)	Dynamic Range (log_{10}(copies/µL))	R^2
0	3.28×10^6	1.31×10^8	1.60	0.886
-1	3.28×10^6	2.62×10^8	1.90	0.960
-2	2.62×10^4	2.62×10^9	5.00	0.986
-3	2.62×10^4	1.31×10^9	4.70	0.990
-4	3.28×10^4	1.31×10^9	4.60	0.986
-5	6.55×10^4	6.55×10^8	4.00	0.979

Table D.3. Amplification curve mapping. Minimum and maximum concentrations are defined as the M gene template concentration prior to which converted data falls outside a 2-fold change threshold.

Method	Cycle	$C_{RNA,\ min}$ (copies/µL)	$C_{RNA,\ max}$ (copies/µL)	Dynamic Range (log_{10}(copies/µL))	R^2
Cycle threshold analysis	NA	2.62×10^4	2.62×10^9	5.00	0.991
SCFE	17	2.62×10^5	2.62×10^9	4.00	0.812
SCFE	18	1.32×10^5	2.62×10^9	4.30	0.800
SCFE	19	6.55×10^4	2.62×10^9	4.60	0.989
SCFE	20	2.62×10^4	1.31×10^9	4.70	0.990
SCFE	21	2.62×10^4	1.31×10^9	4.70	0.981
SCFE	22	3.28×10^5	6.55×10^8	4.30	0.962
SCFE	23	6.55×10^4	6.55×10^8	4.00	0.938

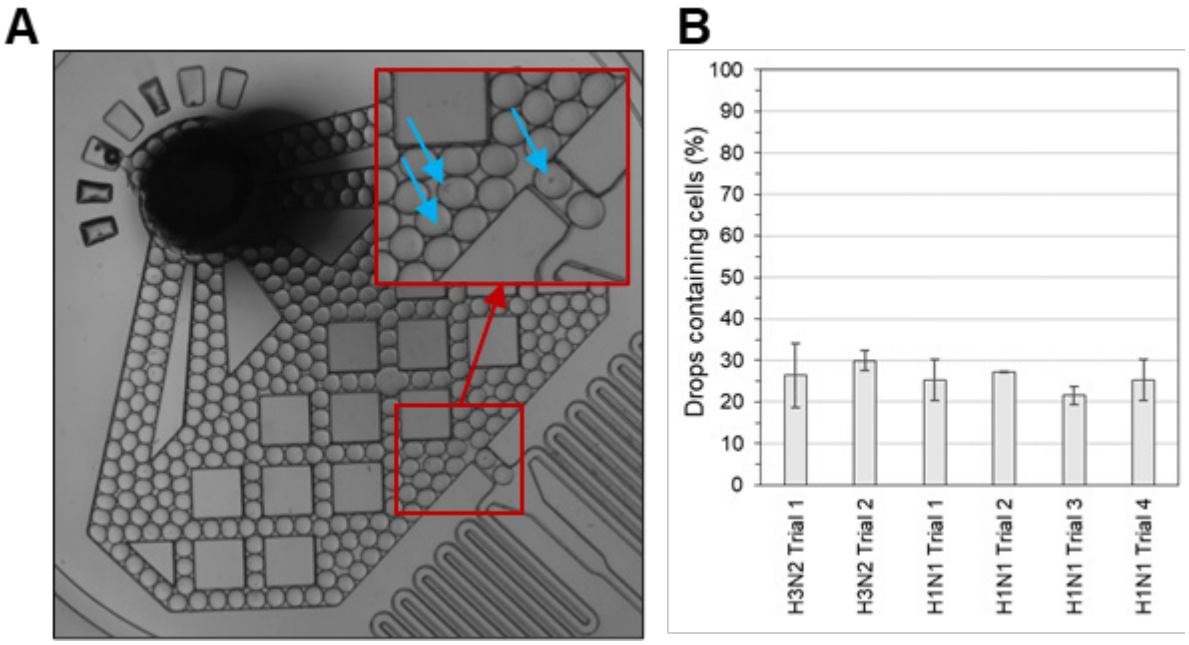


Figure D.1. Cell loading measurements. (A) Images are taken at the start and end of each burst size experiment. Blue arrows in the inset indicate cells inside drops. (B) Cell loading is determined by counting the percentage of drops that contain cells (mean = 25% ± 4%). Cell loading in drops follows a Poisson distribution.[208] For a population of drops with 25% containing cells, we estimate the Poisson mean (λ) to be ≈0.29 cells/drop. In this case, ≈75% of drops are empty, ≈21.5% of drops contain one cell, ≈3% contain two cells, and ≈0.5% of drops contain three or more cells.

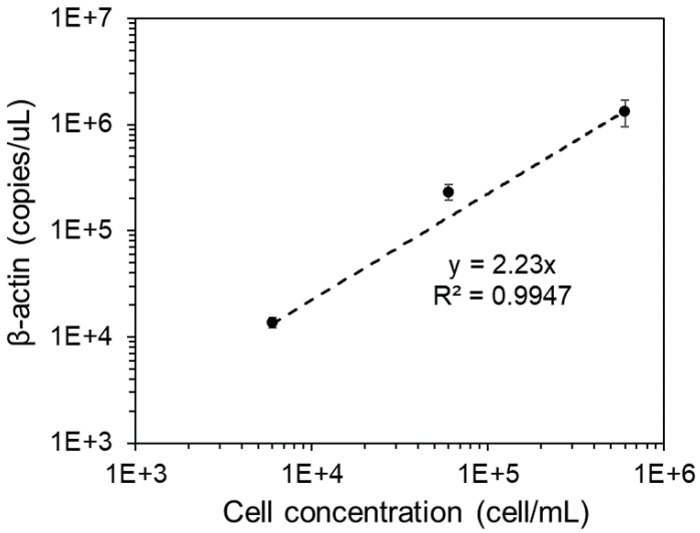


Figure D.2. β-actin released from cells as measured by bulk RT-qPCR when lysed during the RT step of the RT-qPCR assay. β-actin concentration correlates with the cell concentration in suspension after 24 h of incubation. Error bars represent one standard deviation.

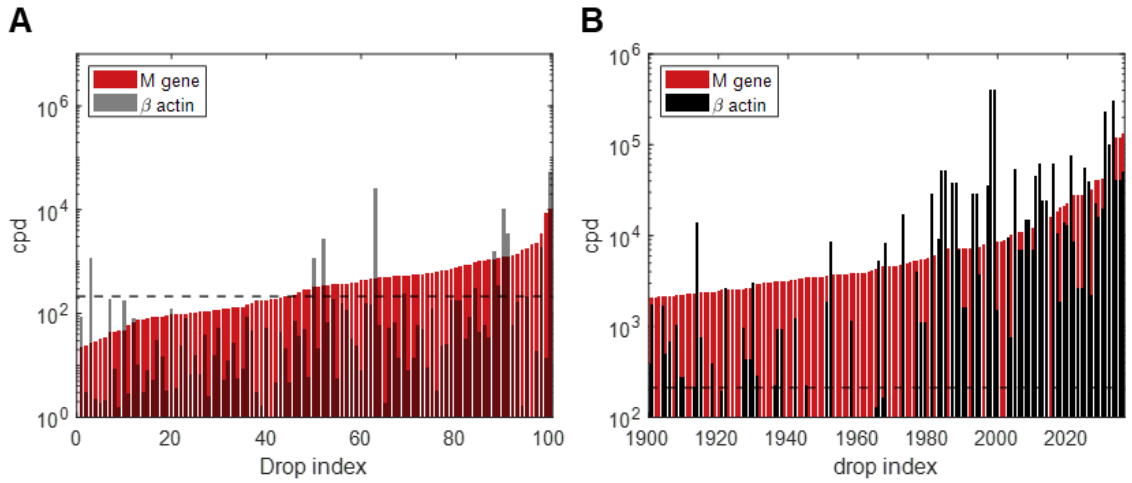


Figure D.3: Example of β-actin filtering of burst size data. (A) H1N1 (replicate 3) drop data arranged in order of increasing RNA contained in each drop prior to β-actin filtering (dashed black line). (B) zoomed in region of (A). A large proportional of the drops containing the most vRNA also contain high levels of cellular RNA.

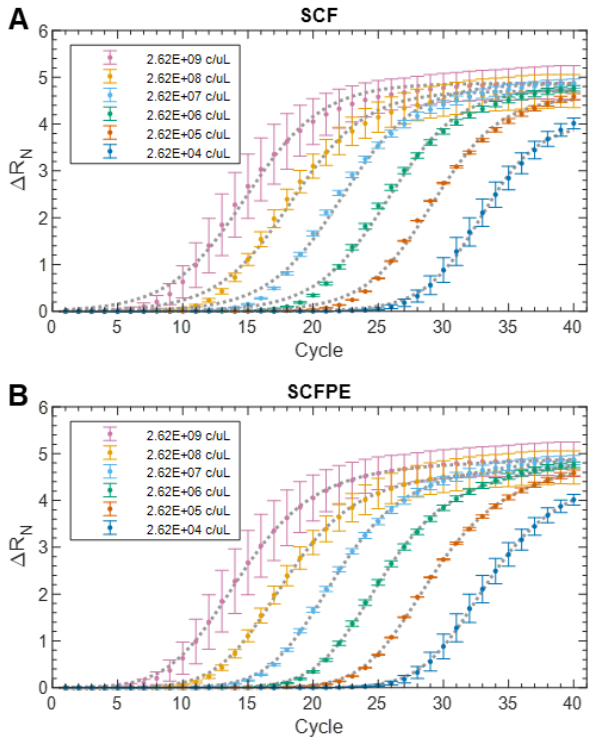


Figure D.4: (A) SCF and (B) SCFPE methods (dashed gray lines) applied to the M gene dilution series amplification curves (colored datapoints). SCFPE provides a better fit to the data at the lower ($\Delta R_N < 1$) and upper ($\Delta R_N > 4$) regions of the amplification curves. The average R^2 values for SCF and SCFPE are 0.9975 and 0.9996, respectively. Error bars represent one standard deviation.

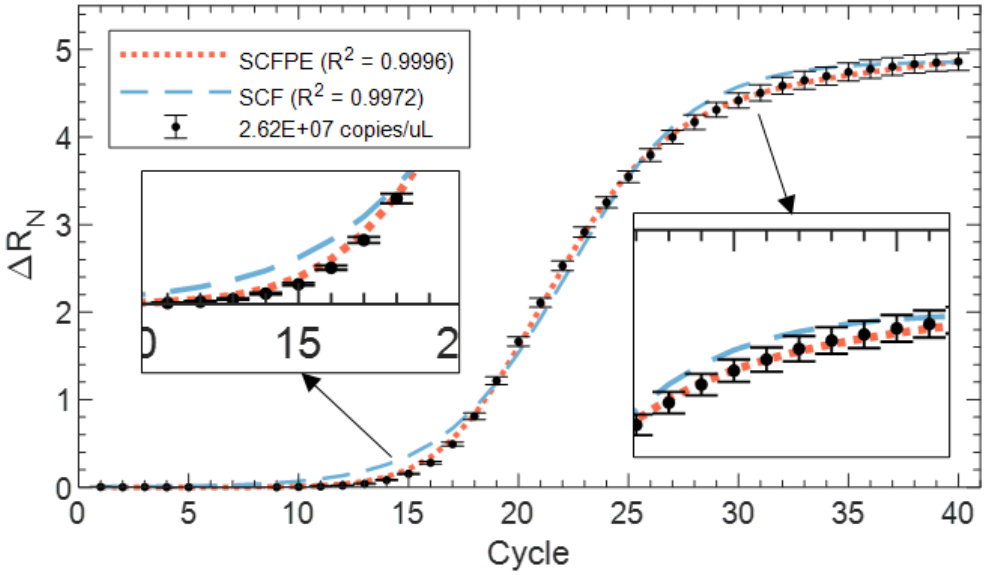


Figure D.5: Zoomed in comparison of SCFPE (red dotted line) and SCF (blue dashed line) fits to bulk qPCR data (black datapoints). The asymmetric nature of SCFPE provides a better fit than SCF at the exponential and plateau phases of the amplification curve. The zoomed in sections highlight this better fit. Error bars represent one standard deviation.

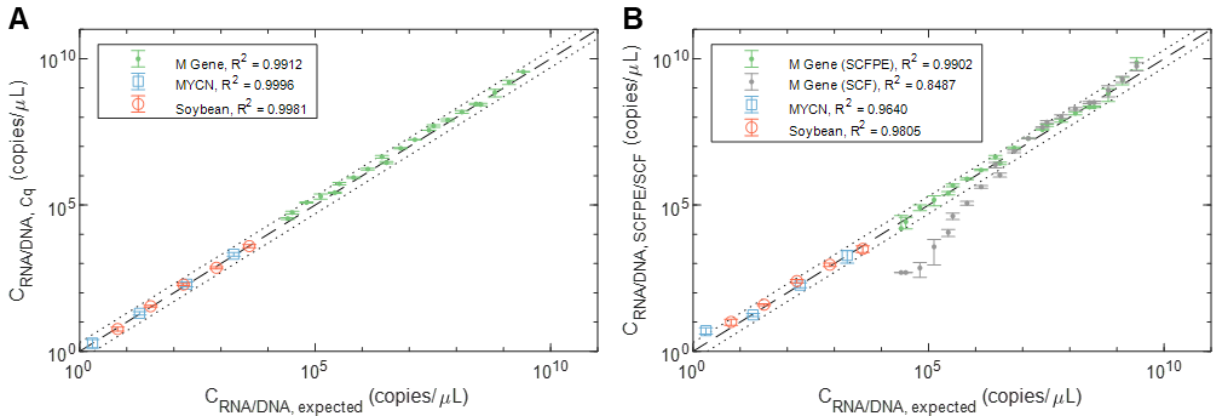


Figure D.6: Method comparison for bulk M gene (green/gray dot), MYCN gene (blue square), and soybean gene (red circle) qPCR datasets. Conversion of the bulk qPCR datasets with the (A) cycle threshold analysis and (B) SCFPE provides a linear response between the measured and expected RNA or DNA concentration for both methods ($R^2 > 0.9912$ and 0.9640, respectively). 2-fold change error is represented by dotted gray lines. Conversion of the M gene dataset with SCF (gray dot) does not provide a linear response across the dilution series ($R^2 = 0.8487$) with many data falling outside the 2-fold change error. For each dilution, there were three, 94, or 18 replicates for the M gene, MYCN, or soybean datasets, respectively. Error bars represent one standard deviation.

APPENDIX E

DROPSOAC: STABILIZING MICROFLUIDIC DROPS FOR TIME-LAPSE QUANTIFICATION OF SINGLE-CELL BACTERIAL PHYSIOLOGY

APPENDIX E

DROPSOAC: STABILIZING MICROFLUIDIC DROPS FOR TIME-LAPSE QUANTIFICATION OF SINGLE-CELL BACTERIAL PHYSIOLOGY

Contribution of Authors and Co-Authors

Subsection of Manuscript in Appendix E

Author: Shawna L. Pratt

Contributions: SP designed the study, conducted experiments, analyzed the data, and wrote the manuscript

Co-Author: Geoffrey K. Zath

Contributions: GZ analyzed the data and contributed to manuscript writing

Co-Author: Tatsuya Akiyama

Contributions: TA designed the study, conducted experiments, and contributed to manuscript writing

Co-Author: Kerry S. Williamson

Contributions: KW designed the study, conducted experiments, and contributed to manuscript writing

Co-Author: Michael J. Franklin

Contributions: MF designed the study and wrote the manuscript.

Co-Author: Connie B. Chang

Contributions: CC designed the study and wrote the manuscript

Manuscript Information

Shawna L. Pratt, Geoffrey K. Zath, Tatsuya Akiyama, Kerry S. Williamson, Michael J. Franklin, Connie B. Chang

Frontiers in Microbiology

Status of Manuscript:
____ Prepared for submission to a peer-reviewed journal
____ Officially submitted to a peer-reviewed journal
____ Accepted by a peer-reviewed journal
_X__ Published in a peer-reviewed journal

Frontiers Media SA
September 2019 Issue, Volume 10, Article 2112
DOI: 10.3389/fmicb.2019.02112

Note: Only the sections regarding the growth heterogeneity of *Pseudomonas Aeruginosa* from the main manuscript have been included here to highlight my contributions to this publication.

Image Processing and Analysis

The 4D image stacks, composed of three spatial dimensions and time, acquired from confocal laser scanning microscopy (CLSM) imaging of *P. aeruginosa* in drops were processed with the Fiji[209] distribution of ImageJ[210]. A summed z-projection of the GFP channel was used to combine the pixel values of all focal planes, capturing fluorescence from bacteria at all locations within the drop. Drop size measurements for each device preparation method were collected with a custom MATLAB script using the brightfield channel. The Fiji plugin TrackMate[211] was used to identify fluorescent cells in drops and track the change in pixel intensity from the GFP channel, frame by frame, as the cells grew. Pixel intensity is linearly correlated with the concentration of cells within the drops over the range of the PMT output on the confocal microscope. The tracking data collected from TrackMate was then loaded into a custom MATLAB script to plot growth curves for each drop, calculate a maximum growth rate (μ_{max}), and calculate the lag phase length. Maximum growth rate was calculated from the slope of the linear portion of the growth curve when the natural log of the fluorescence was plotted against time. The lag phase length was determined from the time at the start of image acquisition until the fluorescence within a drop rose above background noise and was tracked by TrackMate. The frequency of cell resuscitation in drop growth assays was determined using TrackMate data. To quantify numbers of cells that resuscitated, the number of drops in which pixel intensity value was low, but non-zero and constant for the duration of incubation was compared to the number of drops in which fluorescence value increased during incubation.

Growth Heterogeneity of *Pseudomonas Aeruginosa* with Single Cells as Inocula

To demonstrate the utility of the DropSOAC device for studying growth heterogeneity in *P. aeruginosa* populations, we compare the differences in regrowth of *P. aeruginosa* PAO1 and *P. aeruginosa* (Δ*hpf*), that is deleted for the hibernation promoting factor, following 4 days of starvation.[212] The two strains of *P. aeruginosa* were washed in PBS and incubated in PBS for 4 days at 37 °C. Day four starved cultures were then encapsulated in drops containing TSB regrowth medium, with approximately one cell in every 17 drops. The drops were injected into the DropSOAC capsule, and the capsule was incubated at 37 °C in a stage-top incubator. Drops were imaged every 30 min for 21.5 h using CLSM (Figure E.1A). The drops maintained consistent positions and geometry within the device during timelapse imaging. At time zero, the average drop diameter was 19.6 μm ± 1.4 μm, and after 21.5 h, the average drop diameter was 19.9 μm ± 1.7 μm.

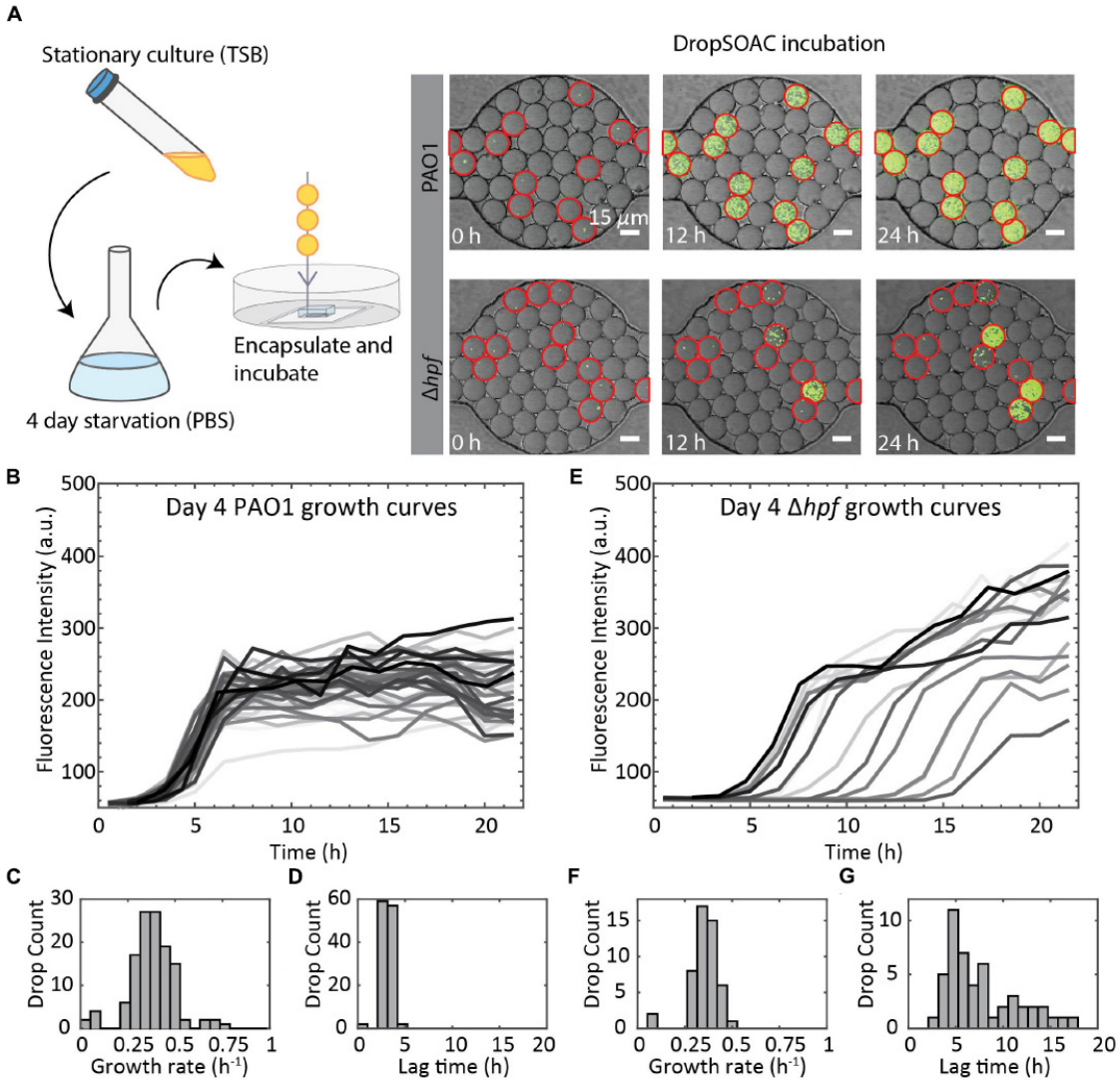


Figure E.1. Summary of *P. aeruginosa* PAO1 and Δ*hpf* growth resuscitation studies. (A) Cells were starved in PBS for 4 days. After starvation, cells were resuspended in TSB media and encapsulated in drops using a 15 μm drop maker. Drops are incubated in a DropSOAC capsule soaked in water-saturated oil and imaged using confocal laser scanning microscopy. Growth was monitored as increased fluorescence. Many of the Δ*hpf* cells show delayed growth or no growth following starvation, which can be seen from the image at 12 h. Drops circled in red contain cells. Scale bars are 15 μm. (B) Single cell growth curves of *P. aeruginosa* PAO1 following 4 d of starvation. Image shows 80 out of a total of 210 cells analyzed from one field of view, with non-growing cells omitted. (C) Histogram showing the distribution of maximum growth rates for *P. aeruginosa* PAO1 following starvation ($N = 210$). (D) Histogram showing the distribution of lag phase length of *P. aeruginosa* PAO1 ($N = 210$). (E) Single cell growth curves of *P. aeruginosa* Δ*hpf* following 4 d of starvation. Image shows 85 out of a total of 218 cells analyzed from one field of view, with non-growing cells omitted. (F) Histogram showing the distribution of maximum growth rates for *P. aeruginosa* Δ*hpf* following starvation ($N = 218$). (G) Histogram showing the distribution of lag phase length of *P. aeruginosa* Δ*hpf* ($N = 218$).

We quantified single-cell growth of bacteria cultured in microfluidic drops using the increase in fluorescence intensities over time for *P. aeruginosa* PAO1 and its Δ*hpf* mutant derivative (Figure E.1A). The growth curves were used to calculate the distributions of maximum growth rates, and the length of time required for individual cells to recover from starvation (lag phase). Following 4 days of starvation, *P. aeruginosa* PAO1 regrew in TSB drops with most cells entering exponential phase at approximately 4 h. The drops inoculated with single cells were completely filled with bacteria by 8 h, as indicated by a homogenous, bright fluorescence signal in the entire drop. Regrowth of PAO1 (Figure E.1B) had an average growth rate of 0.39 h^{-1} ± 0.11 h^{-1} (Figure E.1C) and an average lag phase length of 3.10 h ± 0.62 h (Figure E.1D). By contrast, the drops containing the day four starved Δ*hpf* cells had varying levels of fluorescence output at each time point (Figure E.1E). Analysis of the Δ*hpf* growth curves yielded an average maximum growth rate of 0.36 h^{-1} ± 0.08 h^{-1} (Figure E.1F). By comparison, the growth rate of PAO1 (pMF230) and Δ*hpf* (pMF230) is 0.784 h^{-1} ± 0.042 h^{-1} and 0.689 h^{-1} ± 0.067 h^{-1} when cultured in TSB media in bulk. For the Δ*hpf* cells that were capable of regrowth in drops, the growth rate was similar to that of PAO1. Despite consistent growth rates within the Δ*hpf* population, there was a wide distribution of lag times over the course of the 21.5 h incubation period. The lag times for the Δ*hpf* cells capable of resuscitation ranged from 3 h to 17.5 h (Figure E.1E) with an average lag phase length of 7.71 h ± 3.98 h (Figure E.1G). Most day four starved Δ*hpf* cells, approximately 86.6% ± 2.5%, did not resuscitate in drops following starvation. Cells that did not resuscitate from starvation were not included in the statistical analyses for growth rate and lag phase length. For each strain, three fields of view were monitored, resulting in approximately 3000 drops and over 200 cells imaged per strain.

The DropSOAC Method Allows for Analysis of Single Cell Growth Kinetics and Quantification of Heterogeneity in Microbial Populations

Using the DropSOAC device to stabilize drops, we were able to monitor growth heterogeneity within clonal populations of *P. aeruginosa* PAO1 and its Δ*hpf* mutant derivative. Our results show that PAO1 has a small standard deviation for the lag time, and that growth curves were tightly clustered. We are also able to track cells that did not grow. Though the average growth rate of both the wild-type and the Δ*hpf* mutant cells were similar under these conditions (0.38 h^{-1} ± 0.12 h^{-1} and 0.36 h^{-1} ± 0.08 h^{-1}), the lag time following 4 days of starvation differed. Consistent with our previous study, [212] 86.6% ± 2.5% of the Δ*hpf* mutant cells were unable to recover from starvation and remained as single cells. The cells that recovered had extended and variable lag times, ranging from 3 h to 17.5 h. The Δ*hpf* strain lacks the hibernation promotion factor protein, a ribosomal accessory protein that helps maintain ribosome integrity during starvation. The heterogeneity in lag time in the Δ*hpf* mutant indicates that different cells have varied ability to perform *de novo* protein synthesis and grow following starvation. [212]

APPENDIX F

IMAGE ANALYSIS MATLAB SCRIPT FOR MEASURING DROP DIAMETER AND MULTICHANNEL FLUORESCENCE

A MATLAB (R2020a) script was written to measure the diameter and fluorescence intensity of drops imaged on an epifluorescence microscope. Drops are identified in images using the 'imfindcircles' function in MATLAB which uses a Circular Hough Transform (CHT) based algorithm to find circles in an image.[213] A schematic of the steps involved in CHT are shown in Figure F.1. Foreground pixels of high gradient are designated as being candidate pixels and are allowed to cast votes (Figure F.1A). The candidate pixels vote in a pattern which forms a full curve of a fixed radius. The votes of the candidate pixels belonging to the curve center tend to accumulate at the accumulator array bin corresponding to the circle's center (Figure F.1B). Circle centers are estimated by detecting the peaks in the accumulator array. This information is then used to calculate the circle's radius. Additional post-processing of the CHT algorithm output is performed in the image analysis script to clean up the data (e.g. overlapping circles or incorrectly identified circles). An example application of the drop image analysis script is shown in Figure F.2. An epifluorescence image of PCR drops post-thermocycling (Figure F.2A) is processed with the script to identify the locations of drops (Figure F.2B), measure the average fluorescence intensity of each drop (Figure F.2C), and measure the drop radius (Figure F.2D). The script can also be used with more complex images that have multiple channels. For example in Figure F.3, drops containing *E. coli* that express the green fluorescence protein (GFP) are identified in the brightfield channel (Figure F.3A-B) and the corresponding fluorescence measurements (Figure F.3C) are used to distinguish between drops containing cells and empty drops (Figure F.3D). To access the MATLAB script files, please contact either Geoffrey Zath (geoffrey.zath@gmail.com) of Dr. Connie Chang (connie.chang@montana.edu).

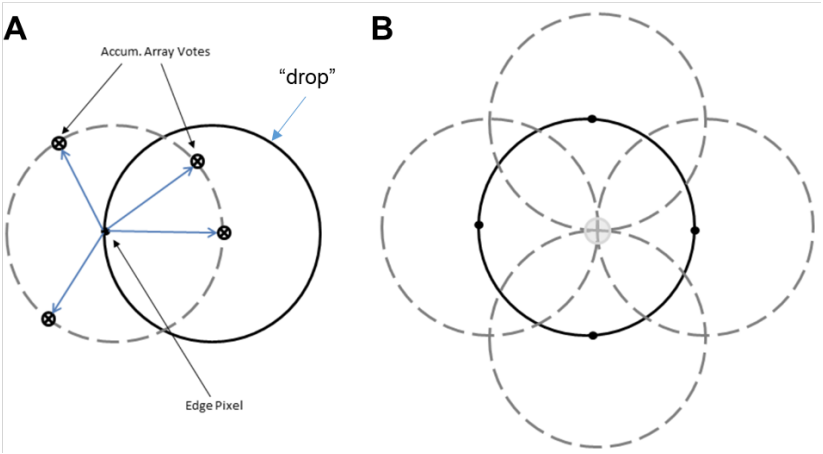


Figure F.1. Circle Hough Transform schematic. (A) Circles, or drops, in the image are tested using an initial guess of the radius range. (B) Once votes have been cast for candidate pixels, the circle center and radius are identified for each circle in the image. Image: https://www.mathworks.com/help/images/ref/imfindcircles.html

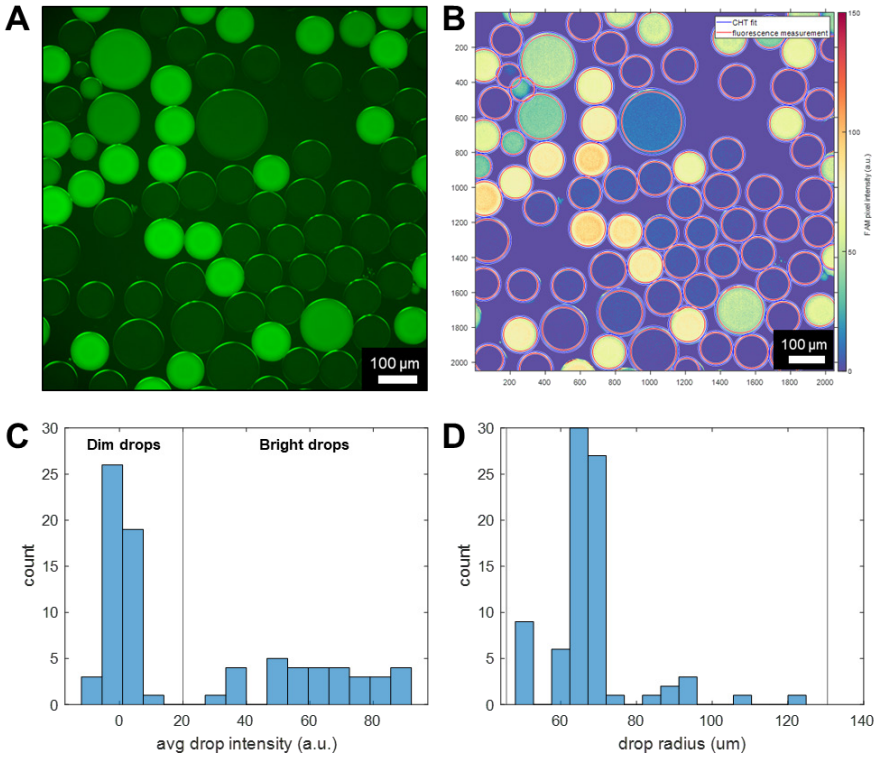


Figure F.2. (A) Epifluorescence image of PCR drops post-thermocycling. Presence of amplified Influenza A virus M gene RNA in a drop is indicated by an increase in fluorescence from the green FAM TaqMan probe. (B) Identification of drops with the drop image analysis MATLAB script. (C) Histogram of average fluorescence intensity in each drop with a threshold indicating dim and bright drops. (D) Histogram of drop radius. The upper and lower bounds indicate the range of radii used in the CHT algorithm.

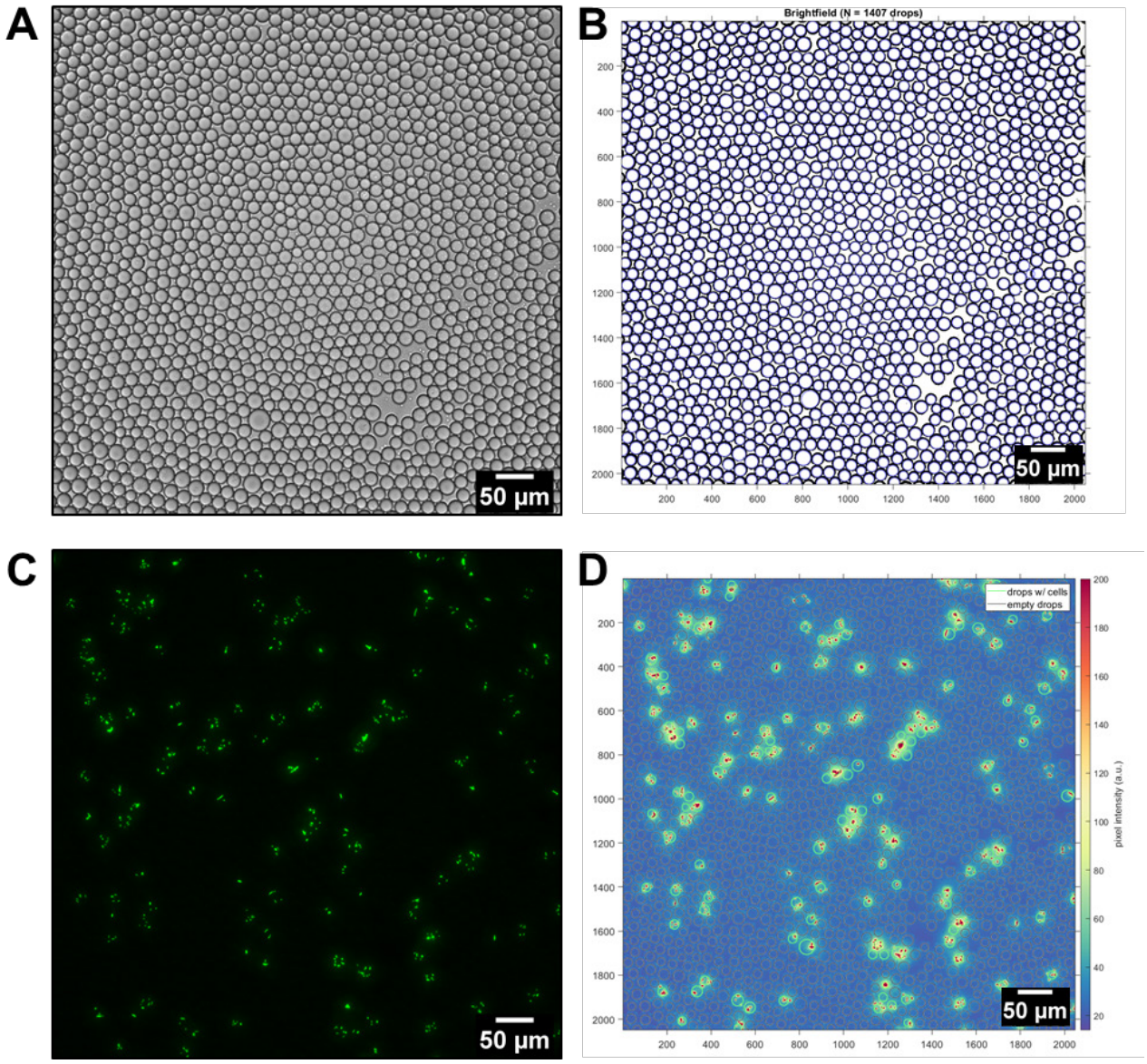


Figure F.3. (A) Brightfield image of drops containing *E. coli*. (B) Identification of drops in the brightfield channel using the drop image analysis MATLAB script. (C) Epifluorescence image of the drops in (A) with *E. coli* expressing GFP. (D) Drops containing cells are identified with the initial identification of drops in the brightfield channel and with thresholds set on the measured fluorescence from the GFP signal. Drops containing cells are outlined with green circles and empty drops are outlined with gray circles.

APPENDIX G

STATISTICS BASED MODEL FOR TRACKING THE LOADING OF CELLS AND VIRUS WHILE PASSAGING WITH THE EVOLUTION CHIP

Introduction

The influenza virus infects millions every year with over 23,000 annual deaths in the United States[214] and over 300,000 annual deaths worldwide.[215] The flu vaccine is the major form of prevention for the public; however, a virus can adapt over the course of a flu season, thereby decreasing the effectiveness of the vaccine. While there are currently available FDA-approved antiviral drugs on the market such at oseltamivir (Tamiflu), zanamivir (Relenza), and peramivir (Rapivab), they are unable to react to an evolving virus while the patient is sick. Therefore, a more dynamic treatment is needed.

One approach to producing a dynamic treatment is to use a form of the wild type virus against itself, capitalizing on a class of interfering particles that arise naturally through virus replication.[202] During virus replication, many incomplete virus mutants are created that are unable to complete their own replication, and are otherwise inactive, without the simultaneous infection of a wild type virus.[203] These mutant viruses have been given the name Defective Interfering Particles (DIPs).[202] DIPs replicate preferentially at the expense of the wild type virus by outcompeting for the interaction with viral replicative machinery.[216] This competition leads to a reduction in infectious virus formation and release. DIPs that are maintained for multiple rounds of replication are thought to be an effective therapy and are given the name Therapeutic Interfering Particles (TIPs). To escape TIP treatment, a virus must undergo multiple mutations that include genome regions common to the TIP. However, the nature of TIPs allows them to match the mutations and keep pace with the virus. The challenge we face in finding a TIP is the multitude of infection events with virus and various DIPs that need to be performed to determine efficacy.

We are specifically interested in finding TIP candidates for influenza type A (H1N1). We plan to passage, or subculture, MDCK cells with wild type virus over multiple rounds using drop-based microfluidics. By creating microscale emulsions, we can isolate single cells and viruses in a drop to observe their interactions in a high throughput manner with large sample sizes.[81, 217, 218] The encapsulation of cells has been utilized in drop-based microfluidic systems for long term cell growth,[90, 219] drop-based PCR,[3, 220-225] and drop sorting[20, 101, 226, 227]. Drop-based microfluidics has been used for the passaging of cancer cells[228] and studying norovirus infection behavior,[229, 230] yet to our knowledge, the passaging of MDCK cells and influenza viruses has not been studied at the microfluidic scale. While DIPs (and therefore TIPs) will arise naturally, in general, viral evolution in a bulk experiment leads to competition and low diversity. By moving to the microscale, we will reduce competition and greatly increase the DIP diversity which will increase the potential of finding a TIP candidate. We plan to quantify the virus and DIP interactions with drop-based qPCR (see Chapters 4-6) in the search for these TIP candidates.

The utility of drop-based microfluidics is in its high-throughput and isolating nature; a biological sample can be encapsulated into drop microenvironments at kilohertz rates. By using drop-based microfluidics, our goal is to increase the throughput of TIP identification and increase the potential diversity of candidates when compared to traditional bench-scale passaging methods. We aim to do this with a two-step approach: first, develop a drop-based microfluidic method for the passaging of MDCK cells, influenza viruses, and DIPs in drops (Appendix G); and second, develop a drop-based qPCR method to quantify virus and DIP within each drop (see Chapters 4-6). We plan to use these devices for up to five cell passages and compare our results to parallel bulk experiments performed in a well plate. Through this approach we will identify

TIPs from successful DIPs. We foresee the integration of these technologies providing a fully closed-loop system for the long-term passaging of cells, viruses, and DIPs/TIPs on a microfluidic device.

The proposed work has potential benefits in industry and healthcare for new vaccine development. The methods developed here can be used to improve the understanding of other viral systems that are important in industry and healthcare such as HIV, Zika, and West Nile. The virus and cell passaging technology can be commercialized, scaled-up, and adapted for other cell lines and virus types to allow for the development of anti-viral therapies in other laboratory systems. Furthermore, the proposed system would allow for the study of cell-to-cell heterogeneity which is unobtainable with standard laboratory methods.

Objective: Develop a Drop-Based Microfluidic Platform for the Continual Passaging of MDCK Cells and Influenza Virus in Drops

The first step is to develop a platform for the passaging of MDCK cells and the influenza virus in drops for a period of one to five days. We currently have a microfluidic device called the evolution chip that splits an incoming drop and merges the primary volume with a stream of fresh cells while the secondary volume is used for analysis (e.g. drop-based qPCR). The primary volume contains newly replicated virus; by adding fresh cells we can perform passaging similar to bench scale methods. The merged primary portion is then incubated, and the process repeated after the next round of replication. An example of drop merging on the evolution chip is presented in Figure G.1. This system will be used to observe virus and DIP competition over many replications. In addition, we will model the distributions of cells and viruses in drops over multiple passages to ensure a stable viral load is maintained in the system. The reduced sample

volume of these drops, a thousand-fold decrease from microtiter wells, allows for many more infection events to be created and quantified than would be practical for traditional passaging performed by hand.

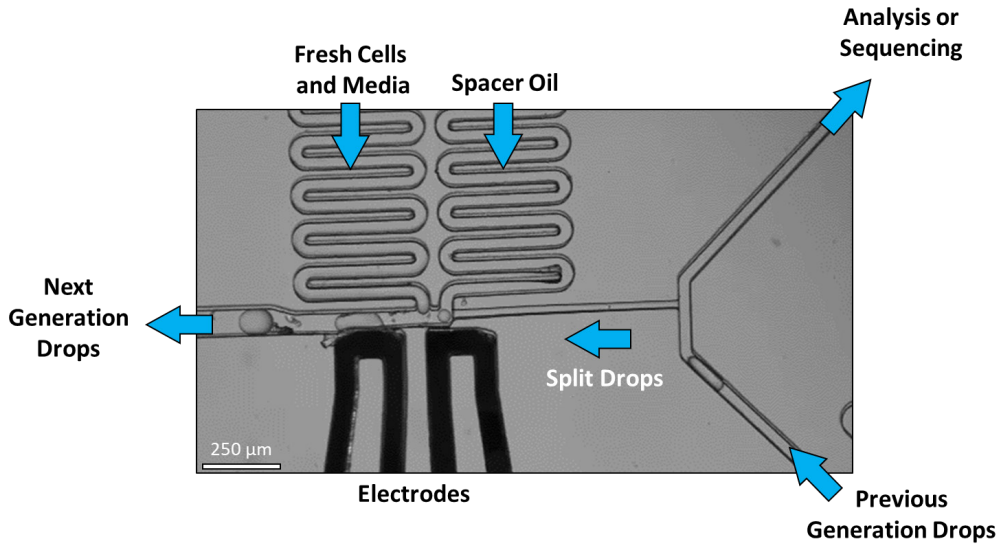


Figure G.1. High-speed video capture of drop merging on the evolution chip. The split drop volume enters and merges with a fresh cell stream. The black electrodes on the bottom of the image apply an electric field to destabilize the drop interface to allow for merging.

Preliminary Results

Evolution Chip Drop Loading Model. Preliminary work on a Poisson drop loading model has been performed for passaging with the evolution chip. The model currently loads cells and viruses based on different Poisson distributions. The model assumes an ideal system where a virus always infects and replicates if a cell is present in the drop. The Poisson distribution equation is shown below,

$$P = \frac{\lambda^k e^{-\lambda}}{k!}$$

where λ is the average particle concentration in a drop (e.g. cell or virus), k takes integer values 0, 1, 2, etc., and P is the probability of drops containing k particles per drop. Cells are loaded at a

user specific ‘cells per drop’ value and viruses loaded based on a user specified ‘MOI’ value. MOI, or multiplicity of infection, is the ratio of infectious viruses to cells. We currently load drops at each passage with the same cell concentration. The model tracks the split fraction of each drop that passes from one passage to the next and calculates the virus burst size after each infection event. Virus burst size is the ratio of viral genomes output per infected cell. Examples of decreasing and stable viral load in drops over 10 passages are shown in Figure G.2. It is apparent that a higher cell loading maintains a stable viral load due to each drop likely having a cell and therefore the virus is always able to replicate during each passage. Another value of note is the PCR cycle dynamic range required to distinguish background viral genomes from those produced from an infection event. We use an adapted equation from Tao et al.[230] to calculate this value,

$$\Delta N = \log_2(f * B_s) - \log_2(\max\{\lambda_v * R_g, 1\})$$

where ΔN is the PCR cycle dynamic range, f is the drop split fraction, B_s is the viral burst size, λ_v is the number viruses per drop, and R_g is the ratio of viral genomes to PFU (plaque forming units). The dynamic range is important as it will determine our success in finding virus/DIP ratios in downstream qPCR analysis. We want a high dynamic range otherwise it will be difficult to distinguish between background genomes (virus leftover from a previous passage) and current passage genomes.

In addition to particle loading in drops, the model also converts the bulk sample MOI into an effective drop MOI (see Figure G.3). Due to the picoliter sized drops, when a sample volume is encapsulated the particles in that sample become partitioned into individual containers. This partitioning nature of drops can lead to few drops with cell/virus combinations. For example, at a

bulk MOI of less than 1 and at less than 1 cell per drop the limit of MOI is 1, no matter the bulk MOI that is being encapsulated (see upper left of Figure G.3). These theoretical results will be verified with controlled experiments.

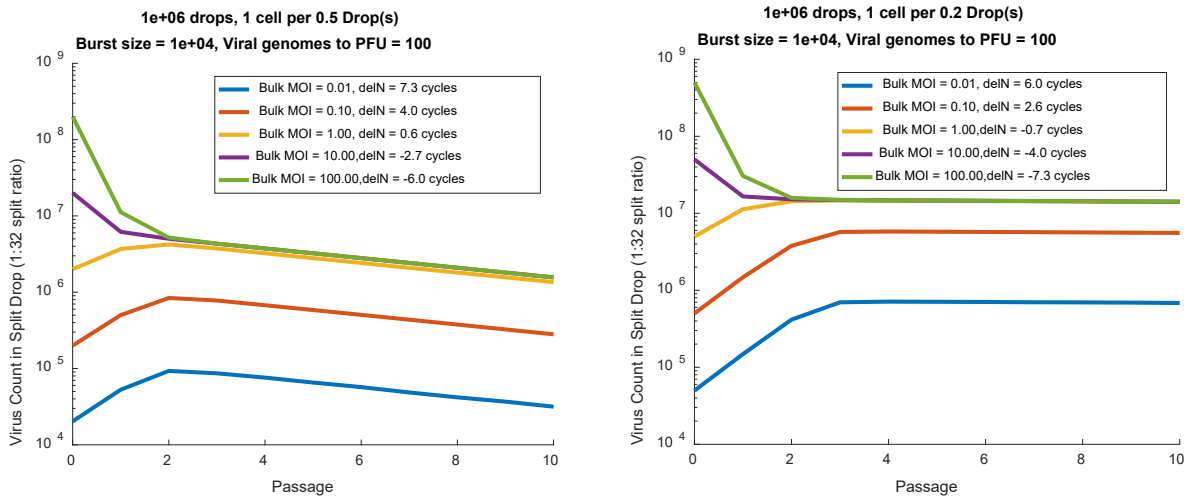


Figure G.2. Modeled viral load in drops. (left) Decreased viral load due to low cell loading in drops. (right) Stable viral load due to high cell loading.

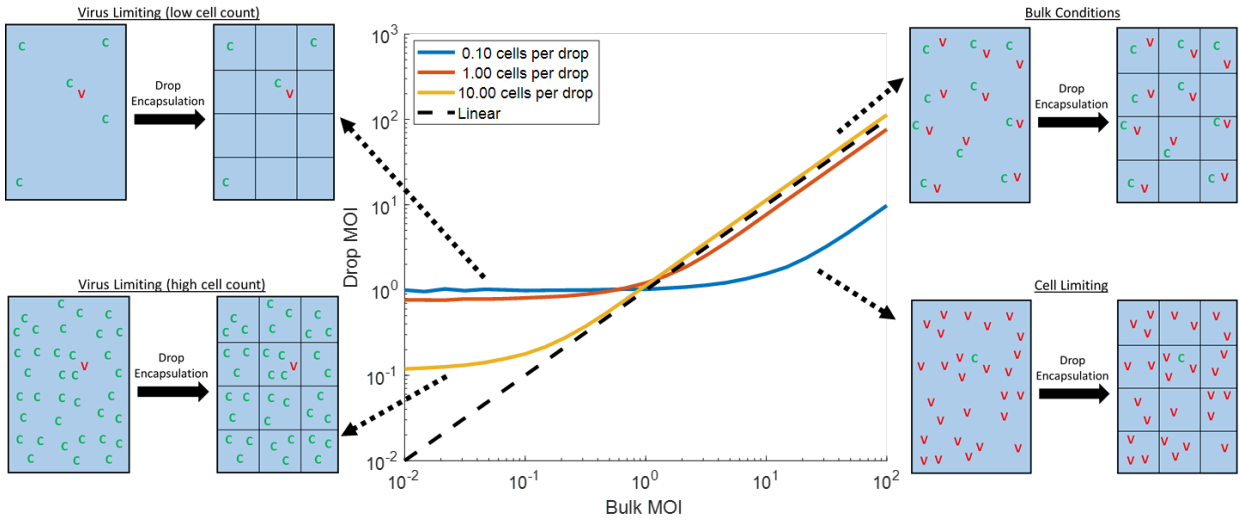


Figure G.3. Relationship between multiplicity of infection (MOI) from a bulk sample encapsulated into a drop. Cells per drop is a function of cell concentration and drop size.

Initial test of the evolution chip. We have performed an initial test run of the evolution chip with a parallel experiment performed in bulk. MDCK cells were encapsulated at a concentration of 1 cell per 100 μm diameter drop (1.9e6 cells/mL) at an MOI of 1. The drops were then incubated at 37 °C for 24 hours prior to the evolution chip operation. For each cell passage, drops were injected into the evolution chip where the smaller primary portion was split and merged with a fresh cell stream (1.9e6 cells/mL) and collected for another 24 hours of incubation. The remaining secondary volume of the drop was collected off chip and later broken for qPCR analysis. Three cell passages were performed before cellular material accumulated in the drops and caused them to become unstable and coalesce. From our qPCR results, we concluded there was little to no replication of virus within the drop system. The lack of replication is evident in Figure G.4 where a 1/8 dilution (device split ratio) applied passage to passage from the 24-hour time point follows the viral copy concentration very closely. Furthermore, if we turn off virus replication in the evolution chip model then it closely predicts the trend we observed. The initial offset between the bulk and microfluidic results may be due to the process of breaking drops which had been previously reported[231] and not due to varying infection dynamics as we would expect both zero time points to be similar. We do not expect there to be an offset once qPCR analysis has transitioned to a drop-based method. The evolution chip model does not consider this offset effect, but an option may be added if we continue to break drops for analysis. We are currently transitioning from using adherent to spinners MDCK cells as we expect this will promote infection in drops.

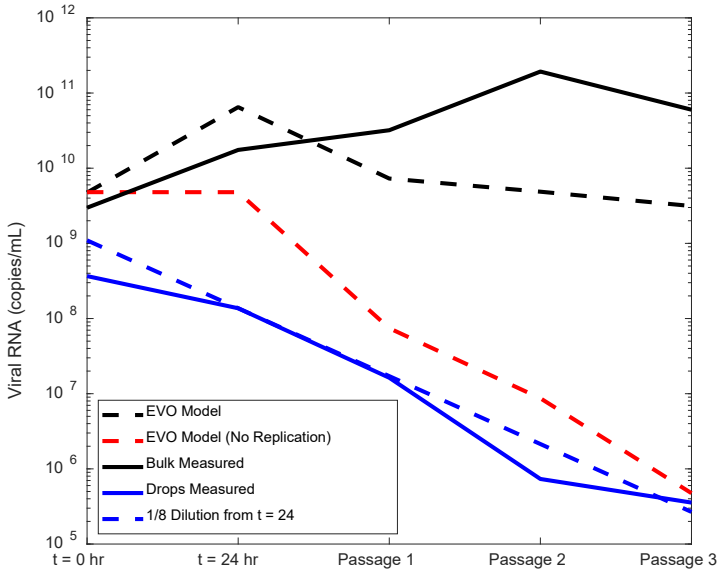


Figure G.4. Comparison of data obtained from the evolution chip, bulk passaging, and model predictions. There appears to have been little to no replication in drops and this is confirmed with our model prediction without replication. The viral copy number in the drop system appears to have been diluted passage to passage due to the splitting of the initial drops and merging of the fresh cell stream following the 1/8 split ratio on the device.

Task 1: Poisson Statistics-Based Cell/Virus Drop Loading Model

A model for the loading of cell, virus, and DIP in drops over multiple passages was written in MATLAB to determine experimental parameters such as flow rates, cell/virus/DIP concentrations, and split drop ratios. The model is based on the Poisson distribution of particles that occurs during drop encapsulation.[20] A diagram of the model is shown in Figure G.5. At drop encapsulation, a random Poisson distribution of cells and viruses is calculated to determine the number of cells and viruses to place in each drop. After each cell passage, a small portion of the drop is split and merged with fresh cells and then virus growth is calculated based on a theoretical viral burst size (viral genomes output per infected cell). These drops then repeat the split and merge process for the desired number of passages. The main purpose of this model is to ensure experimental conditions will achieve a stable viral load passage to passage.

We plan on incorporating parameters such as viral burst size (see Chapter 6), ratio of viral genomes to infectious particles, and the cyclical nature of DIP production for the influenza virus. We will measure these parameters in bulk and in drops. Output from the model using placeholder values of the above-mentioned parameters can be found in the above Preliminary Results section. To access the MATLAB script files, please contact either Geoffrey Zath (geoffrey.zath@gmail.com) of Dr. Connie Chang (connie.chang@montana.edu).

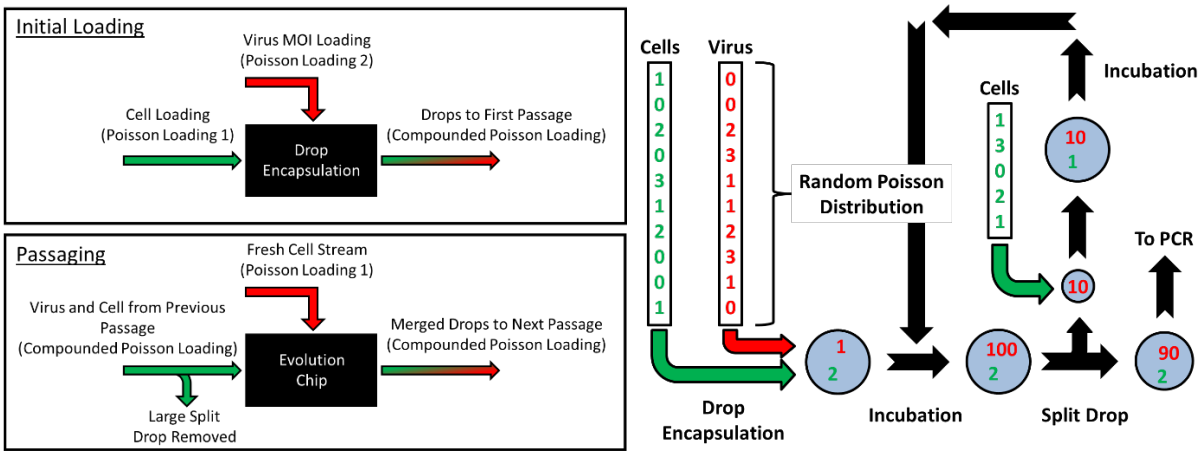


Figure G.5. Process flow of the Poisson statistics-based model at the device level (left) and drop level (right) for cell and virus loading in drops. MOI: multiplicity of infection (ratio of infectious virus to cells).

Task 2: MDCK Cell and Influenza Virus Passaging Study in Drops

Model parameters from Task 1 will be used with the evolution chip to passage MDCK cells with viruses for at least five passages. The secondary volume output of the evolution chip (volume of split drop not being passaged) will either be analyzed with bulk qPCR and/or with a drop-based qPCR method (see Chapter 5 and 6). These experiments will be replicated in bulk using well plates. We expect the drop results to include greater DIP diversity than from bulk due to increased virus lineage diversity from decreased competition in the isolated drop environment.

APPENDIX H

MATLAB SCRIPT FOR COUNTING FLUORESCENT PARTICLES CONTAINED IN DROPS FROM RAW TIME TRACE DETECTION DATA

At low fluorescent particle loading in drops (e.g. <10 particles per drop), the variability of the fluorescence intensity between drops becomes high (data not shown). The ability to count particles in drops allows for a direct measurement of discrete particles, such as cells, rather than relying on the fluorescence intensity. Previous work has demonstrated the ability to count single GFP *E. coli* cells in drops when measured with a flow-based fluorescence detection method.[232] We show a similar ability by counting single green fluorescent microbeads in drops. Green and red fluorescent microbeads were encapsulated in drops at approximately 4 and 100 particles per drop, respectively, and the fluorescence was measure with a flow-based detection method (Figure H.1A).[20] The red microbeads provided a strong fluorescence signal for identifying each drop in the time trace fluorescence data. The 'findpeaks' function in MATLAB (R2020a) was used to identify the location of drops using the red fluorescence data. The same function was then used to count the green fluorescence peaks within each drop (Figure H.1B). The distribution of particles counted per drop from 1400 drops is presented in Figure H.1C (blue Xs) with a fit to a Poisson distribution of five particles per drop (orange line). The agreement between the measured counts and Poisson fit is expected as particle loading in drops is assumed to follow Poisson statistics.[20] This particle counting method has potential as a high-throughput drop-based cell counter that provides a more accurate count than traditional methods (e.g. hemocytometer) due to the large sample size. To access the MATLAB script files, please contact either Geoffrey Zath (geoffrey.zath@gmail.com) of Dr. Connie Chang (connie.chang@montana.edu).

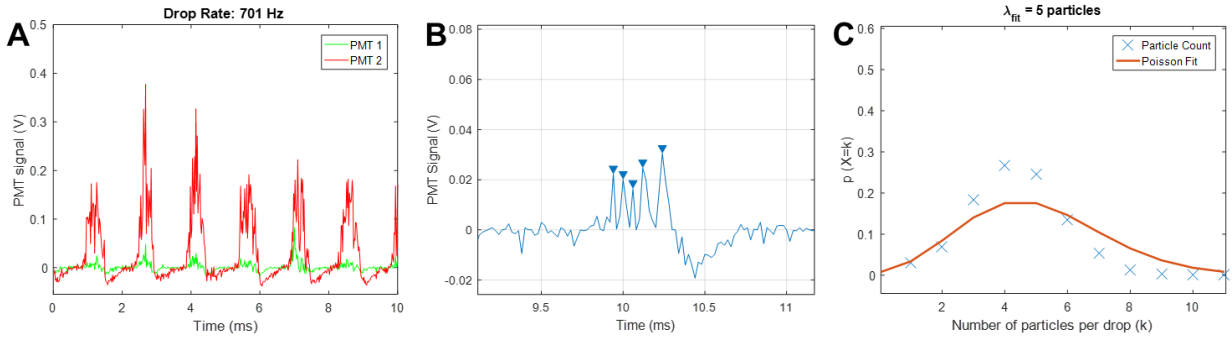


Figure H.1. (A) Raw time trace fluorescence data collected from high-throughput detection of drops. Drops contain 4 particles per drop of green fluorescent microbeads (PMT 1) and 100 particles per drop of red fluorescence microbeads (PMT 2). (B) Example of the MATLAB function 'findpeaks' identifying the signal peaks of green microbeads measured in PMT 1. (C) The distribution of the measured count of green microbeads in drops (blue Xs) compared to a Poisson distribution of five particles per drop (orange line).

APPENDIX I

MODEL FOR SIMULATING DROP DETECTION DATA

A model was written in MATLAB (R2020a) to simulate fluorescent drop detection data. The purpose of the model is to help better interpret the data collected from drop detection. The model allows the user to determine how the contents of a drop (e.g. fluorescent microbeads or cells) affects the raw time trace fluorescence data being collect. The model simulates drops containing variable amounts of fluorescent particles (Figure I.1A-B). The drops "flow across" a Gaussian laser beam profile and the fluorescence intensity of each particle is recorded as the beam intensity at the respective particle's location (Figure I.1A-B). The fluorescence intensity is summed in the y-direction, analogous to time, to provide a peak fluorescence value. To simulate drops flowing in a microfluidic channel (x-direction), a matrix containing alternating "full" and "empty" drops is created. This simulates time trace fluorescence detection data where white noise is added to better approximate real-world conditions (Figure I.1C-D). The simulated time trace data of 100 particles per drop (Figure I.1D) are similar to the measured time trace data collected from drops containing approximately 100 red fluorescent microbeads per drop (Figure I.2A-B). To access the MATLAB script files, please contact either Geoffrey Zath (geoffrey.zath@gmail.com) of Dr. Connie Chang (connie.chang@montana.edu).

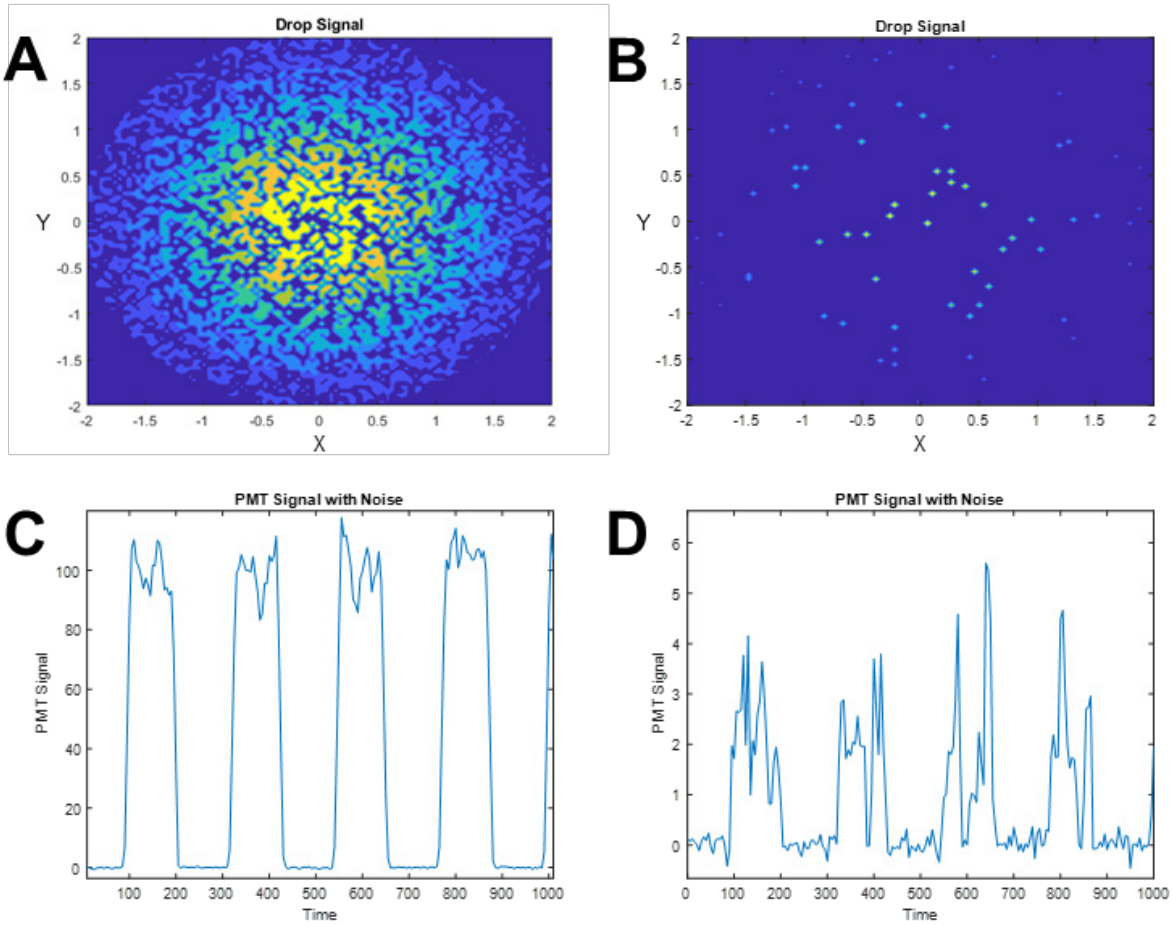


Figure I.1. Simulated fluorescence profile of a drop flowing across a laser with (A) 5000 particles per drop and (B) 100 particles per drop. Fluorescence intensity from low to high is indicated as a color scale from blue to yellow. Simulated time trace fluorescence detection data of drops flowing across a laser with (C) 5000 particles per drop and (D) 100 particles per drop. A small amount of white noise has been added to each drop to approximate real-world conditions.

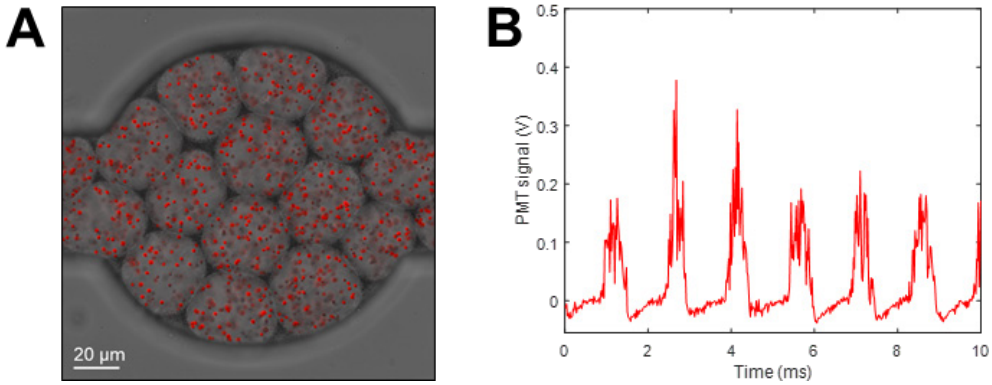


Figure I.2. (A) Fluorescence image of red fluorescent microbeads in drops at approximately 100 particles per drop. (B) Measured time trace fluorescence detection data of drops from (A).

APPENDIX J

MODEL FOR PREDICTING THE COALESCENCE EVENTS OF DROPS

A model was written in MATLAB (R2020a) to simulate drop coalescence over time. Specifically, this "coalescence cascade" model predicts how different combinations of pre-coalesced and coalesced drops combine over time. A schematic of this process is shown in Figure J.1. Pre-coalesced drops from a drop maker (Level 1 drops) coalesce with each other to become Level 2 drops in Event 1 with a probability P_{11}. In Event 2, Level 1 and 2 drops coalesce to form Level 3 drops with a probability P_{12}. In Event 3, Level 2 drops coalesce to form Level 4 drops with a probability P_{22}. To reduce model complexity, it is assumed that Events 1-3 are the primary occurrences of drop coalescence. The simulation is propagated N times to produce greater numbers of coalesced drops (i.e. coalescence cascade). Measured drop volume data from PCR drops after thermocycling (Figure J.2A) are used to compare to the model output (Figure J.2B). The model can create a similar distribution of drop volumes compared to those measured after tuning the model parameters. With further development of the model code, values for P_{11}, P_{12}, and P_{22} can be fit to the measured data and allow for quantifying the degree of coalescence in a sample. This may be useful when screening for additives to improve drop stability as presented in Chapter 4. To access the MATLAB script files, please contact either Geoffrey Zath (geoffrey.zath@gmail.com) of Dr. Connie Chang (connie.chang@montana.edu).

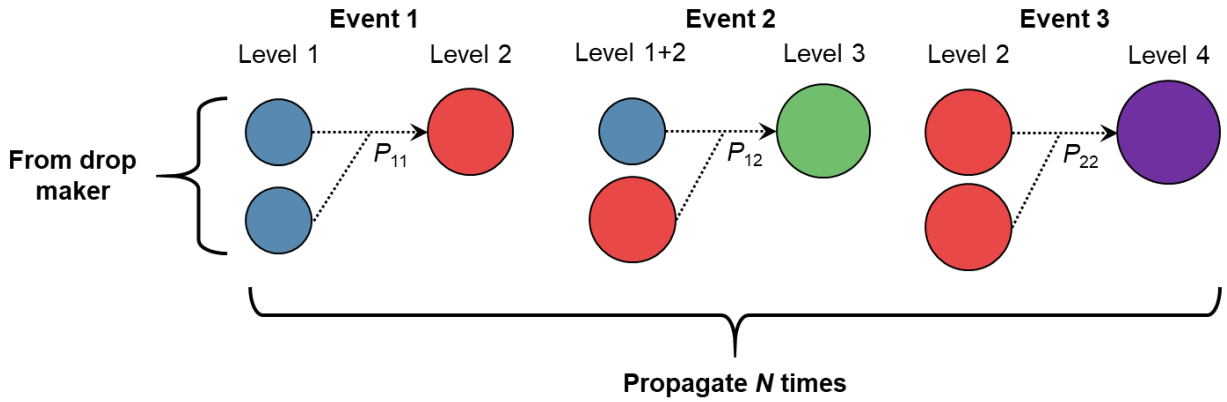


Figure J.1. Schematic of the coalescence cascade model. An initial guess for P_{11}, P_{12}, and P_{22} is made and then the model is propagated N times until the proportions of Level 1, 2, 3, and 4 drops match the measured data.

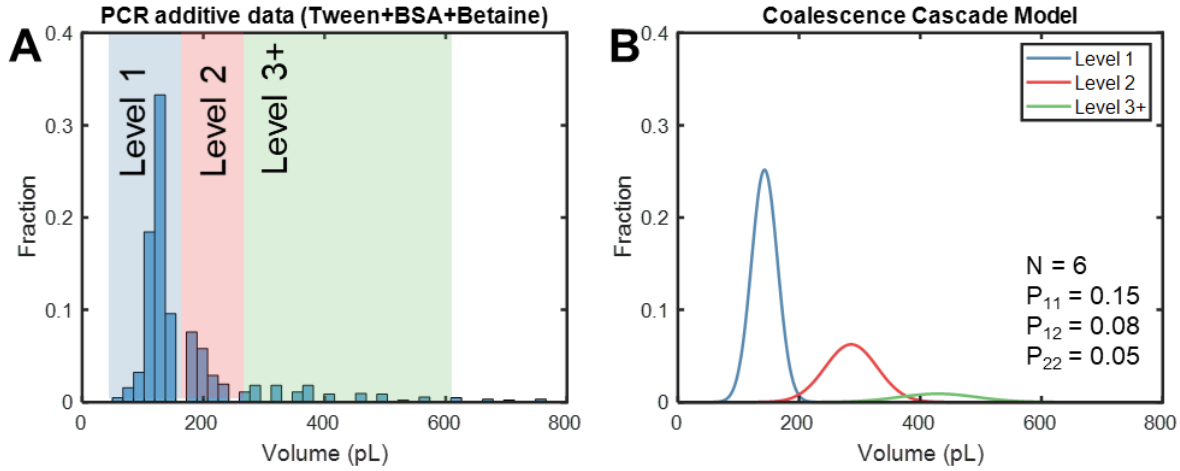


Figure J.2. (A) Measured drop volumes from PCR drops after thermocycling. Approximate regions for each level of coalescence are indicated on the histogram. Levels 3 and 4 are grouped together as Level 3+. (B) Coalescence cascade model output shows a similar distribution of drop volumes after tuning of the model parameters.

REFERENCES CITED

1. Holtze, C.; Rowat, A. C.; Agresti, J. J.; Hutchison, J. B.; Angile, F. E.; Schmitz, C. H.; Koster, S.; Duan, H.; Humphry, K. J.; Scanga, R. A.; Johnson, J. S.; Pisignano, D.; Weitz, D. A., Biocompatible surfactants for water-in-fluorocarbon emulsions. *Lab Chip* **2008,** *8* (10), 1632-9.

2. Beer, N. R.; Hindson, B. J.; Wheeler, E. K.; Hall, S. B.; Rose, K. A.; Kennedy, I. M.; Colston, B. W., On-Chip, Real-Time, Single-Copy Polymerase Chain Reaction in Picoliter Droplets. *Analytical Chemistry* **2007,** *79* (22), 8471-8475.

3. Kiss, M. M.; Ortoleva-Donnelly, L.; Beer, N. R.; Warner, J.; Bailey, C. G.; Colston, B. W.; Rothberg, J. M.; Link, D. R.; Leamon, J. H., High-throughput quantitative polymerase chain reaction in picoliter droplets. *Analytical chemistry* **2008,** *80* (23), 8975-8981.

4. Prakash, R.; Pabbaraju, K.; Wong, S.; Wong, A.; Tellier, R.; Kaler, K., Droplet microfluidic chip based nucleic acid amplification and real-time detection of influenza viruses. *Journal of The Electrochemical Society* **2014,** *161* (2), B3083-B3093.

5. Prakash, R.; Pabbaraju, K.; Wong, S.; Wong, A.; Tellier, R.; Kaler, K., Multiplex, quantitative, reverse transcription PCR detection of influenza viruses using droplet microfluidic technology. *Micromachines* **2015,** *6* (1), 63-79.

6. Beer, N. R.; Wheeler, E. K.; Lee-Houghton, L.; Watkins, N.; Nasarabadi, S.; Hebert, N.; Leung, P.; Arnold, D. W.; Bailey, C. G.; Colston, B. W., On-Chip Single-Copy Real-Time Reverse-Transcription PCR in Isolated Picoliter Droplets. *Analytical Chemistry* **2008,** *80* (6), 1854-1858.

7. Norian, H.; Kymissis, I.; Shepard, K. In *Integrated CMOS quantitative polymerase chain reaction lab-on-chip*, 2013 Symposium on VLSI Circuits, IEEE: 2013; pp C220-C221.

8. Hua, Z.; Rouse, J. L.; Eckhardt, A. E.; Srinivasan, V.; Pamula, V. K.; Schell, W. A.; Benton, J. L.; Mitchell, T. G.; Pollack, M. G., Multiplexed real-time polymerase chain reaction on a digital microfluidic platform. *Analytical chemistry* **2010,** *82* (6), 2310-2316.

9. Bian, X.; Jing, F.; Li, G.; Fan, X.; Jia, C.; Zhou, H.; Jin, Q.; Zhao, J., A microfluidic droplet digital PCR for simultaneous detection of pathogenic Escherichia coli O157 and Listeria monocytogenes. *Biosensors and Bioelectronics* **2015,** *74*, 770-777.

10. Leung, K.; Zahn, H.; Leaver, T.; Konwar, K. M.; Hanson, N. W.; Pagé, A. P.; Lo, C.-C.; Chain, P. S.; Hallam, S. J.; Hansen, C. L., A programmable droplet-based microfluidic device applied to multiparameter analysis of single microbes and microbial communities. *Proceedings of the National Academy of Sciences* **2012,** *109* (20), 7665-7670.

11. Hatch, A. C.; Fisher, J. S.; Tovar, A. R.; Hsieh, A. T.; Lin, R.; Pentoney, S. L.; Yang, D. L.; Lee, A. P., 1-Million droplet array with wide-field fluorescence imaging for digital PCR. *Lab on a Chip* **2011,** *11* (22), 3838-3845.

12. Rane, T. D.; Chen, L.; Zec, H. C.; Wang, T.-H., Microfluidic continuous flow digital loop-mediated isothermal amplification (LAMP). *Lab on a Chip* **2015,** *15* (3), 776-782.

13. Sciancalepore, A. G.; Polini, A.; Mele, E.; Girardo, S.; Cingolani, R.; Pisignano, D., Rapid nested-PCR for tyrosinase gene detection on chip. *Biosensors and Bioelectronics* **2011,** *26* (5), 2711-2715.

14. Eastburn, D. J.; Sciambi, A.; Abate, A. R., Ultrahigh-throughput mammalian single-cell reverse-transcriptase polymerase chain reaction in microfluidic drops. *Analytical chemistry* **2013,** *85* (16), 8016-8021.

15. Hayes, C. J.; Dalton, T. M., Microfluidic droplet-based PCR instrumentation for high-throughput gene expression profiling and biomarker discovery. *Biomolecular Detection and Quantification* **2015,** *4*, 22-32.

16. White, A. K.; VanInsberghe, M.; Petriv, O. I.; Hamidi, M.; Sikorski, D.; Marra, M. A.; Piret, J.; Aparicio, S.; Hansen, C. L., High-throughput microfluidic single-cell RT-qPCR. *Proceedings of the National Academy of Sciences* **2011,** *108* (34), 13999-14004.

17. VanInsberghe, M.; Zahn, H.; White, A. K.; Petriv, O. I.; Hansen, C. L., Highly multiplexed single-cell quantitative PCR. *PLOS ONE* **2018,** *13* (1), e0191601.

18. Zhu, Y.; Zhang, Y.-X.; Liu, W.-W.; Ma, Y.; Fang, Q.; Yao, B., Printing 2-Dimentional Droplet Array for Single-Cell Reverse Transcription Quantitative PCR Assay with a Microfluidic Robot. *Scientific Reports* **2015,** *5*, 9551.

19. Schaerli, Y.; Wootton, R. C.; Robinson, T.; Stein, V.; Dunsby, C.; Neil, M. A.; French, P. M.; DeMello, A. J.; Abell, C.; Hollfelder, F., Continuous-flow polymerase chain reaction of single-copy DNA in microfluidic microdroplets. *Analytical chemistry* **2008,** *81* (1), 302-306.

20. Mazutis, L.; Gilbert, J.; Ung, W. L.; Weitz, D. A.; Griffiths, A. D.; Heyman, J. A., Single-cell analysis and sorting using droplet-based microfluidics. *Nature protocols* **2013,** *8* (5), 870-91.

21. Hindson, B. J.; Ness, K. D.; Masquelier, D. A.; Belgrader, P.; Heredia, N. J.; Makarewicz, A. J.; Bright, I. J.; Lucero, M. Y.; Hiddessen, A. L.; Legler, T. C., High-throughput droplet digital PCR system for absolute quantitation of DNA copy number. *Analytical chemistry* **2011,** *83* (22), 8604-8610.

22. Milbury, C. A.; Zhong, Q.; Lin, J.; Williams, M.; Olson, J.; Link, D. R.; Hutchison, B., Determining lower limits of detection of digital PCR assays for cancer-related gene mutations. *Biomolecular detection and quantification* **2014,** *1* (1), 8-22.

23. Pfaffl, M. W. J. A. o. q. P., Quantification strategies in real-time PCR. **2004,** *1*, 89-113.

24. Kubista, M.; Andrade, J. M.; Bengtsson, M.; Forootan, A.; Jonák, J.; Lind, K.; Sindelka, R.; Sjöback, R.; Sjögreen, B.; Strömbom, L. J. M. a. o. m., The real-time polymerase chain reaction. **2006,** *27* (2-3), 95-125.

25. Hatch, A. C.; Ray, T.; Lintecum, K.; Youngbull, C., Continuous flow real-time PCR device using multi-channel fluorescence excitation and detection. *Lab on a Chip* **2014,** *14* (3), 562-568.

26. Gevertz, J. L.; Dunn, S. M.; Roth, C. M., Mathematical model of real-time PCR kinetics. *Biotechnology and bioengineering* **2005,** *92* (3), 346-355.

27. Rutledge, R., Sigmoidal curve-fitting redefines quantitative real-time PCR with the prospective of developing automated high-throughput applications. *Nucleic acids research* **2004,** *32* (22), e178-e178.

28. Tao, Y.; Rotem, A.; Zhang, H.; Chang, C. B.; Basu, A.; Kolawole, A. O.; Koehler, S. A.; Ren, Y.; Lin, J. S.; Pipas, J. M.; Feldman, A. B.; Wobus, C. E.; Weitz, D. A., Rapid, targeted and culture-free viral infectivity assay in drop-based microfluidics. *Lab Chip* **2015,** *15* (19), 3934-3940.

29. Hatori, M. N.; Kim, S. C.; Abate, A. R., Particle-templated emulsification for microfluidics-free digital biology. *Analytical chemistry* **2018,** *90* (16), 9813-9820.

30. Hajji, I.; Serra, M.; Geremie, L.; Ferrante, I.; Renault, R.; Viovy, J. L.; Descroix, S.; Ferraro, D., Droplet microfluidic platform for fast and continuous-flow RT-qPCR analysis devoted to cancer diagnosis application. *Sensor Actuat B-Chem* **2020,** *303*, 127171.

31. Pekin, D.; Skhiri, Y.; Baret, J.-C.; Le Corre, D.; Mazutis, L.; Salem, C. B.; Millot, F.; El Harrak, A.; Hutchison, J. B.; Larson, J. W., Quantitative and sensitive detection of rare mutations using droplet-based microfluidics. *Lab on a chip* **2011,** *11* (13), 2156-2166.

32. Zhong, Q.; Bhattacharya, S.; Kotsopoulos, S.; Olson, J.; Taly, V.; Griffiths, A. D.; Link, D. R.; Larson, J. W., Multiplex digital PCR: breaking the one target per color barrier of quantitative PCR. *Lab on a Chip* **2011,** *11* (13), 2167-2174.

33. Rutledge, R. G.; Stewart, D. J. B. b., A kinetic-based sigmoidal model for the polymerase chain reaction and its application to high-capacity absolute quantitative real-time PCR. **2008,** *8* (1), 47.

34. Liu, W.; Saint, D. A. J. B.; communications, b. r., Validation of a quantitative method for real time PCR kinetics. **2002,** *294* (2), 347-353.

35. Liu, W.; Saint, D. A. J. A. b., A new quantitative method of real time reverse transcription polymerase chain reaction assay based on simulation of polymerase chain reaction kinetics. **2002,** *302* (1), 52-59.

36. Thorsen, T.; Roberts, R. W.; Arnold, F. H.; Quake, S. R., Dynamic pattern formation in a vesicle-generating microfluidic device. *Physical review letters* **2001,** *86* (18), 4163.

37. Gruner, P.; Riechers, B.; Orellana, L. A. C.; Brosseau, Q.; Maes, F.; Beneyton, T.; Pekin, D.; Baret, J.-C., Stabilisers for water-in-fluorinated-oil dispersions: Key properties for microfluidic applications. *Current opinion in colloid & interface science* **2015,** *20* (3), 183-191.

38. Studer, A.; Hadida, S.; Ferritto, R.; Kim, S.-Y.; Jeger, P.; Wipf, P.; Curran, D. P., Fluorous Synthesis: A Fluorous-Phase Strategy for Improving Separation Efficiency in Organic Synthesis. *Science* **1997,** *275* (5301), 823-826.

39. Scott, R. L., The Solubility of Fluorocarbons1. *Journal of the American Chemical Society* **1948,** *70* (12), 4090-4093.

40. Lipinski, C. A.; Lombardo, F.; Dominy, B. W.; Feeney, P. J., Experimental and computational approaches to estimate solubility and permeability in drug discovery and development settings1PII of original article: S0169-409X(96)00423-1. The article was originally published in Advanced Drug Delivery Reviews 23 (1997) 3–25.1. *Advanced Drug Delivery Reviews* **2001,** *46* (1), 3-26.

41. Gollan, F.; Clark, L., Organ perfusion with fluorocarbon fluid. *Physiologist* **1966,** *9* (191), H292.

42. Andjus, R.; Suhara, K.; Sloviter, H. A., An isolated, perfused rat brain preparation, its spontaneous and stimulated activity. *Journal of applied physiology* **1967,** *22* (5), 1033-1039.

43. Geyer, R. P., Fluorocarbon-polyol artificial blood substitutes. *New England Journal of Medicine* **1973,** *289* (20), 1077-1082.

44. Pan, M.; Rosenfeld, L.; Kim, M.; Xu, M.; Lin, E.; Derda, R.; Tang, S. K. Y., Fluorinated Pickering Emulsions Impede Interfacial Transport and Form Rigid Interface for the Growth of Anchorage-Dependent Cells. *ACS Applied Materials & Interfaces* **2014,** *6* (23), 21446-21453.

45. Chowdhury, M. S.; Zheng, W.; Kumari, S.; Heyman, J.; Zhang, X.; Dey, P.; Weitz, D. A.; Haag, R., Dendronized fluorosurfactant for highly stable water-in-fluorinated oil emulsions with minimal inter-droplet transfer of small molecules. *Nat. Commun.* **2019,** *10* (1), 4546.

46. Baret, J.-C., Surfactants in droplet-based microfluidics. *Lab on a Chip* **2012,** *12* (3), 422-433.

47. Bourrel, M.; Graciaa, A.; Schechter, R. S.; Wade, W. H., The relation of emulsion stability to phase behavior and interfacial tension of surfactant systems. *J Colloid Interface Sci* **1979,** *72* (1), 161-163.

48. Butt, H.-J.; Butt, H.-J. B.; Graf, K.; Kappl, M., *Physics and chemistry of interfaces*. John Wiley & Sons: 2003.

49. Bibette, J.; Calderon, F. L.; Poulin, P., Emulsions: basic principles. *Reports on Progress in Physics* **1999,** *62* (6), 969.

50. Bibette, J.; Morse, D.; Witten, T.; Weitz, D., Stability criteria for emulsions. *Physical review letters* **1992,** *69* (16), 2439.

51. Courtois, F.; Olguin, L. F.; Whyte, G.; Theberge, A. B.; Huck, W. T.; Hollfelder, F.; Abell, C., Controlling the retention of small molecules in emulsion microdroplets for use in cell-based assays. *Analytical chemistry* **2009,** *81* (8), 3008-3016.

52. Skhiri, Y.; Gruner, P.; Semin, B.; Brosseau, Q.; Pekin, D.; Mazutis, L.; Goust, V.; Kleinschmidt, F.; El Harrak, A.; Hutchison, J. B.; Mayot, E.; Bartolo, J.-F.; Griffiths, A. D.; Taly, V.; Baret, J.-C., Dynamics of molecular transport by surfactants in emulsions. *Soft Matter* **2012,** *8* (41), 10618.

53. Sandoz, P. A.; Chung, A. J.; Weaver, W. M.; Di Carlo, D., Sugar Additives Improve Signal Fidelity for Implementing Two-Phase Resorufin-Based Enzyme Immunoassays. *Langmuir* **2014,** *30* (23), 6637-6643.

54. Woronoff, G.; El Harrak, A.; Mayot, E.; Schicke, O.; Miller, O. J.; Soumillion, P.; Griffiths, A. D.; Ryckelynck, M., New generation of amino coumarin methyl sulfonate-based fluorogenic substrates for amidase assays in droplet-based microfluidic applications. *Anal Chem* **2011,** *83* (8), 2852-7.

55. Discher, D. E.; Janmey, P.; Wang, Y.-l., Tissue Cells Feel and Respond to the Stiffness of Their Substrate. *Science* **2005,** *310* (5751), 1139-1143.

56. Malisova, B.; Tosatti, S.; Textor, M.; Gademann, K.; Zürcher, S., Poly(ethylene glycol) Adlayers Immobilized to Metal Oxide Substrates Through Catechol Derivatives: Influence of Assembly Conditions on Formation and Stability. *Langmuir* **2010,** *26* (6), 4018-4026.

57. Hey, M. J.; Ilett, S. M.; Davidson, G., Effect of temperature on poly(ethylene oxide) chains in aqueous solution. A viscometric, 1H NMR and Raman spectroscopic study. *Journal of the Chemical Society, Faraday Transactions* **1995,** *91* (21), 3897-3900.

58. Colegate, D. M.; Bain, C. D., Adsorption kinetics in micellar solutions of nonionic surfactants. *Physical review letters* **2005,** *95* (19), 198302.

59. Derkach, S.; Krägel, J.; Miller, R., Methods of measuring rheological properties of interfacial layers (Experimental methods of 2D rheology). *Colloid journal* **2009,** *71* (1), 1-17.

60. Jin, F.; Balasubramaniam, R.; Stebe, K. J., Surfactant adsorption to spherical particles: The intrinsic length scale governing the shift from diffusion to kinetic-controlled mass transfer. *The journal of adhesion* **2004,** *80* (9), 773-796.

61. Dai, B.; Leal, L. G., The mechanism of surfactant effects on drop coalescence. *Physics of fluids* **2008,** *20* (4), 040802.

62. Tan, Y.-C.; Ho, Y. L.; Lee, A. P., Droplet coalescence by geometrically mediated flow in microfluidic channels. *Microfluidics and Nanofluidics* **2007,** *3* (4), 495-499.

63. Trotta, M.; Gasco, M. R.; Morel, S., Release of drugs from oil-water microemulsions. *Journal of Controlled Release* **1989,** *10* (3), 237-243.

64. Gruner, P.; Riechers, B.; Semin, B.; Lim, J.; Johnston, A.; Short, K.; Baret, J. C., Controlling molecular transport in minimal emulsions. *Nat Commun* **2016,** *7*, 10392.

65. Calderó, G.; García-Celma, M. J.; Solans, C.; Plaza, M.; Pons, R., Influence of Composition Variables on the Molecular Diffusion from Highly Concentrated Water-in-Oil Emulsions (Gel−Emulsions). *Langmuir* **1997,** *13* (3), 385-390.

66. Babak, V. G.; Stébé, M.-J.; Fa, N., Physico-chemical model for molecular diffusion from highly concentrated emulsions. *Mendeleev Communications* **2003,** *13* (6), 254-256.

67. Fa, N.; Babak, V. G.; Stébé, M.-J., The release of caffeine from hydrogenated and fluorinated gel emulsions and cubic phases. *Colloids and Surfaces A: Physicochemical and Engineering Aspects* **2004,** *243* (1), 117-125.

68. Thiam, A. R.; Bremond, N.; Bibette, J., From Stability to Permeability of Adhesive Emulsion Bilayers. *Langmuir* **2012,** *28* (15), 6291-6298.

69. Ariyaprakai, S.; Dungan, S. R., Influence of surfactant structure on the contribution of micelles to Ostwald ripening in oil-in-water emulsions. *J Colloid Interface Sci* **2010,** *343* (1), 102-108.

70. Tadros, T., Surfactants in pharmaceutical formulations. *Applied Surfactants: Principles and Applications* **2005,** *13*.

71. Schmitz, C. H.; Rowat, A. C.; Köster, S.; Weitz, D. A., Dropspots: a picoliter array in a microfluidic device. *Lab on a Chip* **2009,** *9* (1), 44-49.

72. Etienne, G.; Kessler, M.; Amstad, E., Influence of fluorinated surfactant composition on the stability of emulsion drops. *Macromolecular Chemistry and Physics* **2017,** *218* (2), 1600365.

73. Etienne, G.; Vian, A.; Biocanin, M.; Deplancke, B.; Amstad, E., Cross-talk between emulsion drops: how are hydrophilic reagents transported across oil phases? *Lab Chip* **2018,** *18* (24), 3903-3912.

74. Wen, L.; Papadopoulos, K. D., Visualization of water transport in W1/O/W2 emulsions. *Colloids and surfaces A: Physicochemical and engineering aspects* **2000,** *174* (1-2), 159-167.

75. Bahtz, J.; Gunes, D. Z.; Hughes, E.; Pokorny, L.; Riesch, F.; Syrbe, A.; Fischer, P.; Windhab, E. J., Decoupling of mass transport mechanisms in the stagewise swelling of multiple emulsions. *Langmuir* **2015,** *31* (19), 5265-5273.

76. Bahtz, J.; Gunes, D. Z.; Syrbe, A.; Mosca, N.; Fischer, P.; Windhab, E. J., Quantification of spontaneous W/O emulsification and its impact on the swelling kinetics of multiple W/O/W emulsions. *Langmuir* **2016,** *32* (23), 5787-5795.

77. Bochner de Araujo, S.; Merola, M.; Vlassopoulos, D.; Fuller, G. G., Droplet coalescence and spontaneous emulsification in the presence of asphaltene adsorption. *Langmuir* **2017,** *33* (40), 10501-10510.

78. Chen, Y.; Wijaya Gani, A.; Tang, S. K., Characterization of sensitivity and specificity in leaky droplet-based assays. *Lab Chip* **2012,** *12* (23), 5093-103.

79. Janiesch, J. W.; Weiss, M.; Kannenberg, G.; Hannabuss, J.; Surrey, T.; Platzman, I.; Spatz, J. P., Key factors for stable retention of fluorophores and labeled biomolecules in droplet-based microfluidics. *Anal Chem* **2015,** *87* (4), 2063-7.

80. Loveday, E. K.; Zath, G. K.; Bikos, D. A.; Jay, Z. J.; Chang, C. B., Screening of Additive Formulations Enables Off-Chip Drop Reverse Transcription Quantitative Polymerase Chain Reaction of Single Influenza A Virus Genomes. *Analytical Chemistry* **2021**.

81. Agresti, J. J.; Antipov, E.; Abate, A. R.; Ahn, K.; Rowat, A. C.; Baret, J.-C.; Marquez, M.; Klibanov, A. M.; Griffiths, A. D.; Weitz, D. A., Ultrahigh-throughput screening in drop-based microfluidics for directed evolution. *Proceedings of the National Academy of Sciences* **2010,** *107* (9), 4004-4009.

82. Guo, M. T.; Rotem, A.; Heyman, J. A.; Weitz, D. A., Droplet microfluidics for high-throughput biological assays. *Lab on a Chip* **2012,** *12* (12), 2146-2155.

83. Kulesa, A.; Kehe, J.; Hurtado, J. E.; Tawde, P.; Blainey, P. C., Combinatorial drug discovery in nanoliter droplets. *Proceedings of the National Academy of Sciences* **2018,** *115* (26), 6685-6690.

84. Ackerman, C. M.; Myhrvold, C.; Thakku, S. G.; Freije, C. A.; Metsky, H. C.; Yang, D. K.; Simon, H. Y.; Boehm, C. K.; Kosoko-Thoroddsen, T.-S. F.; Kehe, J. J. N., Massively multiplexed nucleic acid detection with Cas13. *Nature* **2020**, 1-6.

85. Scheler, O.; Makuch, K.; Debski, P. R.; Horka, M.; Ruszczak, A.; Pacocha, N.; Sozański, K.; Smolander, O.-P.; Postek, W.; Garstecki, P. J. S. r., Droplet-based digital antibiotic susceptibility screen reveals single-cell clonal heteroresistance in an isogenic bacterial population. *Scientific Reports (Nature Publisher Group)* **2020,** *10* (1), 1-8.

86. Klein, A. M.; Mazutis, L.; Akartuna, I.; Tallapragada, N.; Veres, A.; Li, V.; Peshkin, L.; Weitz, D. A.; Kirschner, M. W. J. C., Droplet barcoding for single-cell transcriptomics applied to embryonic stem cells. *Cell* **2015,** *161* (5), 1187-1201.

87. Rotem, A.; Ram, O.; Shoresh, N.; Sperling, R. A.; Goren, A.; Weitz, D. A.; Bernstein, B. E., Single-cell ChIP-seq reveals cell subpopulations defined by chromatin state. *Nature biotechnology* **2015,** *33* (11), 1165-72.

88. Rotem, A.; Ram, O.; Shoresh, N.; Sperling, R. A.; Schnall-Levin, M.; Zhang, H.; Basu, A.; Bernstein, B. E.; Weitz, D. A., High-throughput single-cell labeling (Hi-SCL) for RNA-Seq using drop-based microfluidics. *PloS one* **2015,** *10* (5), e0116328.

89. Macosko, E. Z.; Basu, A.; Satija, R.; Nemesh, J.; Shekhar, K.; Goldman, M.; Tirosh, I.; Bialas, A. R.; Kamitaki, N.; Martersteck, E. M., Highly parallel genome-wide expression profiling of individual cells using nanoliter droplets. *Cell* **2015,** *161* (5), 1202-1214.

90. Brouzes, E.; Medkova, M.; Savenelli, N.; Marran, D.; Twardowski, M.; Hutchison, J. B.; Rothberg, J. M.; Link, D. R.; Perrimon, N.; Samuels, M. L., Droplet microfluidic technology for single-cell high-throughput screening. *Proceedings of the National Academy of Sciences* **2009,** *106* (34), 14195-200.

91. Abate, A. R.; Hung, T.; Sperling, R. A.; Mary, P.; Rotem, A.; Agresti, J. J.; Weiner, M. A.; Weitz, D. A., DNA sequence analysis with droplet-based microfluidics. *Lab on a Chip* **2013,** *13* (24), 4864-9.

92. Chen, C. H.; Miller, M. A.; Sarkar, A.; Beste, M. T.; Isaacson, K. B.; Lauffenburger, D. A.; Griffith, L. G.; Han, J., Multiplexed protease activity assay for low-volume clinical samples using droplet-based microfluidics and its application to endometriosis. *Journal of the American Chemical Society* **2013,** *135* (5), 1645-8.

93. Kehe, J.; Kulesa, A.; Ortiz, A.; Ackerman, C. M.; Thakku, S. G.; Sellers, D.; Kuehn, S.; Gore, J.; Friedman, J.; Blainey, P. C., Massively parallel screening of synthetic microbial communities. *Proceedings of the National Academy of Sciences* **2019,** *116* (26), 12804-12809.

94. Miller, O. J.; El Harrak, A.; Mangeat, T.; Baret, J. C.; Frenz, L.; El Debs, B.; Mayot, E.; Samuels, M. L.; Rooney, E. K.; Dieu, P.; Galvan, M.; Link, D. R.; Griffiths, A. D., High-resolution dose-response screening using droplet-based microfluidics. *Proceedings of the National Academy of Sciences* **2012,** *109* (2), 378-83.

95. Kaminski, T. S.; Jakiela, S.; Czekalska, M. A.; Postek, W.; Garstecki, P., Automated generation of libraries of nL droplets. *Lab on a Chip* **2012,** *12* (20), 3995-4002.

96. Rane, T. D.; Zec, H. C.; Wang, T.-H., A serial sample loading system: interfacing multiwell plates with microfluidic devices. *Journal of laboratory automation* **2012,** *17* (5), 370-377.

97. Clausell-Tormos, J.; Griffiths, A. D.; Merten, C. A., An automated two-phase microfluidic system for kinetic analyses and the screening of compound libraries. *Lab on a Chip* **2010,** *10* (10), 1302-1307.

98. Bui, M.-P. N.; Li, C. A.; Han, K. N.; Choo, J.; Lee, E. K.; Seong, G. H., Enzyme kinetic measurements using a droplet-based microfluidic system with a concentration gradient. *Analytical chemistry* **2011,** *83* (5), 1603-1608.

99. Lim, J.; Caen, O.; Vrignon, J.; Konrad, M.; Taly, V.; Baret, J.-C., Parallelized ultra-high throughput microfluidic emulsifier for multiplex kinetic assays. *Biomicrofluidics* **2015,** *9* (3), 034101.

100. Bawazer, L. A.; McNally, C. S.; Empson, C. J.; Marchant, W. J.; Comyn, T. P.; Niu, X.; Cho, S.; McPherson, M. J.; Binks, B. P.; deMello, A.; Meldrum, F. C., Combinatorial microfluidic droplet engineering for biomimetic material synthesis. *Science Advances* **2016,** *2* (10).

101. Baret, J. C.; Miller, O. J.; Taly, V.; Ryckelynck, M.; El-Harrak, A.; Frenz, L.; Rick, C.; Samuels, M. L.; Hutchison, J. B.; Agresti, J. J.; Link, D. R.; Weitz, D. A.; Griffiths, A. D., Fluorescence-activated droplet sorting (FADS): efficient microfluidic cell sorting based on enzymatic activity. *Lab on a Chip* **2009,** *9* (13), 1850-8.

102. Ester, M.; Kriegel, H.-P.; Sander, J.; Xu, X. In *A density-based algorithm for discovering clusters in large spatial databases with noise*, Kdd, Portland, OR, AAAI Press: Portland, OR, 1996; pp 226-231.

103. Lim, S. W.; Tran, T. M.; Abate, A. R., PCR-Activated Cell Sorting for Cultivation-Free Enrichment and Sequencing of Rare Microbes. *PloS one* **2015,** *10* (1), e0113549.

104. Zhang, H.; Cockrell, S. K.; Kolawole, A. O.; Rotem, A.; Serohijos, A. W.; Chang, C. B.; Tao, Y.; Mehoke, T. S.; Han, Y.; Lin, J. S., Isolation and analysis of rare norovirus recombinants from coinfected mice using drop-based microfluidics. *Journal of virology* **2015,** *89* (15), 7722-7734.

105. Tao, Y.; Rotem, A.; Zhang, H.; Cockrell, S. K.; Koehler, S. A.; Chang, C. B.; Ung, L. W.; Cantalupo, P. G.; Ren, Y.; Lin, J. S. J. C., Artifact-free quantification and sequencing of rare recombinant viruses by using drop-based microfluidics. *ChemBioChem* **2015,** *16* (15), 2167-2171.

106. Cubaud, T.; Mason, T. G., Capillary threads and viscous droplets in square microchannels. *Physics of Fluids* **2008,** *20* (5), 053302.

107. Tice, J. D.; Lyon, A. D.; Ismagilov, R. F., Effects of viscosity on droplet formation and mixing in microfluidic channels. *Analytica chimica acta* **2004,** *507* (1), 73-77.

108. Funfschilling, D.; Debas, H.; Li, H.-Z.; Mason, T., Flow-field dynamics during droplet formation by dripping in hydrodynamic-focusing microfluidics. *Physical Review E* **2009,** *80* (1), 015301.

109. Garstecki, P.; Stone, H. A.; Whitesides, G. M., Mechanism for flow-rate controlled breakup in confined geometries: A route to monodisperse emulsions. *Physical review letters* **2005,** *94* (16), 164501.

110. Garstecki, P.; Fuerstman, M. J.; Stone, H. A.; Whitesides, G. M., Formation of droplets and bubbles in a microfluidic T-junction—scaling and mechanism of break-up. *Lab on a Chip* **2006,** *6* (3), 437-446.

111. Abate, A.; Poitzsch, A.; Hwang, Y.; Lee, J.; Czerwinska, J.; Weitz, D., Impact of inlet channel geometry on microfluidic drop formation. *Physical Review E* **2009,** *80* (2), 026310.

112. Huebner, A.; Srisa-Art, M.; Holt, D.; Abell, C.; Hollfelder, F.; Demello, A.; Edel, J. J. C. c., Quantitative detection of protein expression in single cells using droplet microfluidics. *Chemical communications* **2007,** (12), 1218-1220.

113. McClain, R. L.; Wright, J. C., Description of the role of shot noise in spectroscopic absorption and emission measurements with photodiode and photomultiplier tube detectors: information for an instrumental analysis course. *Journal of Chemical Education* **2014,** *91* (9), 1455-1457.

114. Schottky, W., Über spontane Stromschwankungen in verschiedenen Elektrizitätsleitern. *Annalen der physik* **1918,** *362* (23), 541-567.

115. Nguyen, H. Q.; Baxter, B. C.; Brower, K.; Diaz-Botia, C. A.; DeRisi, J. L.; Fordyce, P. M.; Thorn, K. S., Programmable microfluidic synthesis of over one thousand uniquely identifiable spectral codes. *Advanced optical materials* **2017,** *5* (3), 1600548.

116. Han, M.; Gao, X.; Su, J. Z.; Nie, S., Quantum-dot-tagged microbeads for multiplexed optical coding of biomolecules. *Nature biotechnology* **2001,** *19* (7), 631.

117. Lee, H.; Kim, J.; Kim, H.; Kim, J.; Kwon, S., Colour-barcoded magnetic microparticles for multiplexed bioassays. *Nature materials* **2010,** *9* (9), 745-749.

118. He, X.; Lau, E. H. Y.; Wu, P.; Deng, X. L.; Wang, J. A.; Hao, X. X.; Lau, Y. C.; Wong, J. Y.; Guan, Y. J.; Tan, X. H.; Mo, X. N.; Chen, Y. Q.; Liao, B. L.; Chen, W. L.; Hu, F. Y.; Zhang, Q.; Zhong, M. Q.; Wu, Y. R.; Zhao, L. Z.; Zhang, F. C.; Cowling, B. J.; Li, F.; Leung, G. M., Temporal dynamics in viral shedding and transmissibility of COVID-19. *Nat. Med.* **2020,** *26* (5), 672-675.

119. Furukawa, N.; Brooks, J.; Sobel, J., Evidence supporting transmission of severe acute respiratory syndrome coronavirus 2 while presymptomatic or asymptomatic. *Emerg. Infect. Dis.* **2020,** *26* (7), e1-e6.

120. Maignan, M.; Viglino, D.; Hablot, M.; Masson, N. T.; Lebeugle, A.; Muret, R. C.; Makele, P. M.; Guglielmetti, V.; Morand, P.; Lupo, J.; Forget, V.; Landelle, C.; Larrat, S., Diagnostic accuracy of a rapid RT-PCR assay for point-of-care detection of influenza A/B virus at emergency department admission: A prospective evaluation during the 2017/2018 influenza season. *PLoS One* **2019,** *14* (5), 1-12.

121. Pfefferle, S.; Reucher, S.; Norz, D.; Lutgehetmann, M., Evaluation of a quantitative RT-PCR assay for the detection of the emerging coronavirus SARS-CoV-2 using a high throughput system. *Euro Surveill.* **2020,** *25* (9), 18-22.

122. Thirion, L.; Dubot-Peres, A.; Pezzi, L.; Corcostegui, I.; Touinssi, M.; de Lamballerie, X.; Charrel, R. N., Lyophilized matrix containing ready-to-use primers and probe solution for standardization of real-time PCR and RT-qPCR diagnostics in virology. *Viruses-Basel* **2020,** *12* (2), 1-13.

123. Mackay, I. M.; Arden, K. E.; Nitsche, A., Real-time PCR in virology. *Nucleic Acids Res.* **2002,** *30* (6), 1292-1305.

124. Clementi, M.; Menzo, S.; Bagnarelli, P.; Manzin, A.; Valenza, A.; Varaldo, P. E., Quantitative PCR and RT-PCR in virology. *PCR Methods Appl.* **1993,** *2* (3), 191-196.

125. Hindson, B. J.; Ness, K. D.; Masquelier, D. A.; Belgrader, P.; Heredia, N. J.; Makarewicz, A. J.; Bright, I. J.; Lucero, M. Y.; Hiddessen, A. L.; Legler, T. C.; Kitano, T. K.; Hodel, M. R.; Petersen, J. F.; Wyatt, P. W.; Steenblock, E. R.; Shah, P. H.; Bousse, L. J.; Troup, C. B.; Mellen, J. C.; Wittmann, D. K.; Erndt, N. G.; Cauley, T. H.; Koehler, R. T.; So, A. P.; Dube, S.; Rose, K. A.; Montesclaros, L.; Wang, S.; Stumbo, D. P.; Hodges, S. P.; Romine, S.; Milanovich, F. P.; White, H. E.; Regan, J. F.; Karlin-Neumann, G. A.; Hindson, C. M.; Saxonov, S.; Colston, B. W., High-throughput droplet digital PCR system for absolute quantitation of DNA copy number. *Analytical Chemistry* **2011,** *83* (22), 8604-8610.

126. Beer, N. R.; Wheeler, E. K.; Lee-Houghton, L.; Watkins, N.; Nasarabadi, S.; Hebert, N.; Leung, P.; Arnold, D. W.; Bailey, C. G.; Colston, B. W., On-chip single-copy real-time reverse-transcription PCR in isolated picoliter droplets. *Anal Chem* **2008,** *80* (6), 1854-1858.

127. Kiss, M. M.; Ortoleva-Donnelly, L.; Beer, N. R.; Warner, J.; Bailey, C. G.; Colston, B. W.; Rothberg, J. M.; Link, D. R.; Leamon, J. H., High-throughput quantitative polymerase chain reaction in picoliter droplets. *Anal Chem* **2008,** *80* (23), 8975-8981.

128. Kim, S. C.; Clark, I. C.; Shahi, P.; Abate, A. R., Single-cell RT-PCR in microfluidic droplets with integrated chemical lysis. *Anal Chem* **2018,** *90* (2), 1273-1279.

129. Hopken, M. W.; Piaggio, A. J.; Pabilonia, K. L.; Pierce, J.; Anderson, T.; Abdo, Z., Predicting whole genome sequencing success for archived avian influenza virus (Orthomyxoviridae) samples using real-time and droplet PCRs. *J. Virol. Methods* **2020,** *276*, 113777.

130. Prakash, R.; Pabbaraju, K.; Wong, S.; Wong, A.; Tellier, R.; Kaler, K. V. I. S., Droplet microfluidic chip based nucleic acid amplification and real-time detection of influenza viruses. *Journal of the Electrochemical Society* **2014,** *161* (2), B3083-B3093.

131. Basu, A. S., Digital assays part I: Partitioning statistics and digital PCR. *SLAS Technol.* **2017,** *22* (4), 369-386.

132. Gruner, P.; Riechers, B.; Semin, B.; Lim, J.; Johnston, A.; Short, K.; Baret, J. C., Controlling molecular transport in minimal emulsions. *Nat. Commun.* **2016,** *7*, 10392.

133. Skhiri, Y.; Gruner, P.; Semin, B.; Brosseau, Q.; Pekin, D.; Mazutis, L.; Goust, V.; Kleinschmidt, F.; El Harrak, A.; Hutchison, J. B., Dynamics of molecular transport by surfactants in emulsions. *Soft Matter* **2012,** *8* (41), 10618-10627.

134. Rane, T. D.; Chen, L.; Zec, H. C.; Wang, T. H., Microfluidic continuous flow digital loop-mediated isothermal amplification (LAMP). *Lab Chip* **2015,** *15* (3), 776-782.

135. Labanieh, L.; Nguyen, T. N.; Zhao, W. A.; Kang, D. K., Floating droplet array: An ultrahigh-throughput device for droplet trapping, real-time analysis and recovery. *Micromachines* **2015,** *6* (10), 1469-1482.

136. Pompano, R. R.; Liu, W. S.; Du, W. B.; Ismagilov, R. F., Microfluidics using spatially defined arrays of droplets in one, two, and three dimensions. *Annu. Rev. Anal. Chem.* **2011,** *4*, 59-81.

137. Nakano, M.; Komatsu, J.; Matsuura, S.; Takashima, K.; Katsura, S.; Mizuno, A., Single-molecule PCR using water-in-oil emulsion. *J. Biotechnol.* **2003,** *102* (2), 117-124.

138. Zhang, F.; Liao, P.; Sun, Y.; Chen, Z.; Pang, Y.; Huang, Y., Surfactant and Oil Formulations for Monodisperse Droplet Emulsion PCR. *Lab Chip* **2020,** *20*, 2328-2333.

139. Shu, B.; Wu, K. H.; Emery, S.; Villanueva, J.; Johnson, R.; Guthrie, E.; Berman, L.; Warnes, C.; Barnes, N.; Klimov, A.; Lindstrom, S., Design and performance of the CDC real-time reverse transcriptase PCR swine flu panel for detection of 2009 A (H1N1) pandemic influenza virus. *J Clin Microbiol* **2011,** *49* (7), 2614-9.

140. Piorkowski, G.; Baronti, C.; de Lamballerie, X.; de Fabritus, L.; Bichaud, L.; Pastorino, B. A.; Bessaud, M., Development of generic Taqman PCR and RT-PCR assays for the detection of DNA and mRNA of beta-actin-encoding sequences in a wide range of animal species. *J. Virol. Methods* **2014,** *202*, 101-105.

141. Spackman, E.; Senne, D. A.; Myers, T. J.; Bulaga, L. L.; Garber, L. P.; Perdue, M. L.; Lohman, K.; Daum, L. T.; Suarez, D. L., Development of a real-time reverse transcriptase PCR assay for type A influenza virus and the avian H5 and H7 hemagglutinin subtypes. *Journal of Clinical Microbiology* **2002,** *40* (9), 3256-3260.

142. Otsu, N., A threshold selection method from gray-level histograms. *IEEE Trans. Syst. Man Cybern. Syst.* **1979,** *9* (1), 62-66.

143. Weingartl, H. M.; Berhane, Y.; Hisanaga, T.; Neufeld, J.; Kehler, H.; Emburry-Hyatt, C.; Hooper-McGreevy, K.; Kasloff, S.; Dalman, B.; Bystrom, J.; Alexandersen, S.; Li, Y.; Pasick, J., Genetic and pathobiologic characterization of pandemic H1N1 2009 influenza viruses from a naturally infected swine herd. *J. Virol.* **2010,** *84* (5), 2245-2256.

144. Lan, F.; Haliburton, J. R.; Yuan, A.; Abate, A. R., Droplet barcoding for massively parallel single-molecule deep sequencing. *Nat. Commun.* **2016,** *7*, 11784.

145. Azizi, M.; Zaferani, M.; Cheong, S. H.; Abbaspourrad, A., Pathogenic bacteria detection using RNA-Based loop-mediated isothermal-amplification-assisted nucleic acid amplification via droplet microfluidics. *ACS Sens.* **2019,** *4* (4), 841-848.

146. Zhang, H. D.; Cockrell, S. K.; Kolawole, A. O.; Rotem, A.; Serohijos, A. W. R.; Chang, C. B.; Tao, Y.; Mehoke, T. S.; Han, Y. L.; Lin, J. S.; Giacobbi, N. S.; Feldman, A. B.; Shakhnovich, E.; Weitz, D. A.; Wobus, C. E.; Pipas, J. M., Isolation and analysis of rare norovirus recombinants from coinfected mice using drop-based microfluidics. *J. Virol.* **2015,** *89* (15), 7722-7734.

147. Kothekar, S. C.; Ware, A. M.; Waghmare, J. T.; Momin, S. A., Comparative analysis of the properties of Tween-20, Tween-60, Tween-80, Arlacel-60, and Arlacel-80. *J. Dispers. Sci. Technol.* **2007,** *28* (3), 477-484.

148. Takei, F.; Akiyama, M.; Nobusawa, K.; Sabani, N. B.; Han, H. W.; Nakatani, K.; Yamashita, I., PCR under low ionic concentration buffer conditions. *ChemistrySelect* **2018,** *3* (3), 973-976.

149. Sasaki, Y.; Miyoshi, D.; Sugimoto, N., Effect of molecular crowding on DNA polymerase activity. *Biotechnol. J.* **2006,** *1* (4), 440-446.

150. Tong, Y.; Lemieux, B.; Kong, H., Multiple strategies to improve sensitivity, speed and robustness of isothermal nucleic acid amplification for rapid pathogen detection. *BMC Biotechnol.* **2011,** *11*, 50.

151. Farell, E. M.; Alexandre, G., Bovine serum albumin further enhances the effects of organic solvents on increased yield of polymerase chain reaction of GC-Rich templates. *BMC Res. Notes* **2012,** *5*, 257.

152. Zhang, Z.; Yang, X.; Meng, L.; Liu, F.; Shen, C.; Yang, W., Enhanced amplification of GC-Rich DNA with two organic reagents. *Biotechniques* **2009,** *47* (3), 775-779.

153. Henke, W.; Herdel, K.; Jung, K.; Schnorr, D.; Loening, S. A., Betaine improves the PCR amplification of GC-Rich DNA sequences. *Nucleic Acids Res.* **1997,** *25* (19), 3957-3958.

154. Hoffmann, E.; Stech, J.; Guan, Y.; Webster, R. G.; Perez, D. R., Universal primer set for the full-length amplification of all influenza A viruses. *Arch. Virol.* **2001,** *146* (12), 2275-2289.

155. Pfaffl, M. W., Quantification strategies in real-time PCR. In *A-Z of Quantitative PCR*, Bustin, S. A., Ed. IUL Press: 2004; pp 87-112.

156. Kubista, M.; Andrade, J. M.; Bengtsson, M.; Forootan, A.; Jonák, J.; Lind, K.; Sindelka, R.; Sjöback, R.; Sjögreen, B.; Strömbom, L., The real-time polymerase chain reaction. *Mol. Aspects Med.* **2006,** *27* (2-3), 95-125.

157. Mazutis, L.; Gilbert, J.; Ung, W. L.; Weitz, D. A.; Griffiths, A. D.; Heyman, J. A., Single-cell analysis and sorting using droplet-based microfluidics. *Nat. Protoc.* **2013,** *8* (5), 870-891.

158. Li, L.; Yu, L.; Wu, T. In *Direct PCR amplification and in situ imaging based on alginate droplets*, 2017 IEEE 30th International Conference on Micro Electro Mechanical Systems (MEMS), 22-26 Jan. 2017; 2017; pp 1252-1255.

159. Yin, K.; Zeng, X.; Liu, W. Z.; Xue, Y. K.; Li, X. R.; Wang, W.; Song, Y. L.; Zhu, Z.; Yang, C. Y., Stable colloidosomes formed by self-assembly of colloidal surfactant for highly robust digital PCR. *Anal. Chem.* **2019,** *91* (9), 6003-6011.

160. Pratt, S. L.; Zath, G. K.; Akiyama, T.; Williamson, K. S.; Franklin, M. J.; Chang, C. B., DropSOAC: Stabilizing microfluidic drops for time-lapse quantification of single-cell bacterial physiology. *Front. Microbiol.* **2019,** *10*, 2112.

161. Akiyama, T.; Williamson, K. S.; Schaefer, R.; Pratt, S.; Chang, C. B.; Franklin, M. J., Resuscitation of *Pseudomonas aeruginosa* from dormancy requires hibernation promoting factor (PA4463) for ribosome preservation. *Proc. Natl. Acad. Sci. U. S. A.* **2017,** *114* (12), 3204-3209.

162. Fischer, A. E.; Wu, S. K.; Proescher, J. B. G.; Rotem, A.; Chang, C. B.; Zhang, H. D.; Tao, Y.; Mehoke, T. S.; Thielen, P. M.; Kolawole, A. O.; Smith, T. J.; Wobus, C. E.; Weitz, D. A.; Lin, J. S.; Feldman, A. B.; Wolfe, J. T., A high-throughput drop microfluidic system for virus culture and analysis. *J. Virol. Methods* **2015,** *213*, 111-117.

163. Heldt, F. S.; Kupke, S. Y.; Dorl, S.; Reichl, U.; Frensing, T., Single-cell analysis and stochastic modelling unveil large cell-to-cell variability in influenza A virus infection. *Nature Communications* **2015,** *6* (1), 8938.

164. Fomsgaard, A. S.; Rosenstierne, M. W., An alternative workflow for molecular detection of SARS-CoV-2-escape from the NA extraction kit-shortage, Copenhagen, Denmark, March 2020. *Euro Surveill.* **2020,** *25* (14), 6-9.

165. Hayden, R.; Gu, Z.; Sam, S.; Sun, Y.; Tang, L.; Pounds, S.; Caliendo, A., Comparative evaluation of three commercial quantitative cytomegalovirus standards by use of digital and real-time PCR. *Journal of clinical microbiology* **2015,** *53* (5), 1500-1505.

166. Quan, P.-L.; Sauzade, M.; Brouzes, E., dPCR: a technology review. *Sensors* **2018,** *18* (4), 1271.

167. Hindson, B. J.; Ness, K. D.; Masquelier, D. A.; Belgrader, P.; Heredia, N. J.; Makarewicz, A. J.; Bright, I. J.; Lucero, M. Y.; Hiddessen, A. L.; Legler, T. C.; Kitano, T. K.; Hodel, M. R.; Petersen, J. F.; Wyatt, P. W.; Steenblock, E. R.; Shah, P. H.; Bousse, L. J.; Troup, C. B.; Mellen, J. C.; Wittmann, D. K.; Erndt, N. G.; Cauley, T. H.; Koehler, R. T.; So, A. P.; Dube, S.; Rose, K. A.; Montesclaros, L.; Wang, S.; Stumbo, D. P.; Hodges, S. P.; Romine, S.; Milanovich, F. P.; White, H. E.; Regan, J. F.; Karlin-Neumann, G. A.; Hindson, C. M.; Saxonov, S.; Colston, B. W., High-throughput droplet digital PCR system for absolute quantitation of DNA copy number. *Anal Chem* **2011,** *83* (22), 8604-10.

168. Hatch, A. C.; Ray, T.; Lintecum, K.; Youngbull, C. J. L. o. a. C., Continuous flow real-time PCR device using multi-channel fluorescence excitation and detection. **2014,** *14* (3), 562-568.

169. Hayes, C. J.; Dalton, T. M. J. B. d.; quantification, Microfluidic droplet-based PCR instrumentation for high-throughput gene expression profiling and biomarker discovery. **2015,** *4*, 22-32.

170. Panina, Y.; Germond, A.; David, B. G.; Watanabe, T. M. J. B. b., Pairwise efficiency: a new mathematical approach to qPCR data analysis increases the precision of the calibration curve assay. **2019,** *20* (1), 1-12.

171. Ramakers, C.; Ruijter, J. M.; Deprez, R. H. L.; Moorman, A. F. J. N. l., Assumption-free analysis of quantitative real-time polymerase chain reaction (PCR) data. **2003,** *339* (1), 62-66.

172. Peirson, S. N.; Butler, J. N.; Foster, R. G. J. N. a. r., Experimental validation of novel and conventional approaches to quantitative real-time PCR data analysis. **2003,** *31* (14), e73-e73.

173. Rutledge, R. J. N. a. r., Sigmoidal curve-fitting redefines quantitative real-time PCR with the prospective of developing automated high-throughput applications. **2004,** *32* (22), e178-e178.

174. Spiess, A.-N.; Feig, C.; Ritz, C. J. B. b., Highly accurate sigmoidal fitting of real-time PCR data by introducing a parameter for asymmetry. **2008,** *9* (1), 221.

175. Tellinghuisen, J.; Spiess, A.-N. J. B. d.; quantification, qPCR data analysis: better results through iconoclasm. **2019,** *17*, 100084.

176. Mazutis, L.; Gilbert, J.; Ung, W. L.; Weitz, D. A.; Griffiths, A. D.; Heyman, J. A., Single-cell analysis and sorting using droplet-based microfluidics. *Nat Protoc* **2013,** *8* (5), 870-91.

177. Ruijter, J. M.; Pfaffl, M. W.; Zhao, S.; Spiess, A. N.; Boggy, G.; Blom, J.; Rutledge, R. G.; Sisti, D.; Lievens, A.; De Preter, K. J. M., Evaluation of qPCR curve analysis methods for reliable biomarker discovery: bias, resolution, precision, and implications. **2013,** *59* (1), 32-46.

178. Lievens, A.; Van Aelst, S.; Van den Bulcke, M.; Goetghebeur, E. J. N. a. r., Enhanced analysis of real-time PCR data by using a variable efficiency model: FPK-PCR. **2012,** *40* (2), e10-e10.

179. Batsch, A.; Noetel, A.; Fork, C.; Urban, A.; Lazic, D.; Lucas, T.; Pietsch, J.; Lazar, A.; Schömig, E.; Gründemann, D. J. B. b., Simultaneous fitting of real-time PCR data with efficiency of amplification modeled as Gaussian function of target fluorescence. **2008,** *9* (1), 95.

180. Alvarez, M. J.; Vila-Ortiz, G. J.; Salibe, M. C.; Podhajcer, O. L.; Pitossi, F. J. J. B. b., Model based analysis of real-time PCR data from DNA binding dye protocols. **2007,** *8* (1), 85.

181. Eastburn, D. J.; Sciambi, A.; Abate, A. R. J. A. c., Ultrahigh-throughput Mammalian single-cell reverse-transcriptase polymerase chain reaction in microfluidic drops. **2013,** *85* (16), 8016-8021.

182. Tao, Y.; Rotem, A.; Zhang, H.; Chang, C. B.; Basu, A.; Kolawole, A. O.; Koehler, S. A.; Ren, Y.; Lin, J. S.; Pipas, J. M. J. L. o. a. c., Rapid, targeted and culture-free viral infectivity assay in drop-based microfluidics. **2015,** *15* (19), 3934-3940.

183. Krammer, F.; Smith, G. J. D.; Fouchier, R. A. M.; Peiris, M.; Kedzierska, K.; Doherty, P. C.; Palese, P.; Shaw, M. L.; Treanor, J.; Webster, R. G.; Garcia-Sastre, A., Influenza. *Nat Rev Dis Primers* **2018,** *4* (1), 3.

184. Dolan, P. T.; Whitfield, Z. J.; Andino, R., Mapping the Evolutionary Potential of RNA Viruses. *Cell Host & Microbe* **2018,** *23* (4), 435-446.

185. Brooke, C. B., Population diversity and collective interactions during influenza virus infection. *Journal of virology* **2017,** *91* (22), e01164-17.

186. Schulte, M. B.; Andino, R., Single-cell analysis uncovers extensive biological noise in poliovirus replication. *Journal of virology* **2014,** *88* (11), 6205-6212.

187. Heldt, F. S.; Kupke, S. Y.; Dorl, S.; Reichl, U.; Frensing, T. J. N. c., Single-cell analysis and stochastic modelling unveil large cell-to-cell variability in influenza A virus infection. **2015,** *6* (1), 1-12.

188. Kupke, S. Y.; Ly, L.-H.; Börno, S. T.; Ruff, A.; Timmermann, B.; Vingron, M.; Haas, S.; Reichl, U. J. V., Single-Cell Analysis Uncovers a Vast Diversity in Intracellular Viral Defective Interfering RNA Content Affecting the Large Cell-to-Cell Heterogeneity in Influenza A Virus Replication. **2020,** *12* (1), 71.

189. Sun, J.; Vera, J. C.; Drnevich, J.; Lin, Y. T.; Ke, R.; Brooke, C. B. J. P. p., Single cell heterogeneity in influenza A virus gene expression shapes the innate antiviral response to infection. **2020,** *16* (7), e1008671.

190. Russell, A. B.; Trapnell, C.; Bloom, J. D. J. E., Extreme heterogeneity of influenza virus infection in single cells. **2018,** *7*, e32303.

191. Zhu, Y.; Yongky, A.; Yin, J., Growth of an RNA virus in single cells reveals a broad fitness distribution. *Virology* **2009,** *385* (1), 39-46.

192. Brooke, C. B.; Ince, W. L.; Wrammert, J.; Ahmed, R.; Wilson, P. C.; Bennink, J. R.; Yewdell, J. W. J. J. o. v., Most influenza a virions fail to express at least one essential viral protein. **2013,** *87* (6), 3155-3162.

193. Delbrück, M., The burst size distribution in the growth of bacterial viruses (bacteriophages). *Journal of bacteriology* **1945,** *50* (2), 131.

194. Cummings, K. W.; Levy, D. N.; Wodarz, D., Increased burst size in multiply infected cells can alter basic virus dynamics. *Biology direct* **2012,** *7* (1), 16.

195. Ke, R.; Lewin, S. R.; Elliott, J. H.; Perelson, A. S., Modeling the effects of vorinostat in vivo reveals both transient and delayed HIV transcriptional activation and minimal killing of latently infected cells. *PLoS pathogens* **2015,** *11* (10).

196. Pawelek, K. A.; Huynh, G. T.; Quinlivan, M.; Cullinane, A.; Rong, L.; Perelson, A. S., Modeling within-host dynamics of influenza virus infection including immune responses. *PLoS computational biology* **2012,** *8* (6).

197. Tao, Y.; Rotem, A.; Zhang, H.; Chang, C. B.; Basu, A.; Kolawole, A. O.; koehler, S.; Ren, Y.; Lin, J. S.; Pipas, J. M.; Feldman, A. B.; Wobus, C.; Weitz, D. A., Rapid, targeted and culture-free viral infectivity assay in drop-based microfluidics. *Lab on a Chip* **2015**.

198. Gini, C. J. R. i. M. d. m. s., Variabilità e mutabilità. **1912**.

199. Stray, S. J.; Air, G. M., Apoptosis by influenza viruses correlates with efficiency of viral mRNA synthesis. *Virus research* **2001,** *77* (1), 3-17.

200. Pinilla, L. T.; Holder, B. P.; Abed, Y.; Boivin, G.; Beauchemin, C. A. J. J. o. v., The H275Y neuraminidase mutation of the pandemic A/H1N1 influenza virus lengthens the eclipse phase and reduces viral output of infected cells, potentially compromising fitness in ferrets. **2012,** *86* (19), 10651-10660.

201. Weingartl, H. M.; Berhane, Y.; Hisanaga, T.; Neufeld, J.; Kehler, H.; Emburry-Hyatt, C.; Hooper-McGreevy, K.; Kasloff, S.; Dalman, B.; Bystrom, J.; Alexandersen, S.; Li, Y.; Pasick, J., Genetic and pathobiologic characterization of pandemic H1N1 2009 influenza viruses from a naturally infected swine herd. *J. Virol.* **2010,** *84* (5), 2245-56.

202. Huang, A. S.; Baltimore, D., Defective viral particles and viral disease processes. *Nature* **1970,** *226* (5243), 325.

203. Perrault, J., Origin and Replication of Defective Interfering Particles. In *Initiation Signals in Viral Gene Expression*, Shatkin, A. J., Ed. Springer Berlin Heidelberg: Berlin, Heidelberg, 1981; pp 151-207.

204. Lim, S. W.; Tran, T. M.; Abate, A. R. J. P. o., PCR-activated cell sorting for cultivation-free enrichment and sequencing of rare microbes. **2015,** *10* (1), e0113549.

205. Russell, A. B.; Elshina, E.; Kowalsky, J. R.; Te Velthuis, A. J.; Bloom, J. D. J. J. o. v., Single-cell virus sequencing of influenza infections that trigger innate immunity. **2019,** *93* (14).

206. Hamamatsu Specification sheet for H10723-20 photomultiplier tube. https://www.hamamatsu.com/resources/pdf/etd/H10723_TPMO1064E.pdf.

207. Schindelin, J.; Rueden, C. T.; Hiner, M. C.; Eliceiri, K. W., The ImageJ ecosystem: An open platform for biomedical image analysis. *Mol. Reprod. Dev.* **2015,** *82* (7-8), 518-29.

208. Mazutis, L.; Gilbert, J.; Ung, W. L.; Weitz, D. A.; Griffiths, A. D.; Heyman, J. A. J. N. p., Single-cell analysis and sorting using droplet-based microfluidics. **2013,** *8* (5), 870-891.

209. Schindelin, J.; Arganda-Carreras, I.; Frise, E.; Kaynig, V.; Longair, M.; Pietzsch, T.; Preibisch, S.; Rueden, C.; Saalfeld, S.; Schmid, B., Fiji: an open-source platform for biological-image analysis. *Nature methods* **2012,** *9* (7), 676.

210. Rueden, C. T.; Schindelin, J.; Hiner, M. C.; DeZonia, B. E.; Walter, A. E.; Arena, E. T.; Eliceiri, K. W., ImageJ2: ImageJ for the next generation of scientific image data. *BMC bioinformatics* **2017,** *18* (1), 529.

211. Tinevez, J.-Y.; Perry, N.; Schindelin, J.; Hoopes, G. M.; Reynolds, G. D.; Laplantine, E.; Bednarek, S. Y.; Shorte, S. L.; Eliceiri, K. W., TrackMate: An open and extensible platform for single-particle tracking. *Methods* **2017,** *115*, 80-90.

212. Akiyama, T.; Williamson, K. S.; Schaefer, R.; Pratt, S.; Chang, C. B.; Franklin, M. J., Resuscitation of Pseudomonas aeruginosa from dormancy requires hibernation promoting factor (PA4463) for ribosome preservation. *Proceedings of the National Academy of Sciences* **2017,** *114* (12), 3204-3209.

213. Atherton, T. J.; Kerbyson, D. J. J. I.; computing, V., Size invariant circle detection. **1999,** *17* (11), 795-803.

214. Thompson, W. W.; Weintraub, E.; Dhankhar, P.; Cheng, P. Y.; Brammer, L.; Meltzer, M. I.; Bresee, J. S.; Shay, D. K., Estimates of US influenza-associated deaths made using four different methods. *Influenza and other respiratory viruses* **2009,** *3* (1), 37-49.

215. Nair, H.; Brooks, W. A.; Katz, M.; Roca, A.; Berkley, J. A.; Madhi, S. A.; Simmerman, J. M.; Gordon, A.; Sato, M.; Howie, S., Global burden of respiratory infections due to seasonal

influenza in young children: a systematic review and meta-analysis. *The Lancet* **2011,** *378* (9807), 1917-1930.

216. Kirkwood, T. B.; Bangham, C. R., Cycles, chaos, and evolution in virus cultures: a model of defective interfering particles. *Proceedings of the National Academy of Sciences* **1994,** *91* (18), 8685-8689.

217. Guo, M. T.; Rotem, A.; Heyman, J. A.; Weitz, D. A., Droplet microfluidics for high-throughput biological assays. *Lab Chip* **2012,** *12* (12), 2146-55.

218. Rakszewska, A.; Tel, J.; Chokkalingam, V.; Huck, W. T. S., One drop at a time: toward droplet microfluidics as a versatile tool for single-cell analysis. *NPG Asia Materials* **2014,** *6* (10), e133.

219. Akiyama, T.; Williamson, K. S.; Schaefer, R.; Pratt, S.; Chang, C. B.; Franklin, M. J., Resuscitation of Pseudomonas aeruginosa from dormancy requires hibernation promoting factor (PA4463) for ribosome preservation. *Proceedings of the National Academy of Sciences* **2017**.

220. Hatch, A. C.; Fisher, J. S.; Tovar, A. R.; Hsieh, A. T.; Lin, R.; Pentoney, S. L.; Yang, D. L.; Lee, A. P., 1-Million droplet array with wide-field fluorescence imaging for digital PCR. *Lab Chip* **2011,** *11* (22), 3838-45.

221. Prakash, R.; Pabbaraju, K.; Wong, S.; Wong, A.; Tellier, R.; Kaler, K., Multiplex, Quantitative, Reverse Transcription PCR Detection of Influenza Viruses Using Droplet Microfluidic Technology. *Micromachines* **2014,** *6* (12), 63-79.

222. Zhang, Y.; Jiang, H. R., A review on continuous-flow microfluidic PCR in droplets: Advances, challenges and future. *Anal Chim Acta* **2016,** *914*, 7-16.

223. Tanaka, H.; Yamamoto, S.; Nakamura, A.; Nakashoji, Y.; Okura, N.; Nakamoto, N.; Tsukagoshi, K.; Hashimoto, M., Hands-off preparation of monodisperse emulsion droplets using a poly(dimethylsiloxane) microfluidic chip for droplet digital PCR. *Anal Chem* **2015,** *87* (8), 4134-43.

224. Eastburn, D. J.; Sciambi, A.; Abate, A. R., Ultrahigh-throughput Mammalian single-cell reverse-transcriptase polymerase chain reaction in microfluidic drops. *Anal Chem* **2013,** *85* (16), 8016-21.

225. Prakash, R.; Pabbaraju, K.; Wong, S.; Wong, A.; Tellier, R.; Kaler, K. V. I. S., Droplet Microfluidic Chip Based Nucleic Acid Amplification and Real-Time Detection of Influenza Viruses. *Journal of the Electrochemical Society* **2013,** *161* (2), B3083-B3093.

226. Sciambi, A.; Abate, A. R., Accurate microfluidic sorting of droplets at 30 kHz. *Lab Chip* **2015,** *15* (1), 47-51.

227. Clark, I. C.; Thakur, R.; Abate, A. R., Concentric electrodes improve microfluidic droplet sorting. *Lab Chip* **2018**.

228. Liu, L.; Loutherback, K.; Liao, D.; Yeater, D.; Lambert, G.; Estevez-Torres, A.; Sturm, J. C.; Getzenberg, R. H.; Austin, R. H., A microfluidic device for continuous cancer cell culture and passage with hydrodynamic forces. *Lab Chip* **2010,** *10* (14), 1807-13.

229. Fischer, A. E.; Wu, S. K.; Proescher, J. B.; Rotem, A.; Chang, C. B.; Zhang, H.; Tao, Y.; Mehoke, T. S.; Thielen, P. M.; Kolawole, A. O.; Smith, T. J.; Wobus, C. E.; Weitz, D. A.; Lin, J. S.; Feldman, A. B.; Wolfe, J. T., A high-throughput drop microfluidic system for virus culture and analysis. *J Virol Methods* **2015,** *213*, 111-7.

230. Tao, Y.; Rotem, A.; Zhang, H.; Chang, C. B.; Basu, A.; Kolawole, A. O.; Koehler, S. A.; Ren, Y.; Lin, J. S.; Pipas, J. M.; Feldman, A. B.; Wobus, C. E.; Weitz, D. A., Rapid, targeted and culture-free viral infectivity assay in drop-based microfluidics. *Lab Chip* **2015,** *15* (19), 3934-40.

231. Schaerli, Y.; Wootton, R. C.; Robinson, T.; Stein, V.; Dunsby, C.; Neil, M. A. A.; French, P. M. W.; deMello, A. J.; Abell, C.; Hollfelder, F., Continuous-Flow Polymerase Chain Reaction of Single-Copy DNA in Microfluidic Microdroplets. *Analytical Chemistry* **2009,** *81* (1), 302-306.

232. Lu, H.; Caen, O.; Vrignon, J.; Zonta, E.; El Harrak, Z.; Nizard, P.; Baret, J.-C.; Taly, V. J. S. r., High throughput single cell counting in droplet-based microfluidics. **2017,** *7* (1), 1-9.